

AN ABSTRACT OF THE THESIS OF

Bernd D. Schurr for the degree of Master of Science in Geophysics presented on January 7, 1997.

Title: The 1993, Scotts Mills Aftershock Sequence: Moment Tensor Inversion and Joint Hypocenter Determination.

Abstract approved: _____

MS *MS* *MS* *MS* *MS*
Redacted for Privacy

//

JOHN L. HUBBARD

Aftershocks of the moderate 1993, $M_w = 5.5$, Scotts Mills, Oregon, earthquake were well recorded by a dense, temporary array of digital three-component short-period and broadband seismographs. We developed a technique for determining source moment tensors of aftershocks from near-source waveforms. In the narrow 0.5 Hz to 3.0 Hz pass band, local (epicentral distances ≤ 30 km) displacement waveforms are simple, pulse-like P and S arrivals. To determine the moment tensor, we invert vertical P and horizontal S phases in separate windows to allow for independent alignment and weighting. Tests on synthetic and real data show that the method is remarkably robust towards inaccuracies in the Green's functions.

We present focal mechanisms of 41 events with moment magnitude ranging from 1.6 to 3.2. The source mechanisms are highly variable, ranging from pure strike slip to pure thrust. Using P and S arrival times, we relocate the events by simultaneously inverting for all events' hypocentral parameters and station corrections. Even though the fault plane solutions exhibit greatly varying nodal planes, a majority of the events fall on a well defined plane (strike 283° , dip 49°). This plane is broadly consistent with the mainshock mechanism (strike 300° , dip 50° , rake 145°) determined from regional and teleseismic waveforms. Hypocenters are evenly distributed over an area of roughly 20 km^2 , approximately the rupture area inferred from the source duration of the mainshock. The incompatibility of most events' nodal planes with the plane defined by

their locations suggests, however, that the aftershocks did not occur on the fault plane, but tightly around it, outlining the rupture area rather than defining it.

A group of more north-easterly striking thrust events is clearly separated from the major plane. Their clustering and similarity in mechanisms suggests the activation of a secondary fault approximately 3 km north of the main fault plane.

The 34 events defining the major plane revealed stable P-axis orientations while T-axis plunges were variable. We used Gephart's (1990) stress field inversion to obtain principal compressional stress directions. The results indicate a uniform stress field where σ_1 (maximum stress) is oriented $185^\circ/5^\circ$ (azimuth/plunge), and σ_3 (minimum stress) is oriented $278^\circ/29^\circ$. This is in excellent agreement with the regional stress direction. Average T-axis plunges decrease steadily with depth (60° for 11-12 km, 45° for 12-13 km, and 30° for 13-14 km), indicating a change in faulting style from dip-slip to strike-slip mechanisms. This change is probably due to an interchange of intermediate and minimum stress axes at this depth. Applying a Coulomb-Mohr analysis using principal stress directions from the stress inversion, the mainshock exhibits a nearly maximum level of resolved shear stress to normal stress ratio, τ/σ_n , on the north-dipping nodal plane, indicating a high fault strength, whereas the aftershocks all plot below the mainshock τ/σ_n ratio. Many of them have extremely low levels of resolved shear stress on their preferred nodal planes, suggesting low fault strength.

The characteristics of the Scotts Mills aftershock sequence are difficult to explain by remnant stress concentrations on the mainshock rupture plane and popular asperity/barrier-type models. We suggest instead that the aftershocks occurred under an ambient stress, and were triggered by a sudden weakening of the region surrounding the mainshock. For the weakening of the zone adjacent to the slip area we suggest a possible mechanism that is based on dilatancy-diffusion models.

© Copyright by Bernd D. Schurr

January 7, 1997

All Rights Reserved

The 1993, Scotts Mills Aftershock Sequence: Moment Tensor Inversion and Joint
Hypocenter Determination

by

Bernd D. Schurr

A THESIS

submitted to

Oregon State University

in partial fulfillment of
the requirements for the
degree of

Master of Science

Completed January 7, 1997

Commencement June 1997

Master of Science thesis of Bernd Schurr presented on January 7, 1997

APPROVED:

MS
1112
Q
Redacted for Privacy

Major Professor, representing Geophysics

Redacted for Privacy

Dean of the College of Oceanic and Atmospheric Sciences

MS
Redacted for Privacy

Dean of Graduate School

I understand that my thesis will become part of the permanent collection of Oregon State University libraries. My signature below authorizes release of my thesis to any reader upon request.

B
S
Redacted for Privacy

Bernd D. Schurr, Author

ACKNOWLEDGMENTS

This work would not have been possible without the encouragement and enthusiasm of my advisor John Nabelek. He provided me with both freedom and guidance as was necessary to accomplish this work. In addition to his undisputed technical expertise, John has human qualities that are rarely met, I was fortunate to have him as an advisor.

I am also grateful to Drs. Michael Lerner, Anne M. Trehu, and Bob Yeats for reading my thesis and serving on my committee. Drs. Yeats' and Trehu's lectures also contributed significantly to my graduate education.

I want to extend this list with Drs. Dudley Chelton, Y. John Chen, Dave Christie, Gary Egbert, Clayton Paulson, LaVerne Kulm, and Donald Solmon whose classes widened my horizon.

Anne Trehu not only taught me higher-frequency seismology, but also helped me to the invaluable opportunity of spending half a year in the real world of oil, money, and inner city jungle, thank you.

I want to thank Stuart Fagin of Paradigm Geophysical for arousing my interest in exploration seismology and seismic imaging. He was a good advisor in the Texan exile.

Thanks to all the fellow Geophysics students over the years: Albi, Alex, Axel, Beate, Guibiao, Jochen, Kelly, Kurt, Maren, Rugang, Thorsten, Weerachai, and Xiao Qing, your being around, discussions, distractions, and sharing chairs made life much easier. I am particularly grateful to Jochen Braunmiller who patiently answered all my questions; much knowledge contained in this thesis originated from his wise comments and discussions.

From the many friends I shared times and ropes with, I am most grateful to Rachel, Mark, Mitch, Peter, and Tom. With Mitch and Tom, just before finishing this thesis, I shared an adventure that made the prosaic problems of graduate school but a vanishing, hollow echo somewhere behind the stomach.

Thanks to Albrecht for visiting me for a year. Martin and Michael who are still waiting for me to come home. Milena for being in my mind.

My parents, my sister Ulrike, my brothers Rainer and Christof for their uncompromised love that was felt over continents and oceans. Following my being on atlases and globes their love provided a ground without which living in a foreign country would not have been possible.

TABLE OF CONTENTS

1 INTRODUCTION	1
2 MOMENT TENSOR INVERSION OF LOCAL EARTHQUAKE DATA.....	5
2.1 Introduction	5
2.2 Theory	8
2.3 Method	12
2.4 Testing with Synthetic Data	14
2.5 Application to Aftershocks of the 1993 Scotts Mills Earthquake	29
3 EARTHQUAKE LOCATION TECHNIQUES AND THEIR APPLICATION TO THE SCOTTS MILLS AFTERSHOCK SEQUENCE	67
3.1 Single-Event Location.....	67
3.2 Multiple-Event Location	68
3.3 Theoretical basis of JHD.....	70
3.4 Results	75
4 DISCUSSION	84
4.1 Methods	84
4.2 Seismotectonics.....	85
4.3 Stress-Field Considerations.....	90
4.4 Fault Strength Considerations	100
4.5 Implications for Models of Aftershock Generation.....	103
BIBLIOGRAPHY	112
APPENDICES.....	120
Appendix A Observed and Synthetic Waveforms	121
Appendix B Code for Joint Hypocenter Determination	163

LIST OF FIGURES

Figure	Page
2.1.1 Record section of synthetic displacement seismograms at increasing epicentral distances	7
2.3.1 Schematic view of inversion windows.....	13
2.4.1 Velocity model WO94 used to calculate “observed” seismograms.	16
2.4.2 “Observed” and synthetic seismograms for a dip slip source in the two frequency bands: A) 0.5 Hz - 10 Hz, and B) 0.5 Hz - 3 Hz	18
2.4.2 (continued) “Observed” and synthetic seismograms for a strike-slip source in the two frequency bands: C) 0.5 Hz - 10 Hz, and D) 0.5 Hz - 3 Hz	19
2.4.3 “Observed” and synthetic seismograms for a dip-slip source in the two frequency bands: A) 0.5 Hz - 10 Hz, and B) 0.5 Hz - 3 Hz	21
2.4.3 (continued) “Observed” and synthetic seismograms for a strike-slip source in the two frequency bands: C) 0.5 Hz - 10 Hz, and D) 0.5 Hz - 3 Hz	22
2.4.4 “Observed” and synthetic seismograms for a dip-slip source in the two frequency bands: A) 0.5 Hz - 10 Hz, and B) 0.5 Hz - 3 Hz	24
2.4.5 Schematic view of the changed event-receiver geometry (dotted lines) caused by a mislocated epicenter	26
2.4.6 “Observed” and synthetic seismograms for the station geometry sketched in <i>Figure 2.4.5</i> in the frequency band 0.5 Hz - 3 Hz for A) a dip-slip source, and D) a strike-slip source	27
2.5.1 Map of all stations used in this study	32
2.5.2 A trace of station CAL before and after data processing	34
2.5.3 Velocity model used to calculate Green’s functions	36
2.5.4 Modeling of low velocity layers (LVL’s).....	37
2.5.5 Variance of the solution versus low pass cut off for top: event 13, and bottom: event 18	40

LIST OF FIGURES (CONTINUED)

Figure	Page
2.5.6 A) All traces used in the inversion in the 0.7 - 10.0 Hz pass band for event 13.....	42
2.5.6 (continued) B) All traces used in the inversion, in the 0.7 - 5.0 Hz pass band for event 13.....	43
2.5.6 (continued) C) All traces used in the inversion, in the 0.7 - 3.0 Hz pass band for event 13.....	44
2.5.6 (continued) D) All traces used in the inversion, in the 0.7 - 2.0 Hz pass band for event 13.....	45
2.5.7 A) All traces used in the inversion, in the 1.0 - 10.0 Hz pass band for event 18.....	46
2.5.7 (continued) B) All traces used in the inversion, in the 1.0 - 5.0 Hz pass band for event 13.....	47
2.5.7 (continued) C) All traces used in the inversion, in the 1.0 - 3.0 Hz pass band for event 18.....	48
2.5.7 (continued) D) All traces used in the inversion, in the 1.0 - 2.0 Hz pass band for event 18.....	49
2.5.8 Variance versus deviation from the best-fit double couple solution in three frequency bands for A) event 13, and B) event 18.....	51
2.5.9 Top: Location and mechanisms for event 38 and 39. Bottom: Observed seismograms for both events, that show clear distinction in waveforms and amplitudes.	53
2.5.10 Maps showing event (star), station geometry and fault plane solutions for different station distributions for A) event 13, and B) event 18	55
2.5.11 First motion fault plane solutions from Thomas <i>et al.</i> (1996) (left), and the solutions derived in this thesis by waveform modeling (right).....	57
2.5.12 Map of all focal mechanisms determined in this thesis.	63

LIST OF FIGURES (CONTINUED)

Figure	Page
2.5.13 Graph showing moment magnitude estimate versus coda duration magnitude estimate	65
3.4.1 Map of the stations used for <i>JHD</i>	76
3.4.2 Map showing station corrections as circles, with their radii proportional to size of the correction term.....	77
3.4.3 A) Map showing <i>JHD</i> relocations (circles).....	80
3.4.3 B) Right: Vertical cross section along line A, perpendicular to the best-fit plane. Left: Vertical cross section of <i>JHD</i> relocated events.....	81
3.4.4 All 41 relocated earthquakes with focal mechanisms from Chapter 2 (lower-hemisphere, equal area projection).....	83
4.2.1 Three published mainshock mechanisms: Solid - from regional waveforms, dashed - from body waves, and dotted - from first motion polarities.....	86
4.2.2 The Scotts Mills area.....	88
4.2.3 Map of aeromagnetic anomalies in the Northern Willamette Valley (from Blakeley <i>et al.</i> , 1996)	89
4.3.1 Composite plot of P (pressure, filled circles) and T (tension, open circles) axes from all investigated events (lower-hemisphere, equal-area projection)	91
4.3.2 Rose section-diagrams showing the distribution of plunges and azimuths of the pressure (P) and tension (T) axes for the investigated events.....	92
4.3.3 Cross sectional view perpendicular to the best-fit plane (location of the surface projection of this cross-section is shown in Figure 4.2.2)	94
4.3.4 Maximum and minimum stress axes (σ_1 and σ_3) from stress tensors that fall into the 68% and 95% confidence limits (stereo-net projection).....	96
4.3.5 Focal mechanisms are displayed with their plunges graphed versus hypocentral depth	98

LIST OF FIGURES (CONTINUED)

Figure	Page
4.3.6 Rose diagrams of T-axis plunges for three different depth slices	99
4.3.7 Estimates of absolute stresses as a function of depth.....	101
4.4.1 Mohr circles for three stress tensors within the 95% confidence limit	102
4.5.1 The aftershocks investigated in this study projected onto the best-fitting fault plane.....	105
4.5.2 Change in the static stress field predicted by simple Griffith crack.....	107
4.5.3 Synoptic model of fault zone and outline of mechanism for aftershock generation	110

LIST OF TABLES

Table	Page
2.4.1 Station parameters used in synthetic tests	15
2.4.2 Results of Synthetic Testing.....	17
2.5.1 Station parameters	31
2.5.2 Velocity Model.....	35
2.5.3 Source parameters for 41 aftershocks of the 1993, Scotts Mills earthquake.....	59
3.4.1 Station Parameter and Corrections	78
3.4.2 Event Parameters from JHD.....	82
4.3.1 Stress tensor inversion results	95

LIST OF APPENDIX FIGURES

Figure	Page
A.1	Observed (solid lines) and synthetic (dashed lines) seismograms (event 1) 122
A.2	Observed (solid lines) and synthetic (dashed lines) seismograms (event 2) 123
A.3	Observed (solid lines) and synthetic (dashed lines) seismograms (event 3) 124
A.4	Observed (solid lines) and synthetic (dashed lines) seismograms (event 4) 125
A.5	Observed (solid lines) and synthetic (dashed lines) seismograms (event 5) 126
A.6	Observed (solid lines) and synthetic (dashed lines) seismograms (event 6) 127
A.7	Observed (solid lines) and synthetic (dashed lines) seismograms (event 7) 128
A.8	Observed (solid lines) and synthetic (dashed lines) seismograms (event 8) 129
A.9	Observed (solid lines) and synthetic (dashed lines) seismograms (event 9) 130
A.10	Observed (solid lines) and synthetic (dashed lines) seismograms (event 10) 131
A.11	Observed (solid lines) and synthetic (dashed lines) seismograms (event 11) 132
A.12	Observed (solid lines) and synthetic (dashed lines) seismograms (event 12) 133
A.13	Observed (solid lines) and synthetic (dashed lines) seismograms (event 13) 134
A.14	Observed (solid lines) and synthetic (dashed lines) seismograms (event 14) 135
A.15	Observed (solid lines) and synthetic (dashed lines) seismograms (event 15) 136
A.16	Observed (solid lines) and synthetic (dashed lines) seismograms (event 16) 137
A.17	Observed (solid lines) and synthetic (dashed lines) seismograms (event 17) 138
A.18	Observed (solid lines) and synthetic (dashed lines) seismograms (event 18) 139
A.19	Observed (solid lines) and synthetic (dashed lines) seismograms (event 19) 140
A.20	Observed (solid lines) and synthetic (dashed lines) seismograms (event 20) 141
A.21	Observed (solid lines) and synthetic (dashed lines) seismograms (event 21) 142

LIST OF APPENDIX FIGURES (CONTINUED)

Figure	Page
A.22	Observed (solid lines) and synthetic (dashed lines) seismograms (event 22) 143
A.23	Observed (solid lines) and synthetic (dashed lines) seismograms (event 23) 144
A.24	Observed (solid lines) and synthetic (dashed lines) seismograms (event 24) 145
A.25	Observed (solid lines) and synthetic (dashed lines) seismograms (event 25) 146
A.26	Observed (solid lines) and synthetic (dashed lines) seismograms (event 26) 147
A.27	Observed (solid lines) and synthetic (dashed lines) seismograms (event 27) 148
A.28	Observed (solid lines) and synthetic (dashed lines) seismograms (event 28) 149
A.29	Observed (solid lines) and synthetic (dashed lines) seismograms (event 29) 150
A.30	Observed (solid lines) and synthetic (dashed lines) seismograms (event 30) 151
A.31	Observed (solid lines) and synthetic (dashed lines) seismograms (event 31) 152
A.32	Observed (solid lines) and synthetic (dashed lines) seismograms (event 32) 153
A.33	Observed (solid lines) and synthetic (dashed lines) seismograms (event 33) 154
A.34	Observed (solid lines) and synthetic (dashed lines) seismograms (event 34) 155
A.35	Observed (solid lines) and synthetic (dashed lines) seismograms (event 35) 156
A.36	Observed (solid lines) and synthetic (dashed lines) seismograms (event 36) 157
A.37	Observed (solid lines) and synthetic (dashed lines) seismograms (event 37) 158
A.38	Observed (solid lines) and synthetic (dashed lines) seismograms (event 38) 159
A.39	Observed (solid lines) and synthetic (dashed lines) seismograms (event 39) 160
A.40	Observed (solid lines) and synthetic (dashed lines) seismograms (event 40) 161
A.41	Observed (solid lines) and synthetic (dashed lines) seismograms (event 41) 162

LIST OF APPENDIX TABLES

Table	Page
B.1 JHD Input data	163
B.2 JHD Output data.....	164

The 1993, Scotts Mills Aftershock Sequence: Moment Tensor Inversion and Joint Hypocenter Determination

Chapter 1

INTRODUCTION

If we could know in advance when and where an earthquake would occur, we could equip the nominal site with a myriad of instruments, and record dense, high-quality seismic, geodetic, electro-magnetic and other data. These data could then be used to study later in detail this short lived phenomenon. However, despite all efforts from seismologists worldwide, earthquakes are still almost as unforeseeable as they were a hundred years ago. This unpredictability limits the analysis of most earthquakes to dominantly seismic data that are recorded at distant and often sparsely distributed observatories. Yet we know that almost every shallow, tectonic earthquake of any significant size is followed by numerous smaller events, which we call aftershocks. The occurrence of aftershocks is a universally observed phenomena. In fact, they are the only case where we can predict earthquakes with high probability in a spatially and temporally restricted framework, and consequently are able to timely set up arrays of seismic stations to monitor this transient activity. Besides the rewarding possibility of studying earthquakes from a close distance alone, aftershocks also permit inferences on the, typically by at least one magnitude unit bigger (Utsu 1971), mainshock by which they were caused. The geometry of their locations often delineate the mainshock rupture plane, or they cluster at rupture complexities (e.g. Bakun, King, and Cockerham, 1986), but are also observed at locations distinctly different from the mainshock slip area (e.g., Das and Scholz, 1982). Though it seems clear that aftershocks are caused by stress changes in the mainshock rupture enclosing volume, the mechanisms that induce these changes are not completely understood, and are probably as various as the characteristics

of different earthquakes themselves. The extremely diverse aftershock sequence of the Loma Prieta, California earthquake (Oppenheimer, 1990), for example, was incompatible with the customary view of aftershocks being the response to mainshock induced shear stresses; instead Beroza and Zoback (1990) suggested that aftershocks were triggered by a mainshock induced decrease in shear strength of the fault zone.

In this thesis I study in detail earthquakes from the aftershock sequence following the moderate $M_w = 5.5$, 1993 Scotts Mills, Oregon earthquake (Nabelek and Xia, 1996). Each of the investigated earthquakes will be described by its location and its focal mechanism. Deducing this information from seismic data is a major area of research in its own right. Consequently a good part of this thesis is devoted to the development of two techniques that invert seismic data for source and hypocentral parameters. With the combined results that follow from this analyses we hope to describe the stress field that triggered the aftershocks, to infer information about the causal relationship between the main event and its aftershock series, and to relate this earthquake sequence to the geology and tectonics of that region.

The Scotts Mills earthquake is of particular interest as it occurred in an area of peculiarly low historic seismicity. Indeed, the Scotts Mills event was the largest earthquake to occur in Oregon in more than a century, although, later that same year, two $M_w = 6.0$ earthquakes near the town of Klamath Falls disputed it the right to bear this title. By the investigation of this rare event, we hope to learn more about stresses acting in Western Oregon's crust, as well as to assess the risk for future earthquakes in this region.

I used seismic data recorded from a dense, temporary array of digital short period and broadband seismographs that were deployed in a multi-institutional (U.S. Geological Survey, Oregon State University, and University of Oregon) effort the day after the mainshock. The seismic stations recorded between one and three weeks. This is also the time period encompassed by the events studied in this thesis. The data are of very high quality, which forms the ground to the development of techniques, that can be applied to similar earthquakes in future studies.

We retrieve source parameters by means of a waveform inversion, rather than the customary inspection of first arrival polarities. This method is well established for moderate to large earthquakes, but has rarely been applied to small earthquakes recorded at short epicentral distances. The waveform inversion uses seismograms at all three recorded components, and thus takes full advantage of modern, digital, three component seismometry. The efficient use of data allows the determination of focal mechanisms even if the event is recorded by only few stations. The establishment of this method has widespread applications, because it allows a detailed analysis of earthquake mechanics from data sets where this was formerly not possible.

In order to interpret the implications of the earthquake's focal mechanisms, we have to assign each event the most accurate location possible within the sequence. We therefore expand the commonly used single-event location method and perform a *joint hypocenter determination* (JHD) (Douglas, 1967). The JHD method inverts, in addition to the hypocentral coordinates, for station corrections that absorb travel time errors due to a heterogeneous crust, that are common to all events. This method has been proved to give a more focused picture to clustered seismicity in many applications.

The following chapter, Chapter 2, describes the moment tensor inversion for local earthquakes, and as such is the main part of this thesis. Chapter 2.2 is dedicated to the theoretical background, the forward and the inverse problem of the moment tensor method. In Chapter 2.3, I discuss the particularities of its implementation for local earthquakes. Synthetic modeling has been performed to investigate the inversion's susceptibility to an erroneous crustal structure and epicenter mislocations. The results are displayed in Chapter 2.4. The moment tensor method has been applied to 41 aftershocks of the Scotts Mills sequence, the results are presented in Chapter 2.5. There I also describe in detail the field data and the data processing that preceded the analysis. Particular emphasis will be given to the resolution and uncertainties of the inversion results. Chapter 3 deals with the problem of locating the earthquakes. First, I juxtapose different methods employed to solve this classic inverse problem, then the mathematical grounds of the joint hypocenter determination are derived. The results of the relocation are presented in Chapter 3.4. In Chapter 4, the outcome of the previous two chapters are

combined. I subdivide the discussion in seismotectonics, stress and strength considerations, and the implications to models of aftershock generation. The stress part will be dealt with rather elaborately, because of its important geophysical implications. Along with statistical methods to describe the stress field defined by the earthquake focal mechanisms, we perform a stress field inversion following the method of Gephart and Forsyth (1984). At last a model will be suggested that attempts to explain the unusual characteristics of this earthquake sequence. Best-fit synthetic and observed waveforms of all investigated events are appended in Appendix A. Appendix B embraces a description of the input and output of the JHD code as well as a listing of the same.

Chapter 2

MOMENT TENSOR INVERSION OF LOCAL EARTHQUAKE DATA**2.1 Introduction**

Focal mechanisms of weak earthquakes are of importance in the understanding of regional and small-scale tectonics. In regions lacking large-scale seismicity they are often the only means to estimate regional stress directions. Recurrence intervals for small earthquakes are shorter than for large earthquakes. In seismically active areas, this allows for the compilation of representative data ensembles of earthquake mechanisms and maximum and minimum stress directions in relatively short time windows. These data give insight in the temporal and spatial distribution of stresses in the earth's crust (e.g., Iio, 1996). Alternatively, aftershock studies, with the use of focal mechanisms and precise hypocenter locations, can reveal complex fault interactions and crustal-scale tectonics (e.g., Beroza and Zoback, 1993; Fan *et al.*, 1993; Harmsen, 1994; Hauksson 1994; Braunmiller *et al.*, 1995).

Despite widespread availability of digital three-component data, the commonly used technique to estimate fault orientation and slip direction of small earthquakes is still the observation of first motion polarities. Because this technique utilizes only a very small part of the seismogram, namely the polarity of the first arrival, many observations along with the knowledge of local velocity structure are necessary to determine accurate first motion mechanisms. Unfortunately, weak earthquakes rarely have a sufficient number of recordings. The description of the seismic source as a point source through the moment tensor provides a concept that is able to yield source parameters from few observations. While moment tensor inversion techniques are now routinely used to obtain source parameters from long period body- and surface-waves recorded at teleseismic and regional distances (e.g., Dziewonski and Woodhouse, 1983; Nabelek, 1984; Ritsema and Lay, 1993; Nabelek and Xia, 1995), only a few attempts have been

made to apply this technique to short-period data from local earthquakes (e.g., Saikia and Herrmann, 1985 and 1986; Koch 1991a and 1991b; Mao *et al.*, 1994).

A seismogram can be understood as consisting of the contributions of source, path, and receiver-site. For moderate and large earthquakes, seismic energy can be observed at long enough wavelengths that a gross velocity model describes the earth's response well enough to yield satisfactory results (e.g., Ritsema and Lay, 1993). In comparison, locally recorded seismograms of small earthquakes have to be analyzed at higher frequencies (≥ 1 Hz) for the signal to emerge from ambient noise. To still succeed in separating source from path, this would imply a knowledge of detail in crustal structure that can rarely be achieved. Figure 2.1.1 shows a record section of synthetic displacement seismograms calculated for a dip-slip source buried at 12 km depth in a layered upper crust (see inset in Figure 2.1.1 for crustal model) at increasing epicentral distances. The waveforms at the near source sites are simple. Whereas at distances smaller than 14 km, the direct *P* and *S* arrivals are the dominant phases, multiples and converted phases due to complex interactions in the layered crust become more apparent at increasing epicentral distances. It is this simplicity of waveforms recorded at short epicentral distances that allows us to model seismic waveforms, even if the structural model for the region under study is poorly known for the scale of wavelengths contained in the seismic data.

Stump and Johnson (1977) were the first to apply a moment tensor inversion technique to local body waves. Though they did not apply it to field data, their synthetic examples were calculated for a local station geometry, demonstrating the general feasibility of the method for this type of data. Saikia and Herrmann (1985, 1986) used waveform modeling for four Miramichi aftershocks and three Arkansas swarm earthquakes. Trying to fit the entire seismograms on all three components at frequencies up to 15 Hz, they posed high demands on the crustal model used for calculating the synthetic Green's functions, and did not always succeed in matching amplitude ratios and wave shapes. Koch (1991b) inverted local aftershock seismograms of the 1980, Mammoth Lake earthquakes in the frequency domain for time dependent moment tensor components. However, considering data in a 1 to 20 Hz pass band, waveforms were not well matched. To avoid the complexities in wave shapes encountered when inverting

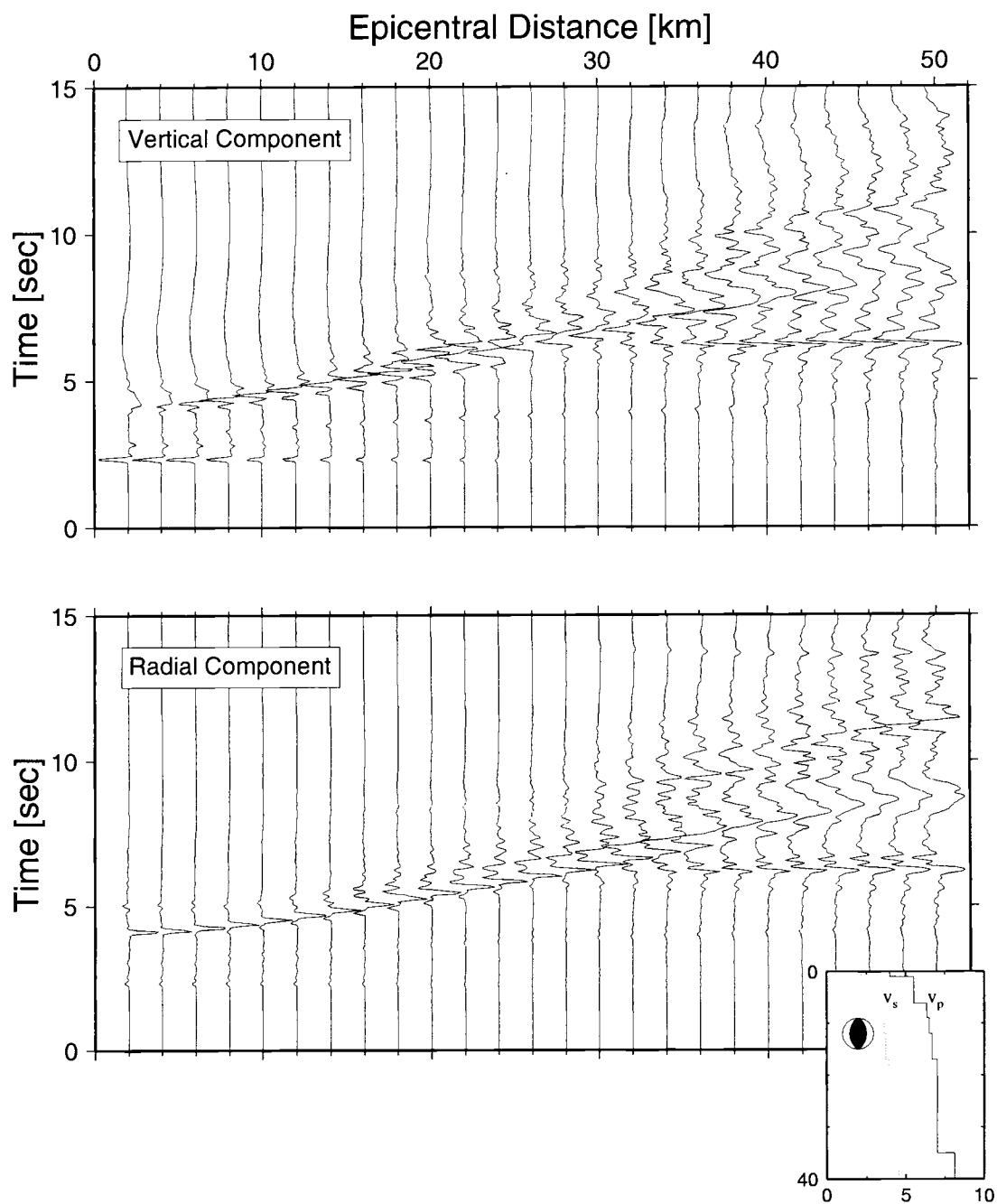


Figure 2.1.1 Record section of synthetic displacement seismograms at increasing epicentral distances. Each trace is scaled to its maximum amplitude. Time axis was reduced with 5.5 km/s. The inset shows the velocity model that was used to calculate seismograms.

whole locally recorded seismograms, Schwartz (1995) inverted amplitude ratios. However, the derived solutions are not unique, and first motion polarities have to be used to resolve the ambiguity in the sense of motion on the nodal planes.

In this thesis I adapt a technique routinely used for regional waveform modeling in the Pacific Northwest (Nabelek and Xia, 1995), and apply it to near-source data. In a narrow frequency band, where displacement waveforms are simple, pulse-like arrivals, we model P and S phases in separate time windows allowing appropriate alignment of the observed and theoretical waveforms. This method proves to be remarkably robust in the presence of non-Gaussian noise resulting from inaccurate Green's functions.

I extensively test the method with synthetic and real data, exemplify the inversion on two Scotts Mills events, and present the results of 39 more aftershocks of the same sequence.

2.2 Theory

We try to extract properties of the seismic source from recorded seismograms. Therefore we have to establish a mathematical model of the source that can be described with a manageable number of parameters, and find its displacement field. The concept of equivalent body forces (Burridge and Knopoff, 1965) leads to the moment tensor (Gilbert, 1970), which can be used to describe the most general seismic sources, but is especially useful for point sources. Within this formalism, the relation between displacement (the seismogram) and source (the moment tensor) is simple and the separation of the latter becomes feasible. The average point source parameters are extracted from the data by fitting waveform and amplitude information of P and S waves with synthetic seismograms in a least square sense. Because the seismogram is a non-linear function of the source parameters (i.e., displacement is a convolution of the source-time-function with Green's function multiplied by the Moment Tensor), the inverse solution is found iteratively.

2.2.1 Mathematical representation of seismic sources

The displacement $\mathbf{u}(\mathbf{x}, t)$, at location \mathbf{x} and time t , in the n_{th} -direction can be written as an integral of the time domain convolution of the seismic moment tensor density m_{pq} and the elastodynamic Green's function \mathbf{G} over the fault surface Σ (see Aki and Richards, 1980 for a derivation):

$$u_n(\mathbf{x}, t) = \iint_{\Sigma} m_{pq}(\xi, t) * \frac{\delta G_{np}(\mathbf{x}, t, \xi, 0)}{\delta \xi_q} d\Sigma \quad (2.1).$$

If \mathbf{u} is observed at wavelengths much greater than the scale of Σ , than the waves excited from different places on Σ are approximately in phase and Σ can be considered as a point, simplifying equation (2.1) to

$$u_n(\mathbf{x}, t) = M_{pq} * G_{np,q} \quad (2.2),$$

where the moment tensor components are $M_{pq}(t) = \iint_{\Sigma} m_{pq} d\Sigma$. If we further assume that the elements of M_{pq} share the same time dependence $\Omega(t)$, equation (2.2) can be written as

$$u_n(\mathbf{x}, t) = M_{pq} \left(\Omega(t) * G_{np,q} \right).$$

2.2.2 Synthetic Displacement Seismograms for a homogeneous full space

The displacement field everywhere is uniquely determined by the slip on the fault. To calculate the displacement seismograms $\mathbf{u}(\mathbf{x}, t)$ for a source with moment tensor \mathbf{M} and time function $\Omega(t)$, we need the corresponding Green's function \mathbf{G} . To infer some basic properties of \mathbf{G} , I write down the solution for an infinite homogeneous full space in

spherical coordinates r , θ , and ϕ (for the derivation of this solution see again., Aki and Richards, 1980):

$$\begin{aligned} \mathbf{u}(\mathbf{x}, t) = & \frac{1}{4\pi\rho} \mathbf{A}^N \frac{1}{r^4} \int_{r/\alpha}^{r/\beta} \tau \dot{\mathbf{M}}_0(t - \tau) d\tau \\ & + \frac{1}{4\pi\rho\alpha^2} \mathbf{A}^{IP} \frac{1}{r^2} \dot{\mathbf{M}}_0\left(t - \frac{r}{\alpha}\right) + \frac{1}{4\pi\rho\beta^2} \mathbf{A}^{IS} \frac{1}{r^2} \dot{\mathbf{M}}_0\left(t - \frac{r}{\beta}\right) \\ & + \frac{1}{4\pi\rho\alpha^3} \mathbf{A}^{FP} \frac{1}{r} \ddot{\mathbf{M}}_0\left(t - \frac{r}{\alpha}\right) + \frac{1}{4\pi\rho\beta^3} \mathbf{A}^{FS} \frac{1}{r} \ddot{\mathbf{M}}_0\left(t - \frac{r}{\beta}\right) \end{aligned} \quad (2.3),$$

where \mathbf{A} are simple trigonometric functions describing the radiation patterns.

The solution (2.3) can be separated into three parts by relative decay with source to receiver distance. The so-called near-field term is for short source durations approximately proportional to $1/r^3$, the intermediate terms to $1/r^2$, and the far-field term decays, as expected for a spherical wavefront with $1/r$. From the radiation patterns, it can be seen that the far-field P wave consists only of longitudinal motion, and the S wave only of transverse motion. In the far-field, displacements are proportional to the derivative of the moment tensor time-function. In contrast, for intermediate-field and near-field displacements, both P and S , involve both longitudinal and transverse components. Near-field motion arrives at the P -arrival time and is approximately active until the arrival of the S wave. The expressions near- and far-field do not indicate a static distance between source and receiver, but are dependent on the wavelength under observation. The far-field is anywhere a few wavelengths away from the source and the near-field at all positions within a fraction of a wavelength from the source (Aki and Richards, 1980). At positions in between those, the relative magnitude of the terms is difficult to assess, and neither of the terms might dominate. The dimensionless ratio $f \cdot r/v$ denotes the number of wavelengths contained in r for a wave with frequency f traveling with velocity v , and helps to determine which part of the wavefield is encountered. For a frequency of 0.5 Hz, hypocentral distance $r = 12$ km and a shear wave velocity of $\beta = 3$ km/s, the number of wavelengths in r is two. Here the near- and

intermediate-field terms might not be negligible. If they are not included in the calculation of the Green's functions, the data must be high-pass filtered.

In this thesis Green's functions are computed by a discrete summation over horizontal wave numbers (Bouchon, 1981 and 1982). This solution of the wave equation for a layered half-space is exact, and includes all of the discussed wavefield characteristics.

2.2.3 Inverse Problem

If data \mathbf{d} and model parameter \mathbf{p} are normally distributed, the linear inverse problem can be solved by the principle of maximum likelihood. The maximum likelihood inverse is found by minimizing

$$\chi^2 = [\mathbf{d} - \mathbf{m}(\mathbf{p})]^T \mathbf{C}_{d_0}^{-1} [\mathbf{d} - \mathbf{m}(\mathbf{p})] ,$$

where \mathbf{d} is an array of all digitized, observed seismograms within a specified time window, \mathbf{m} is an array of all synthetic seismograms, predicted from the model parameters \mathbf{p} : the six moment tensor components m_{11} , m_{22} , m_{33} , m_{12} , m_{13} , m_{23} , (five, if a deviatoric constraint is imposed), the scalar seismic moment M_0 , and the amplitude weights of the n isosceles triangles used to parametrize the source time function. \mathbf{C}_{d_0} are *a priori* estimates of the data-covariance. This solution is equivalent to the well known least squares solution, with the weighting matrix being the inverse of the covariance matrix (Menke, 1984). To stabilize the inversion, a damping factor is used to lessen the effect of small eigenvalues on the inversion result.

2.3 Method

At short epicentral distances, in a narrow frequency pass-band, displacement waveforms are simple, distinct, pulse-like P and S arrivals, little contaminated by other crustal phases (see Figure 2.1.1). We window these parts of the seismogram, which bear most information from the source and are least dependent on crustal structure and each other, namely direct P and SH and SV phases on the Z, T, and R component seismograms respectively (Figure 2.3.1). If we were to, for example, model the direct P phase in addition on the radial component, no information on the source would be gained, because its amplitude relative to the P arrival on the vertical component is solely governed by energy partitioning at the free surface, which in turn depends on crustal structure and event location. The same is true for later crustal phases, their information on the source is immediately coupled to the direct arrivals by crustal structure. From the three major phases, the SV phase is most sensitive to crustal heterogeneity, and its limited use will be discussed in the next two chapters. Within the windows, we allow for separate aligning and weighting of the seismograms. Independent alignment of the two phases is crucial because the one-dimensional velocity model used in generating the synthetics can not account for exact arrival times for both P and S phases at all recording stations, yet, a minor error in traveltimes can lead, at high frequencies, to the skipping of a whole cycle, thus making the inversion results meaningless. The separate weighting is important, since in the least squares inversion, we try to minimize the squared differences in amplitudes between synthetics and data. Because S amplitudes are often an order of magnitude larger than P amplitudes¹, if weighted equally, they were allowed an emphasis on the solution, that is not justified by their information content. The weighting was chosen so that the weighted variance of P and S was roughly equal. It should be noted that, by cutting the seismogram into two halves, we lose the depth information included in the relative P to S traveltimes, but by doing so, gain, to some order, independence from velocity structure.

¹ In fact if we bring equation 2.3 to our memory, we remember, that the far-field amplitude ratio of P and S arrival is $(v_p/v_s)^3$, which for a Poisson solid is about 5.2.

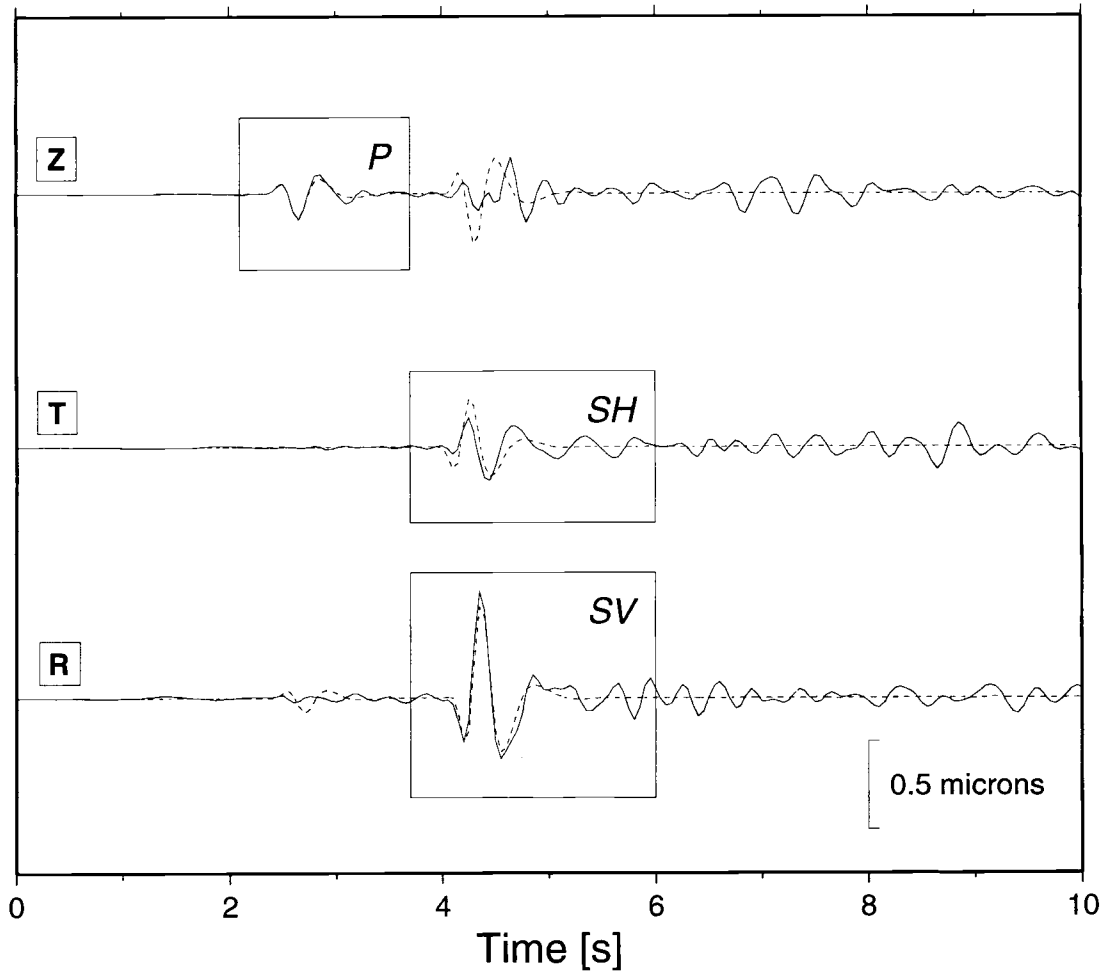


Figure 2.3.1 Schematic view of inversion windows. Only the highlighted parts of the seismograms are used in the inversion.

However, we recover this valuable information in the next chapter, when inverting separately for hypocentral coordinates, where both P and S arrival times are used whenever possible. The inversion technique is the same as in Nabelek and Xia (1995) and Xia (1993), which again is based on Nabelek's (1984) body wave inversion, and is described there in much detail. Although implemented and in theory possible, I do not invert for the source time history. For earthquakes of such small size, in the considered frequency band ($\leq 5\text{Hz}$), the source-time-function is not resolvable and becomes a simple step-function. Effects of fault finiteness are also neglected and the inversion seeks only the first order moment tensor and scalar seismic moment, which describes the source in its average (point source) properties. For all inversions a deviatoric constraint was applied, and the deviatoric moment tensor was decomposed into its double couple (DC) and compensated linear vector dipole (CLVD) components.

2.4 Testing with Synthetic Data

The least-squares solution to the inverse problem is unbiased if the data are contaminated by additive, normally-distributed noise. However, the effect of inaccurate Green's functions due to uncertainties in crustal velocities and mislocated hypocenters, is much more severe and difficult to assess. To estimate the susceptibility of the inversion method to those two sources of error, I constructed a set of synthetic data for a given station distribution, and used them subsequently as "observed" data. To simulate the geometry of our field data, coordinates of a subset of five stations from the temporary array deployed to monitor the Scotts Mills aftershock activity were used. The five stations were specifically selected for two reasons. Since these stations were running very reliably during the first days of the earthquake sequence, when most of the analyzed events originated, the information gathered from the synthetic data can be applied directly to our field data. Secondly, the stations were well distributed, having good azimuthal coverage, as well as spanning epicentral distances from few kilometers (three stations are well within the earthquake cluster), to more than 20 km from the cluster's focal point

(station OSU1 is one of the most distant stations used in the analysis). The station parameters are summarized in Table 2.4.1. The source was placed at the same epicentral coordinates as event 18 of the analyzed sequence, in the center of the cluster, at a depth of 13 km.

Table 2.4.1 Station parameters used in synthetic tests

station name	azimuth [°]	distance [km]
OST	335	5.64
OSU1	55	22.65
OSU2	279	13.00
OSU4	150	3.16
SMI	80	4.51

azimuth - event - station azimuth, measured clockwise from north. Distance is epicentral distance.

I investigated two source types, a 45° dip-slip and a vertical strike-slip. Most events analyzed roughly fell into one of those two categories. Seismograms for these two types were calculated for a seismic moment $M_0 = 2.16 \cdot 10^{19}$ dyn-cm, corresponding to a moment magnitude $M_w = 2.0$, and a simple triangular source time function of 0.025 s length, which also was the sampling interval. The seismograms were generated for the velocity model shown in Figure 2.4.1. This model (from now on referred to as model "WO94") is based on refraction data in Western Oregon and Washington (Trehu *et al.*, 1994), and was used by Nabelek and Xia (1995) for regional waveform modeling of the mainshock. When investigating site-effects, I added shallow low velocity-layers at sites OSU4 and SMI, simulating a weathering layer or slow sediments (see inset in Figure 2.4.1, this model will be referred to as "WO94LV").

2.4.1 The Effect of Crustal Structure on Inversion Results

Four experiments were conducted to investigate the influence of crustal structure on inversion results. The four sets of "observed" data (seismograms for the two sources calculated for the models WO94 and WO94LV respectively) were inverted using Green's

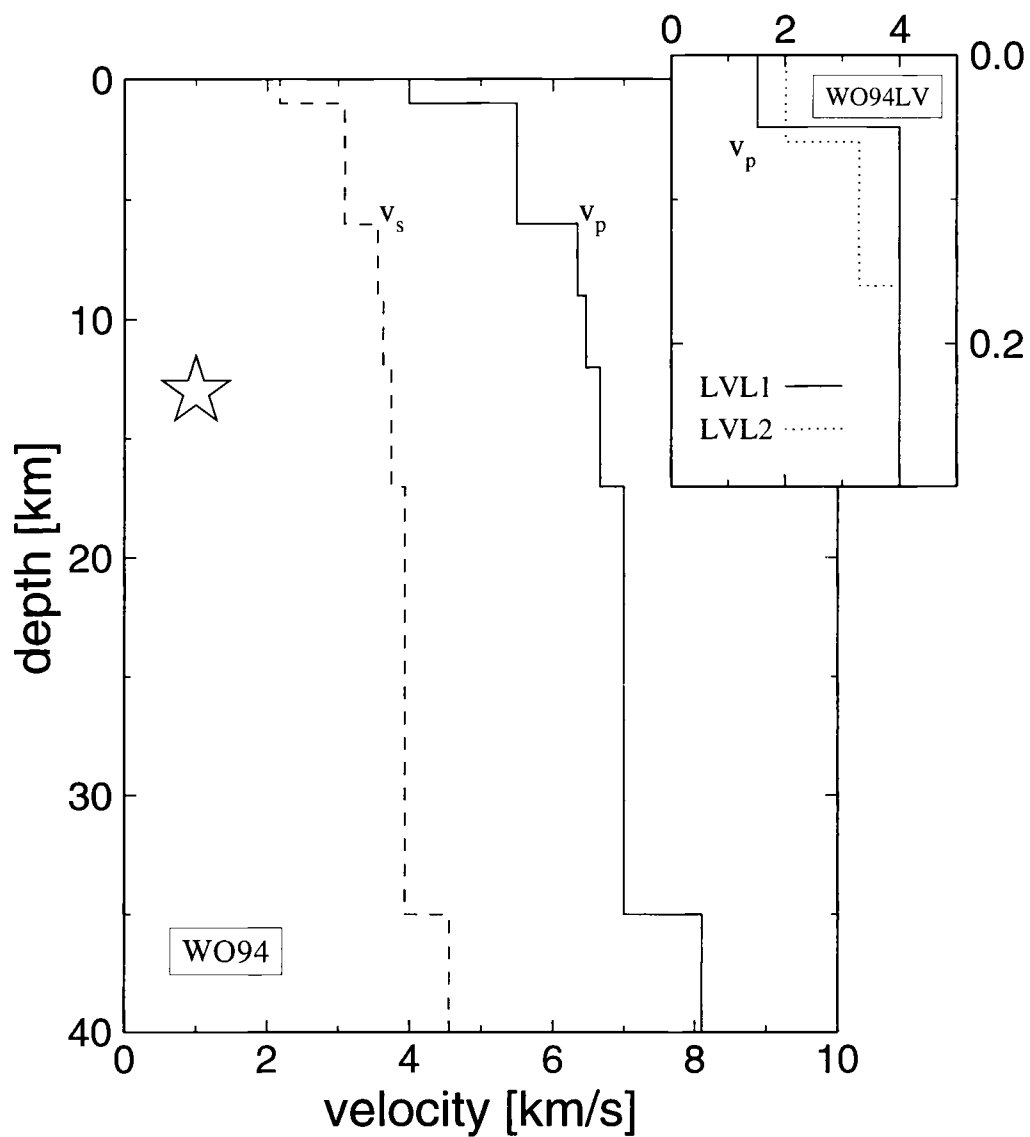


Figure 2.4.1 Velocity model WO94 used to calculate “observed” seismograms. Inset is model WO94LV, which was used at stations OSU4 (LVL1) and SMI (LVL2). The star indicates the depth where the event was placed.

functions computed, (1) for a half space having an average velocity of model WO94, (referred to as "HSA"), and (2), a half space having 10 percent lower velocity as model HSA (referred to as "HSS"). The inversions were carried out in the two frequency bands 0.5 - 10 Hz and 0.5 - 3 Hz, SV phases included and excluded, respectively. All permutations of these realizations are summarized in Table 2.4.2.

Table 2.4.2 Results of Synthetic Testing

model synth	model obs	source [DS/SS]	low pass [Hz]	SV [+/-]	strike/dip/rake [°]	M_0/M_w	DC [%]	variance
HSA	WO94	DS	10	-	90.7/45.1/90.3	1.20/1.99	94.3	0.1397
		DS	10	+	95.7/44.6/90.5	1.35/2.02	84.1	0.2651
		DS	3	-	90.5/45.2/90.3	1.30/2.01	94.4	0.0479
		DS	3	+	90.6/45.1/90.5	1.40/2.03	82.4	0.2598
		SS	10	-	134.3/87.9/179.6	1.39/2.03	97.6	0.0950
		SS	10	+	48.4/88.1/357.8	1.40/2.03	99.9	0.1733
		SS	3	+	45.5/89.2/358.3	1.42/2.03	99.6	0.1334
		SS	3	-	133.7/87.5/179.5	1.39/2.03	97.3	0.0667
	WO94LV	DS	10	-	89.6/45.5/86.9	1.47/2.05	88.6	0.2520
		DS	10	+	96.3/43.9/90.5	1.67/2.08	73.7	0.3389
		DS	3	-	89.3/45.7/86.2	1.37/2.02	88.6	0.1359
		DS	3	+	92.1/44.2/90.9	1.69/2.09	73.3	0.3335
		SS	10	-	45.7/87.6/0.0	1.46/2.04	98.6	0.1833
		SS	10	+	48.4/84.3/358.4	1.56/2.06	98.8	0.2413
		SS	3	-	45.5/87.9/0.3	1.44/2.04	99.4	0.1662
		SS	3	+	45.8/84.9/359.4	1.58/2.07	96.7	0.2158
HSS	WO94	DS	3	-	90.2/45.2/90.3	0.94/1.92	97.2	0.0437
		SS	3	-	133.7/87.5/179.6	1.03/1.94	97.9	0.0642
	WO94LV	DS	3	-	88.9/45.6/86.1	0.99/1.93	91.6	0.1357
		SS	3	-	45.4/87.9/0.5	1.06/1.95	99.7	0.1638
MISLO	WO94	DS	3	-	86.2/52.8/82.1	1.16/1.98	57.9	0.0521
		DS	3	+	85.7/51.8/83.5	1.27/2.00	56.8	0.2754
		SS	3	-	314.6/76.7/192.5	1.22/1.99	89.3	0.1467
		SS	3	+	315.1/76.8/190.7	1.28/2.0	89.2	0.1997
	WO94LV	DS	3	-	90.2/53.9/77.4	1.21/1.99	41.6	0.1323
		DS	3	+	89.5/49.6/85.3	1.60/2.07	45.4	0.3527
		SS	3	-	317.9/71.8/191.1	1.21/1.99	88.8	0.2904
		SS	3	+	317.5/73.5/188.0	1.36/2.02	94.0	0.3202

HSA - half space with average velocity of WO94. HSS - half space having 10% slower velocity than HSA. MISLO - event is misplaced 3km to the north. WO94 - layered velocity model of Figure 2.4.1. WO94LV - same model as WO94 with a low velocity top included (see inset Figure 2.4.1). DS - dip-slip source with strike=90°, dip=45°, and rake=90°. SS - strike-slip source with strike=45°, dip=90°, and rake=0°. Low pass - cut-off frequency for a 3-pole Butterworth filter. SV - "-" if SV phase was excluded, "+" if SV was included in inversion. strike/dip/rake - of best DC-inversion-solution. M_0 - in 10^{19} dyn-cm. M_w - moment magnitude. DC - double-couple portion of moment tensor. Variance of fit.

Separate alignments for P and S arrivals were allowed in all inversions. The seismograms are simple and consist mainly of direct P and S arrival (Figure 2.4.2). The

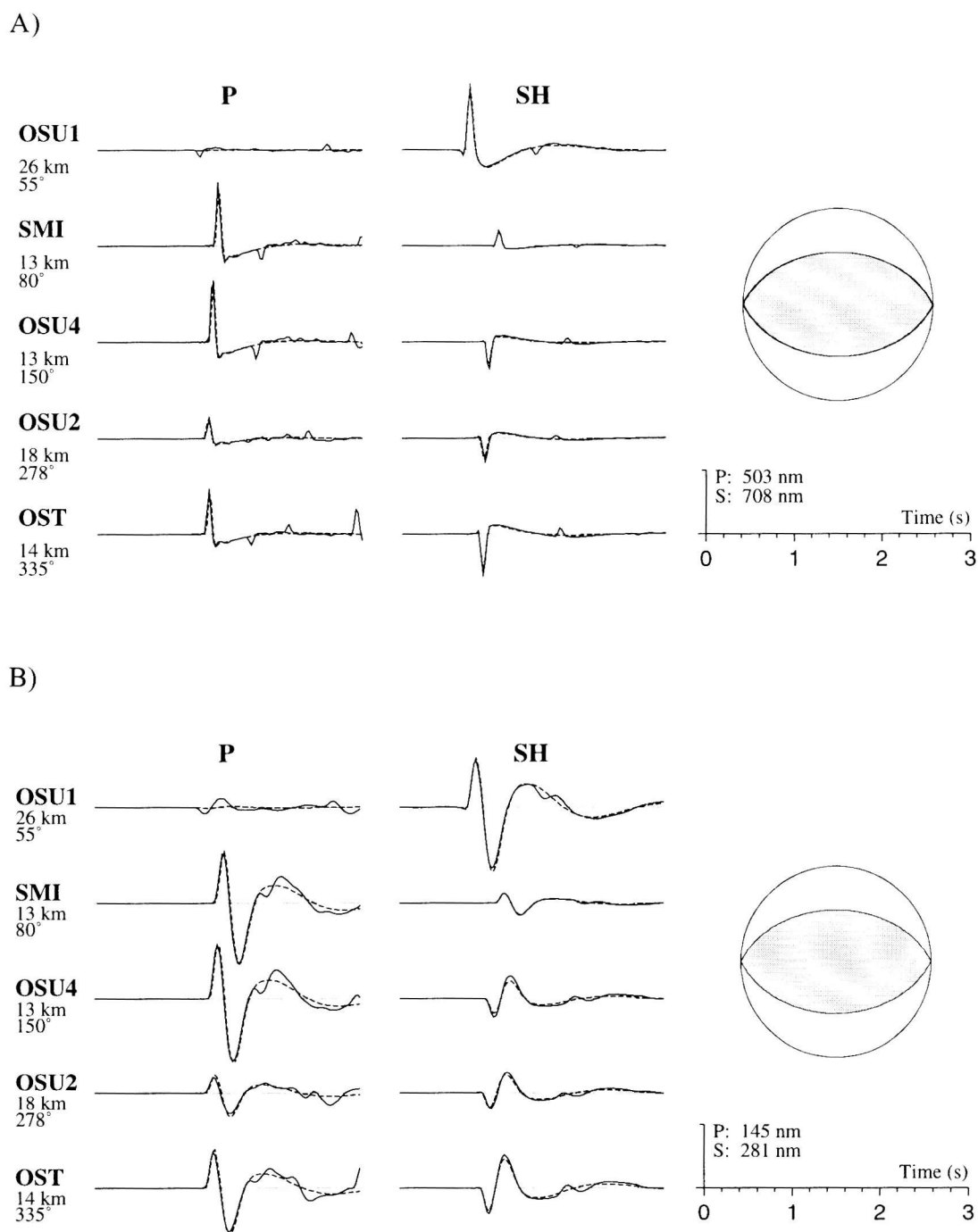
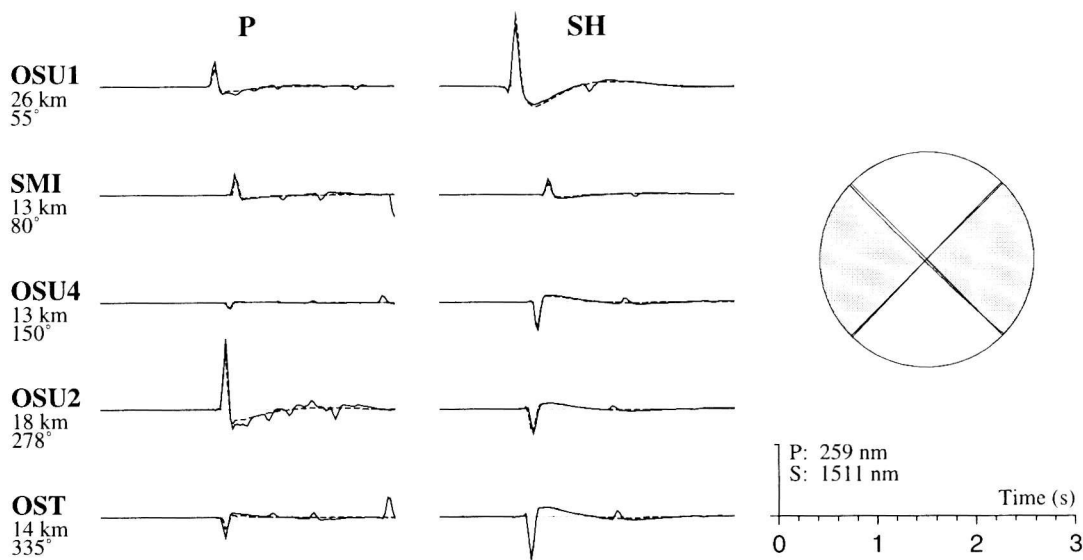


Figure 2.4.2 “Observed” and synthetic seismograms for a dip slip source in the two frequency bands: A) 0.5 Hz - 10 Hz, and B) 0.5 Hz - 3 Hz . Synthetic seismograms are calculated for a half space. The mechanism derived in the inversions (shaded) fully match the true mechanisms (transparent).

C)



D)

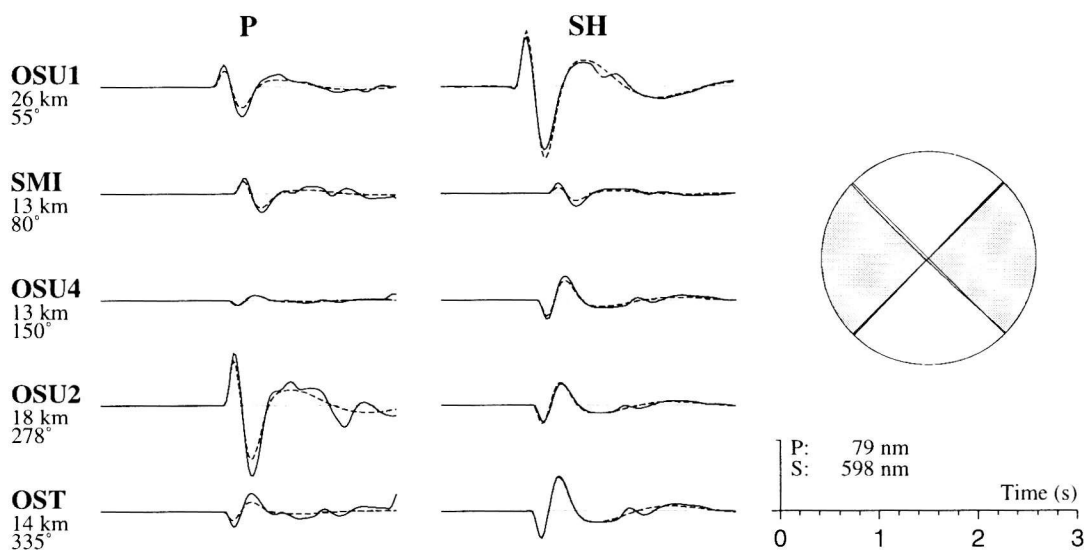
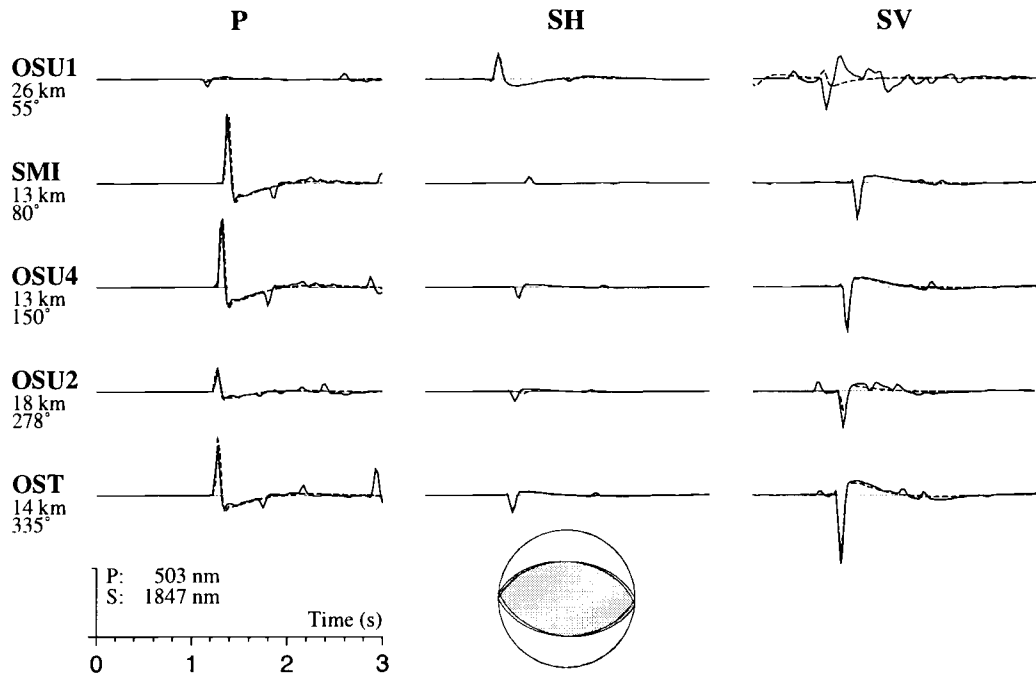


Figure 2.4.2 (continued) “Observed” and synthetic seismograms for a strike-slip source in the two frequency bands: C) 0.5 Hz - 10 Hz, and D) 0.5 Hz - 3 Hz. Synthetic seismograms are calculated for a half-space. The mechanisms derived in the inversions (shaded) completely match the true mechanisms (transparent).

pulse shape is just the impulse response of the applied filter. Using the vertical component for the direct P , and the transverse for the SH wavetrains, all source parameters are well recovered (errors $< 1^\circ$ for strike-slip, $< 3^\circ$ for dip-slip source), with only a minor deviation from a pure DC (CLVD part $< 3\%$ for strike-slip, and $< 6\%$ for dip-slip source) in both frequency bands. Both amplitudes and waveforms are well matched by the model HSA; reflections and phase-conversions are minor and do not bias the solution.

Inclusion of radial-component SV phases has a different effect on the two source types tested. The strike-slip solution has a much higher variance now, but strike, dip, and rake of the source are well recovered and the DC-portion is high. For the dip-slip mechanism the strike is off by six degrees in the high frequency inversion, and the CLVD-part of the moment tensor is considerable with 16 percent. At lower frequencies, the source parameters converge to the correct solution, but CLVD portion stays high. Looking at the seismograms (Figure 2.4.3) these effects can be understood and some important properties of the SV waves can be learned. The SV waves are simple and well-matched in both amplitude and shape for the near-epicenter-stations OSU4, SMI, and OST, whereas they become more complicated with increasing epicentral distance. For the near-stations, rays depart from the source under a very steep angle. Reflection and conversion amplitudes are small, and energy partitioning between the vertical and radial component at the free surface is well modeled by a half-space. For the more distant station OSU2, synthetic amplitudes are too small because the half space does not bend rays like a layered model, resulting in a too small angle of emergence at the receiver site (see Figure 2.4.3). At epicentral distances of the order of those of site OSU1, complex wave interactions in the layered crust dominate the radial seismogram, causing a complete mismatch between observed and synthetics. Since OSU1 is nodal for the strike-slip source, the bias in the solution is less severe there. In summary, source parameters are well recovered with a simplified earth model, and SV -phases do not improve the solution, and are difficult to match at epicentral distances larger than about one depth-length.

A)



B)

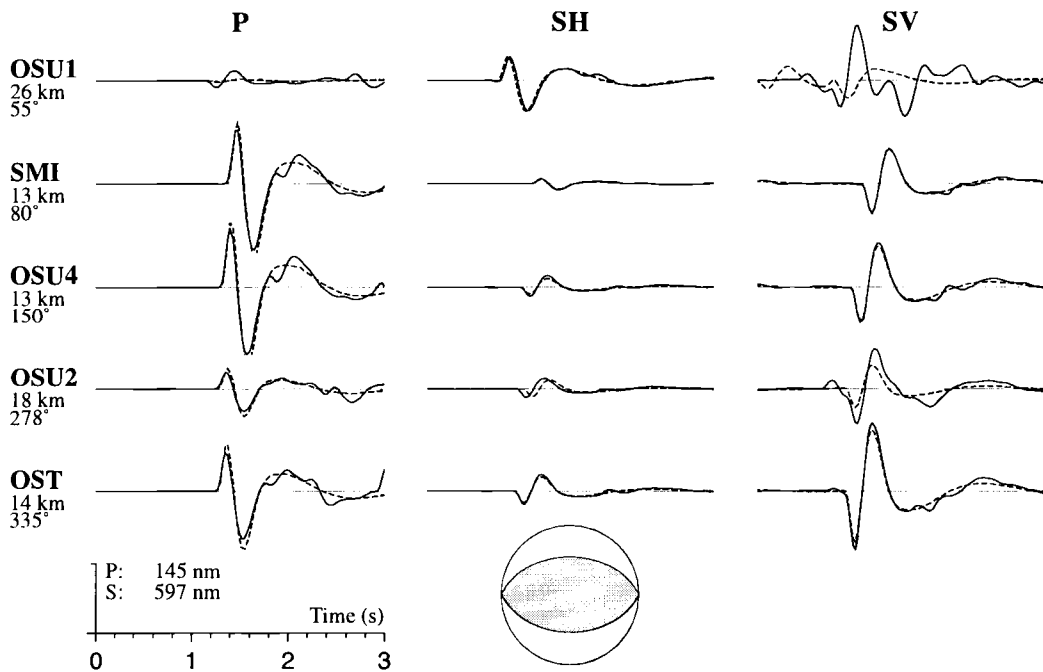
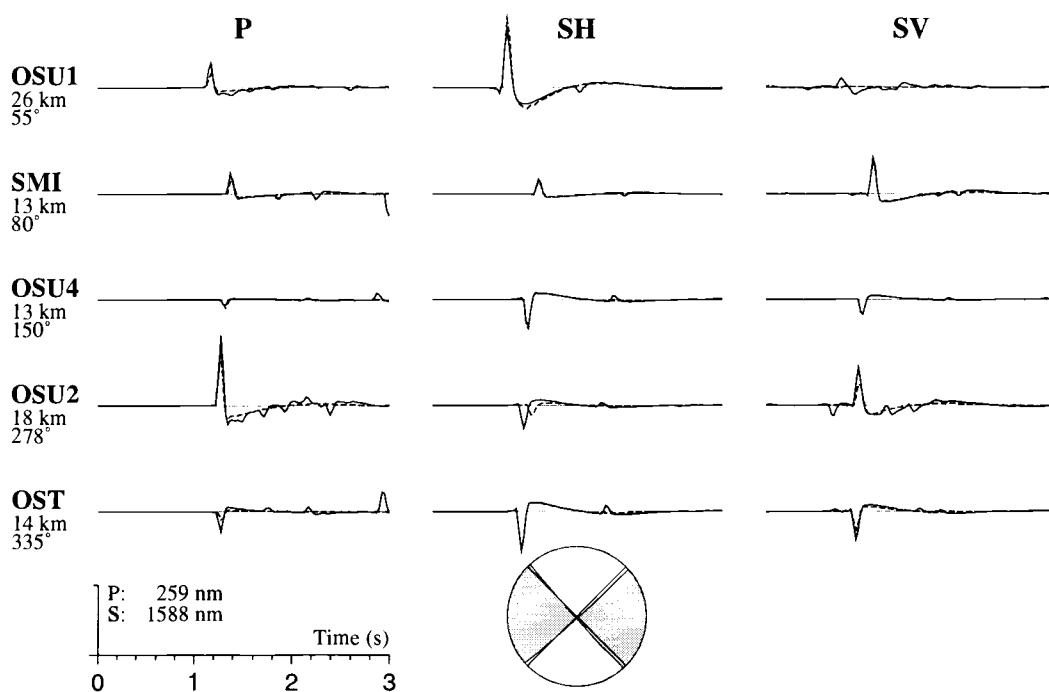


Figure 2.4.3 “Observed” and synthetic seismograms for a dip-slip source in the two frequency bands: A) 0.5 Hz - 10 Hz, and B) 0.5 Hz - 3 Hz . True mechanism is shown transparent, retrieved mechanism is superimposed in shaded grey. Now *SV* phases are included in the inversion. Note the bad fit for the distant station OSU1.

C)



D)

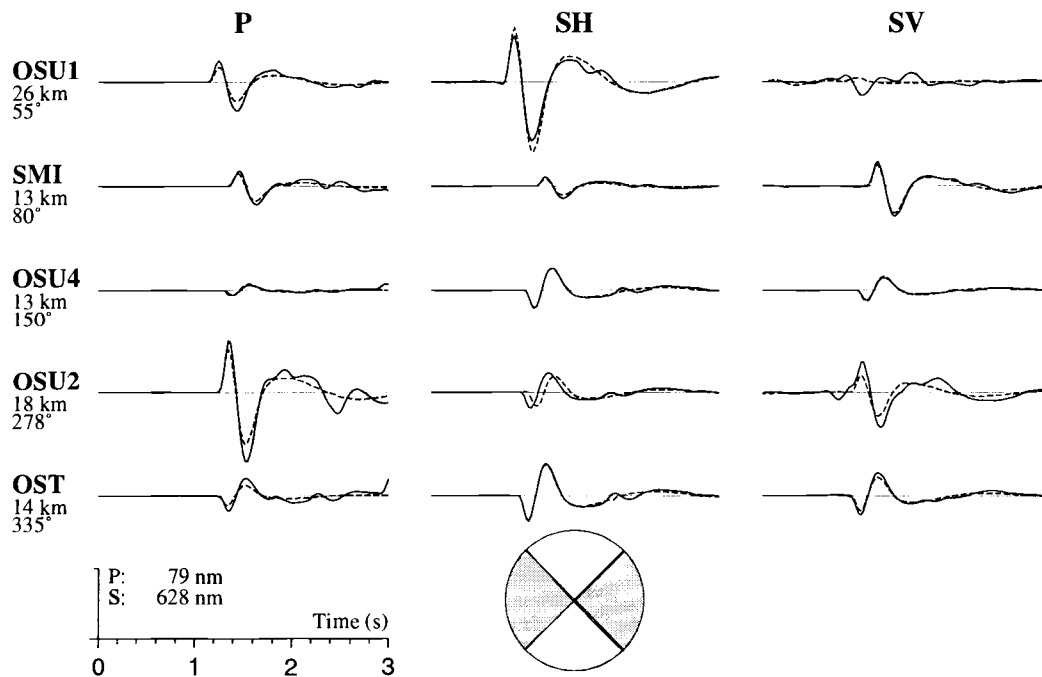
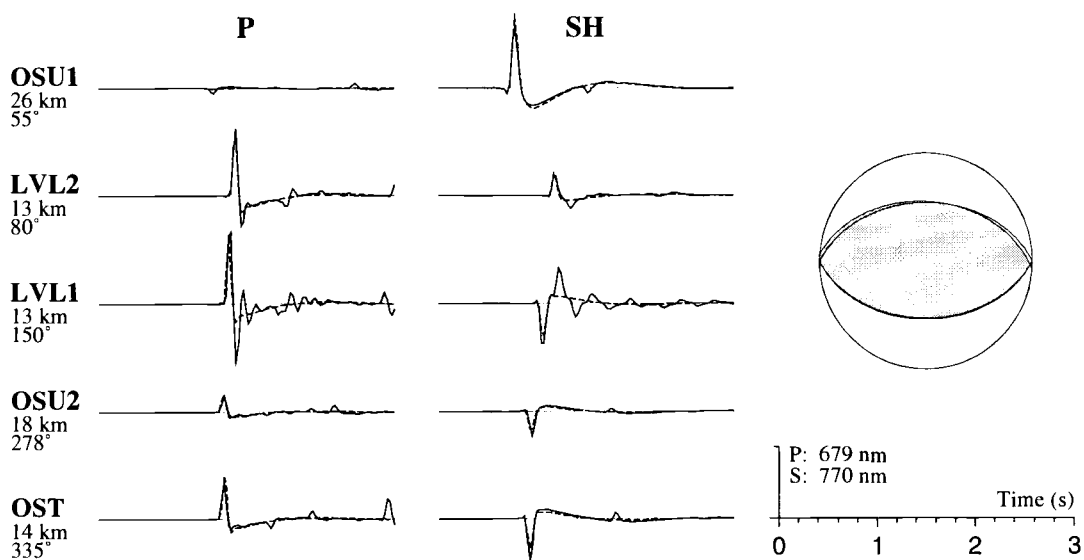


Figure 2.4.3 (continued) “Observed” and synthetic seismograms for a strike-slip source in the two frequency bands: C) 0.5 Hz - 10 Hz, and D) 0.5 Hz - 3 Hz. True mechanism is shown transparent, retrieved mechanism is superimposed shaded gray. *SV* for OSU1 is nodal, and has less influence on inversion.

In a second experiment the half-space P and S velocities for computing synthetic Green's functions were decreased by 10 percent. This affected mainly the travel times, causing a considerable misalignment of phases (0.62 s for P , and 0.88 s for S arrival at OSU1). However, after realignment strike, dip, and rake were recovered accurately, leaving only the seismic moment underestimated, which is to be expected, since amplitudes depend reciprocally on velocities.

To examine site-effects, the receiver structure at two sites was altered by adding a single 50-m-thick layer of very low velocities at station OSU4, and a 60m and 100m thick layer of low velocities at station SMI to WO94 (see Figure 2.4.1). Site-effects are usually referred to as the contribution of that part of the path that is not common to all the stations. They are most often caused by shallow, heterogeneous layers of weathered rock, unconsolidated sediments, gravels, or soils. The effect of low velocity layers (LVL's) is five fold: (1) The distinct velocity change at the base of the LVL sharply bends seismic rays, so that they impinge nearly vertically on the surface, regardless of their direction of travel beneath the LVL. (2) The very high impedance contrast at the base of the LVL causes strong multiple reflections and phase conversions. (3) The slow velocities have disproportional large effects on amplitudes and travel times. (4) Because of the low velocity, wavelengths are short and hence much smaller features produce scattering and other noise, and (5) the absorption of seismic energy is high in this zone (Sheriff and Geldart, 1983). All of these effects are often encountered in field data, with points (4) and (5) being less significant for the wavelengths observed in this data set. Site-effects are difficult to correct for, and if one cannot restrict oneself to frequencies, low enough that thin layers become transparent, it must be hoped that the effects are averaged out by observations at many sites. The effect of amplification and reverberation is well seen in the test data (Figure 2.4.4). Even though it cannot be modeled with a half space, the bias in the solution is small, resulting mainly in a higher variance and an increase in CLVD component. The CLVD increase is needed to model high amplitudes at OSU4 and SMI, which cannot be achieved by changing the DC-mechanism with simultaneously matching amplitudes at the other sites. The higher amplitudes at the two sites also cause a slight

A)



B)

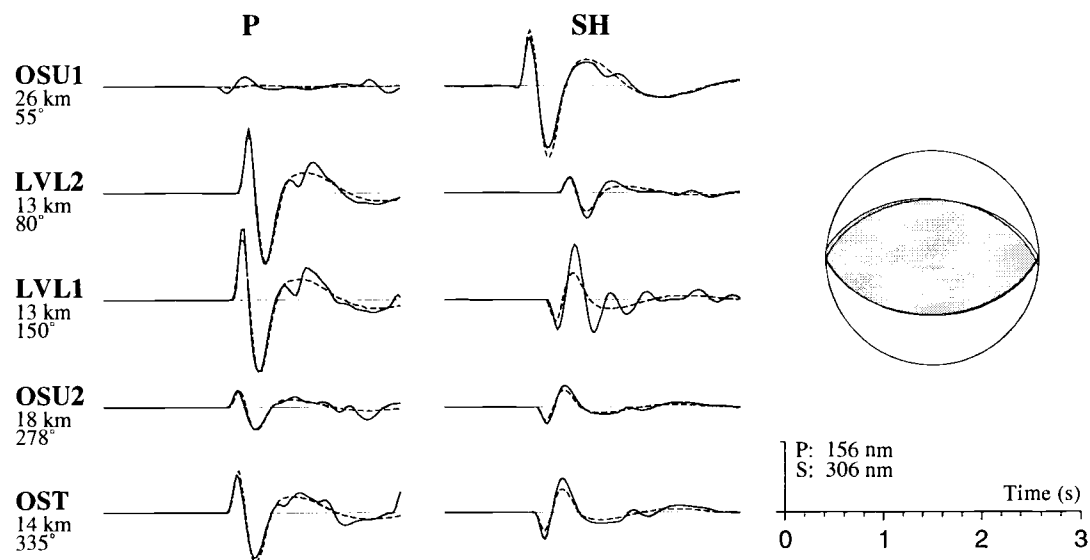


Figure 2.4.4 “Observed” and synthetic seismograms for a dip-slip source in the two frequency bands: A) 0.5 Hz - 10 Hz, and B) 0.5 Hz - 3 Hz. Now at sites OSU4 (LVL1) and SMI (LVL2), a zone of low seismic speed was included. Reverberations within these layers are well visible. However, the effect decreases at lower frequencies. The mechanisms derived in the inversions (shaded) still match well with the true mechanisms (transparent).

overestimation of the seismic moment. Most importantly, all the effects become mitigated at lower frequencies (Table 2.4.2).

2.4.2 *Effects of Hypocentral Errors on Inversion Results*

Inaccurate hypocenter locations cause erroneous arrival times. An incorrect depth provokes errors in the relative timing of phases (e.g., P , pP , sP , and S , pS , sS), whereas, lateral mispositioning of the event changes the event-station-azimuth, which results in inconsistencies in the radiation pattern. The effect of erroneous arrival times is easily corrected by a linear time shift of the seismograms. In contrast, the effect of incorrect depths is non-linear and causes serious problems in most waveform inversion methods. However, because in the method described in this thesis only direct P and S arrival are modeled, and they are allowed to align independently, the correction is easily done by simple time shifts between synthetic P and S seismograms. This leaves the error introduced by lateral mispositioning of the event. In many instances observations are made from far enough distances that uncertainties in epicentral coordinates cause small enough changes in event-receiver-azimuth that they are negligible. If, however, earthquakes are recorded in the proximity of their epicenters, small location errors can considerably change the relative positions of stations and event, and severely bias the source parameter estimates. To investigate these effects, Green's functions were calculated for a source placed three kilometers north of the correct event location (Figure 2.4.5), changing station azimuths as much as 26° . Figure 2.4.6 shows waveforms and the obtained DC-mechanisms (shaded, the correct solution is shown transparent). Focal mechanism parameters deviate from the correct solution by up to 13° , but the general type of faulting is still recovered. The inversion shifts the nodal planes, but cannot find a mechanism consistent with the observed radiation patterns for both P and SH waves, leaving some of the seismograms unmatched (see Figure 2.4.6). An increase in CLVD component can also be observed. This is especially severe for the dip-slip mechanism, where the DC-part in the moment tensor comprises less than 60 percent. For

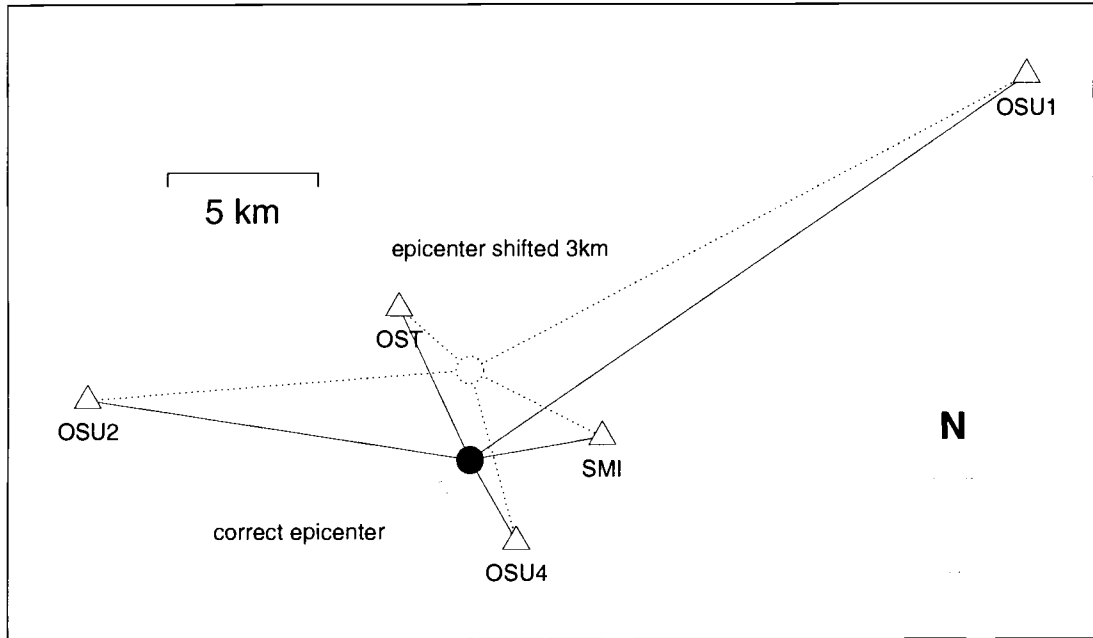


Figure 2.4.5 Schematic view of the changed event-receiver geometry (dotted lines) caused by a mislocated epicenter. This new geometry was used to calculate Green's functions in a synthetic experiment.

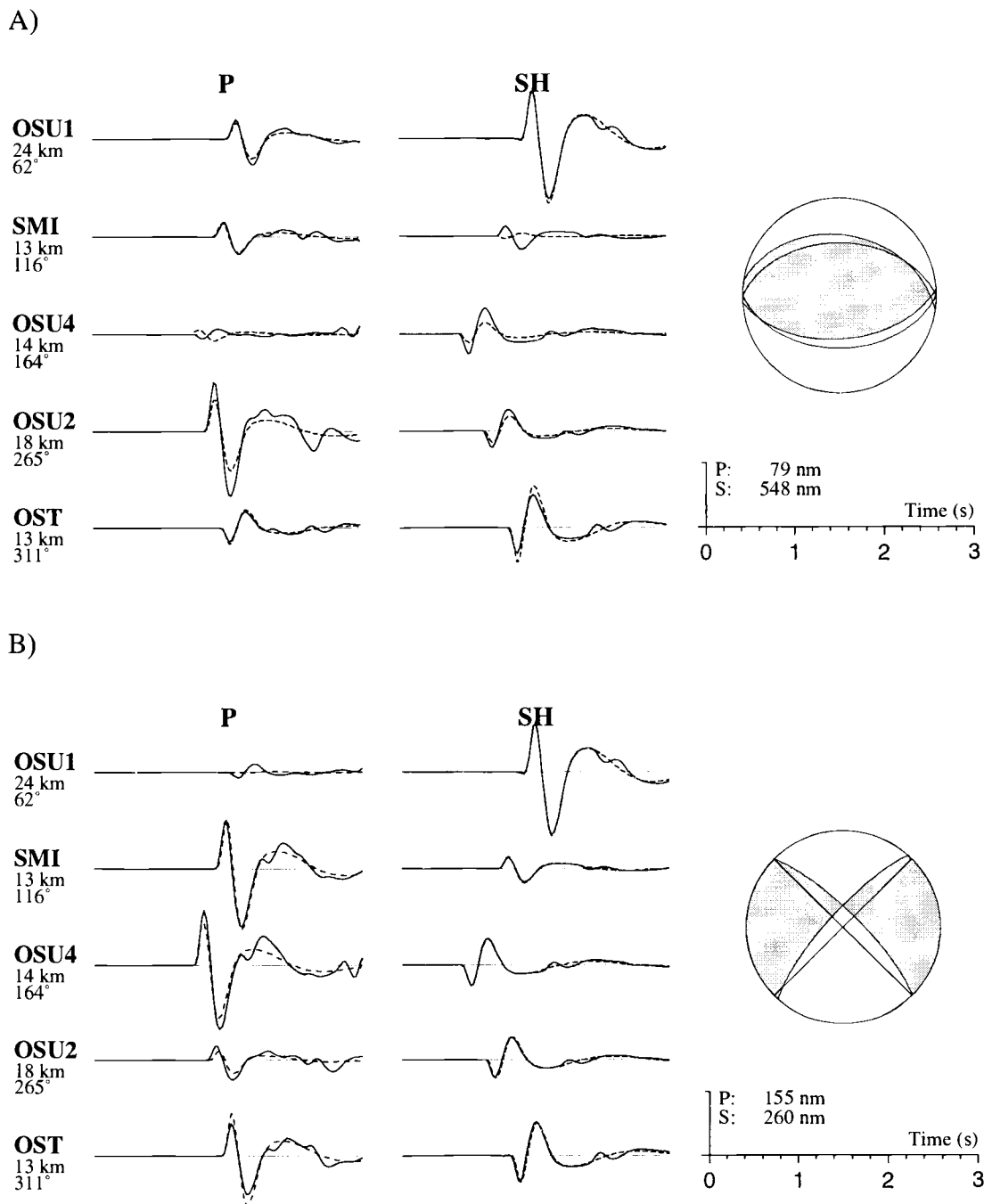


Figure 2.4.6 “Observed” and synthetic seismograms for the station geometry sketched in Figure 2.4.5 in the frequency band 0.5 Hz - 3 Hz for A) a dip-slip source, and B) a strike-slip source. Some of the waveforms are not matched. The mechanisms derived in the inversions (shaded) differ considerably from the true mechanisms (transparent).

the data set used in this study, a lateral mislocation of three kilometers is unlikely, but in situations where station coverage is less dense, errors of this magnitude can not be ruled out.

2.4.3 Summary and Discussion

I tested sensitivity of the moment tensor inversion to erroneous crustal structure and lateral epicenter mislocation for two source types with synthetic data. The "observed" seismograms were calculated for a layered structure and a local station geometry (epicentral distances ≤ 25 km). All inversions were done with Green's functions calculated for a half space. The estimate of source orientation is remarkably insensitive to simplified earth models. Strike, dip, and rake were well recovered, even when the velocity model used did not reflect the average properties of the correct structure. *P* and *SH* waveforms are simple and well-matched by the half-space-model at the epicentral distances investigated. The inclusion of *SV* waves did not improve the estimate of source parameters. Moreover, because they are most sensitive to crustal heterogeneity, they are difficult to model if the velocity model is not known in detail; this is especially true with increasing epicentral distance. The addition of LVL's at two sites did not severely degrade the inversion results. Of all parameters, the seismic moment was most sensitive to crustal velocities. For the noise-free data, the inversion performed equally well in the two tested frequency bands. From all tested scenarios, the bias in the solution resulting from an incorrect epicenter location was strongest. But despite the introduction of gross errors in epicenter coordinates, the general type of faulting, summarized by the DC-part of the moment tensor, was well described. It is interesting to see that misfit between data and synthetics caused by inaccurate Green's functions is often projected into the CLVD component of the moment tensor, leaving the DC parameters strike, dip, and rake relatively undisturbed.

2.5 Application to Aftershocks of the 1993 Scotts Mills Earthquake

The technique to retrieve source parameters from recorded seismograms described in the previous chapters was applied to 41 events of the Scotts Mills aftershock sequence. The analyzed events had moment magnitudes ranging from $M_w = 1.6$ to $M_w = 3.2$, and were recorded by at least 3 and at most 15 stations of a temporary array of digital, three-component seismographs. It is evident that for events with only a small number of recordings, traditional methods using *P*-wave polarities for faulting parameter retrieval, would not have been applicable. For four events, which were recorded from the temporary network as well as the Pacific Northwest Regional Seismic Network (PNSN), first motion mechanisms have been published by Thomas and colleagues (1996). Their results compare favorably with the ones derived by waveform inversion in this thesis. The earthquake sequence shows a remarkable variability in their source mechanisms, the north-south compression as maximum stress being the only consistent feature. Such non-uniformity in focal mechanisms is not expected for aftershocks if they are believed to occur on a common fault plane in the aftermath of the mainshock. It is important to show that the differences in mechanisms are not caused by a lack of resolution or by artifacts introduced by the recording geometry, but are indeed required by the data. I will pay special attention to the choice of the frequency band in which the inversion is performed most advantageously. Most of this analysis will be exemplified with two events, number 13 and 18. Their focal mechanisms exhibit the two endmembers in the scale of observed mechanisms, specifically, a thrust on a dipping plane, and a vertical strike slip. Both events had very good station coverage (15 and 12 recordings respectively), and well constrained mechanisms. With the help of those two events, I will investigate the effects of the frequency band and the recording geometry on the inversion, as well as try to establish bounds on the resolution of the faulting parameters.

2.5.1 Data and Data Preparation

The Scotts Mills aftershock sequence is arguably one of the best recorded earthquake series of its kind. Starting hours after the mainshock, teams from U.S. Geological Survey (USGS), University of Oregon (UO), and Oregon State University (OSU) started to deploy 28 three-component, digital seismographs. Investigators from USGS Denver placed seven DR-200 recorders equipped with three-component short-period (SP) sensors (Sprengnether S6000). Five instruments (ILG, DIE, HOL, SAT, WIL) were set up in a linear array, radiating west from the aftershock cluster, to investigate site-response characteristics in the Willamette River flood plain (Carver *et al.*, 1993). The DR-200 seismograph units recorded for about one week. A team from USGS Menlo Park deployed seven GEOS recorders equipped with two sets of three-component sensors, a SP-velocity-transducer (Mark Products L-22), and a force-balanced accelerometer. These instruments stayed in the field for about three weeks. On March 31, four GEOS stations were relocated to sites initially occupied by DR-200 instruments (SMI, OST, CAL, BYR); there they recorded simultaneously until the DR-200 instruments were removed on April 1. USGS Golden investigators deployed four REFTEK stations with both SP-velocity-transducers (Mark Products L-22) and strong-motion sensors. Three seismographs (WA1, WB1, and WC1) were set up as a Tri-Partite array. The fourth (BC1) REFTEK had only a strong-motion sensor. UO deployed three REFTEK recorders together with three-component broadband (BB) seismometers (Guralp CMG-ESP). Investigators from OSU set up three BB sensors (Streckeisen STS-2) and REFTEK recorders. All the BB-sites collected data for approximately one week.

All SP-instruments were programmed to record in a trigger mode 200 samples per second (sps). The BB stations recorded continuously 50 sps (except station DPUO, which ran in a triggered mode). All station parameters are summarized in Table 2.5.1. A map of all stations is shown in Figure 2.5.1.

The horizontal velocity seismograms were rotated from north- and east- to radial- and transverse-component using single-event locations. Trend and mean were removed from the data. The data were then windowed with a five-second-long Hanning taper

Table 2.5.1 Station parameters

Station Name	Recorder Type	# of Channels (vel./acc.)	Type of velocity sensor	Sensor nat. freq. [Hz]	North Latitude	West Longitude	Elevation [m]	Date Installed	Date Removed
ANG	GEOS	3/3	SP/L-22	2.0/80.0 ¹	45.056	122.775	128	3/30	4/14
BC1	REFTEK	0/3	_____	50.0	45.029	122.618	192	3/27	4/01
BYR	DR-200	3/0	SP/L-22	2.0/80.0 ¹	44.999	122.519	660	3/28	4/01
BYR	GEOS	3/3	SP/L-22	2.0/80.0 ¹	44.999	122.519	660	4/01	4/15
CAL	DR-200	3/0	SP/S6000	2.1/1.7 ²	44.951	122.558	615	3/26	4/01
CAL	GEOS	3/3	SP/L-22	2.0/80.0 ¹	44.951	122.558	615	4/01	4/14
CHR	GEOS	3/3	SP/L-22	2.0/80.0 ¹	45.128	122.452	349	3/27	3/30
CHUO	REFTEK	3/0	BB/CMG-ESP	0.033-25 ³	45.355	122.989	100	3/27	4/03
DIE	DR-200	3/0	SP/S6000	2.1/1.7 ²	45.040	122.784	64	3/27	4/01
DPUO	REFTEK	3/0	BB/CMG-ESP	0.033-25 ³	45.101	122.522	100	3/26	4/01
GLDO	GEOS	3/0	SP/L-22	2.0/80.0 ¹	45.109	122.634	91	3/26	3/29
HOL	DR-200	3/0	SP/S6000	2.1/1.7 ²	45.044	122.741	92	3/27	4/01
ILG	DR-200	3/0	SP/S6000	2.1/1.7 ²	45.043	122.817	52	3/27	3/28
LAN	DR-200	3/0	SP/S6000	2.1/1.7 ²	45.064	122.587	207	3/26	4/01
LOM	DR-200	3/0	SP/S6000	2.1/1.7 ²	44.984	122.637	277	3/26	4/01
MAQ	GEOS	3/3	SP/L-22	2.0/80.0 ¹	45.058	122.678	116	3/27	3/30
MHS	GEOS	3/3	SP/L-22	2.0/80.0 ¹	45.144	122.576	117	3/27	3/30
OST	DR-200	3/0	SP/S6000	2.1/1.7 ²	45.080	122.634	159	3/26	4/01
OST	GEOS	3/3	SP/L-22	2.0/80.0 ¹	45.080	122.634	159	3/31	4/11
OSU1	REFTEK	3/0	BB/STS-2	0.01-25 ³	45.149	122.369	400	3/26	3/29
OSU2	REFTEK	3/0	BB/STS-2	0.01-25 ³	45.052	122.766	130	3/26	4/01
OSU4	REFTEK	3/0	BB/STS-2	0.01-25 ³	45.009	122.584	320	3/25	3/29
SAT	DR-200	3/0	SP/S6000	2.1/1.7 ²	45.038	122.709	181	3/27	4/01
SIV	GEOS	3/3	SP/L-22	2.0/80.0 ¹	44.979	122.723	308	3/27	4/14
SMI	DR-200	3/0	SP/S6000	2.1/1.7 ²	45.041	122.548	415	3/26	4/01
SMI	GEOS	3/3	SP/L-22	2.0/80.0 ¹	45.041	122.548	415	3/31	4/14
WA1	REFTEK	3/3	SP/L-22	2.0/50.0 ¹	45.047	122.833	56	3/27	4/01
WB1	REFTEK	3/3	SP/L-22	2.0/50.0 ¹	45.047	122.836	56	3/27	4/01
WHUO	REFTEK	3/0	BB/CMG-ESP	0.033-25 ³	45.183	122.737	100	3/26	4/02
WIL	DR-200	3/0	SP/S6000	2.1/1.7 ²	45.040	122.673	216	3/27	3/29
YOD	GEOS	3/3	SP/L-22	2.0/80.0 ¹	45.145	122.681	67	3/27	3/30

¹ velocity/acceleration² vertical/horizontal component³ flat instrument response

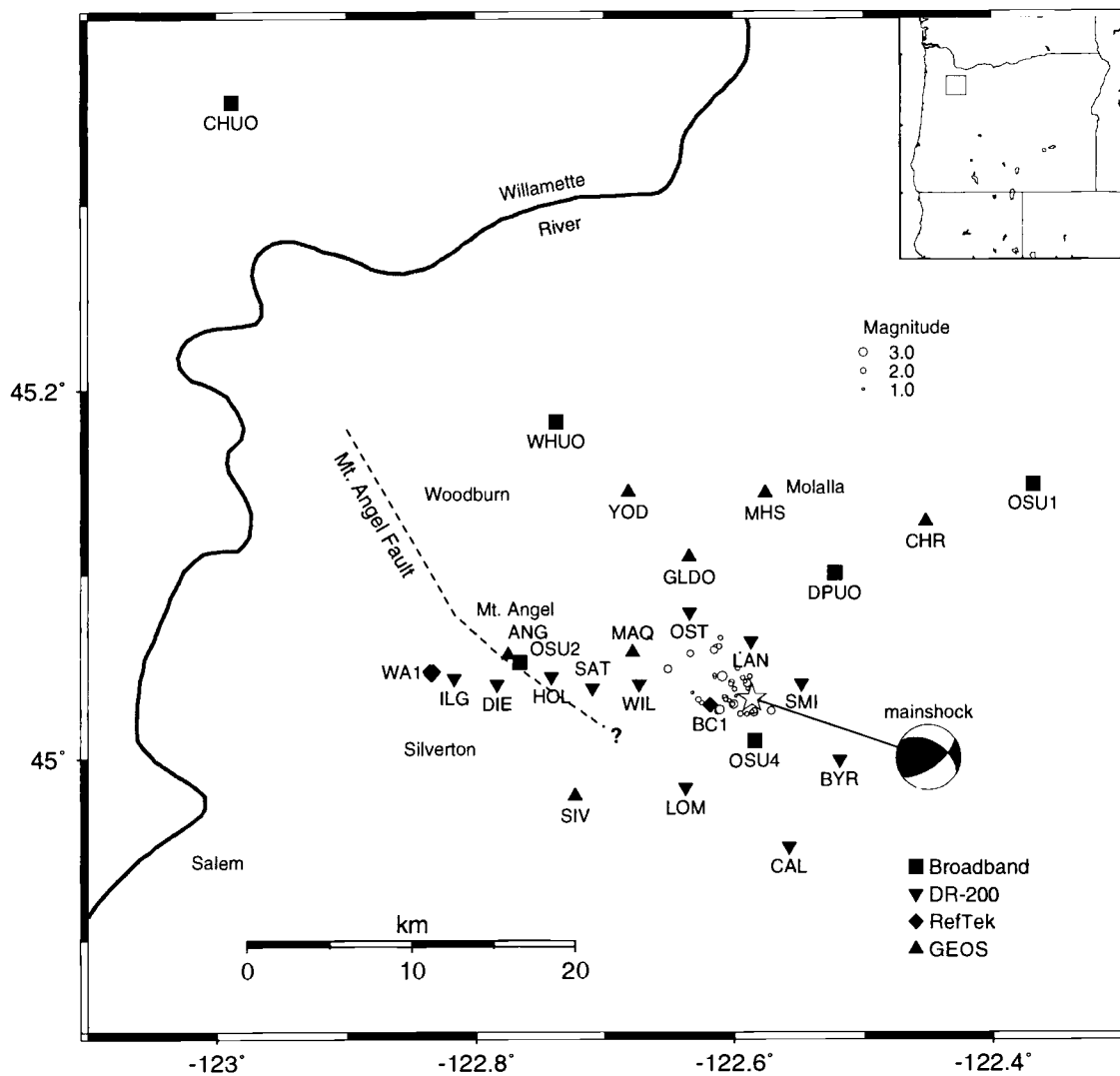


Figure 2.5.1 Map of all stations used in this study. Location of aftershocks and the mainshock are also indicated.

before being converted into ground displacement. This conversion was done by deconvolving the seismometer response from the velocity records. The SP sensors are conventional spring mass seismometers. If the inductance of the coil is ignored, the transfer function for a velocity input is given by

$$H(s) = \frac{s^2}{s^2 + 2\beta\omega_0 s + \omega_0^2},$$

where β is the fraction of critical damping, and ω_0 is the natural frequency in radians. Thus there are two zeros at $s=0$ and two poles at

$$s = -\beta\omega_0 \pm i\omega_0\sqrt{1-\beta^2}.$$

The time series were then filtered with a 3-pole Butterworth filter with corners at 0.1 Hz and 5.0 Hz, down-sampled to 20 sps, and finally, starting from the origin time, cut into a 25.6-s-long displacement record. An example of a SP seismogram before and after processing is shown in Figure 2.5.2.

The inversion time window for the P -wavetrain starts just from before the P -arrival and ends just before the S -arrival. The inversion window for the S -wavetrain starts at the end of the P -window and lasts twice the time of the P -window; hence the inversion is covering the entire seismogram.

2.5.2 Velocity Model

To compute Green's functions for the Scotts Mills aftershocks, I adapted the crustal model from Thomas and colleagues (1996). This same model was also used in locating the aftershocks. It's P velocities are based on a 1-D model routinely used for hypocenter locations in the Puget Sound Basin (Crosson, 1976) (Table 2.5.2). To match S arrivals of the Scotts Mills events, they increased v_p/v_s ratio from 1.73 to 1.78 (Thomas *et al.*, 1996).

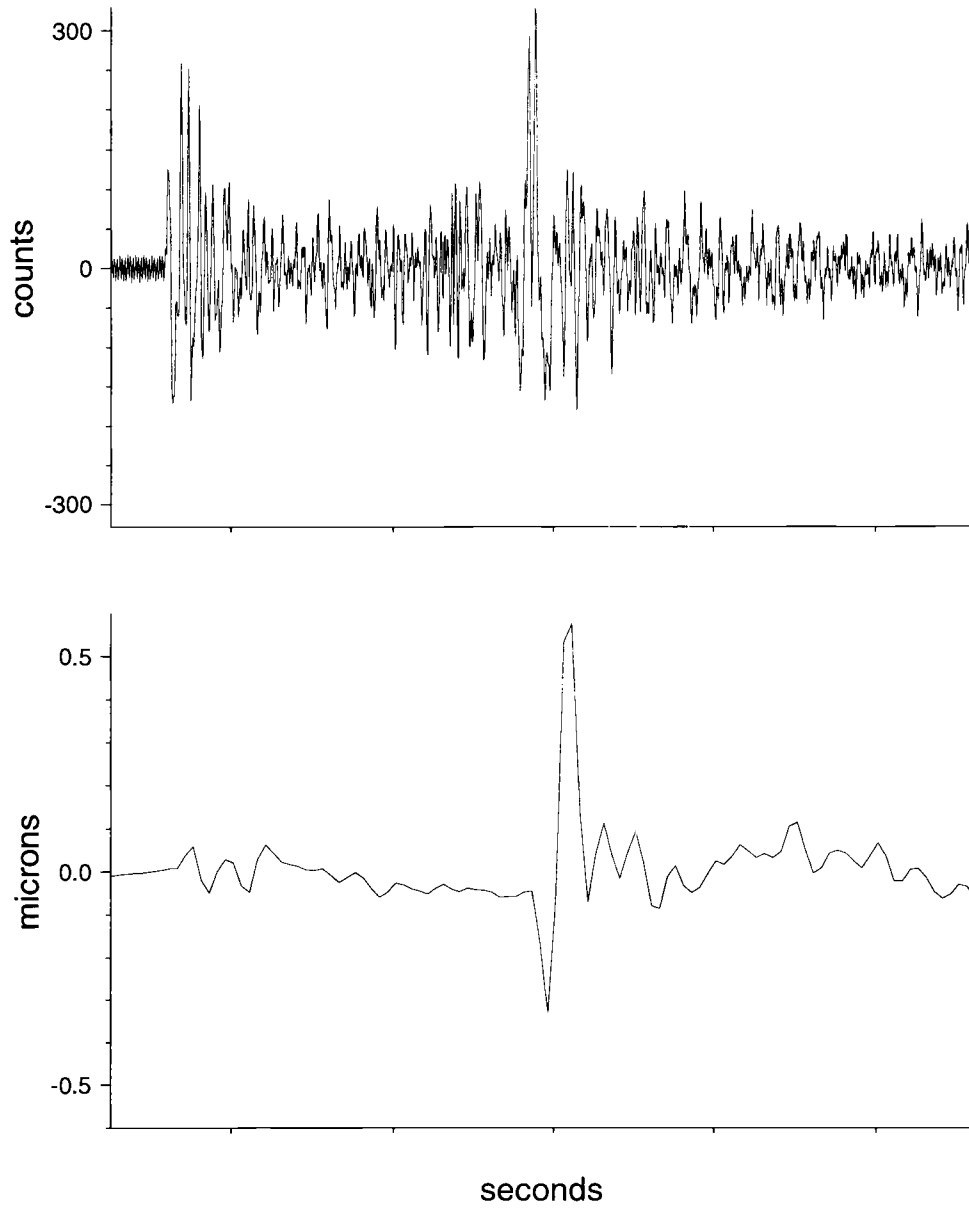


Figure 2.5.2 A trace of station CAL before and after data processing.

The densities were estimated using Nafe-Drake's velocity-density-relation (Nafe and Drake, 1957). Attenuation was also included, but Q values, taken from Nabelek and Xia (1995), are not well constrained; their effect, however should be limited for the short

Table 2.5.2 Velocity Model

depth [km]	v_p [km/s]	v_s [km/s]	density [g/cm ³]	Q_p	Q_s
0.05	1.51	0.56	1800	30	20 ¹
0.06	2.02	0.67	2000	20	15 ²
0.16	3.29	1.315	2200	20	15 ²
10	5.36	3.01	2620	225	100
16	6.61	3.71	2870	225	100
22	6.70	3.76	2910	225	100
32	6.91	3.88	3000	225	100
35	7.11	3.99	3020	225	100
38	7.16	4.02	3020	225	100
∞	7.75	4.35	3020	225	100

¹ Only for OSU4

² Only for SMI

travel paths. This velocity model succeeded well in minimizing travel time residuals when I inverted for hypocentral parameters. Since first arrivals at all stations used in the analysis come from up-going rays, the main contributions to the synthetic seismograms will be caused by their origin's overlying structure. For most events' depths, this consists only of two layers (see Figure 2.5.3).

Our model describes the earth merely in its average properties, and we find a similar situation as in the synthetic example described in Chapter 2.4. Guided from the findings there, I use *SV* only if their signal is not contaminated by complicated phases generated in a heterogeneous crust, and if the amplitude partitioning at the free surface is reasonably well modeled. At stations OSU4 and SMI, I added shallow LVL's to model high amplitudes and strong reverberations. Their thickness and velocity was found by crude modeling of amplitude and phase of first and multiple arrivals. Figure 2.5.4 shows observed and synthetic seismograms, with the LVL's included and excluded in the model, plotted on top of each other. For the modeling I used events that had a good station

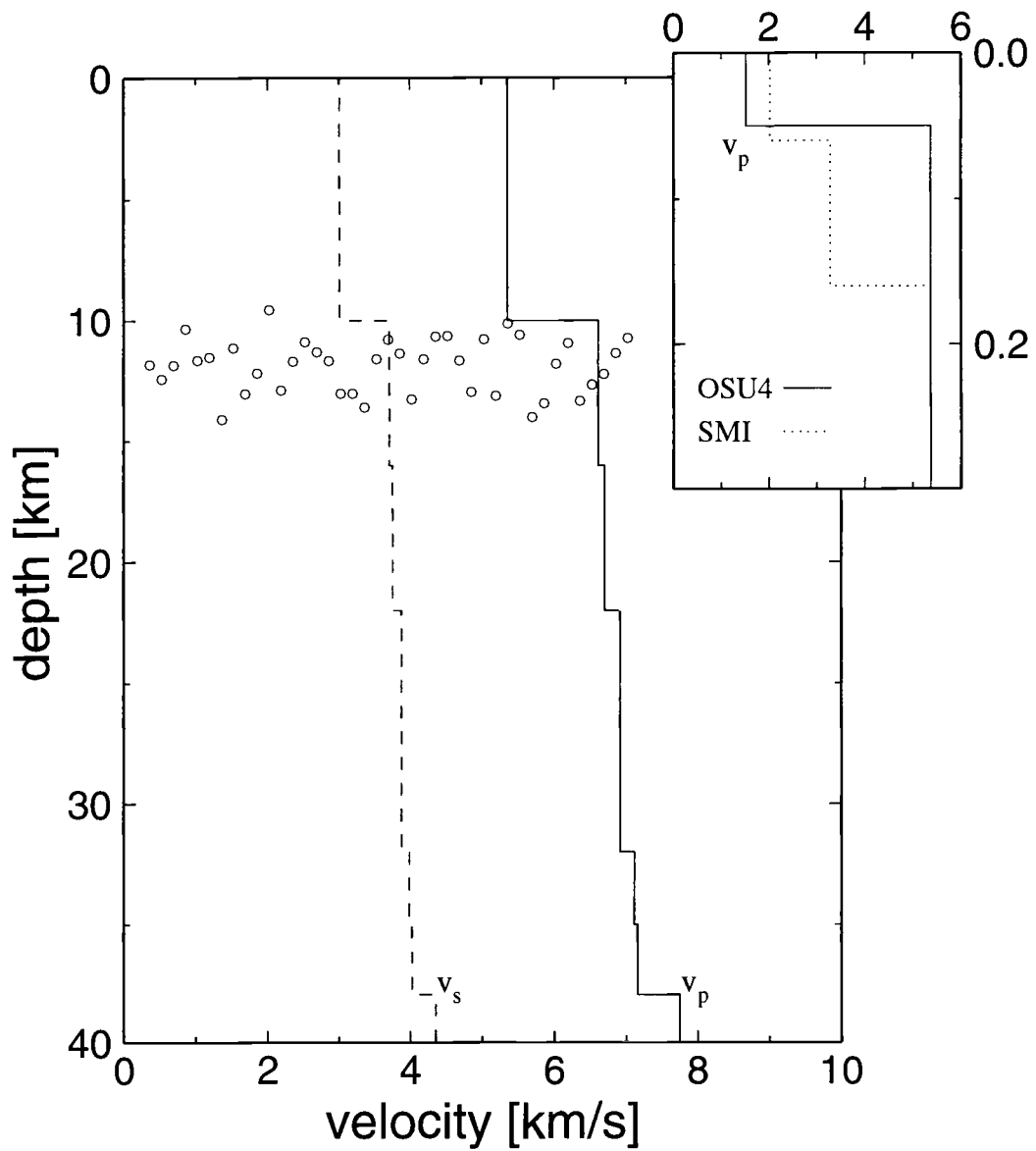


Figure 2.5.3 Velocity model used to calculate Green's functions. Inset shows shallow structure, that was used at stations OSU4 and SMI. Open circles show depths of events investigated in this study (x-coordinates are arbitrary).

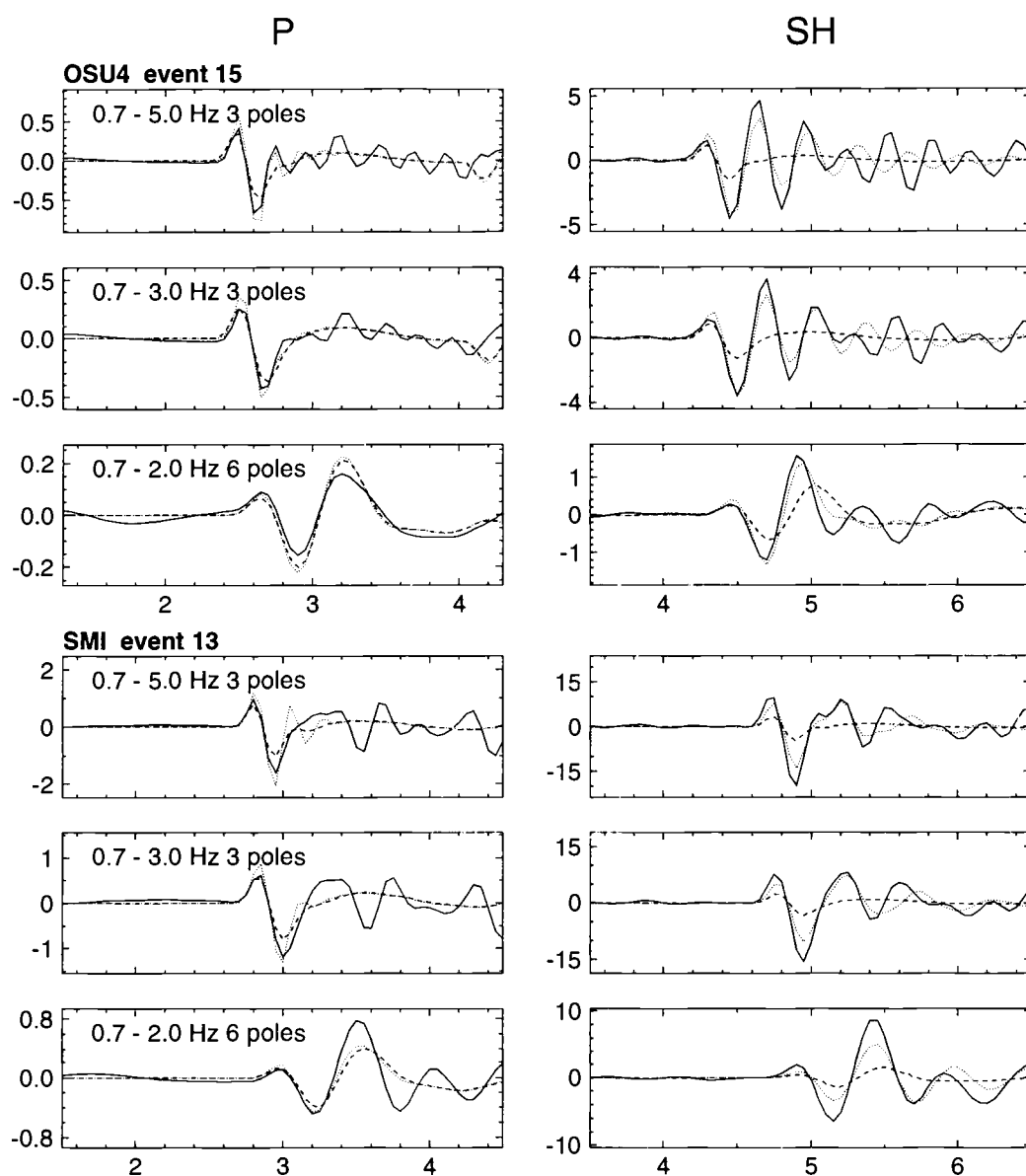


Figure 2.5.4 Modeling of low velocity layers (LVL's). Observed traces (solid), synthetic traces with LVL's included (dotted), and synthetic traces with LVL's excluded (dashed) are shown for two events in three different frequency pass bands. The reverberations in the LVL's match the observed seismograms in both amplitude and phase. Their effect gets damped at lower frequencies.

coverage, and derived the moment tensor for the synthetics without using the investigated stations in the inversion. The shallow P velocities (Table 2.5.2) are consistent with values found in a high resolution seismic reflection study in the area (L. M. Liberty, personal communication, 1996). A high Poisson's ratio was necessary to match corresponding S amplitudes (0.42 at OSU4, and 0.44 at SMI). Such high v_p/v_s ratios, however, are not unusual, and often found in shallow, unconsolidated sediments above the water table (e.g., Ward, 1990, pp. 48). The model with LVL's included fits the data significantly better, with both amplitudes and phase matched reasonably well. The effect of the LVL's decreases with decreasing frequency, although it is still perceptible even if the wavelengths are longer than the scale of structural dimensions (Figure 2.5.4). There is an inherent ambiguity in modeling thickness and velocity of the layers; and their true values might not be well resolved, however, since our main interest is not to infer structure, but to remove a possible bias in the least squares solution caused by large amplitude misfits, we are content with the derived model.

2.5.3 The Choice of the Frequency Band

In general, one should use as broad of a frequency range as workable, to keep as much information in the data as possible. However, there are several factors limiting the frequency range of the data in the analysis. An upper limit on the spectrum is set by the sampling rate, with which the data was digitized. In order to avoid aliasing, high frequencies are limited to the Nyquist frequency. The broadband data were sampled at 50 sps, resulting in a 25 Hz Nyquist frequency, the velocities on the short period sensors were recorded with 200 sps, yielding a 100 Hz Nyquist frequency. A second restriction imposed on the high end of the spectrum is related to the point source approximation used to describe the source. To avoid the effects of a finite fault and rupture duration, one has to stay below the events' corner frequencies. For an assumed rupture duration of 0.1 seconds, the corner frequency would be about 20 Hz. This is a lower bound, since

rupture times of earthquakes, with magnitudes in the range discussed here, are expected to be shorter.

The lower end of the spectrum is controlled by the seismographs transfer function. Whereas the BB sensor's response on ground motion is flat for all frequencies of interest contained in the data, the SP instrument acts like a high-pass filter. Even though we deconvolve the instrument response from the records, there is a lower limit in the spectrum, recorded by these instruments. With the sensor's natural frequency of approximately 2 Hz, we do not expect to record periods much higher than 10 seconds.

However, in practice the factors limiting the frequency range are somewhat different, restricting our analysis to a much narrower band than would be allowed under the conditions outlined above. The lower corner in the spectrum will be dictated by the signal power, and is very much dependent on the size of the event. Small events do not radiate a lot of energy at low frequencies, and microseismic noise easily overwhelms the signal. In order to obtain an acceptable signal to noise ratio, the seismograms had to be high-pass filtered with a Butterworth filter with corners between 0.5 Hz and 1.0 Hz, depending on the size of the event.

The choice of the cut off at high frequencies depends on our ability to simulate the observed seismograms. The earth model we use to explain the data, is, at best, a very low-pass filtered version of the real earth. Based on these crude assumptions, we will not be able to fit high frequency features in the observed seismograms. To bring synthetic and observed seismograms nevertheless to a match, both have to be low-pass filtered. A measure of how much of the data is explained by the model, i.e., the synthetic seismogram, is the variance of the solution.

Figure 2.5.5 shows variance and focal mechanisms for the inversion in frequency bands with the low-pass cut off decreasing from 10 Hz to 2 Hz for events 13 and 18. Event 13 is a thrust with a shallow, and a steeply-dipping nodal plane. The mechanism is well resolved, with the azimuthal range of the recorded seismogram covering nodes for both *P* and *SH* phases (Figure 2.5.6). Its moment magnitude of 2.65 makes it the sixth largest of the 41 analyzed events. Whereas the DC orientation of the source remains

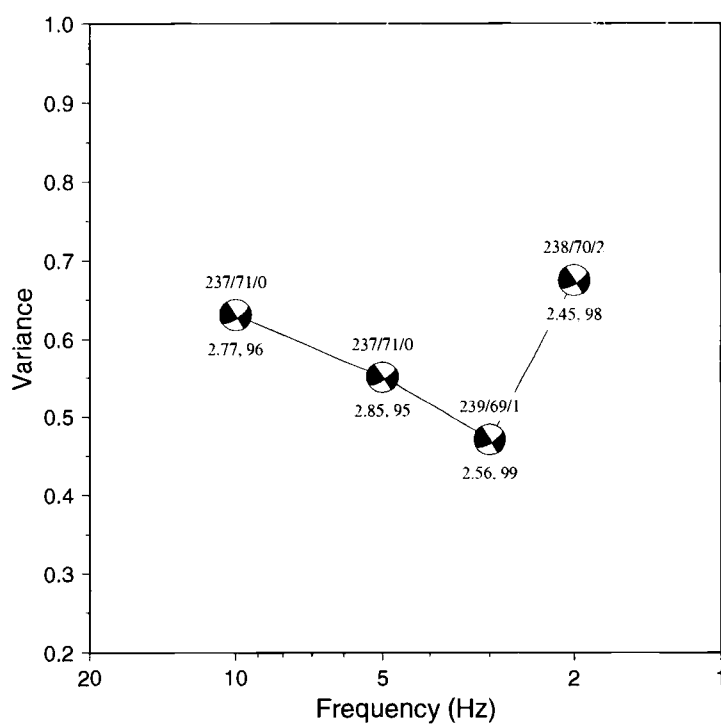
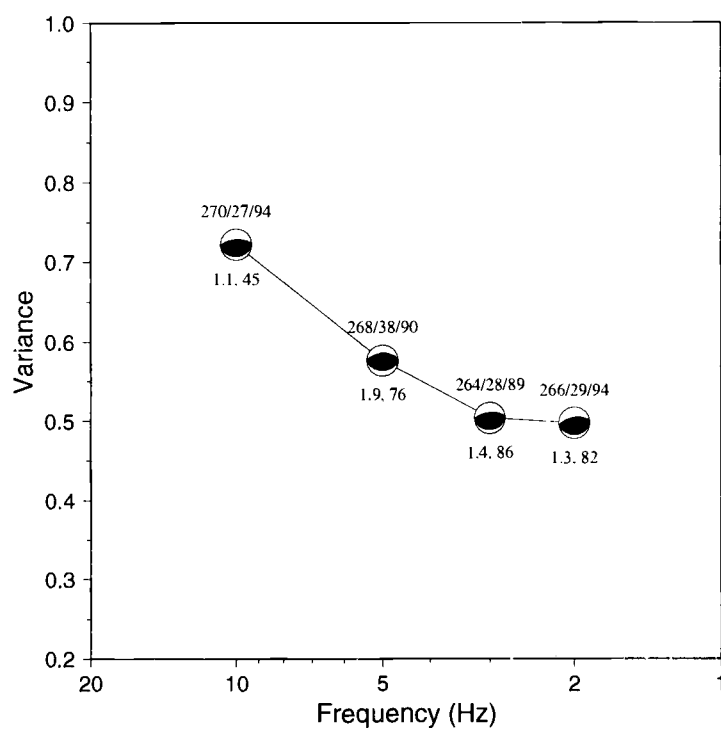


Figure 2.5.5 Variance of the solution versus low pass cut off for top: event 13, and bottom: event 18.

stable, the variance steadily decreases, as the frequency band narrows from 0.7 Hz - 10 Hz to 0.7 Hz - 3 Hz. When the spectrum is further narrowed with a low-pass corner at 2 Hz, the decrease in variance is minor. Since we try to keep the frequency range as broad as possible, by simultaneously explaining as much of the data as possible, the optimum pass-band is 0.7 Hz - 3 Hz. Figure 2.5.6 shows all the traces used in the inversion filtered to the four investigated bands. The improvement in waveform-fit, expressed by the variance, is here easily seen with the naked eye. At high frequencies (10 Hz high-pass), the observed seismograms are complex, consisting of first arrivals, immediately followed by a long coda of later phases which are not modeled by the synthetics at all. Obviously, the earth model used to calculate Green's functions is not sufficient for this frequency band. The match between observed and synthetics significantly improves as the waveforms become simpler at lower frequencies. Now, at frequencies ≤ 3 Hz, the seismograms consist of distinct, simple arrivals, their shape and amplitude well modeled despite our simplistic assumptions about the earth's structure. An attribute, that we already experienced in the preceding chapter with synthetic examples, is the projection of misfit into the CLVD part of the moment tensor, observed in the broadest band, 0.7 - 10 Hz, where the DC comprises only 45 percent of the moment tensor.

Event 18 bears a strike slip mechanism with one steeply dipping and one vertical nodal plane. Again, nodes are covered for *P* and *SH* phases (Figure 2.5.7), tightly constraining the source parameters. At a moment magnitude of 2.22, it is considerably less energetic than the previously shown event, and had to be high-pass filtered at 1.0 Hz to suppress low frequency noise. The variance-frequency plot (Figure 2.5.5 B) shows, once more, a stable mechanism through the range of tested pass-bands. However, now there is a pronounced minimum in variance for the 1 - 3 Hz frequency band. The sudden increase in variance at the 1 - 2 Hz pass-band is explained with a glance at the seismograms (Figure 2.5.7 D). In this narrow band, the weaker event's signal does not have enough power to stand out of the ambient noise. Markedly, the lower amplitude *P* wave is only distinct at anti-nodal stations. Again, the balance between simplicity of the

A)

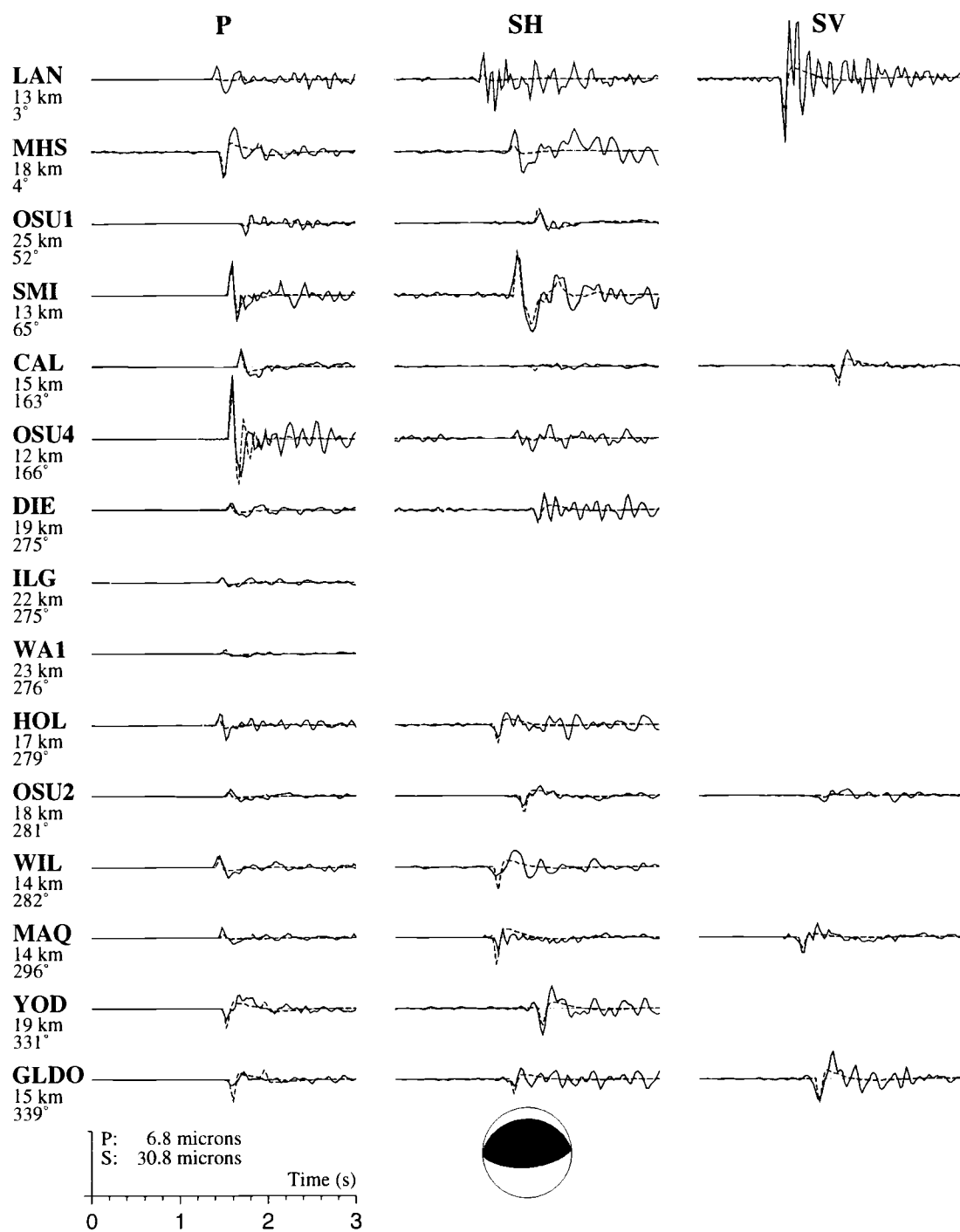


Figure 2.5.6 A) All traces used in the inversion in the 0.7 - 10.0 Hz pass band for event 13.

B)

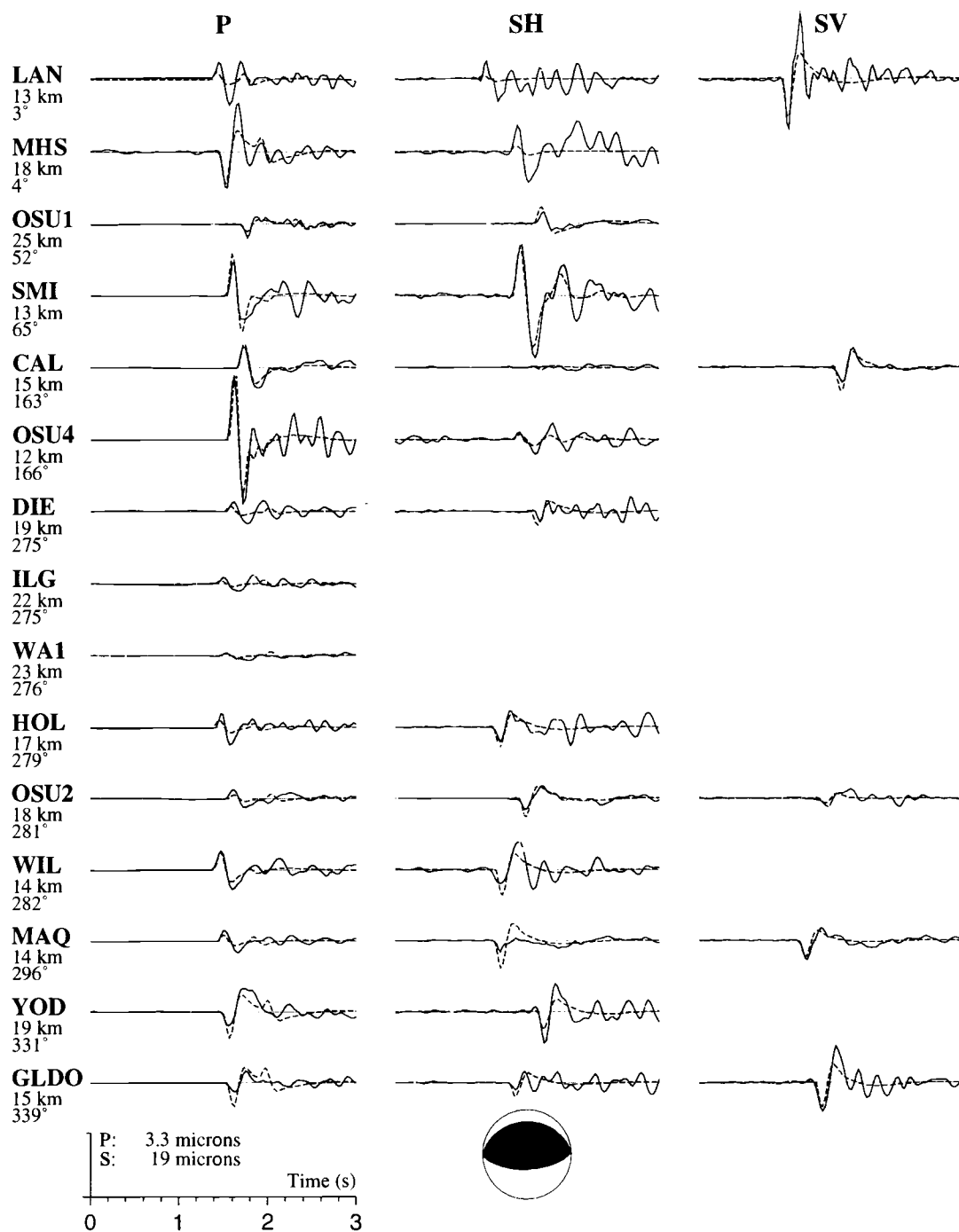


Figure 2.5.6 (continued) B) All traces used in the inversion in the 0.7 - 5.0 Hz pass band for event 13.

C)

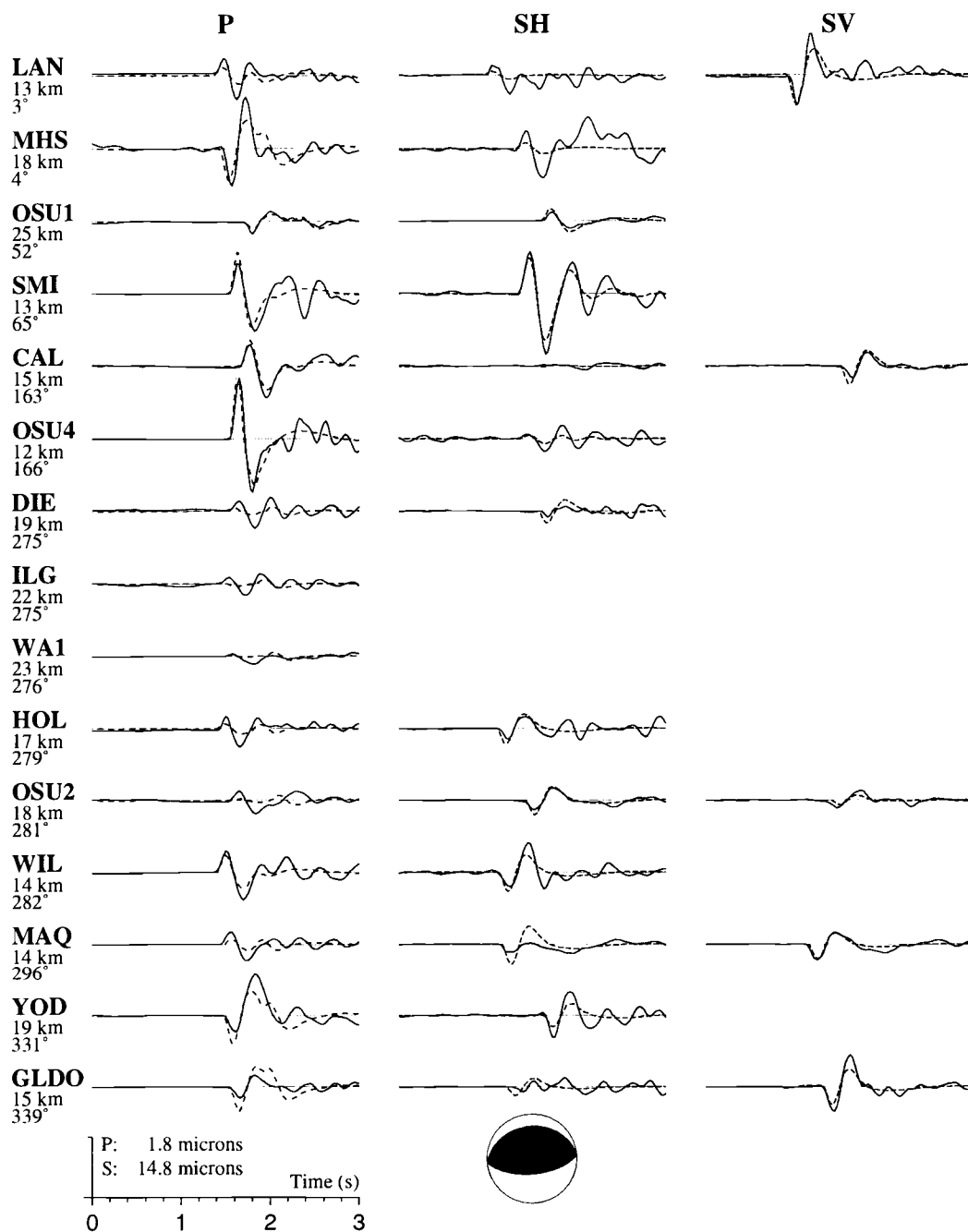


Figure 2.5.6 (continued) C) All traces used in the inversion in the 0.7 - 3.0 Hz pass band for event 13.

D)

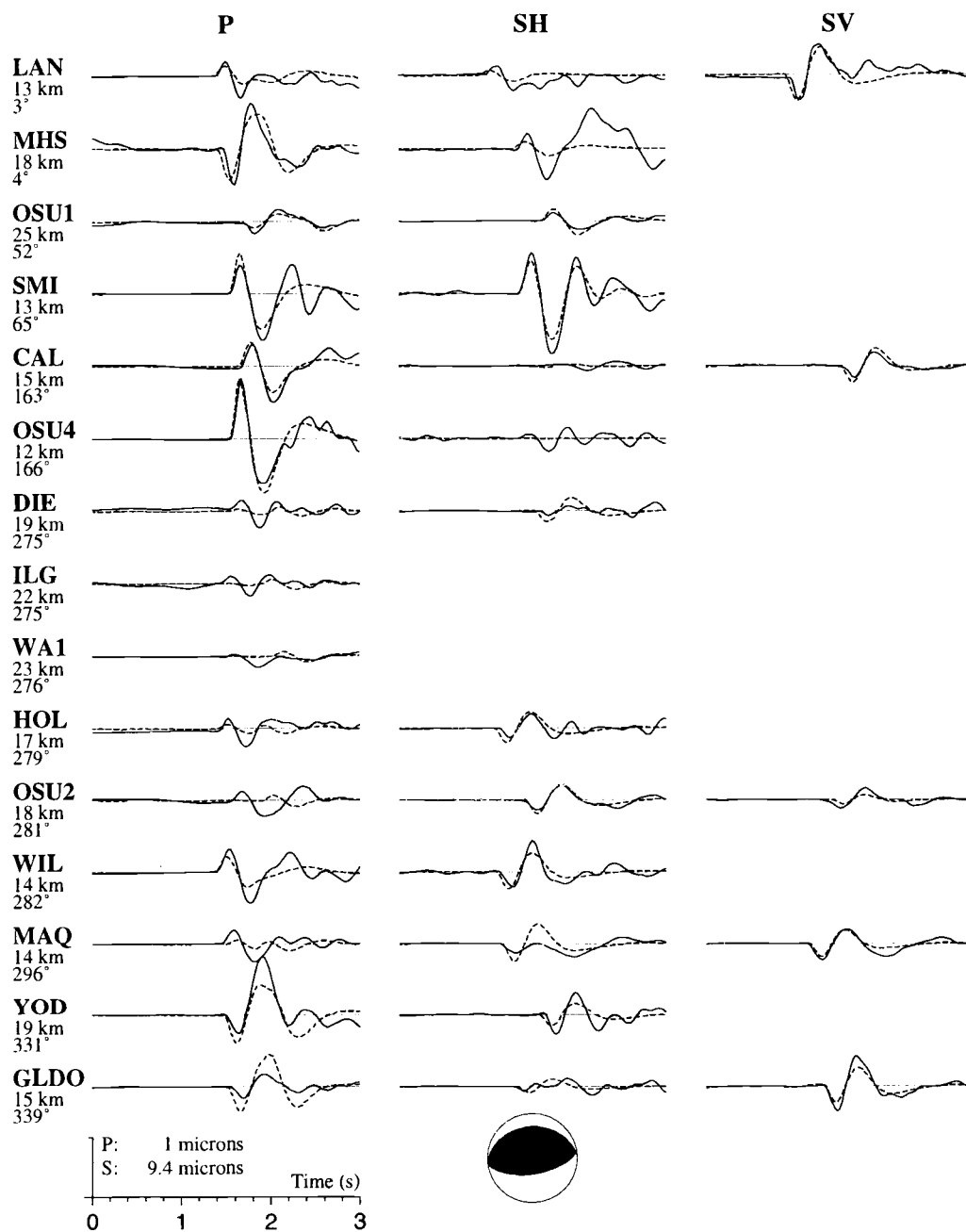


Figure 2.5.6 (continued) D) All traces used in the inversion in the 0.7 - 2.0 Hz pass band for event 13.

A)

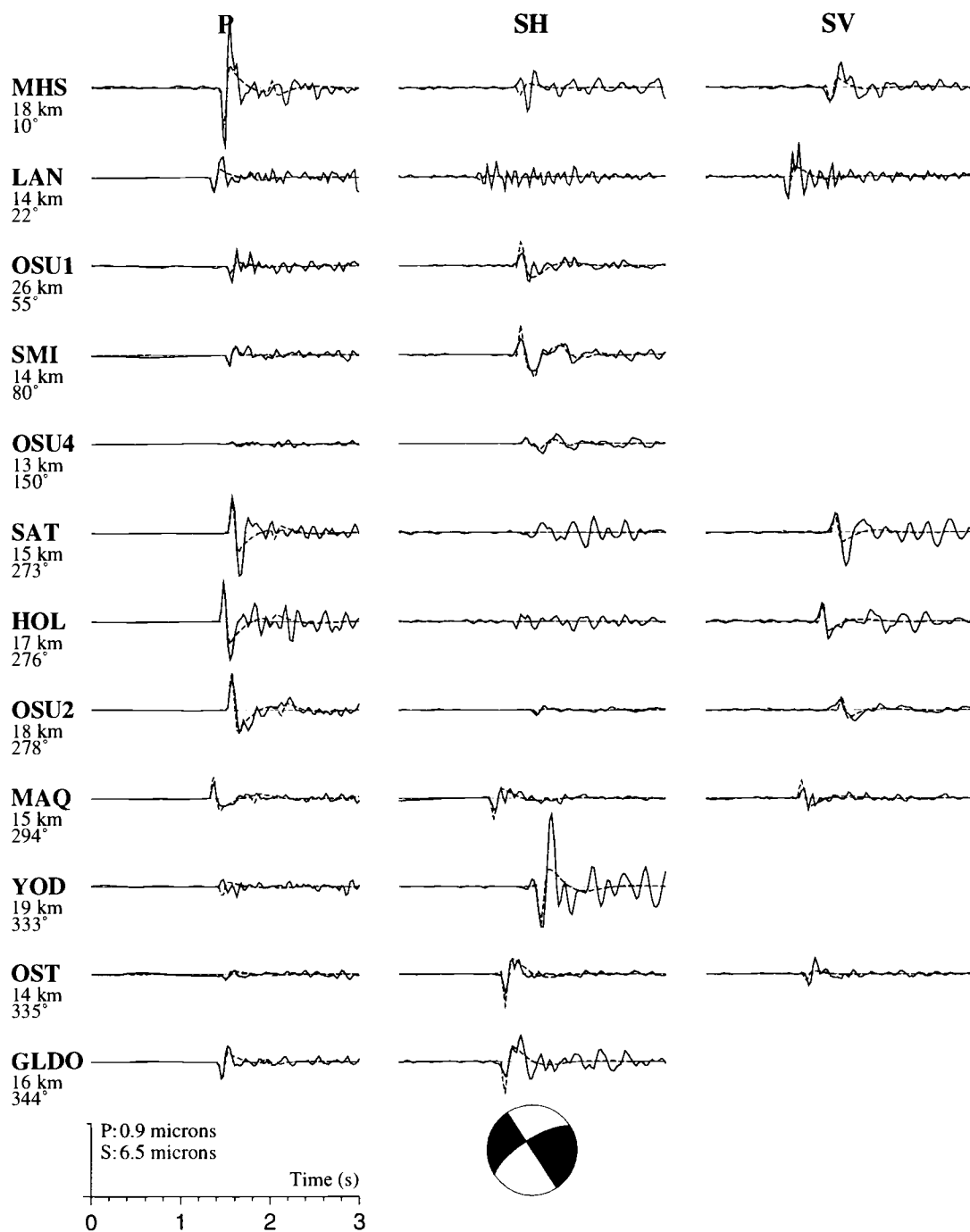


Figure 2.5.7 A) All traces used in the inversion in the 1.0 - 10.0 Hz pass band for event 18.

B)

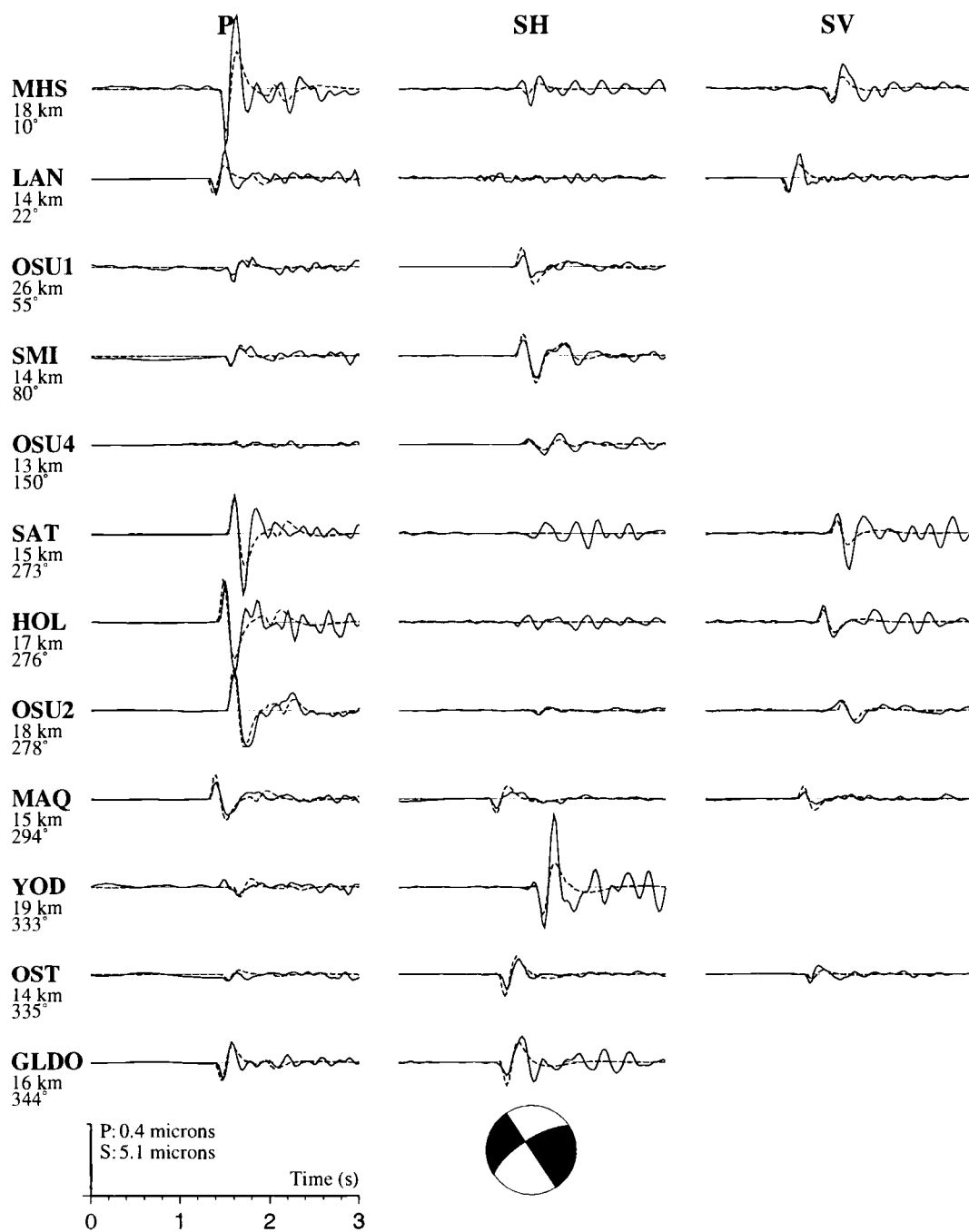


Figure 2.5.7 (continued) B) All traces used in the inversion in the 1.0 - 5.0 Hz pass band for event 13.

C)

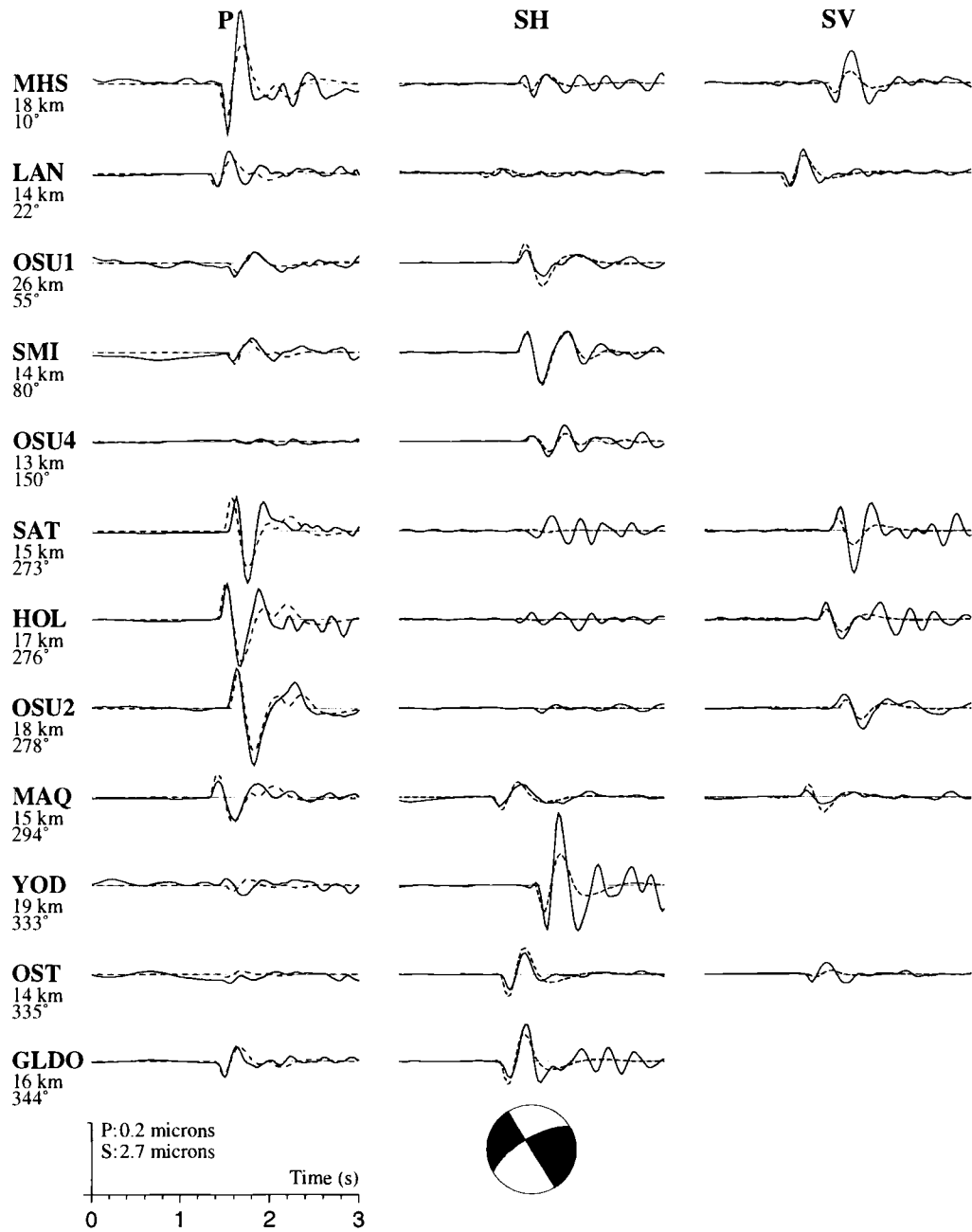


Figure 2.5.7 (continued) C) All traces used in the inversion in the 1.0 - 3.0 Hz pass band for event 18.

D)

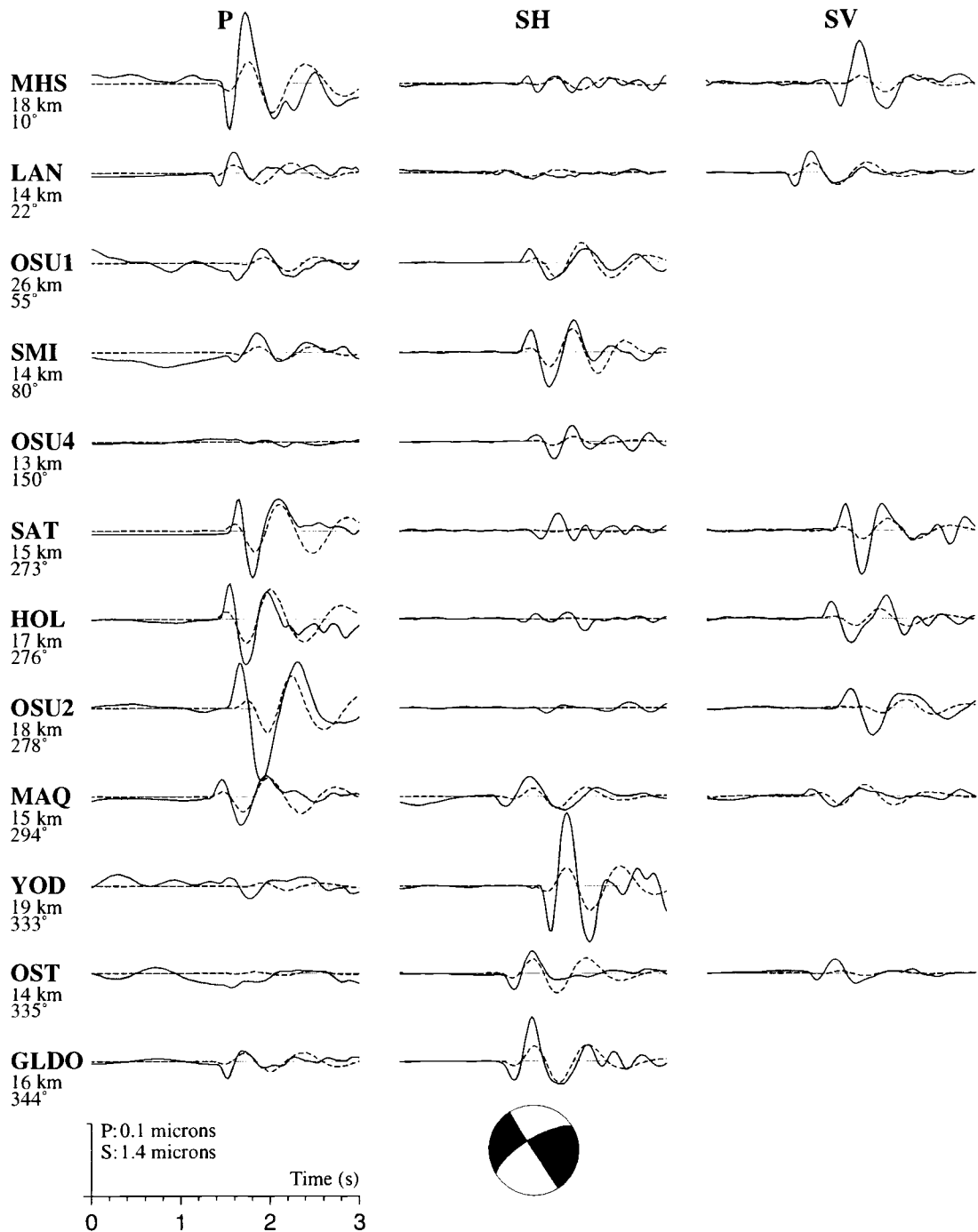


Figure 2.5.7 (continued) D) All traces used in the inversion in the 1.0 - 2.0 Hz pass band for event 18.

waveforms and sufficient signal power is found in the frequency band with a low-pass cut-off at 3.0 Hz.

In summary, we found the narrow frequency band between 0.5 Hz and 3.0 Hz most suitable for the inversion in this study, though in general the cut-offs will depend on the knowledge of crustal structure, noise, data quality, and recording geometry.

2.5.4 Resolution of Faulting Parameters

A major concern is the resolution of the source parameters, i.e., if the variability we see in aftershock focal mechanisms is indeed contained in the data. A glance at the seismograms of the two sample events 13 and 18 (e.g., Figure 2.5.6 A and Figure 2.5.7 A), clearly shows significantly different waveforms recorded at the same stations for similar event locations. Whereas P is nodal at OSU4 for event 18, it is certainly antinodal for event 13, with the opposite being true at station OSU2. There is no doubt that we can distinguish a thrust from a strike slip mechanism. But how well can we constrain, for example, the shallow dip of event 13's one nodal plane? This question is not easily addressed, and the resolution of the focal mechanisms will differ from event to event, depending, for example, on recording geometry and data quality.

2.5.4.1 Variance

To get a rough estimate of uncertainties, I independently perturb the three parameters, strike, dip, and rake, around the best-fitting double-couple solution (Figure 2.5.8 A and 2.5.8 B). The resolution is similar in the three tested frequency bands. For event 13, the dip-angle of the fault plane is best resolved, while the strike is the least resolved parameter. In the frequency band 0.7 - 3.0 Hz, relative to the best-fit, the bounds for a five percent increase in variance are $\pm 13^\circ$ for strike, -8° to $+6^\circ$ for dip, and $\pm 11^\circ$ for rake. For event 18, the strike is more tightly constrained than dip and rake. Relative to the best fit in the 1 - 3 Hz frequency range, the bounds for a five percent variance increase are $\pm 8^\circ$ for strike, -10° to $+9^\circ$ for dip, and -8° to $+9^\circ$ for rake. From these estimates, we

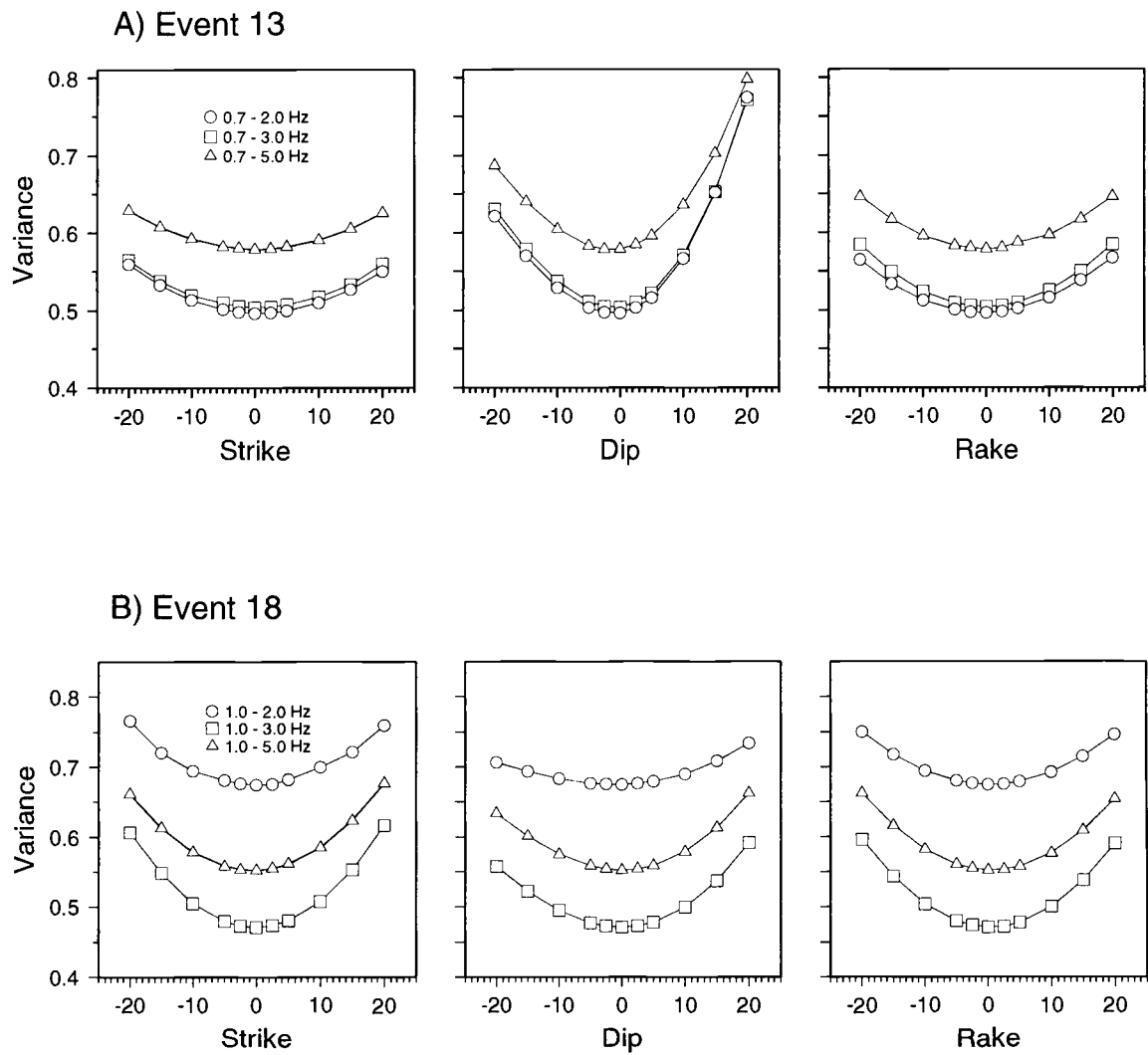


Figure 2.5.8 Variance versus deviation from the best-fit double-couple solution in three frequency bands for A) event 13, and B) event 18.

like to believe that uncertainties in the parameters describing the source orientation are in the range of $\pm 10^\circ$ to $\pm 15^\circ$.

2.5.4.2 T-test

Yet we do not know if a 5% difference in normalized variances is statistically significant. If the data of the time series recorded at individual stations are not statistically independent, using a standard F-test to compare two models by their overall variances might not be opportune (Huang *et al.*, 1986). Huang *et al.* (1986) suggest using the mean square residuals at each station, instead of residuals of individual time samples, to assure statistically independent data.

To compare two models a and b, we take the differences, d_i^{ab} , of the mean squared residuals (r_i^a and r_i^b) at each of the N stations:

$$d_i^{ab} = (r_i^a)^2 - (r_i^b)^2 \quad i = 1, 2, \dots, N,$$

and test the null hypothesis $\mu^{ab} = 0$ by forming the statistics

$$t^{ab} = \frac{\mu^{ab} \sqrt{N}}{\sigma^{ab}},$$

where μ^{ab} and σ^{ab} are the mean and standard deviation of the set of d_i^{ab} respectively. t^{ab} follows the one-sided t-distribution with N-1 degrees of freedom.

For event 13 we will use a t-test to determine a significant change between our best-fit model and models with perturbed source parameters. We find that our best model fits the data significantly better at the 95% confidence level than models with strikes deviating $+7^\circ/-8^\circ$, dips deviating $+20^\circ/-4^\circ$, and rakes deviating $+4^\circ/-8^\circ$. These results indicate that the source parameter are well resolved in the inversion.

2.5.4.3 By Eye

The numbers derived above might be equivocal, and a qualitative look on the data may be more convincing than statistics. Figure 2.5.9 shows some observed seismograms of two small events (event 38, $M_w=1.84$, and event 39, $M_w=1.86$), separated by five hours on April 1, 1993. Their complete source parameters are contained in Table 2.5.3, and all observed and synthetic seismograms used in the inversion are shown in Appendix Figures

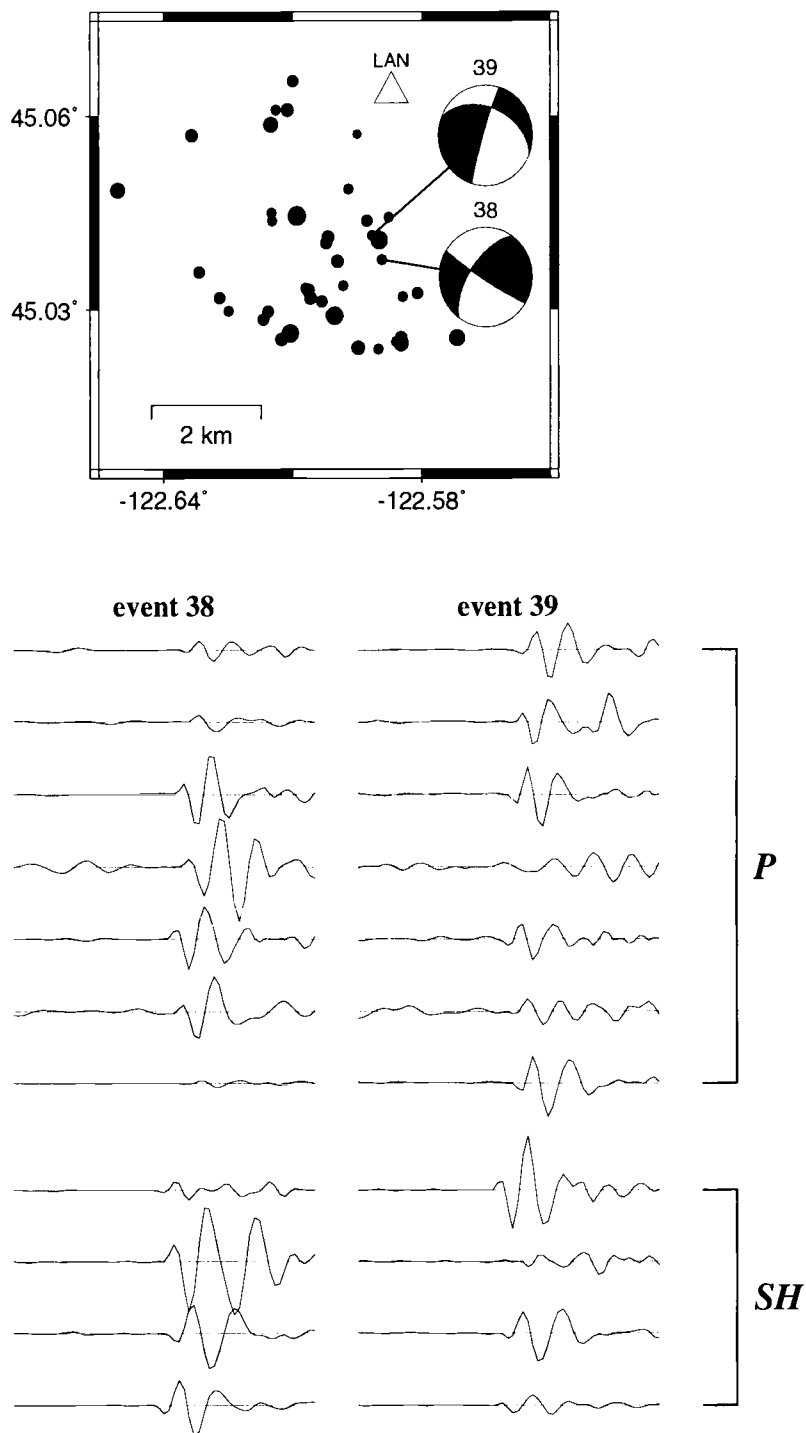


Figure 2.5.9 Top: Location and mechanisms for event 38 and 39. Filled circles are locations of aftershocks investigated in this thesis. Bottom: Observed seismograms for both events, that show clear distinction in waveforms and amplitudes.

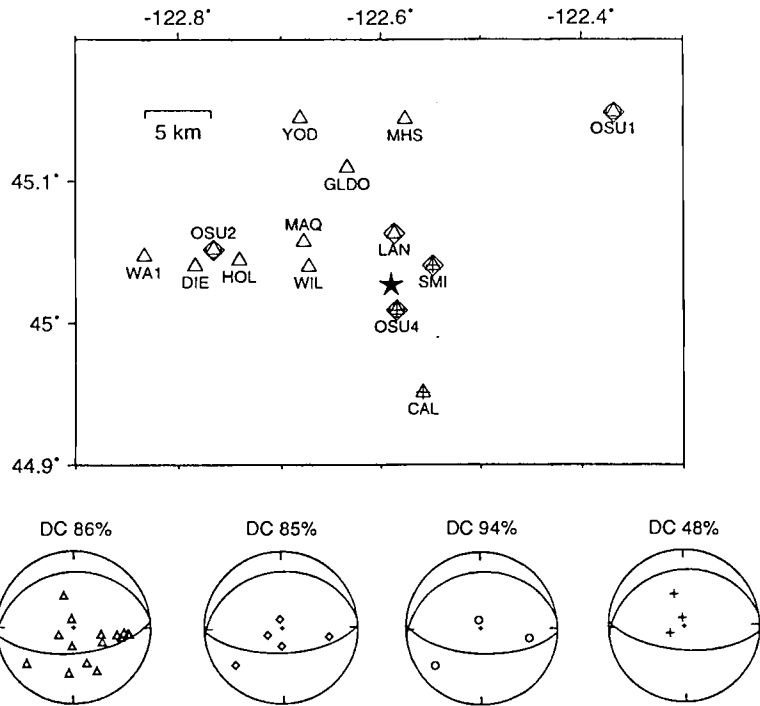
A.38 and A.39. Their map locations (Figure 2.5.9) are very close together, so that their positions relative to the recording stations are about the same, and differences in waveforms should not be caused by different paths or different event-receiver geometry, but can solely be attributed to the source. The beachballs in Figure 2.5.9 ascribe both earthquakes a left lateral strike slip mechanism. A second, more detailed look, however, unveils some distinct differences in the orientations of their nodal planes. We would like to see if these differences can also be perceived as differences in their waveforms. I therefore plotted those traces side by side, that exhibit the greatest distinction, at either P or SH . The traces are scaled to the maximum amplitude in each panel. At many sites, striking differences in amplitudes and waveforms can be beheld. The whole amplitude pattern, constraining the source parameters, is shifted, polarities differ for the two earthquakes at many stations (P polarity clearly differs at SAT, HOL, and OST, SH polarity differs at LAN, SMI, and OST), and one event's nodal station becomes dominant for the other event and vice versa. This example makes clear, that the observed seismograms can not be explained by the same sources, and, that the different mechanisms derived in the inversion are in fact required by the data, thus strengthening our confidence in the results.

2.5.5 The Influence of Recording Geometry on Inversion Results

Because of the ephemeral character of the seismic network and large differences in magnitudes, the station coverage greatly varied for most events' recordings. It is therefore meaningful to learn how varying recording parameters affect the focal parameters derived in the inversion. We revisit events 13 and 18. Their good coverage allows to investigate the effect of changing station geometry. We shall alter the number of stations used in the inversion, and compare the resulting fault plane solutions.

Figure 2.5.10 shows maps for event 13 and 18, with event (star) and station locations. Plotted below the maps are focal mechanisms, with the stations that were used in the inversion projected into the lower hemisphere. Same symbols are used for stations

A)



B)

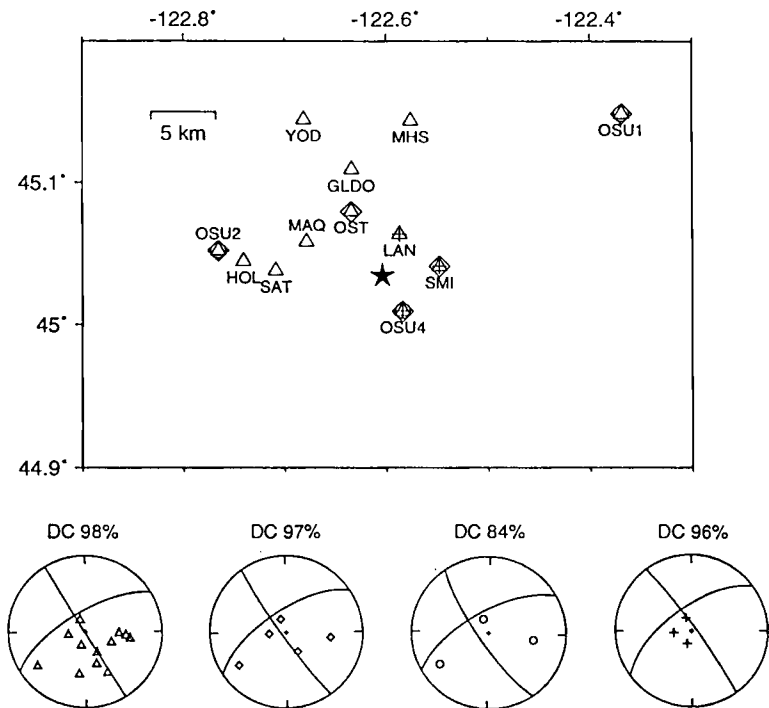


Figure 2.5.10 Maps showing event (star), station geometry, and fault plane solutions for different station distributions for A) event 13, and B) event 18. Symbols for the stations are the same in map and focal sphere.

on the map and in the focal spheres. I use the focal mechanisms, derived by employing all stations (triangles in Figure 2.5.10) in the inversion, as reference, to which the later results will be compared. In a first experiment, the 15 stations for event 13, and the 12 stations for event 18 are reduced to five stations respectively (diamonds in Figure 2.5.10). This new distribution, though with a significantly smaller number of sites, still covers a wide range of azimuths and distances. The resulting mechanism changes only slightly in source orientation (maximum change $\pm 4^\circ$ for both events) and DC portion.

In a second experiment, the number of stations is further decreased, with only three sites remaining in the inversion (circles in Figure 2.5.10). But these stations are still well distributed around the source. The resulting mechanisms are similar to the reference solutions. For event 13, source parameters change by 8° at the most, while for event 18, the solution differs by up to 11° from the reference mechanism.

In a third experiment, I keep the number of stations at three, but degrade their spatial distribution (crosses in Figure 2.5.10). The main effect for event 13 is a strong increase in CLVD part of the moment tensor, whereas the DC mechanism stays similar to the reference, with a maximum change of 10° in source orientation. For event 18, the DC portion stays high, and all source parameters remain within 5° of the reference mechanism, except the rake belonging to the vertical nodal plane, which differs by 46° .

Overall, the mechanisms are robust towards changes in station coverage. In most events' inversions, more than three stations were used, usually with good coverage around the source. Only event 41 had the same, one-sided coverage, as the last realization for event 13 in this test. However, learning from this experiment, the DC mechanism should still be reliable.

2.5.6 Comparison of Four Fault Plane Solutions Derived by Waveform Modeling with Results from a First Motion Study

Thomas and collaborators (1996) published focal mechanisms for 10 aftershocks of the 1993, Scotts Mills earthquake. For four of those only PNSN data was used. For

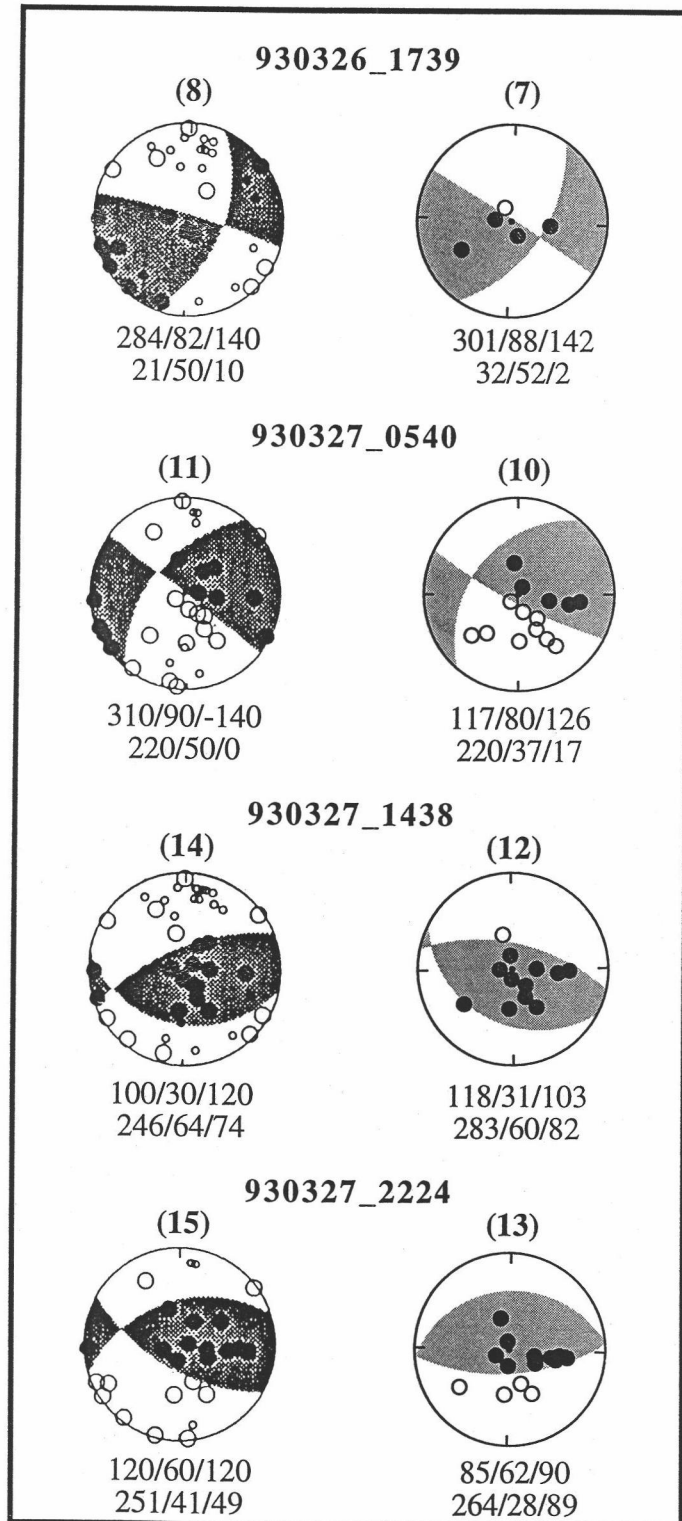


Figure 2.5.11 First motion fault plane solutions from Thomas *et al.* (1996) (left), and the solutions derived in this thesis by waveform modeling (right). The numbers in parentheses are the event numbers referred to in Thomas *et al.* (1996) (left) and the event numbers referred to in this thesis (Table 2.5.3).










another four events with sufficient station coverage by the temporary array, we computed moment tensors. Figure 2.5.11 juxtaposes those four earthquakes, for which both solutions are available. First arrivals are equal-angle-projected into the lower hemisphere. Solid circles represent compressional first motion, open circles dilatational, and larger circles correspond to rays that travel through the upper hemisphere. Overall, the solutions compare well. First motion fault plane solutions for events 970327_1438 and 930327_2224 (events 12 and 13 in Table 2.5.3) however, show a strike slip component, that is not seen in the mechanisms derived by waveform modeling. It is noted, that the strike slip components are mainly required by the compressional first motions of one station for event 970327_1438, and two stations for event 930327_2224. Those stations are roughly between 80 km and 100 km away from the epicenter. At these distances, the interpretation of the first arrival as direct (P_g , travels through the upper focal-hemisphere), or head wave (P_n , travels through the lower focal-hemisphere) becomes ambiguous, and is strongly dependent on the velocity model in use. Correct interpretation, however, is crucial, because the two rays emanate from the focal sphere at different angles. A second point to be made is that amplitudes at westernmost station in the compressional quadrant, WA1, (far right in the focal sphere) are clearly nodal for both events (see Appendix Figures A.12 and A.13), which does not conform with first motion mechanisms, where station WA1 is in the center of the compressional quadrant.

2.5.7 Results

Source parameters for all 41 earthquakes analyzed in this thesis are summarized in Table 2.5.3. Figure 2.5.12 maps the focal mechanisms on their single-event locations. Appendix A contains all observed and synthetic waveforms used in the inversions.

Focal mechanisms for all 41 earthquakes are varied, ranging from pure thrust to pure strike-slip, with common, approximately N-S pressure axis. The DC component of the moment tensors is generally high. Only two events (8 and 26) have DC's comprising less than 50 percent of the moment tensor. Those two events are both within a small

Table 2.5.3 Source parameters for 41 aftershocks of the 1993, Scotts Mills earthquake

	Ev. #	OT date	OT h:m:s	Lat (°N)	Lon (°W)	CD (km)	S/D/R (°)	P(az/pl) (°)	T(az/pl) (°)	M _w /m _c	DC (%)	Stat.'s #
	1	930326	07:35:49	45.024	122.590	11.7	221/70/351 314/81/200	179/21	86/8	1.88/1.8	95	6
	2	930326	08:00:05	45.029	122.600	12.4	148/83/119 250/30/14	214/32	86/44	2.98/2.9	96	6
	3	930326	10:22:51	45.032	122.585	11.8	13/36/186 278/86/306	220/38	339/32	1.84/1.7	57	6
	4	930326	12:45:23	45.030	122.615	10.3	75/36/47 304/65/116	15/16	254/61	1.92/1.7	94	5
	5	930326	12:55:39	45.025	122.613	11.6	123/78/137 225/48/17	180/19	74/39	2.13/2.0	84	5
	6	930326	16:54:31	45.026	122.610	11.5	127/22/139 257/76/73	360/29	145/56	3.04/3.1	61	6
	7	930326	17:39:22	45.044	122.609	14.1	32/52/2 301/88/142	353/24	250/27	3.23/3.1	99	5
	8	930326	18:43:48	45.059	122.615	11.1	61/50/59 284/49/121	172/0	263/67	2.63/2.8	17	6
	9	930326	19:56:44	45.044	122.588	13.0	167/53/22 63/73/140	119/13	19/40	1.74/1.5	70	3

OT - origin time in UTC. CD - centroid depth. Location and origin time were determined by single event location. S/D/R - strike/dip/rake. P - azimuth and plunge of pressure axis. T - azimuth and plunge of tension axis. M_w - moment magnitude. m_c - coda magnitude. DC - double couple percentage. Stat.'s - number of stations used in inversion.

Table 2.5.3 continued












	10	930327	05:40:33	45.027	122.575	12.7	117/80/126 220/37/17	180/26	62/43	2.75/2.6	89	12
	11	930327	06:46:07	45.057	122.633	9.5	21/73/85 217/18/105	115/28	284/62	2.21/2.3	98	12
	12	930327	14:38:58	45.041	122.586	13.8	118/31/103 283/60/82	18/15	172/74	2.91/2.9	87	12
	13	930327	22:24:14	45.027	122.590	12.5	85/62/90 264/28/89	175/12	356/73	2.69/2.5	86	15
	14	930327	23:34:13	45.032	122.603	11.2	232/73/27 134/65/161	1/5	94/31	2.15/1.7	52	11
	15	930328	05:22:56	45.025	122.595	11.4	113/67/126 232/41/36	178/15	67/54	2.37/2.1	80	13
	16	930328	07:43:51	45.029	122.601	11.6	247/17/53 105/76/100	186/31	29/57	2.00/1.8	92	13
	17	930328	08:20:07	45.033	122.607	13.0	186/44/19 65/63/126	130/11	23/56	1.83/1.5	81	7
	18	930328	08:50:56	45.034	122.604	13.6	239/69/1 148/89/159	196/14	102/16	2.21/1.7	99	12
	19	930328	09:03:47	45.032	122.606	13.6	236/75/32 137/59/163	4/11	101/33	2.11/1.6	61	10
	20	930328	13:08:35	45.034	122.598	11.6	130/73/129 241/42/27	192/19	81/48	1.75/1.1	81	6

Table 2.5.3 continued






















	21	930328	15:50:36	45.030	122.625	10.76	298/68/170 32/81/22	163/9	257/22	1.86/1.7	98	9
	22	930328	23:26:18	45.032	122.603	11.4	90/87/103 191/13/12	168/41	13/46	2.07/1.4	77	13
	23	930329	00:16:31	45.041	122.602	13.2	61/49/73 266/44/109	163/3	264/77	2.26/2.0	98	15
	24	930329	02:19:38	45.028	122.590	11.3	98/68/105 242/27/57	176/21	32/64	2.14/2.0	98	8
	25	930329	10:39:59	45.028	122.617	10.6	86/29/77 280/62/97	8/17	212/71	2.04/1.5	100	12
	26	930329	22:47:46	45.061	122.611	10.5	55/48/98 223/48/82	155/6	26/80	2.12/1.9	42	4
	27	930330	07:43:30	45.033	122.581	11.6	296/58/111 80/38/60	11/11	251/69	1.91/1.7	98	7
	28	930330	09:18:07	45.045	122.615	12.9	240/83/319 336/50/189	190/33	295/22	1.89/1.3	51	10
	29	930330	11:36:20	45.036	122.632	10.8	109/72/71 338/26/135	214/25	354/58	1.92/1.1	85	8
	30	930330	11:41:50	45.040	122.602	13.1	219/87/8 129/82/177	354/4	84/7	2.09/1.7	76	7
	31	930330	16:40:48	45.061	122.614	10.1	233/42/116 20/53/69	125/6	233/72	1.86/1.0	81	6

Table 2.5.3 continued

	32	930330	16:56:23	45.065	122.610	10.6	250/45/134 16/60/55	130/8	234/60	2.00/1.6	79	6
	33	930331	08:35:37	45.049	122.597	14.0	222/51/24 116/72/139	173/13	71/42	1.82/1.5	94	5
	34	930331	19:28:08	45.044	122.593	13.4	268/67/59 145/38/140	21/16	136/57	1.95/1.8	66	7
	35	930331	23:43:59	45.044	122.615	11.8	270/39/102 75/52/81	172/7	303/80	1.85/1.0	97	8
	36	930401	04:13:17	45.025	122.586	10.9	101/63/92 277/27/87	190/18	15/72	1.71/1.3	75	7
	37	930401	04:17:43	45.057	122.595	13.3	78/58/108 227/36/64	155/12	29/71	1.61/0.8	69	6
	38	930401	04:36:02	45.038	122.589	12.6	122/85/152 214/62/5	171/16	74/23	1.84/1.2	96	8
	39	930401	09:39:14	45.042	122.591	12.2	197/86/-47 291/43/186	143/35	254/28	1.86/1.2	94	10
	40	930402	16:28:42	45.032	122.627	11.3	59/74/80 273/19/123	157/28	314 /60	2.02/2.1	71	3
	41	930406	09:47:31	45.049	122.65	10.7	128/16/68 330/76/96	55/30	248/59	2.60/2.6	75	3

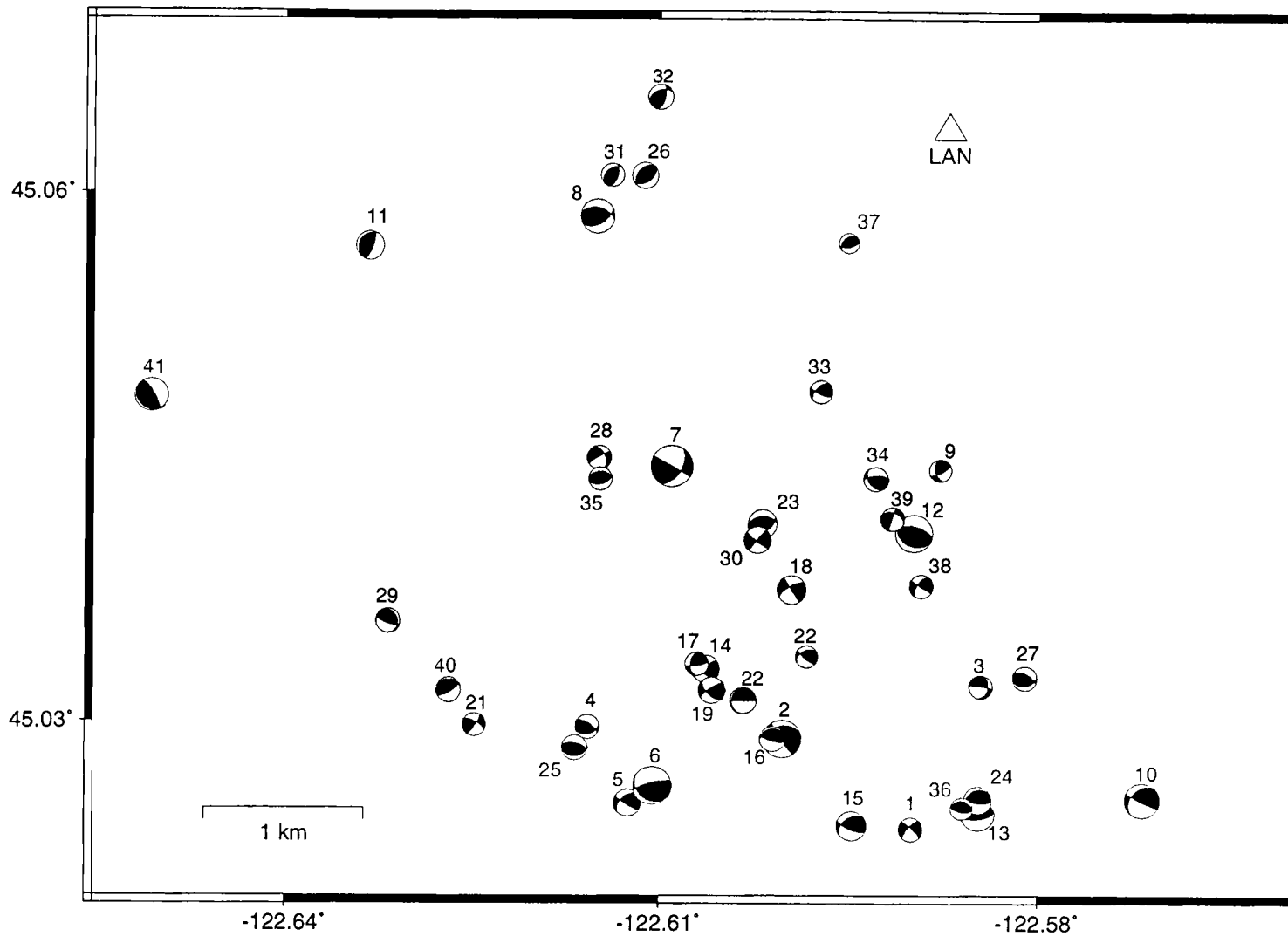


Figure 2.5.12 Map of all focal mechanisms determined in this thesis. Beachballs are sized according to magnitude of the event.

group of earthquakes to the north of the main cluster (see Figure 2.5.12). We have seen that errors in Green's functions, due to an incorrect velocity model or wrongly located epicenters, can be projected into the CLVD part of the solution. Because events 31 and 32, at similar location, have a normal DC component, it is unlikely that the high CLVD part for events 8 and 26 is caused by path effects. Traveltime residuals from hypocenter locations do not show any anomalies, and when relocated with a Joint Hypocenter Determination technique, locations of event 8 and 26 do not move considerably (see next chapter, Figure 3.3.3. A). A physical origin for the high CLVD component of these two events, caused, for example, by a complex rupture geometry, is thus favored.

Moment magnitudes differ at times considerably from coda magnitudes published by Thomas and colleagues (1996) (Figure 2.5.13). Especially for smaller events ($M_w \leq 2.0$), and at later times in the series, coda duration magnitude estimates are often significantly smaller than the magnitudes derived from the seismic moment (e.g., events 14, 18, 19, 20, 22, 25, 28, 29, 31, 32, 35, 36, 37, 38, and 39). A reason could be that small earthquakes, especially at later times when fewer of the temporarily deployed stations were in use, do not have enough recordings to guarantee a reliable magnitude estimate. Crosson (1972) found a deviation of the linear trend used to convert coda lengths into magnitudes derived from Wood-Anderson seismograph recordings for earthquakes in the Puget Sound area recorded by PNSN, with a magnitude smaller than two. This indicates that earthquakes at that size are not completely detected by the network in that area. Thomas and colleagues (1996) found a detection threshold at $m_c \leq 1.7$ for the Scotts Mills series. Another reason could be that the noise level for the small earthquakes is too high to allow for a dependable reading of coda duration.

2.5.8 Summary

Moment tensors were computed for 41 earthquakes recorded by 3 to 15 three-component seismographs. The earthquakes span a range in moment magnitudes from 1.6 to 3.2. The narrow frequency band between approximately 0.5 and 3.0 Hz was found to

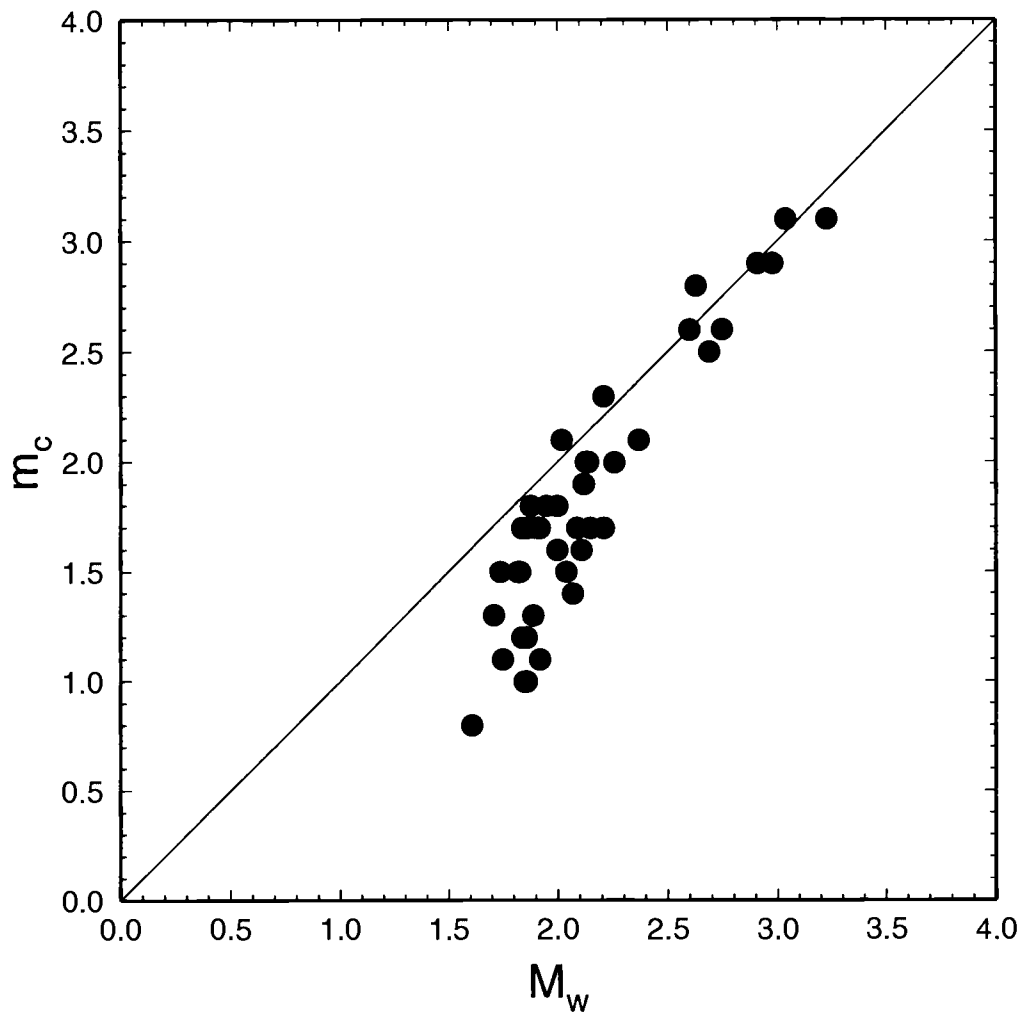


Figure 2.5.13 Graph showing moment magnitude estimate versus coda duration magnitude estimate. Coda durations clearly underestimate magnitudes for events with $M \leq 2$.

be most advantageous for inversion performance. We detected highly variable focal mechanisms, ranging from pure strike slip to pure reverse motion. The variability in mechanisms is believed to be real, and not caused by lack of resolution or varying station geometry. In fact we showed that mechanisms are stable over a wide range of frequencies and recording geometries, and that the resolution of source orientation is about $\pm 10^\circ$.

Chapter 3

EARTHQUAKE LOCATION TECHNIQUES AND THEIR APPLICATION TO THE SCOTTS MILLS AFTERSHOCK SEQUENCE

To interpret the group of focal mechanisms derived in Chapter 2, we have to assign each event as accurate locations within the sequence as possible. It will be especially fruitful to know the events' locations relative to each other. In this chapter different earthquake location techniques will be discussed and compared. Earthquake location algorithms can be divided into two broad groups: single- and multiple-event location techniques. Single-event locations are presented, as well as locations from *joint hypocenter determination* (JHD), a representative of the multiple-event group. The theoretical development of JHD is described in chapter 3.3, the code written for and used in the analysis is appended in Appendix B.

3.1 Single-Event Location

Nearly all earthquake location algorithms are based on Geiger's (1910) iterative, least squares method. In single event location schemes, data of each earthquake are inverted one at a time, as if they were the only event ever recorded. I use the code *lquake* developed at University of Washington for analysis of PNSN data. When picking arrival times, each pick is assigned an uncertainty, which is used as weighting in the inversion. For near stations those uncertainties could be as small as the sampling interval, 0.005 seconds for the SP instruments, and 0.02 seconds for the BB instruments. I used data from the temporary network as well as from PNSN, but down-weighted picks at hypocentral distances r greater than $d = 75$ km, according to $\left(1 + \left(\frac{r}{d}\right)^2\right)^{-1}$. For the three component seismographs of the temporary station array, horizontal records were rotated into event-receiver coordinates (transverse and radial components), to facilitate the

identification of S arrivals. The single event locations were already applied in chapter 4 for calculation of Green's functions, and are there summarized in Table 2.5.3. A map of all event locations together with their mechanisms is displayed in Figure 2.5.12

3.2 Multiple-Event Location

Most earthquake location methods rely on a one-dimensional layered earth model. In reality, the earth's crust is more complicated. Deviations from the assumed simple model cause errors in traveltimes calculations. These errors can be divided, based upon their origin, in three groups: from near the hypocenter, along the path, and from near the station. In a single-event method, it is not possible to discriminate between the three. This changes, however, if more than one earthquake is recorded by several stations. The most rigorous approach would be to invert simultaneously for three dimensional earth structure and hypocenter locations (Thurber, 1983). This method requires many events, very good station coverage, and excessive computer time. A less ambitious way within a one dimensional model is taken by *multiple-event* methods, which are founded on the observation that errors contaminating travel times from earthquake clusters are highly correlated, in particular, travel time errors are nearly constant for events recorded at the same station. These errors are caused by deviations from the simple model assumptions along the path, and at the receiver site, and lumped together into a single effect at each station, commonly called *station correction*. Naturally, the station correction vector s is not known *a priori*, and several different ways have been proposed to deal with this lack of information.

A simple way is to consider only arrival time differences at particular stations to obtain relative locations of events (e.g., Ansell and Smith, 1975). By doing so, site and path effects get shortened out. A drawback, however, is that all events have to be recorded at all stations, which can leave a lot of valuable data unused.

A second set of techniques assumes the station correction to be known for one particular earthquake, the master event. In the *master-event* technique, the station correction vector \mathbf{s} is simply set equal to the residual vector \mathbf{r} of one earthquake (e.g., Evernden 1969, and Thomas *et al.* 1996). The shortcomings of the method are obvious: It requires, that the master event is recorded by every station, which again leads to the deletion of useful data (In this data set event 23 has the most arrivals: 19 P and 15 S picks, which is only 34 of possible 47 picks, this would leave more than one quarter of the arrival time data unused). Secondly, because the corrections are based on a single measurement, they are subject to large uncertainties.

A technique which poses less demands on the data is the *joint hypocenter determination* (JHD) developed by Douglas (1967). Originally used mainly for teleseismic studies (e.g., Jordan and Sverdrup, 1981), it found also application in regional data sets (e.g., Herrmann *et al.*, 1981; Pavlis and Booker, 1983; and Pujol, 1988). In many applications, the resulting hypocenter locations give a more focused picture of seismicity than conventional techniques do (e.g., Schwartz *et al.*, 1989, this thesis). In the JHD method, arrival time data of more than one earthquake are inverted for hypocentral coordinates, origin times, and station corrections simultaneously, and the solution is found in a least squares sense.

In the implementation of JHD in this thesis, we seek station corrections for both P and S arrivals. We use a half space with a fixed P velocity, but invert additionally for v_s/v_p ratio. A half space is chosen for the ease of travel time calculation, and computation of corresponding partial derivatives, which in this case are simple analytical functions (see below). Because a half-space does not bend rays or generate refracted arrivals, we only use nearby stations, for which this effect is negligible. I used only the stations of the temporary array (except CHUO), and the two closest PNSN stations SSO and VG2 in the inversion. The linear system in this inversion problem is ill-conditioned, because the station corrections are linearly dependent on origin times, if earthquakes cluster in a small region. To overcome this problem, side-constraints are usually imposed. This is often done by fixing the location of one master event, or by setting the correction at one station to zero. Because we are additionally inverting for the

v_s/v_p ratio we decided however, to force the sum of P corrections, $\sum s_p$, and the sum of S corrections $\sum s_s$ to be zero.

3.3 Theoretical Basis of JHD

3.3.1 Forward Problem

In the development of the forward problem, I follow closely the notation of Pavlis and Booker (1983). Suppose we recorded arrival times for J earthquakes at N stations. We define the i^{th} measured arrival time for the j^{th} earthquake ($i=1, 2, \dots, I_j$, where $I_j = I_{P_j} + I_{S_j}$, and, I_{P_j} are number of P arrivals, and I_{S_j} are number of S arrivals for the j^{th} earthquake, $j=1, 2, \dots, J$) at the n^{th} station as t_{ij} . Then t_{ij} can be expressed as the functional

$$t_{ij} = t_{0j} + tt(\mathbf{x}_n, \xi_j) + \varepsilon_{ij} \quad (3.1)$$

$$i = 1, 2, \dots, I$$

$$j = 1, 2, \dots, J$$

$$n = 1, 2, \dots, N;$$

where t_{0j} = origin time of j^{th} earthquake,
 $tt(\mathbf{x}_n, \xi_j)$ = travel time from a source at location ξ_j to a receiver at location \mathbf{x}_n ,
 ε_{ij} = error in measuring arrival time t_{ij} .

From the measured arrival times t_{ij} we intend to estimate the spatial locations ξ_j and origin times t_{0j} for the J earthquakes. Because the calculation of travel times $tt(\mathbf{x}_n, \xi_j)$ is based on an idealized earth model, they are inherently inexact. We account for the differences between true travel times, and times calculated from our model by writing

$$tt(\mathbf{x}_n, \xi_j) \approx tt_{\text{model}}(\mathbf{x}_n, \xi_j, c) + s_n + \varepsilon_{ij} \quad (2),$$

where tt_{model} is the travel time calculated by some velocity model, c is v_s/v_p ratio, introduced to determine S velocities from the constant P velocities, and s_n is a constant associated with the n^{th} station, called *station correction*. Equation (2) only holds true in certain cases: If the velocity model is known well at depth, but poorly near the surface, than the terms s_n become equivalent to static corrections used in reflection seismology. Or, if the arrival times t_{ij} are from an earthquake cluster, where $tt(\mathbf{x}_n, \xi_j) - tt_{\text{model}}(\mathbf{x}_n, \xi_j)$ is approximately constant, and s_n describe the average path anomaly between the cluster and a particular station. The station correction vector \mathbf{s} is not known *a priori*, and has to be estimated in addition to the hypocenters ξ_j and the origin times t_{oj} . We follow Douglas (1967), and linearize equation (1) to obtain

$$t_{ij} = \hat{t}_{oj} + tt_{\text{model}}(\mathbf{x}_n, \hat{\xi}_j) + \hat{s}_n + \varepsilon_{ij} + \frac{\partial tt}{\partial x_1} \Big|_{x_n, \hat{\xi}_j} \delta x_1 + \frac{\partial tt}{\partial x_2} \Big|_{x_n, \hat{\xi}_j} \delta x_2 + \frac{\partial tt}{\partial x_3} \Big|_{x_n, \hat{\xi}_j} \delta x_3 + \frac{\partial tt}{\partial c} \Big|_{x_n, \hat{\xi}_j} \delta c + \delta t_{oj} + \delta s_n \quad (3).$$

The carats on $\hat{\xi}$, \hat{t}_o , and \hat{s} denote the best current estimates, about which the truncated Taylor series was expanded.

For a half space, rays are straight, and the i^{th} travel time from the j^{th} earthquake to the n^{th} station is calculated by the non-linear relationship

$$tt_{ij} = \frac{\sqrt{(x_{1n} - \xi_{1j})^2 + (x_{2n} - \xi_{2j})^2 + (x_{3n} - \xi_{3j})^2}}{v} \quad (4),$$

where v is the constant v_p for P arrivals, and $c \cdot v_p$ for S arrivals. Partial derivatives in (3) are easily calculated from (4):

$$\frac{\partial t}{\partial \xi_{kj}} = \frac{-(\hat{x}_{kn} - \hat{\xi}_{kj})}{v^2 t t_{ij}} \quad (k=1,2,3), \quad \frac{\partial t}{\partial t_{oj}} = 1, \quad \frac{\partial t}{\partial s_n} = 1,$$

$$\frac{\partial t}{\partial c} = 0 \text{ for } P \text{ arrival times, and } \frac{\partial t}{\partial c} = -\frac{t t_{ij}}{\hat{c}} \text{ for } S \text{ arrival times.}$$

So the i^{th} residual from the j^{th} earthquake becomes

$$r_{ij} = t_{ij} - \hat{t}_{oj} - t t_{\text{mod } el}(\mathbf{x}_n, \hat{\xi}_j, \hat{c}) - s_n \quad (5).$$

After substituting (3) into (5), the residuals can be written as

$$r_{ij} - \varepsilon_{ij} = \left. \frac{\partial t t}{\partial x_1} \right|_{x_n, \hat{\xi}_j} \delta x_1 + \left. \frac{\partial t t}{\partial x_2} \right|_{x_n, \hat{\xi}_j} \delta x_2 + \left. \frac{\partial t t}{\partial x_3} \right|_{x_n, \hat{\xi}_j} \delta x_3 + \left. \frac{\partial t t}{\partial c} \right|_{x_n, \hat{\xi}_j} + \delta t_{oj} + \delta s_n \quad (6).$$

We do not know, what the reading errors ε_{ij} are, but assume their statistics to be Gaussian. This is really only justified for impulsive arrivals (Buland, 1976), whereas for emerging arrivals the errors tend to be skewed towards a tendency to pick too late (Pavlis and Booker, 1983). Treatment of non-Gaussian errors, however, would be beyond the scope of this thesis. If they are Gaussian, they can be described by their variance σ_{ij}^2 , which is assigned to each arrival time during the picking process according to the quality of the individual data points. The variances are then used to define a set of weights

$$w_{ij} = \frac{1}{\sigma_{ij}^2} \quad (7),$$

to be used in the inversion later on.

After dropping ε_{ij} , equation (6) can be written as the partitioned matrix equation

$$\begin{bmatrix} \mathbf{r}_1 \\ \mathbf{r}_2 \\ \mathbf{r}_3 \\ \vdots \\ \mathbf{r}_j \\ -\sum s_p \\ -\sum s_s \end{bmatrix} = \begin{bmatrix} \mathbf{A}_1 & \mathbf{0} & \mathbf{0} & \cdots & \mathbf{0} & \mathbf{C}_1 & \mathbf{S}_1 \\ \mathbf{0} & \mathbf{A}_2 & \mathbf{0} & \cdots & \mathbf{0} & \mathbf{C}_2 & \mathbf{S}_2 \\ \mathbf{0} & \mathbf{0} & \mathbf{A}_3 & \cdots & \mathbf{0} & \mathbf{C}_3 & \mathbf{S}_3 \\ \vdots & \vdots & \vdots & & \vdots & \vdots & \vdots \\ \mathbf{0} & \mathbf{0} & \mathbf{0} & \cdots & \mathbf{A}_j & \mathbf{C}_j & \mathbf{S}_j \\ \mathbf{0} & \mathbf{0} & \mathbf{0} & \cdots & \mathbf{0} & \mathbf{0} & \mathbf{e}_p \\ \mathbf{0} & \mathbf{0} & \mathbf{0} & \cdots & \mathbf{0} & \mathbf{0} & \mathbf{e}_s \end{bmatrix} \times \begin{bmatrix} \delta \mathbf{h}_1 \\ \delta \mathbf{h}_2 \\ \delta \mathbf{h}_3 \\ \vdots \\ \delta \mathbf{h}_j \\ \delta \mathbf{c} \\ \delta \mathbf{s} \end{bmatrix} \quad (8),$$

where

$\mathbf{r}_j \in \mathbf{R}^1$ = residual vector for j^{th} earthquake, where $I = I_s + I_p$.

$\mathbf{A}_j \in \mathbf{R}^{I \times 4}$ = matrix of partial derivatives for the j^{th} earthquake

$$(A_{il})_j = \left. \frac{\partial t_i}{\partial \xi_l} \right|_{x_n, \dot{\xi}_j} \quad \text{for } l = 1, 2, 3; \quad (A_{i4})_j = 1.$$

$\mathbf{C}_j \in \mathbf{R}^1$ = vector containing partial derivatives after the v_s/v_p ratio for the j^{th} earthquake, i.e., $c_i = 0$ for $1 \leq i \leq I_p$,

$$\text{and, } c_i = \frac{\partial t_i}{\partial c} \quad \text{for } I_p < i \leq I_s.$$

$\mathbf{S}_j \in \mathbf{R}^{I \times 1}$ = diagonal matrix containing partial derivative coefficients for station corrections. Specifically, $s_{il} = \delta_{il}$.

We added two more lines to matrix equation (8), after its construction from (6) was completed. The two lines comprise the two constraints $\sum s_p = 0$, and $\sum s_s = 0$, which are necessary because of the ill-position of the inverse problem.

$\sum s_p \in \mathbf{R}^1$ = sum of previous (from $k-1^{\text{th}}$ iteration) estimates of P station corrections.

$$\begin{aligned} \Sigma_{S_S} \in \mathbb{R}^1 &= \text{sum of previous (from } k-1^{\text{th}} \text{ iteration) estimates of } S \\ &\quad \text{station corrections.} \\ \mathbf{e}_P \in \mathbb{R}^1 &= e_i \text{ equals } \lambda, \text{ for } 1 \leq i \leq I_P, \text{ and } 0 \text{ for } I_P < i \leq I_S. \\ \mathbf{e}_S \in \mathbb{R}^1 &= e_i \text{ equals } \lambda, \text{ for } I_P < i \leq I_S, \text{ and } 0 \text{ for } 1 \leq i \leq I_P. \end{aligned}$$

The size of λ determines the hardness of the constraint. For large values of λ the sum of the station corrections is constrained to zero.

We can write (8) now in the much abbreviated form

$$\mathbf{d} = \mathbf{G}\mathbf{m} \quad (9),$$

where $\mathbf{d} \in \mathbb{R}^{J+2}$, $\mathbf{G} \in \mathbb{R}^{J+2 \times 4J+1}$, and $\mathbf{m} \in \mathbb{R}^{4J+1}$.

3.3.2 Inverse Problem

Assuming Gaussian statistics, we can apply the same criteria as in chapter 2.2: minimizing

$$\chi^2 = [\mathbf{d} - \mathbf{m}(\mathbf{p})]^T \mathbf{C}_{d_0}^{-1} [\mathbf{d} - \mathbf{m}(\mathbf{p})],$$

(where \mathbf{C}_{d_0} are *a priori* estimates of the data-covariance, as from (7) = $\sigma_d^2 \mathbf{I}$) leads to the least squares solution (Menke, 1984):

$$\hat{\mathbf{m}} = [\mathbf{G}^T \mathbf{W} \mathbf{G} + \epsilon^2]^{-1} \mathbf{G}^T \mathbf{W} \mathbf{d}$$

with the weighting matrix \mathbf{W} being the inverse of the covariance matrix \mathbf{C}_{d_0} . ϵ^2 is a damping factor, mitigating the effect of small eigenvalues.

All of the above was implemented in *MATLAB*, and singular value decomposition was used for the actual inversion.

3.4 Results

P and S arrival time data for 25 stations were used to jointly invert for hypocentral parameters of 41 earthquakes and 47 station corrections (25 P corrections and 22 S corrections). In Figure 3.4.1 a map shows station distribution and the number of picks at each site (black columns are P picks, gray columns are S picks). Azimuthal distribution is good, and most stations have more than 10 P and S picks, respectively. SSO and VG2 are PNSN stations, which are equipped with only a vertical component seismometer, station SIV recorded only the vertical component correctly, for these stations no S picks are available. VG2 is with approximately 50 km the most remote station.

The inversion needed only few iterations to converge to a solution. I used the single-event locations, zero station corrections, and $v_p/v_s = 1.78$ as starting model. The inversion showed to be relatively insensitive to the beginning values of the model parameters, if they were kept in reasonable bounds. The cumulative RMS residual of the solution was reduced almost tenfold from 0.3508 s to 0.0364 s.

The inversion found a v_p/v_s ratio of 1.78 for a half-space P velocity of $v_p = 5.5$ km/s. This is a reasonable value and agrees with what other investigators (Thomas *et al*, 1996) found in this area. However, the value was strongly dependent on the fixed P velocity (i.e., v_p/v_s ratio increased approximately linearly with increasing P velocity).

Station corrections are summarized in Table 3.4.1. Station CAL has with 0.21 s the highest P correction, while BYR has the largest S correction with 0.40 s. Figure 3.4.2 shows a station map with the corrections superimposed as circles with their radii proportional to the correction time. Dashed lines stand for S corrections, solid lines for P corrections, and thick lines indicate positive values, whereas thin lines represent negative ones. It is clearly seen that topography is the governing factor for size and sign of the correction terms. As we cross from the valley into the Cascade foothills the correction terms change polarity from negative to positive and become larger with higher station elevation. Even though we include station elevations when calculating travel times, the on average too fast half-space velocities in this upper layer cause too short theoretical

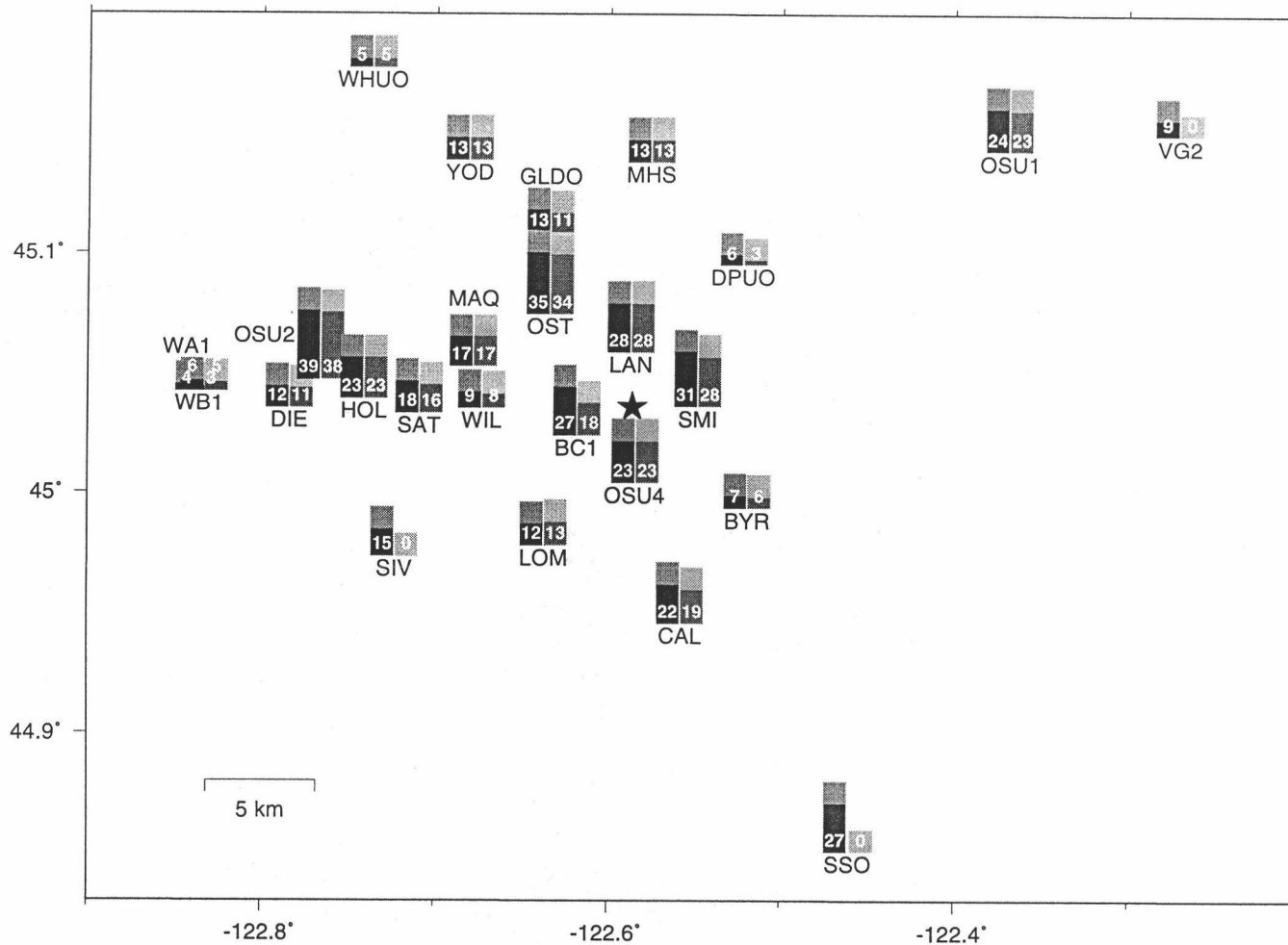


Figure 3.4.1 Map of the stations used for *JHD*. Columns show number of picks at each site. Black columns are for *P* picks, gray columns for *S* picks

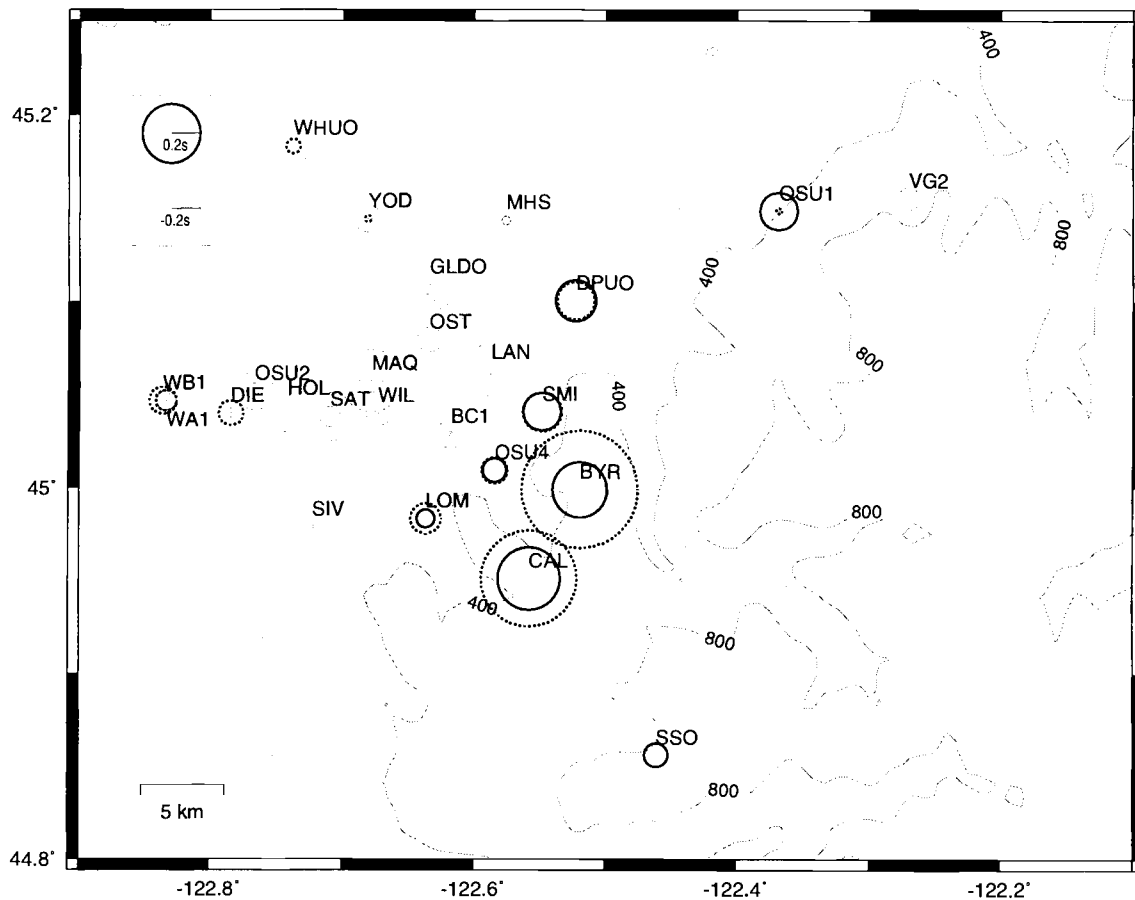


Figure 3.4.2 Map showing station corrections as circles, with their radii proportional to size of the correction term. Solid lines represent P corrections, dashed ones S corrections. Thick lines stand for positive values, thin ones for negative corrections. Note how the corrections change sign, and increase in size when traversing from the Willamette Valley into the Cascade foothills.

travel times which result in positive station corrections. For example, if we have a real velocity of 2.5 km/s in the upper 600 m instead of the assumed 5.5 km/s, the systematic travel time difference at station BYR (660m above sea level) is 0.144 s, which makes up the major portion of the inversion derived 0.187 s. The remainder can be caused by local deviations at the site or an average deviation along the travel path. Station VG2 lies at an elevation of 823 m, yet its station correction is negative. This is, because at larger distances from the source, the average path effect outweighs local effects, and an on average slightly too slow velocity could cause the small negative correction term.

Table 3.4.1 Station Parameter and Corrections.

Station	Latitude [°N]	Longitude [°W]	Elevation. [m]	<i>P</i> - station correction [s]	<i>S</i> - station correction [s]
BC1	45.0289	-122.6180	192	-0.0157	-0.0990
BYR	44.9990	-122.5190	660	0.1878	0.4016
CAL	44.9511	-122.5580	615	0.2148	0.3304
DIE	45.0403	-122.7840	64	-0.0313	0.0856
DPUO	45.1006	-122.5225	100	0.1405	0.1287
GLDO	45.1092	-122.6340	91	-0.0695	-0.1818
HOL	45.0442	-122.7410	92	-0.0740	-0.1799
LAN	45.0636	-122.5870	207	-0.0307	-0.1794
LOM	44.9835	-122.6370	277	0.0624	0.1050
MAQ	45.0577	-122.6780	116	-0.0782	-0.2129
MHS	45.1438	-122.5760	117	-0.0307	-0.0322
OST	45.0797	-122.6340	159	-0.0855	-0.2679
OSU1	45.1488	-122.3686	400	0.1283	0.0199
OSU2	45.0520	-122.7659	130	-0.0553	-0.1296
OSU4	45.0094	-122.5843	320	0.0817	0.0894
SAT	45.0381	-122.7090	181	-0.0700	-0.1666
SIV	44.9790	-122.7230	308	-0.0185	—
SMI	45.0409	-122.5480	415	0.1305	0.1358
WHUO	45.1832	-122.7373	100	-0.1170	0.0482
WIL	45.0402	-122.6730	216	-0.0488	-0.0852
YOD	45.1446	-122.6810	67	-0.0922	0.0234
WA1	45.0471	-122.8335	56	-0.0684	0.0710
WB1	45.0471	-122.8360	56	-0.0643	0.0956
SSO	44.8560	-122.4605	1242	0.0818	—
VG2	45.1556	-122.2708	823	-0.0777	—

A map that shows *JHD* relocation and the shift from the original single-event locations is displayed in Figure 3.4.3 A. The precise values and root mean square residuals of the relocations are documented in Table 3.4.2. *JHD* moves the events in the cluster to the southeast and closer together, and some trends become perceptible. A group of four earthquakes in the north and some scattered events in the east become more isolated from the main cluster. Figure 3.4.3 B shows cross sections along line A, perpendicular to the strike of a best-fitting plane through the events. The planes were found by multivariate least-square regression. For the single-event locations the strike of the best-fit plane is 286° and its dip is 39° . The correlation coefficient of 0.54 is not very good. Although the cross section reveals a trend, the plane, i.e. the dip, is not well resolved. This changes if we look at the cross section of the relocated events. The improvement is quite astonishing, considering the simplicity of the assumptions. The plane is now well focused, and strike and dip are tightly constrained. Four events to the north and two events in the north-west are clearly separated from the plane. Disregarding those six events, a regression coefficient of 0.92 shows strong correlation. The best-fitting plane has a strike of $283^\circ \pm 4^\circ$ and a dip of $49^\circ \pm 4^\circ$ (uncertainties are 95% confidence limits). These parameters were stable using a suite of half-space velocities in the inversion. The two events at the bottom-left (events 18 and 19) were the only events to be located more than one standard deviation away from the best-fit plane. Figure 3.4.4 displays all focal mechanisms in a lower-hemisphere equal-area projection again, now on their new locations.

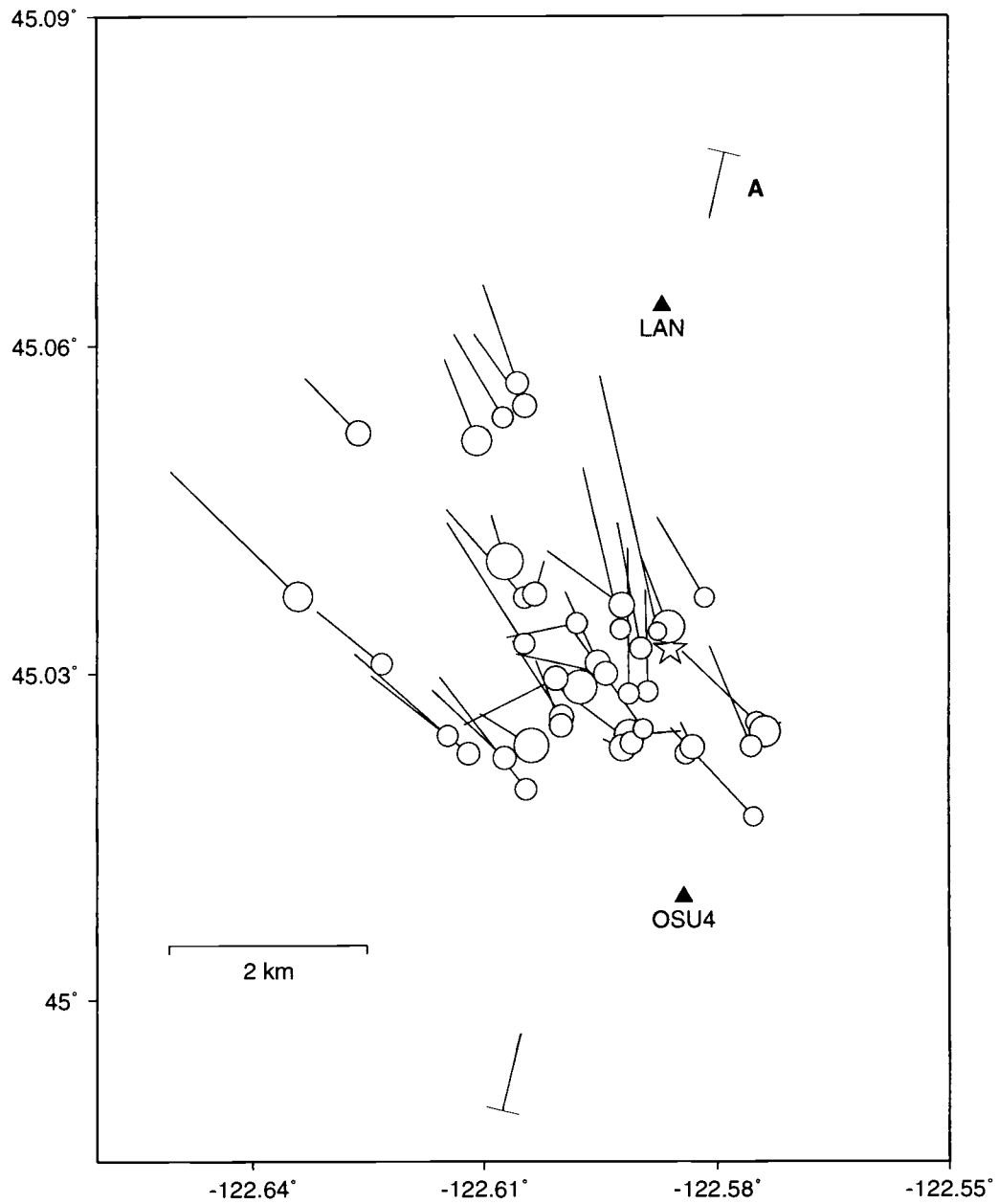


Figure 3.4.3 A) Map showing JHD relocations (circles). Lines point to the original single event locations. The bar A indicates the projection of the cross-sectional plane to the surface, seen in Figure 3.3.3 B.

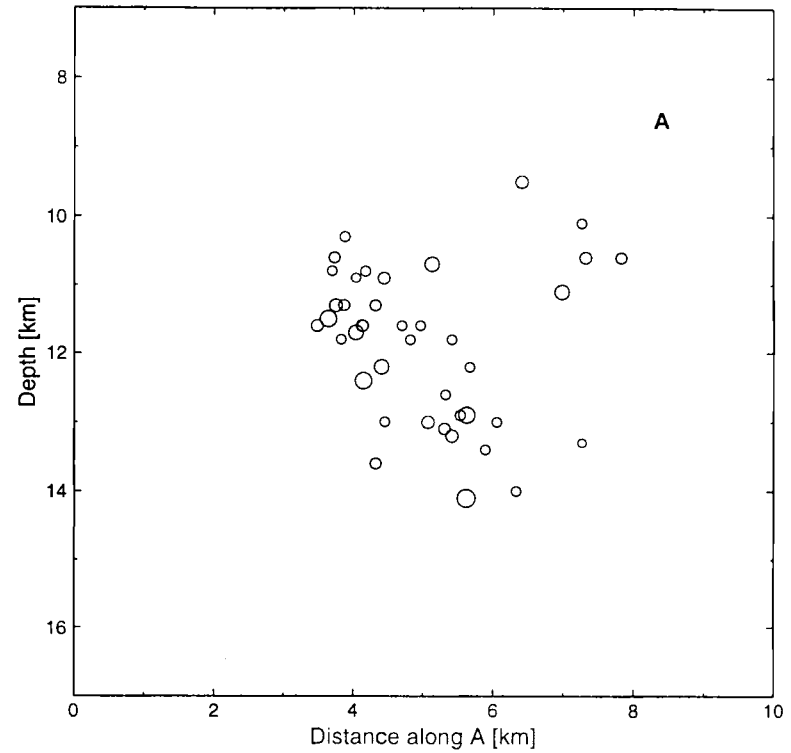
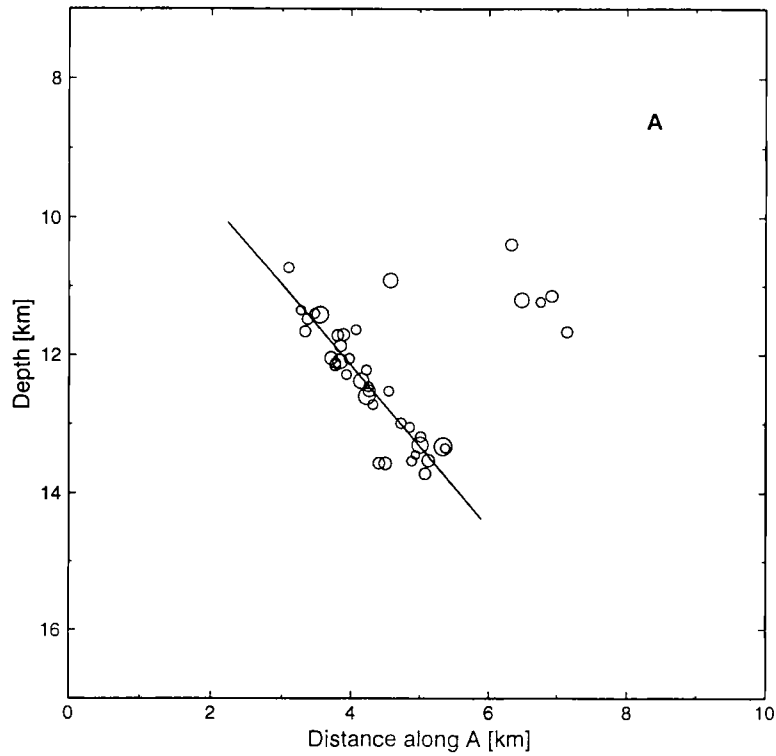


Figure 3.4.3 B) Right: Vertical cross section along line A, perpendicular to the best-fit plane. Locations are from the single-event method. Left: Vertical cross-section of JHD relocated events. The relocated events form a well defined plane. The black line shows the best-fit plane (dip 49°). There is no vertical exaggeration in neither of the plots.

Table 3.4.2 Event Parameters from JHD.

event #	Lat. [°N]	Lon. [°W]	Depth [km]	t_0 [s]	RMS [s]
1	45.0226	-122.5841	12.1	49.35	0.0163
2	45.0287	-122.5976	12.6	65.69	0.0188
3	45.0255	-122.5749	12.2	51.40	0.0220
4	45.0194	-122.6046	10.7	23.09	0.0576
5	45.0295	-122.6007	12.5	39.07	0.0128
6	45.0234	-122.6039	11.4	31.92	0.0377
7	45.0403	-122.6072	13.3	22.16	0.0398
8	45.0513	-122.6109	11.2	48.29	0.0450
9	45.0369	-122.5816	13.3	44.12	0.0182
10	45.0247	-122.5738	12.4	33.24	0.0315
11	45.0520	-122.6263	10.4	7.24	0.0489
12	45.0343	-122.5863	13.3	58.70	0.0380
13	45.0244	-122.5912	12.1	15.76	0.0253
14	45.0260	-122.6000	11.7	13.10	0.0250
15	45.0232	-122.5922	12.1	56.40	0.0332
16	45.0237	-122.5910	12.2	51.22	0.0356
17	45.0346	-122.5980	13.1	7.34	0.0318
18	45.0310	-122.5954	13.6	56.37	0.0459
19	45.0300	-122.5943	13.6	47.53	0.0322
20	45.0249	-122.5895	12.3	34.53	0.0318
21	45.0243	-122.6147	11.4	36.20	0.0420
22	45.0252	-122.6000	11.7	18.67	0.0444
23	45.0363	-122.5922	13.5	31.39	0.0573
24	45.0233	-122.5832	11.9	38.75	0.0200
25	45.0223	-122.6073	11.5	-0.36	0.0352
26	45.0545	-122.6046	11.1	46.16	0.0294
27	45.0233	-122.5756	12.1	30.32	0.0227
28	45.0369	-122.6047	13.2	7.18	0.0388
29	45.0309	-122.6233	11.6	20.04	0.0322
30	45.0373	-122.6034	13.7	50.45	0.0131
31	45.0534	-122.6075	11.2	48.43	0.0362
32	45.0566	-122.6056	11.7	23.11	0.0602
33	45.0340	-122.5924	13.5	37.69	0.0525
34	45.0323	-122.5898	13.0	68.59	0.0309
35	45.0327	-122.6048	12.5	59.13	0.0318
36	45.0168	-122.57530	11.3	17.49	0.0354
37	45.0338	-122.5876	13.4	43.88	0.0270
38	45.0283	-122.5889	12.7	62.40	0.0349
39	45.0282	-122.5914	12.5	14.54	0.0207
40	45.0227	-122.6120	11.7	42.73	0.0251
41	45.0370	-122.6341	10.9	32.00	0.0564

t_0 – Origin time in seconds, for date, hour, and minute of the event refer to Table 2.5.3. RMS – root mean square residual.

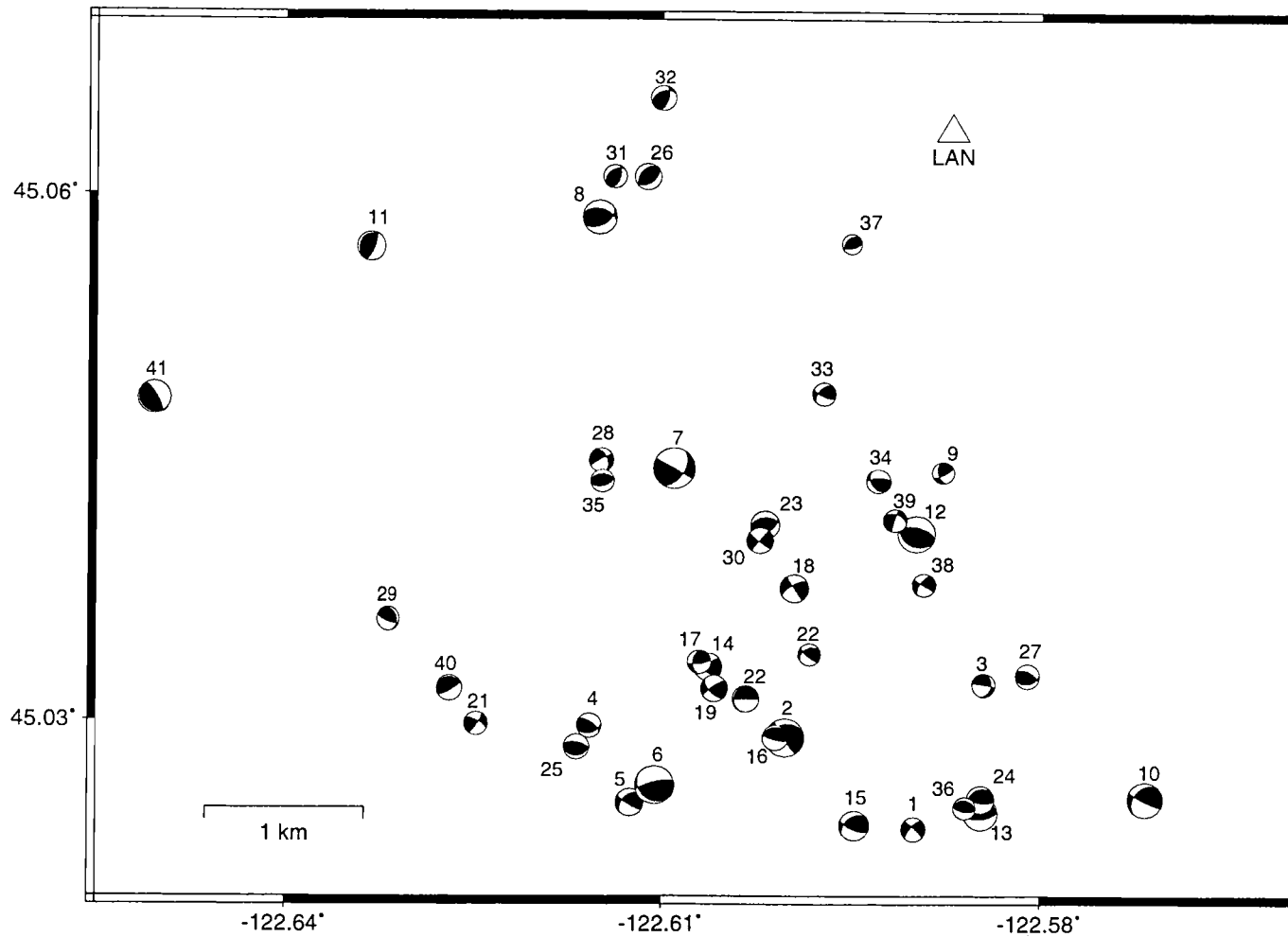


Figure 3.4.4 All 41 relocated earthquakes with focal mechanisms from Chapter 2 (lower-hemisphere, equal area projection).

Chapter 4

DISCUSSION**4.1 Methods**

We developed two techniques to analyze seismic data from local arrays. The Scotts Mills aftershock series was very well instrumented, setting a good ground for a first application and testing of these methods. Both procedures worked remarkably well. The moment tensor technique withstood tests on synthetic and real data with robustness. The inverse solutions were for the most part unbiased by station distribution, erroneous crustal models, and hypocenter locations in the test cases. Although uncertainties are difficult to estimate because data quality and recording geometry for each event differ considerably, based on the tests conducted, we believe that errors in source orientations are for most events smaller than 10° . We showed that waveform inversion methods can be very well applied to small earthquakes, and are a good alternative to conventional first motion techniques. Because they make more efficient use of the data, it is possible to obtain solutions even if the station distribution is sparse. Simple, three-component, short-period velocity transducers were sufficient for our analysis. This has wide implications for future deployments and investigations because, even for small earthquakes, detailed source characteristics can be obtained from relatively few digital, three-component records.

For the joint hypocenter determinations we used both P and S arrival times. Solutions were obtained for a very simple crustal model, i.e., a half-space. Although we did not perform an error analysis, we have reason to believe that the inversion was successful. The fact that the majority of the events collapsed to a well defined plane is unlikely to be fortuitous. We conclude that a one-dimensional model with site and path corrections is sufficient to obtain precise, relative event locations. Even if the events did in fact define a perfect plane, which is highly improbable considering the variety of their focal mechanisms, the scatter of the hypocenter locations would indicate relative location

errors smaller than 500 m. Further confidence is gained due to the correlation of station corrections with surface topography, in a manner that is expected from simple theoretic considerations.

4.2 Seismotectonics

The $M_w = 5.5$, 25 March 1993 Scotts Mills earthquake was the largest earthquake to occur in Oregon in more than a hundred years. Located approximately 35 km east of the state capital Salem, in the foothills of the Cascade Mountains, it was felt strongly throughout the densely populated Willamette Valley, and caused considerable damage amounting to more than \$28 million (Madin *et al.*, 1993). Seismicity in Western Oregon has been peculiarly low (e.g., Jacobsen, 1986) considering its situation above a subduction zone. At 5:35 AM this earthquake not only woke up a large part of the population of Western Oregon, but also raised tremendous earthquake awareness in a region that considered itself in safety several hundred miles north of earthquake-rocked California.

The mainshock mechanism was derived independently from three different data sets. By inversion of regional waveforms (strike = 302° , dip = 48° , rake = 145° , centroid depth = 12-13 km), teleseismic bodywave inversion ($297^\circ/51^\circ/138^\circ$, centroid depth = 14.3 km) (both Nabelek and Xia, 1995), as well as from first motion polarities utilizing PNSN data ($294^\circ/58^\circ/138^\circ$, hypocentral depth = 15.1 km) (Thomas *et al.*, 1996). These mechanisms are shown on an equal area projection in Figure 4.2.1 The location from Thomas *et al.* (1996) places the mainshock at the base of the aftershocks located in this study. Although it is difficult to compare the absolute locations, because they arise from different data sets and velocity models, this would indicate an upward rupture propagation. This is consistent with the difference between the two centroid depths from waveform inversion, which represent an average depth of moment release, and the hypocentral depth, which locates the point of nucleation. All three fault plane solutions are very similar, and their rakes indicate approximately equal amounts of thrust and

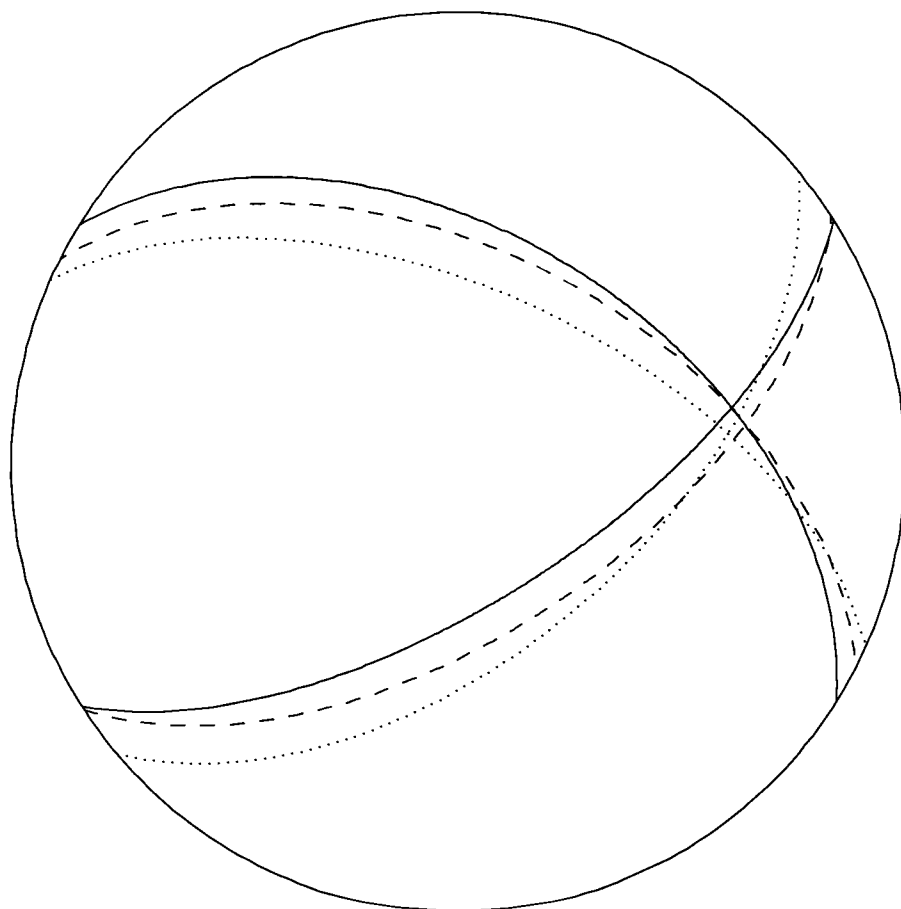


Figure 4.2.1 Three published mainshock mechanisms: Solid - from regional waveforms, dashed - from body waves, and dotted - from first motion polarities.

strike-slip motion. The preferred slip plane strikes northwest and dips to the north. The three planes differ by more than 10° in strike from the plane defined by the relocated aftershock hypocenters (strike = 283° , dip = 49°). The discrepancy is larger than the estimated uncertainties for any of the solutions. It is unclear, however, if a strike of 283° is really inconsistent with the respective data set used to determine the mainshock focal mechanisms, or on the other hand, if a bias was introduced to the aftershock locations by station distribution or station corrections. One should also consider, that the diversity of aftershock mechanisms precludes their occurrence directly on the slip plane, which causes an inherent uncertainty in the determination of the plane by their locations.

There was no surface rupture or ground cracking reported from the Scotts Mills earthquake. Although no mapped fault coincides directly with the mainshock epicenter, the Scotts Mills earthquake has been attributed to the Mt. Angel Fault (MAF) by previous investigators (Madin *et al.*, 1993, Nabelek and Xia, 1995, Thomas *et al.*, 1996). The MAF is part of the Gales Creek - Mt. Angel Structural Zone, the southernmost of several NW-trending, seismically active linear features in NW-Oregon and SW-Washington (Yeats *et al.*, 1996). This NW-trending lineament spatially correlates with a transition from anomalously thick Siletz basement (south) to Siletz terrane of transitional thickness (north), and from lower to higher forearc seismicity (Trehu *et al.*, 1994). Both Gales Creek Fault and MAF are thought to exhibit largely right-lateral strike-slip motion with some local reverse component (Werner *et al.*, 1992). MAF has been mapped based on water wells (Hampton, 1972) and from industry seismic reflection data (Werner *et al.*, 1992) to a length of approximately 25 km. Miocene Columbia River Basalts (CRB) are vertically offset by up to 250 m, whereas younger alluvial deposits show smaller separation, implying continuing post-Miocene deformation. In 1990, a swarm of small ($M \leq 2.5$) earthquakes near Woodburn was attributed to a deep extension of MAF suggesting ongoing deformation (Werner *et al.*, 1992). On high resolution aeromagnetic data collected in 1995 the MAF shows a strong signal. The magnetic anomaly across the fault however cannot be explained solely by displacements of CRB's, but requires significantly offset in deeper Siletz basement (Blakeley *et al.*, 1996). This implies that the MAF may have been active as early as Eocene. The Scotts Mills earthquake sequence

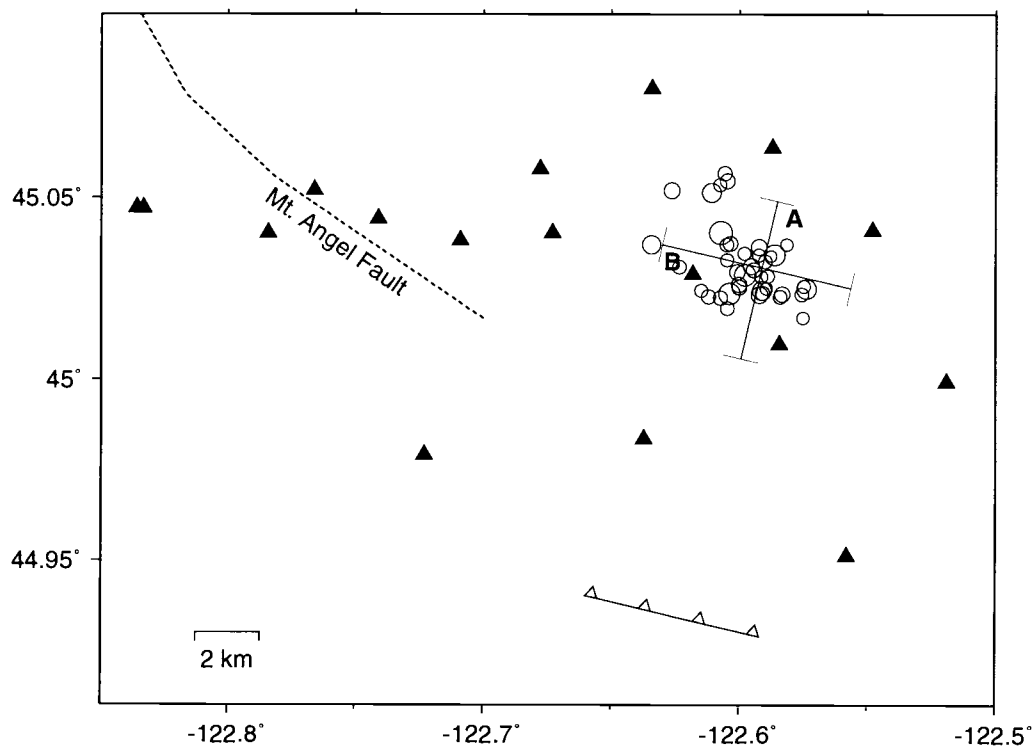


Figure 4.2.2 The Scotts Mills area. Aftershocks are indicated by the empty circles, the triangles locate seismic field stations. The mapped extent of Mount Angel fault (MAF) is indicated by the dashed line. The surface projection of the plane defined by the aftershock locations (barbed line) emanates south-east of MAF. Bars A and B locate the cross-sections that are displayed in Figure 4.3.3 and 4.5.1.

Aeromagnetic Anomalies, Northern Willamette Valley

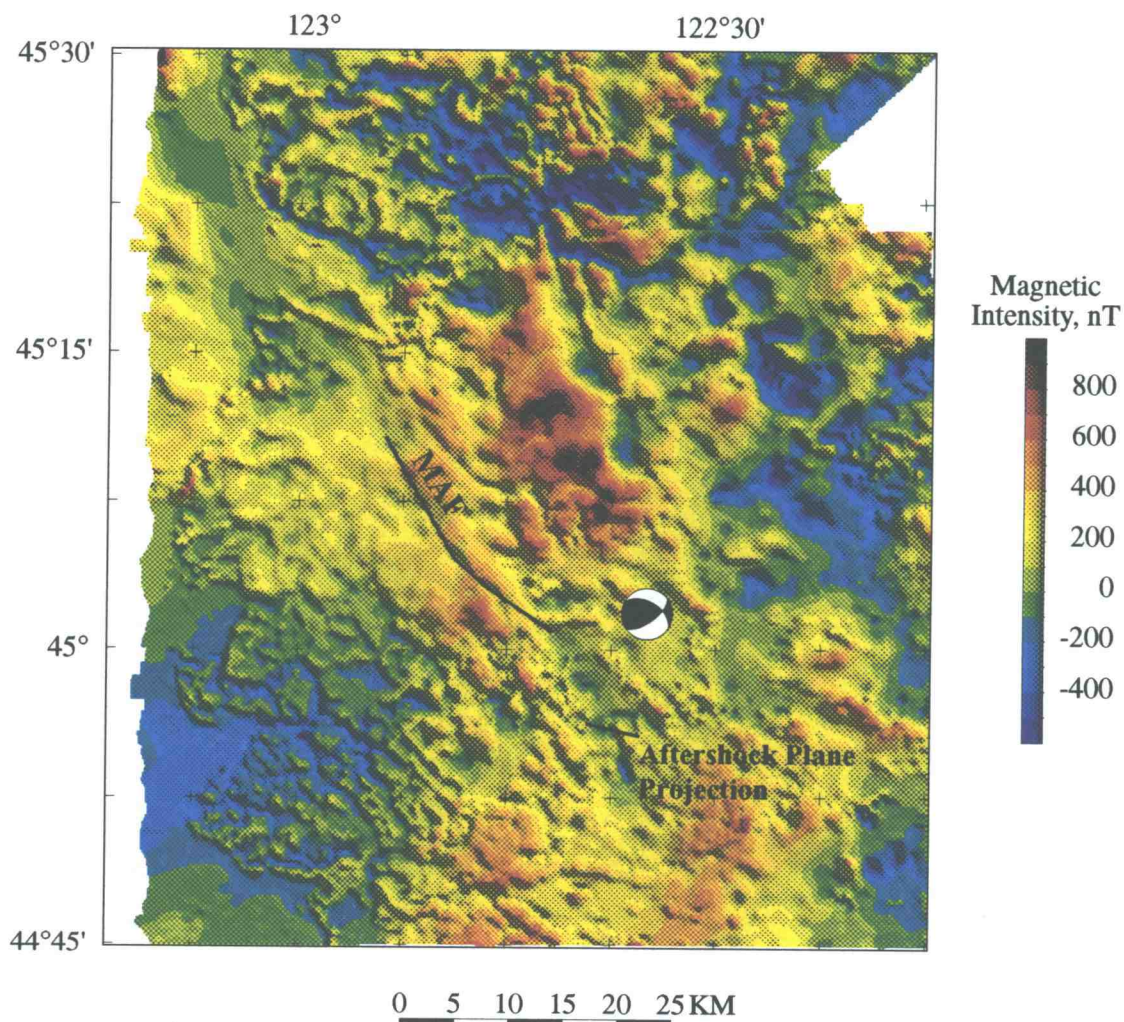


Figure 4.2.3 Map of aeromagnetic anomalies in the Northern Willamette Valley (from Blakeley *et al.*, 1996). Super-imposed is the mapped Mount Angel Fault (from Werner *et al.*, 1992) and the projection of the aftershock plane. MAF clearly correlates with a strong magnetic anomaly. No anomaly coincides with the estimated surface trace of the aftershock plane.

is located about 10 km east of the most southeasterly mapped extent of MAF (Figure 4.2.2). The surface projection of the aftershock plane emanates too far south and with a considerably smaller strike than the southeastern part of MAF as to be easily accepted as a direct extension of it. Both Thomas and colleagues (1996) and Nabelek and Xia (1995) suggested either a single upward curved fault or that the MAF zone is in fact consisting of several parallel faults as suggested by Werner and collaborators (1992) for the northwestern portion of it from a seismic reflection line. On the aeromagnetic data the MAF seems to bend northward when approaching the NE trending Waldo Hills Range Front Fault. Blakeley and colleagues (1996) proposed that the Scotts Mills earthquake may have occurred on a sinistral bend in the MAF. Plotting the surface projection of the aftershock plane on top of the aeromagnetic data, however, shows no clear correlation with an anomaly (Figure 4.2.3), and the relation of the Scotts Mills earthquake to the MAF remains unclear. Displacements on this subsurface fault may be too small as to leave behind a observable magnetic signal.

4.3 Stress-Field Considerations

Besides faulting geometry, a group of focal mechanisms provides information about stresses acting in the crust. In Figure 4.3.1 we show a composite plot of pressure (P) and tension (T) axes from the 41 moment tensors derived in Chapter 2. For a large number of earthquakes, assuming a pervasively fractured crust, the average direction of P and T axes approximate the directions of the principal stresses σ_1 (maximum) and σ_3 (minimum) respectively. The plot shows much greater dispersion for T axes than for P axes. P axes reveal approximately horizontal, N-S maximum compressive stress (Figure 4.3.2). This is in agreement with the regional stress field that Werner *et al.* (1991) found from borehole breakouts in northwestern Oregon. T axes are roughly distributed on a great circle with E-W azimuth, with their plunges ranging from vertical to horizontal. Their distribution shows no preference for either strike-slip or thrust mechanisms, and allows the conclusion that the stress field is approximately uniaxial with $\sigma_1 > \sigma_2 \approx \sigma_3$ at

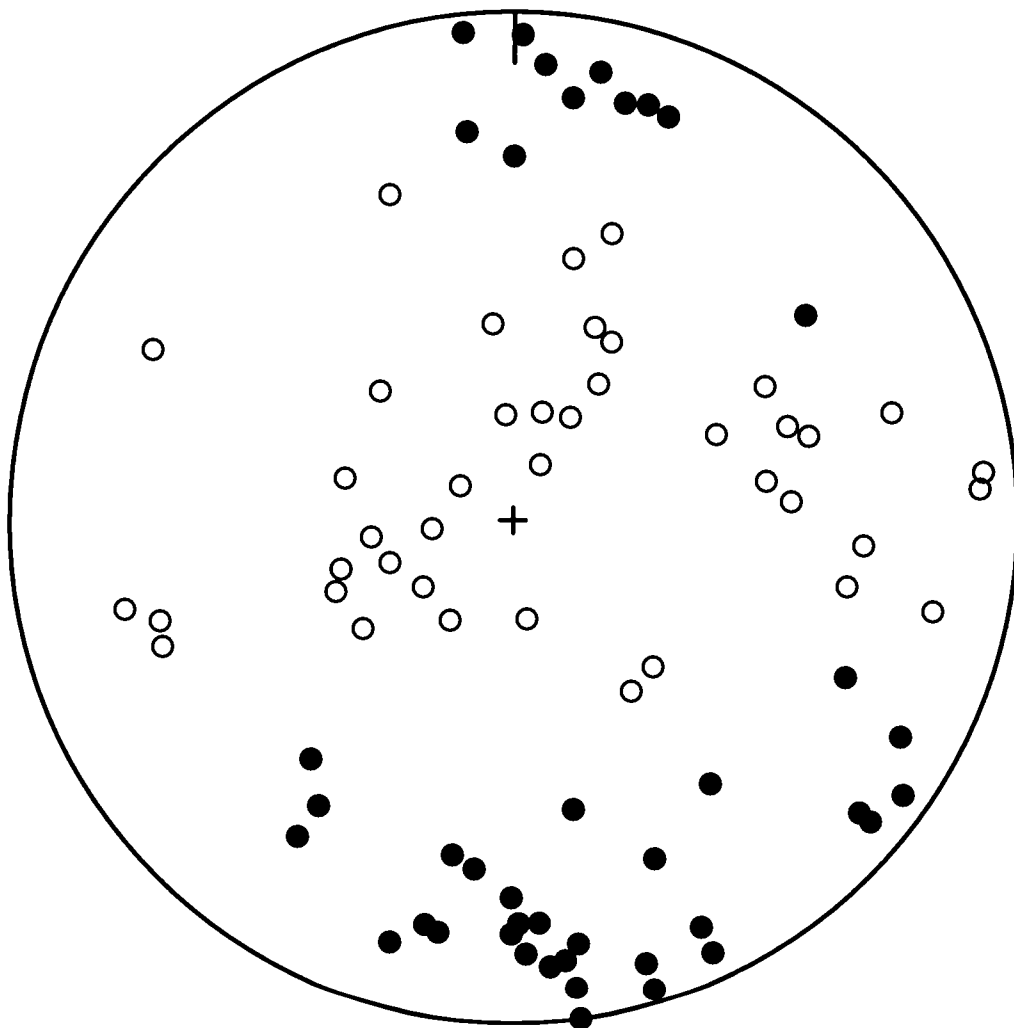
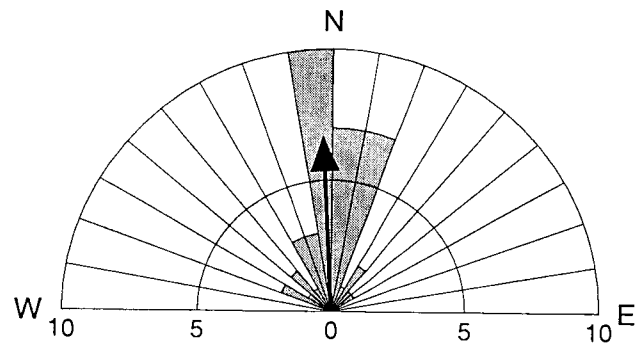
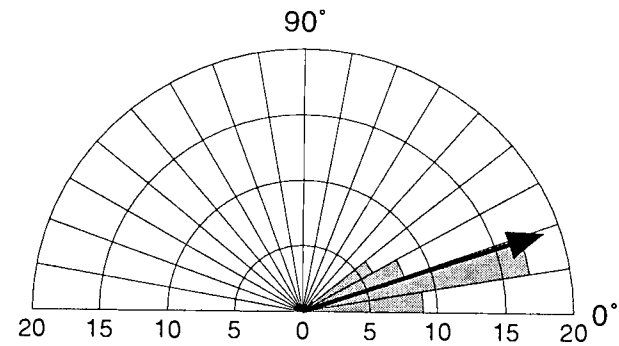


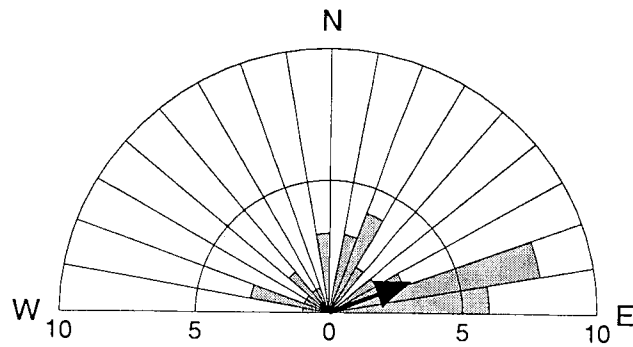
Figure 4.3.1 Composite plot of P (pressure, filled circles) and T (tension, open circles) axes from all investigated events (lower-hemisphere, equal-area projection).



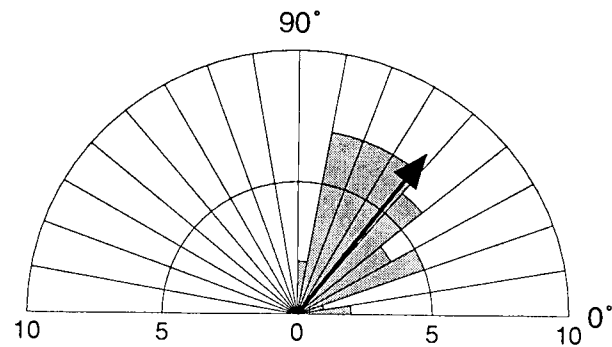
Azimuth of Pressure Axis



Plunge of Pressure Axis



Azimuth of Tension Axis



Plunge of Tension Axis

Figure 4.3.2 Rose section-diagrams showing the distribution of plunges and azimuths of the pressure (P) and tension (T) axes for the investigated events.

that depth range. This observation is in accord with the observed stress field found from focal mechanisms of earthquakes in western Washington (Crosson, 1972; Crosson, 1983; Ma *et al.*, 1991) and Vancouver Island (Wang *et al.*, 1995).

In the following discussion we are primarily interested in the stress field that is described by the 34 moment tensors of those events that define the major plane (Figure 4.3.3). To corroborate the conjecture of a homogenous stress field we perform a stress inversion using the method of Gephart (1990). The inversion is based on two assumptions: 1) A uniform stress field is acting on the study volume, and 2), slip on a given plane follows the direction of resolved shear traction on that plane. The principal stress axes and the ratio of the intermediate stress magnitude to the minimum and maximum stress magnitudes, $R = (\sigma_2 - \sigma_1) / (\sigma_3 - \sigma_1)$, are found in a grid search over possible principal stress directions and magnitude ratios. The misfit is measured by an angular rotation about an arbitrary axis that brings the observed slip direction in coincidence with a, by the stress tensor Φ predicted direction of resolved shear stress on the rotated fault plane. The best Φ is the one that minimizes rotation angles for all mechanisms in a L1-norm. This formulation allows for uncertainties in focal mechanisms as well as the stress tensor. For any given stress tensor Φ , one of each mechanism's two nodal planes will display a better fit and will be selected as the preferred plane. Employing this criterion, no *a priori* knowledge about which of the two nodal planes is the fault plane is required.

Employing the stress inversion on the subset of 34 focal mechanisms, the stress tensor with the following principal stress directions (azimuth plunge) generated a minimum average misfit angle of 6.19° : $\sigma_1 = (185^\circ \ 5^\circ)$, $\sigma_2 = (60^\circ \ 86^\circ)$, $\sigma_3 = (278^\circ \ 29^\circ)$, and a stress magnitude ratio of $R = 0.6$. Inversion results are summarized in Table 4.3.1. The fit to the data is very good, the average misfit angle is smaller than the estimated uncertainties in the orientations of the nodal planes. Only two events (2 and 9) have a misfit angle greater than 20° , and four events (6, 17, 27, 28) greater than 10° . We therefore conclude that the mechanisms are in correspondence with a homogenous stress field with the maximum principal stress axis approximately horizontally striking to the NNE. This is in excellent agreement with the regional stress direction inferred by Werner

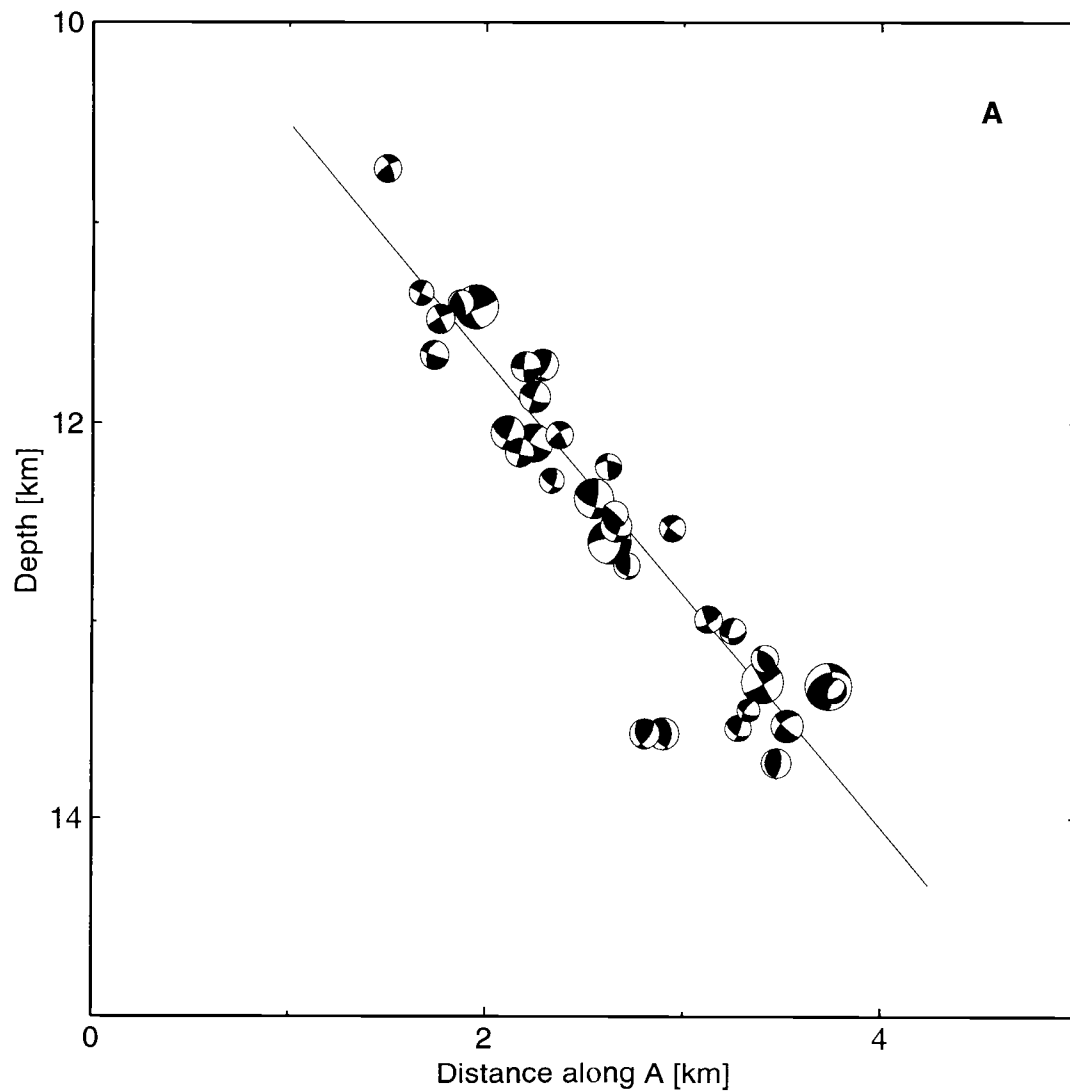


Figure 4.3.3 Cross sectional view perpendicular to the best-fit plane (location of the surface projection of this cross-section is shown in Figure 4.2.2 as line A). Shown are only the 34 events that define the aftershock plane. The black line indicates dip and location of best-fit plane (dip = 49°). Beachballs are back-projected into the cross-sectional plane.

et al. (1991) from borehole data. Figure 4.3.4 shows the best model and models falling within the 95% and 68% confidence limits. Whereas the horizontal NS direction of σ_1 is well constrained, the plunge of σ_3 takes on values ranging from vertical to horizontal in models that are insignificantly different from the best-fit model. The R-value of 0.6 does not fully advocate a uni-axial stress field, for which $R = 1$. Yet, it is not fully understood to what extent this could be an artifact of the inverse algorithm.

Table 4.3.1 Stress tensor inversion results.

ev .#	misfit		original		original		rotated		rotated	
	fault pl. [°]	aux. pl. [°]	fault plane az. [°] dip [°]	aux. plane az. [°] dip [°]	fault plane az. [°] dip [°]	aux. plane az. [°] dip [°]	fault plane az. [°] dip [°]	aux. plane az. [°] dip [°]		
*	1.11	21.17	300.1 48.0	55.0 65.0	300.8 48.1	56.0 64.6				
1	4.66	23.87	220.9 70.0	314.1 81.0	223.2 67.7	317.8 78.8				
2	28.78	40.11	250.1 30.0	148.0 83.1	224.4 49.2	129.0 83.8				
3	3.11	24.92	277.9 86.1	13.3 36.0	275.0 85.0	11.9 35.9				
4	5.98	25.02	74.7 35.8	304.1 64.8	80.1 37.9	310.6 63.6				
5	2.99	11.12	224.6 47.9	123.3 77.8	226.8 45.8	124.9 78.1				
6	13.19	19.64	256.9 75.7	127.5 21.8	269.5 70.8	129.0 24.3				
7	1.69	19.34	32.3 52.0	300.8 88.1	31.5 50.8	299.7 87.8				
9	23.81	38.44	166.7 52.9	63.2 72.8	176.2 29.9	60.6 76.0				
10	2.01	10.27	220.2 37.0	116.9 80.1	218.6 38.6	115.9 80.0				
12	5.66	14.44	118.0 30.9	283.0 59.9	124.0 34.7	285.5 56.7				
13	5.73	16.56	264.0 28.0	85.0 62.0	256.1 30.9	81.6 59.2				
14	1.30	19.13	133.9 65.0	232.1 73.0	133.1 64.2	231.3 73.4				
15	.27	1.61	113.0 67.0	232.1 41.0	112.7 66.9	232.0 41.1				
16	3.69	17.70	105.0 76.2	247.5 17.2	101.4 75.0	246.3 18.1				
17	15.44	42.22	186.2 44.1	64.9 63.2	176.2 29.9	57.5 74.5				
18	.06	26.52	238.7 69.0	148.3 88.9	238.7 69.0	148.2 88.9				
19	.66	19.91	136.9 59.0	236.1 75.1	137.3 59.4	236.5 74.9				
20	8.18	16.62	240.5 41.8	130.2 72.7	233.8 47.5	126.1 71.7				
21	2.30	14.04	31.9 80.9	298.2 68.0	32.9 80.4	298.5 65.9				
22	7.31	14.00	90.0 87.2	192.0 13.0	96.9 89.7	188.4 12.6				
23	9.02	34.74	266.0 43.9	61.0 48.9	276.4 42.5	69.1 50.9				
24	6.10	6.97	241.8 26.8	98.1 67.8	235.1 31.3	95.8 65.3				
25	7.49	18.87	280.0 61.9	85.9 28.9	272.0 62.9	81.0 27.6				
27	10.36	18.51	79.9 37.9	296.1 57.9	90.7 40.9	306.7 55.0				
28	10.07	21.33	336.0 50.0	240.0 83.0	342.9 44.1	247.5 84.8				
30	.43	26.64	128.8 82.0	219.2 87.0	128.6 81.7	219.0 87.3				
33	1.43	10.34	116.2 71.8	221.7 50.9	115.1 70.9	221.2 51.2				
34	1.53	3.16	145.0 38.0	268.0 67.0	143.7 36.8	267.5 67.4				
35	.20	24.34	270.0 39.0	75.0 52.0	270.3 38.9	75.2 52.0				
36	1.37	17.77	101.0 63.0	277.0 27.0	102.4 63.4	278.0 26.7				
37	13.57	29.52	227.0 36.0	78.0 58.0	237.3 25.2	82.8 67.0				
38	9.92	14.50	121.7 85.1	214.3 62.0	115.4 78.2	211.1 64.8				
39	.48	39.28	196.9 86.1	291.1 43.0	197.4 86.1	291.6 42.8				
40	2.31	37.24	272.9 19.0	59.0 74.0	276.3 17.5	60.8 75.6				

* - mainshock

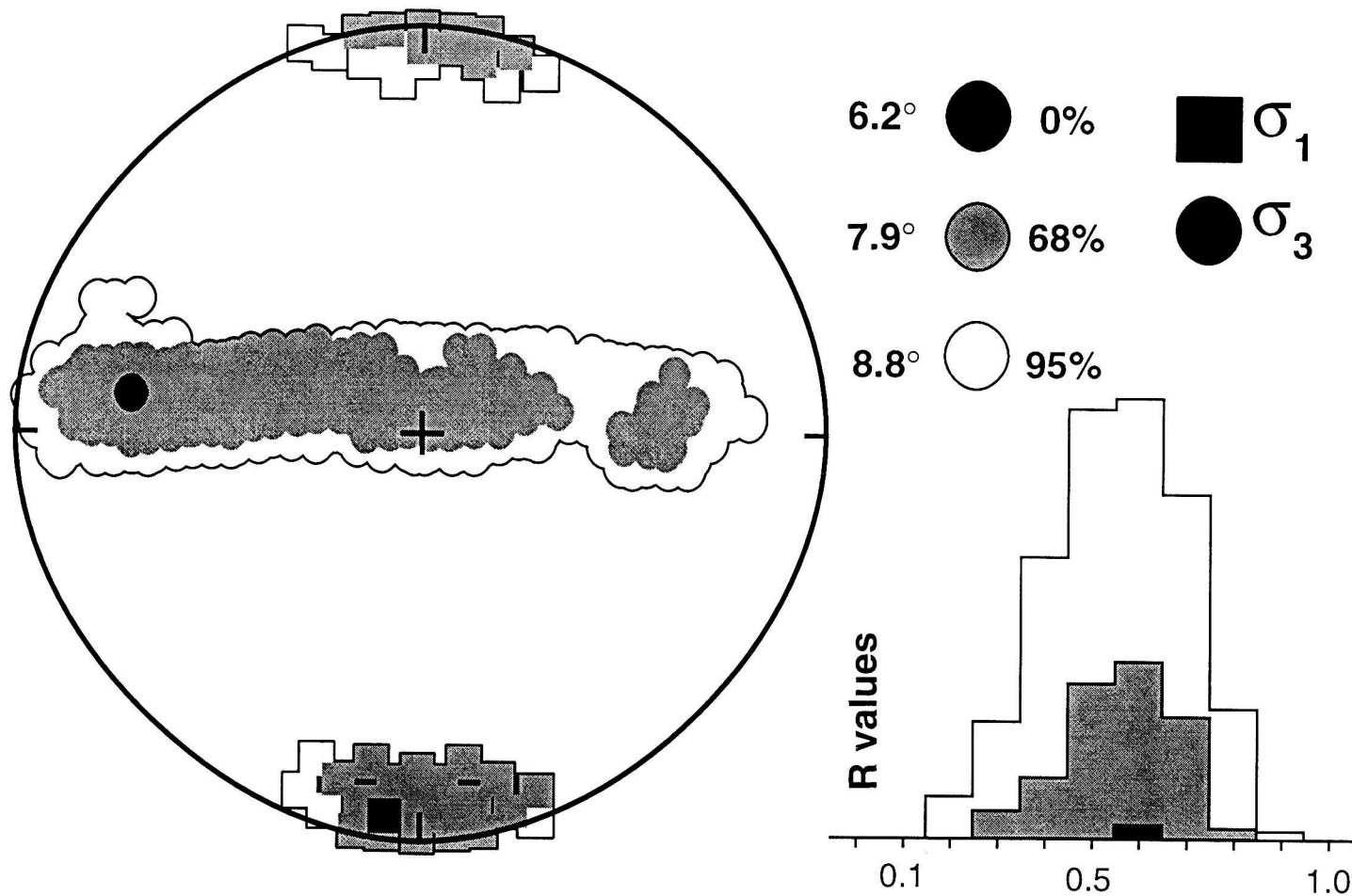


Figure 4.3.4 Maximum and minimum stress axes (σ_1 and σ_3) from stress tensors that fall into the 68% and 95% confidence limits (stereo-net projection). Whereas σ_1 is well constrained by the focal mechanisms, σ_3 directions girdle on a great circle with plunges ranging from sub-horizontal to sub-vertical.

We will further investigate if T-axis plunges change as a function of depth. Figure 4.3.5 shows all focal mechanisms in a T-axis-plunge versus depth graph. Even though there is significant scatter, a trend from deeper strike-slip events to shallower dip-slip events is perceptible. To quantify this relationship, T axis plunges were binned in three depth slices and displayed in a rose diagram (Figure 4.3.6). The rotation of the T- axes with depth is clearly visible, and we obtain average values of about 60° for events shallower than 12 km, 45° for events between 12 and 13 km, and 30° for events deeper than 13 km. A similar relationship was reported by Vetter and Ryall (1983) for the Basin and Range province. They attributed the primary strike-slip motion for shallow events, and the oblique or normal slip motion for deeper events, to the increasing overburden pressure, which results in a rotation of the P-axis from horizontal to vertical. Iio (1996) found a transition from widely distributed T-axis plunges to primarily horizontal plunges with increasing depth in the Kinki district in Japan. He inferred that minimum horizontal stress and vertical stress have a similar magnitude at depths below where the transition occurs, and that minimum horizontal stress is less than the vertical stress above. He concluded that this change is related to the transition from a brittle to a semi-brittle regime.

In our case the rotation of the tension axis is probably a result of increasing overburden pressure (σ_v). This is sketched in Figure 4.3.7: σ_v increases according to $\rho \cdot g \cdot z$, while the minimum horizontal stress σ_h grows at a smaller rate because of the rigidity of rock. The interchange of σ_2 and σ_3 (point 1 in Figure 4.3.7) occurs approximately between 12 km and 13 km, where oblique mechanisms dominate. We obtain an absolute estimate of σ_2 and σ_3 at this depth by setting the average crustal density $\rho = 2700 \text{ kg/m}^3$, depth $z = 12.5 \text{ km}$, and $g = 9.81 \text{ m/s}^2$: $\sigma_2 \approx \sigma_3 = \rho \cdot g \cdot z = 331 \text{ MPa}$. We can also estimate σ_1 at this depth: We write the shear stress τ acting on the fault plane as, $\tau = \frac{\sigma_1 + \sigma_3}{2} \sin 2\delta$, and the normal stress as $\sigma_n = \frac{\sigma_1 + \sigma_3}{2} + \frac{\sigma_1 - \sigma_3}{2} (1 - 2\cos^2 \delta)$, where $\delta = 50^\circ$ is the fault dip. We can write the effective stress $\sigma_n' = \sigma_n - P_0$, where P_0 is the pore pressure, which assuming it to be hydrostatic is approximately $0.4 \times \sigma_v$. Because the fault moved we can apply Byerlee's Law (Byerlee, 1978): $\tau = 0.5 + 0.6 \sigma_n'$, and solve for σ_1 .

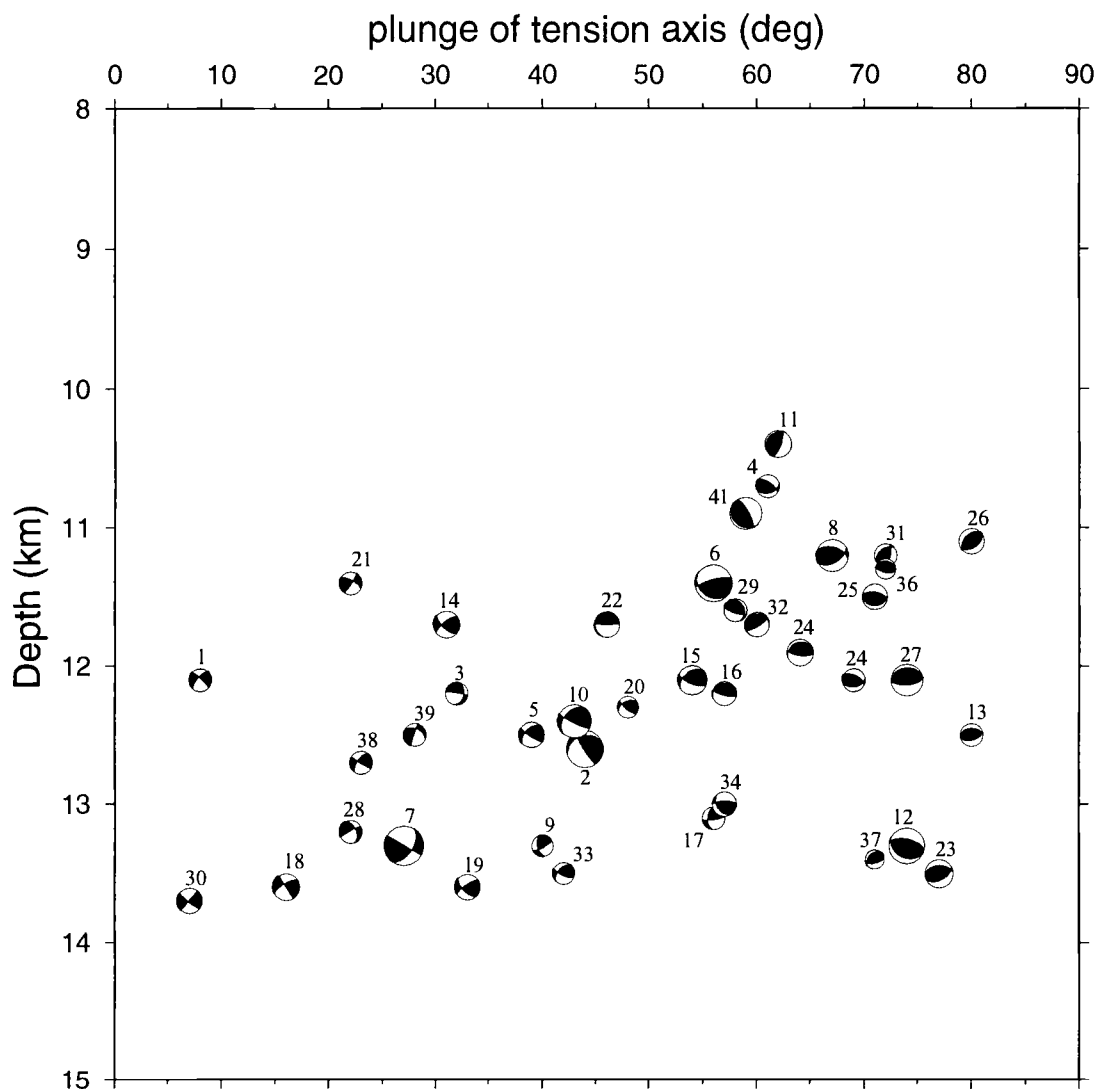


Figure 4.3.5 Focal mechanisms are displayed with their plunges graphed versus hypocentral depth. In this plot strike-slip mechanisms (left) are separated from dip-slip mechanisms (right), and a systematic change of deformation style with depth is revealed.

Plunge of Tension Axis

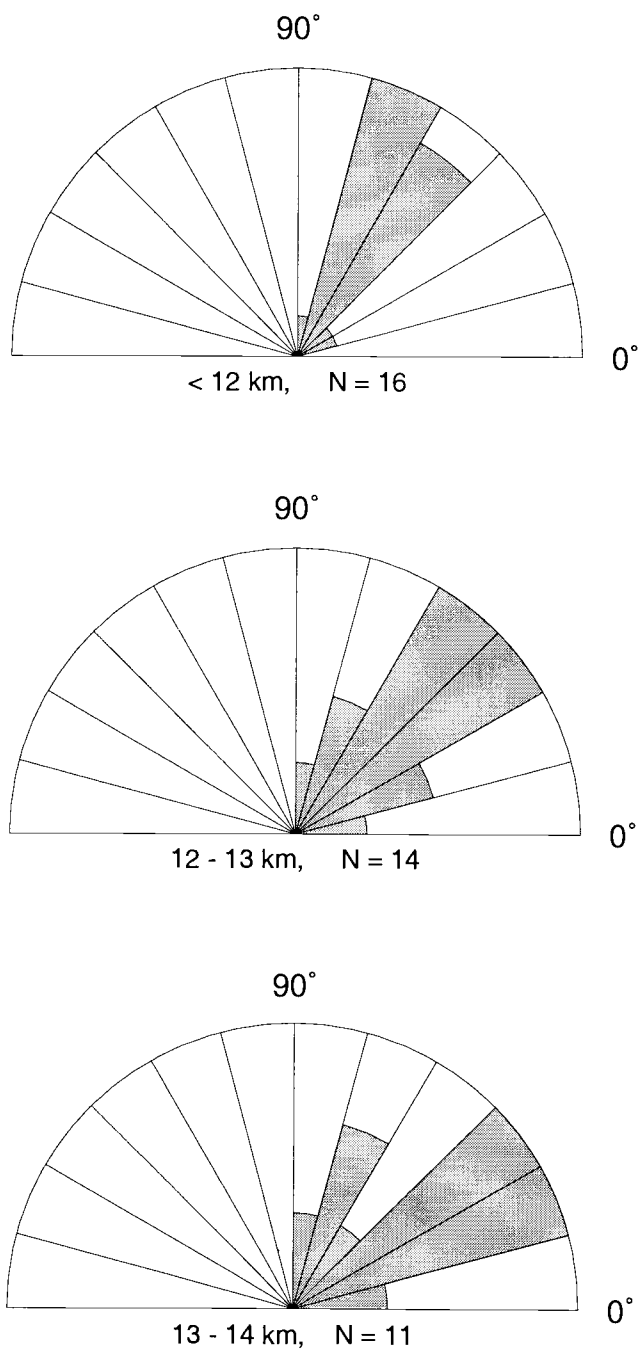


Figure 4.3.6 Rose diagrams of T-axis plunges for three different depth slices. T-axes rotate from an average 60° to 30° with increasing depth.

By doing so we obtain an estimate for the maximum horizontal stress at 12.5 km: $\sigma_1 \approx 375$ MPa (point 2 in Figure 4.3.7). To obtain a more complete picture we estimate stresses also at 5 km depth. $\sigma_3 = \sigma_v$ is easily calculated with $\rho \cdot g \cdot z = 132$ MPa at 5 km depth (point 3 in Figure 4.3.7). For an estimate of σ_1 we take Mc Garr's (1980) empirical relationship of maximum shear stresses for crustal rocks in compressional regimes from hydro-fracture measurements: $\tau = \frac{\sigma_1 - \sigma_3}{2} = 4.2 + 8.66z$. Solving for σ_1 , an upper bound on the maximum principal stress σ_1 at 5 km depth is 227 MPa (point 4 in Figure 4.3.7). Because at shallow depths dip-slip mechanisms are predominant, a tri-axial stress field with $\sigma_1 > \sigma_2 > \sigma_3$ is assumed. Thus we estimate the intermediate principal stress at 5 km depth simply as $\sigma_2 = \frac{\sigma_1 + \sigma_3}{2} = 180$ MPa (point 5 in Figure 4.3.7). Below 15 km in Figure 4.3.7, stresses are assumed to follow a plastic flow law. We are aware of the fact that these are merely crude estimates of absolute stresses, always under the assumption that the aftershock moment tensors describe the regional stress field, which is not in general true.

4.4 Fault Strength Considerations

Several of our mechanisms exhibit severely misoriented planes (i.e., thrusts on very low-angle or very steep planes) on which failure is not easily explained by a Coulomb criterion unless modifications to the model, such as fault confined elevated pore pressures are allowed (e.g., Hubbert and Rubey, 1959). Gephart's inversion does not invoke a friction criterion, thus nodal planes with low resolved shear stresses are not discarded. To illustrate this we can construct an unscaled Mohr circle (Jaeger and Cook, 1969) from the principal stresses and the value of R (Gephart and Forsyth, 1984). In Figure 4.4.1 Mohr circles were computed for the best-fit stress tensor and two other tensors within the 95% confidence limit that have unchanged σ_1 -axes, but σ_3 -axes plunging, 45° and 90° . These stress fields represent deformation styles ranging from right-lateral strike-slip, over oblique, to predominant thrust, and thus are in accordance with the predominantly

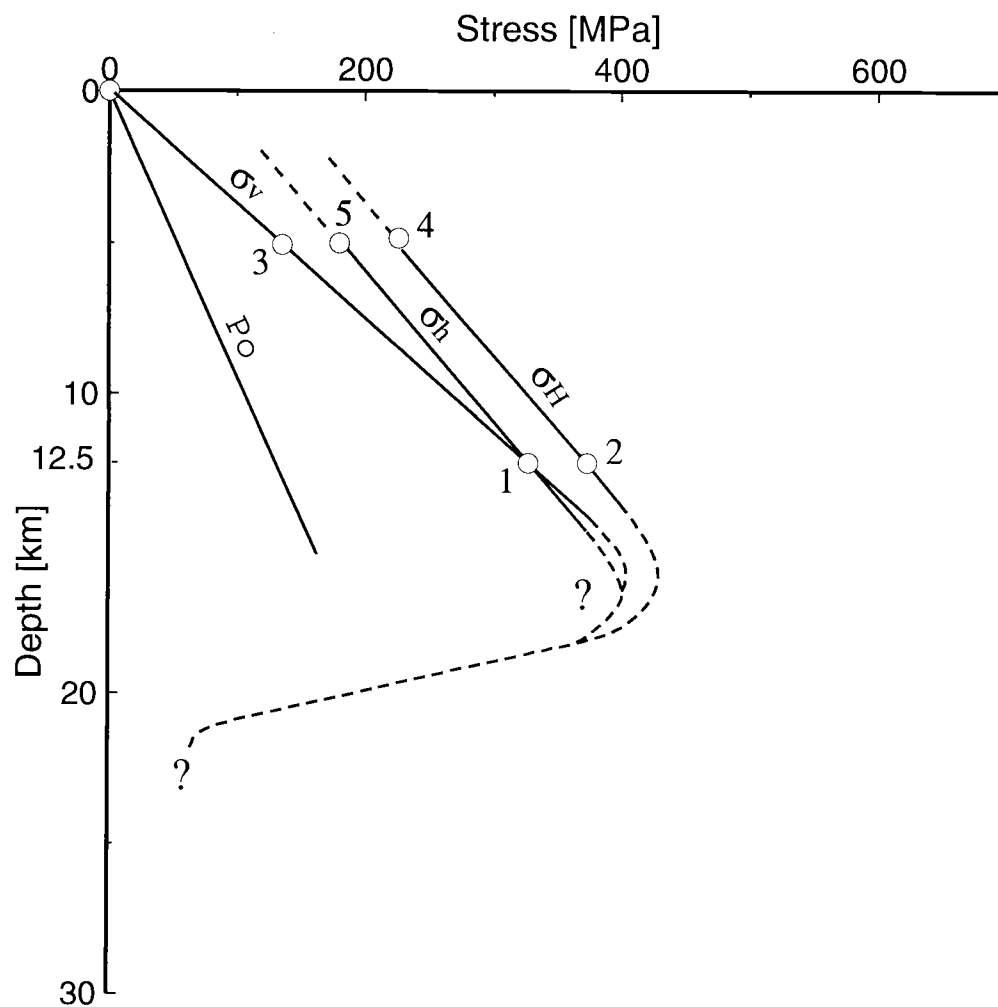


Figure 4.3.7 Estimates of absolute stresses as a function of depth. σ_v is overburden stress, σ_h is minimum horizontal stress, and σ_H is maximum horizontal stress. P_0 is hydrostatic pore pressure. See description of points in the text.

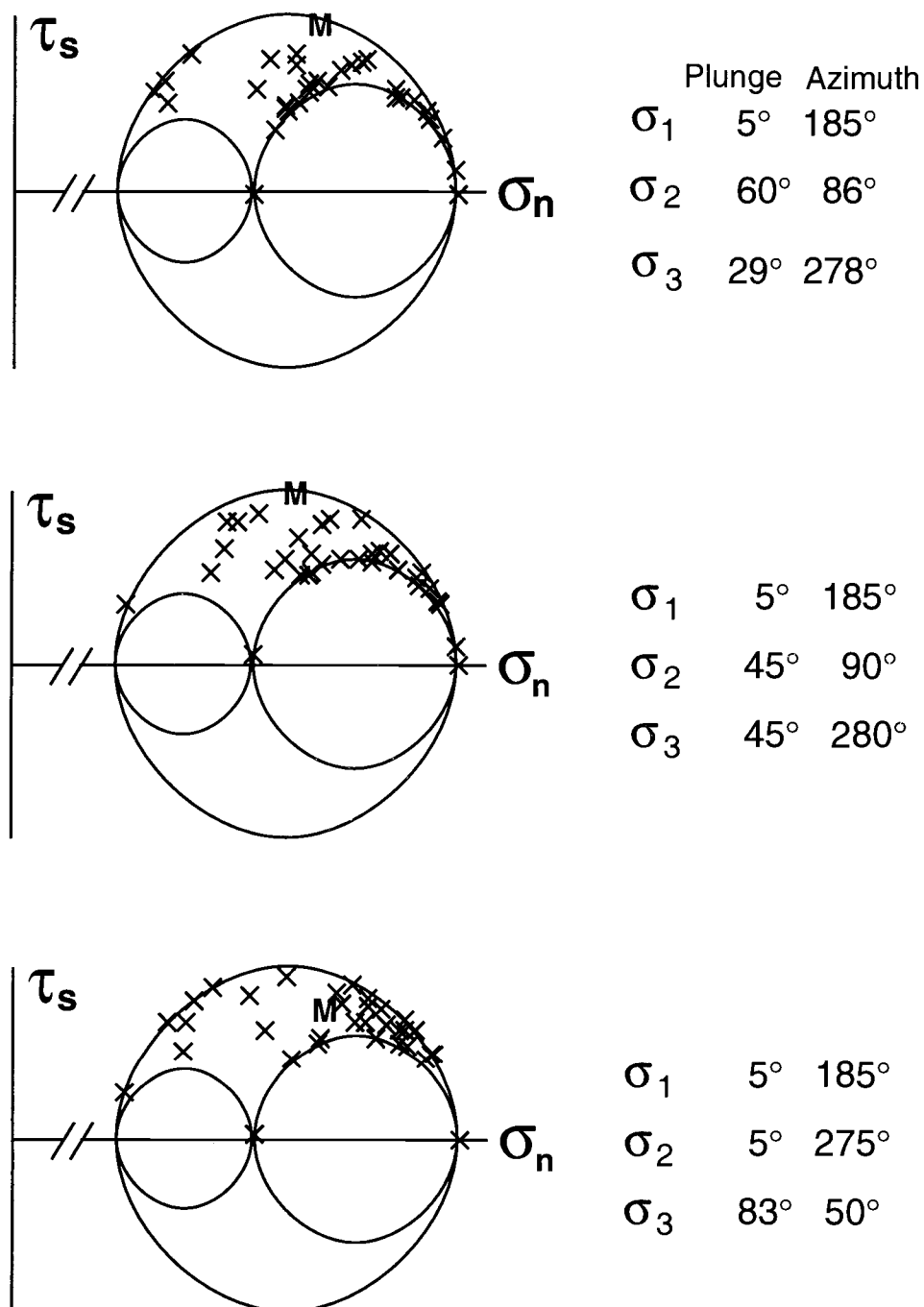


Figure 4.4.1 Mohr circles for three stress tensors within the 95% confidence limit. The top one corresponds to the best-fit stress tensor, the other two have respectively steeper σ_3 axes, whereas the σ_1 direction remains unchanged. Each cross figures the relative magnitudes of resolved shear stress (τ) and normal stress (σ_n) on the preferred nodal plane of an aftershock focal mechanism. The "M" represents stresses on the north-dipping fault plane of the mainshock.

oblique mainshock. Each cross represents normal stress and resolved shear traction on one event's preferred nodal plane for the respective Φ , the "M" represents the mainshock. Assuming a homogeneous stress field, the data clearly indicate variations in apparent fault strength. Many crosses fall just above the principal planes, which under a simple frictional criterion do not represent suitable planes unless the faults are extremely weak. For the stress tensors representing strike-slip and oblique deformation, the ratio of shear traction to normal stress is nearly at a maximum level. The aftershocks plot mostly below the mainshock, suggesting, under the assumption of a uniform stress field, much lower fault strengths. For a fault, the failure criterion can be expressed by the simple relationship

$$\tau_s = C + \mu (\sigma - p) \quad (4.1)$$

(e.g., Byerlee, 1978), where C is a cohesion term, μ is the coefficient of internal friction, a measure of failure resistance, and p is the pore pressure. From (4.1) we see that rupture for small values of shear traction can only occur if the pore pressure is elevated. For some events $\tau \approx 0$, and pore pressures would have to be lithostatic to permit displacement on the fault.

4.5 Implications for Models of Aftershock Generation

Because aftershocks occur as a direct aftermath to the mainshock, they have to stand in a causal relationship to it. Two commonly cited models that suggest such a relationship are the barrier model (Das and Aki, 1979), and the asperity model (Kanamori and Stewart, 1978). A patch of high strength on a rupture plane, that will impede or arrest slip is denoted a barrier. While stress is decreased in the areas of high slip it will increase in the unbroken barriers. Aftershocks are thought to be a response to this increased stress, and represent partial failure of the barriers. An asperity, in contrast, is a zone of high stress accumulation. In this model the strong, high-stressed asperities break during the mainshock. Stress is then transferred from slip areas to the surroundings,

triggering aftershocks there. Whereas the barrier model starts out with a homogeneous pre-mainshock stress field and leaves behind a heterogeneous stress field, the stress field in the asperity model is heterogeneous before the mainshock and the post-mainshock stresses are homogeneous. In both models aftershocks will concentrate around areas of high slip as a response to static stress changes there. This pattern has been observed for many earthquakes, e.g. Coyote Lake 1979 and Morgan Hill 1984 (Oppenheimer *et al.*, 1990; Bakun, King and Cockerham, 1986), Imperial Valley 1979, North Palm Springs 1986, Borah Peak 1983 (Mendoza and Hartzell, 1988).

The aftershocks investigated in this thesis are relatively evenly distributed over an area of approximately 20 km² (Figure 4.5.1). In the pattern no obvious gaps are indicating areas of high coseismic slip. Nabelek and Xia (1995) estimated a rupture area of approximately 28 km² (they used a circular crack model and deduced a rupture radius of 3 km) from the source duration of the mainshock. Unfortunately a slip distribution for this earthquake is not available. But from the mainshock hypocentral and centroid depths we can assume an upward rupture. All the aftershocks lie just above the mainshock hypocentral depth, considering their spatial distribution and the estimated mainshock rupture area, this would put them within the slip region, and not on the perimeter of it, as would be expected by the asperity and barrier models. This is inconsistent with the observation of Mendoza and Hartzell (1988) who observe that the site of mainshock rupture is largely aseismic. If aftershocks would be caused by mainshock induced stress changes surrounding the slipped zone, or at unbroken barriers in the slipped zone, their mechanisms should be similar to that of the mainshock, an oblique thrust on a WNW striking and northerly dipping plane. But none of the aftershocks in this sequence bears such a mechanism. Instead thrusts and strike slip mechanisms on shallowly dipping and vertical planes are dominant.

If we assume, that the mainshock completely relieved the tectonic stress, then the aftershocks could be the response to changes in static stresses produced by the mainshock dislocation. Six events to the northwest of the cluster are clearly separated from the major plane (Figure 3.3.3 B). Five of them (events 8, 11, 26, 31, and 32) form a group of relatively shallow northeast striking dip slip events. Their clustering and similarity in

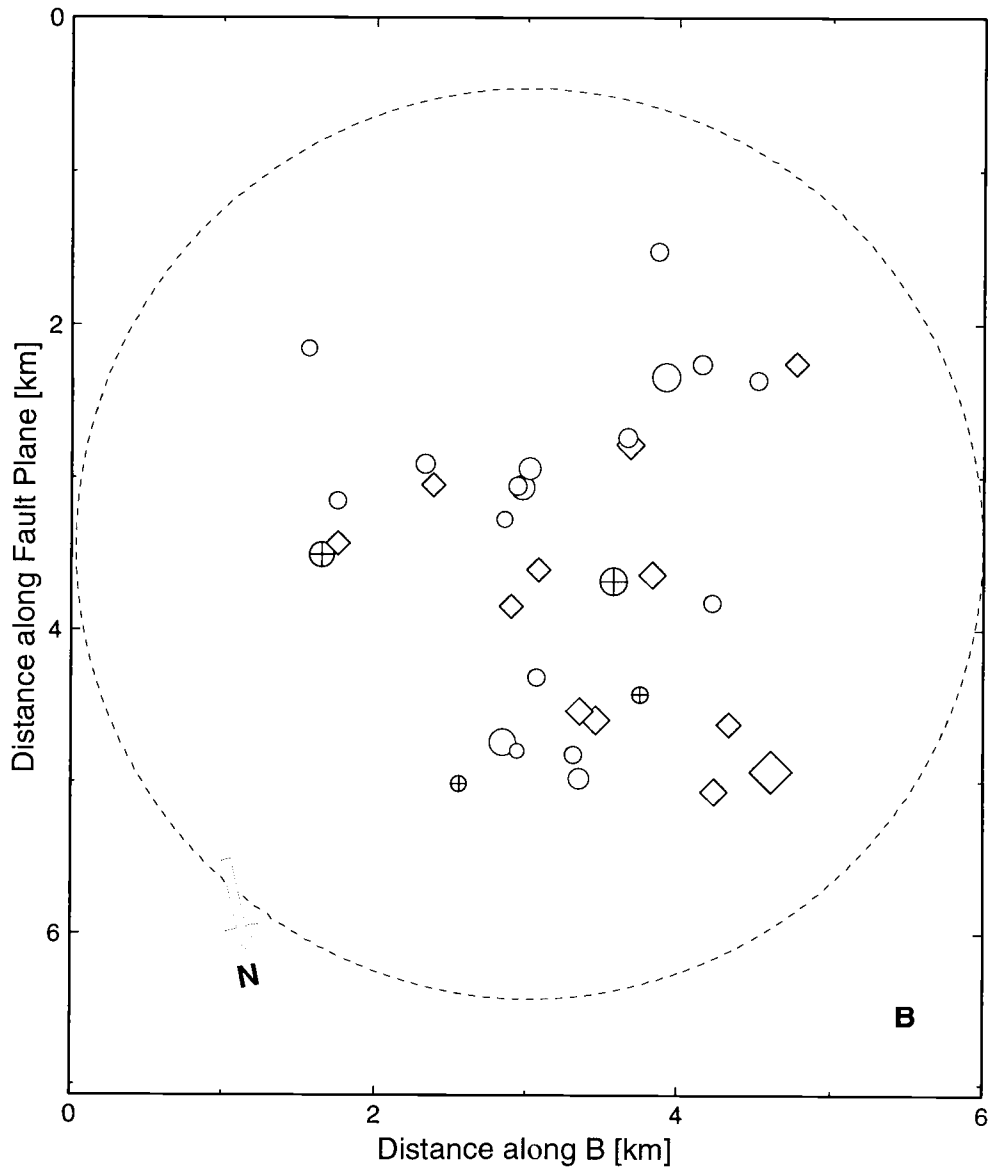


Figure 4.5.1 The aftershocks investigated in this study projected onto the best-fitting fault plane. Symbols are keyed by mechanism style: circles ... predominant thrust, diamonds ... predominant right lateral strike-slip, \oplus ... oblique slip. The dashed circle circumscribes the rupture area from the mainshock source duration inferred rupture area. The exact location of the rupture area is not known, and the circle is centered arbitrarily inside the cluster.

mechanism suggests that they are occurring on a single separated plane to the north of the major slip plane. This conclusion is supported by their NW-SE trending compression axis which differs from the mostly NS trending axes of the events forming the major plane as well as from the regional NS compressional stress field (Werner *et al.*, 1991). These four earthquakes are located about three kilometers off the main fault plane in perpendicular direction (Figure 3.3.3 B). This is about half the rupture length inferred from the other aftershock locations, and exactly where an increase in shear stress is predicted from simple crack or dislocation models (e.g., Kostrov and Das, 1984). The change in a static shear stress field due to a Griffith shear crack is shown in Figure 4.5.2 (from Das and Scholz, 1982). Although the predicted increase in off the plane is only about 10 per cent of the stress drop on the crack, Das and Scholz (1982) found several examples from strike-slip earthquakes, where off fault aftershock clusters occurred at the predicted locales. If the shear stress increase falls on a place of a preexisting weakness, the stimulus could be enough for the fault to reach the yield stress and rupture. However, no stress increase is predicted adjacent to the dislocation (Figure 4.5..2), hence the majority of the events is not explained by such model.

Deschamps and King (1984) explain the variability in aftershock mechanisms of the Campania-Lucania (Italy) event by volume changes due to rupture of a non-planar surface. The Scotts Mills event however, does not show any indication of such complexity.

The most enigmatic feature of this earthquake sequence is that the majority of events seem to sharply define a plane with only little scatter, even though their focal mechanisms are extremely diverse. Because almost none of the mechanisms has a nodal plane that agrees within the uncertainties with the mainshock slip plane (Figure 4.3.3), the aftershocks cannot have occurred on the slip plane but must have ruptured tightly around it on adjacent secondary structures. This is not easily explained by remnant stress concentrations on the mainshock rupture plane or barrier/asperity type models. We found several other characteristics of the Scotts Mills sequence that defy explanation by generic aftershock models:

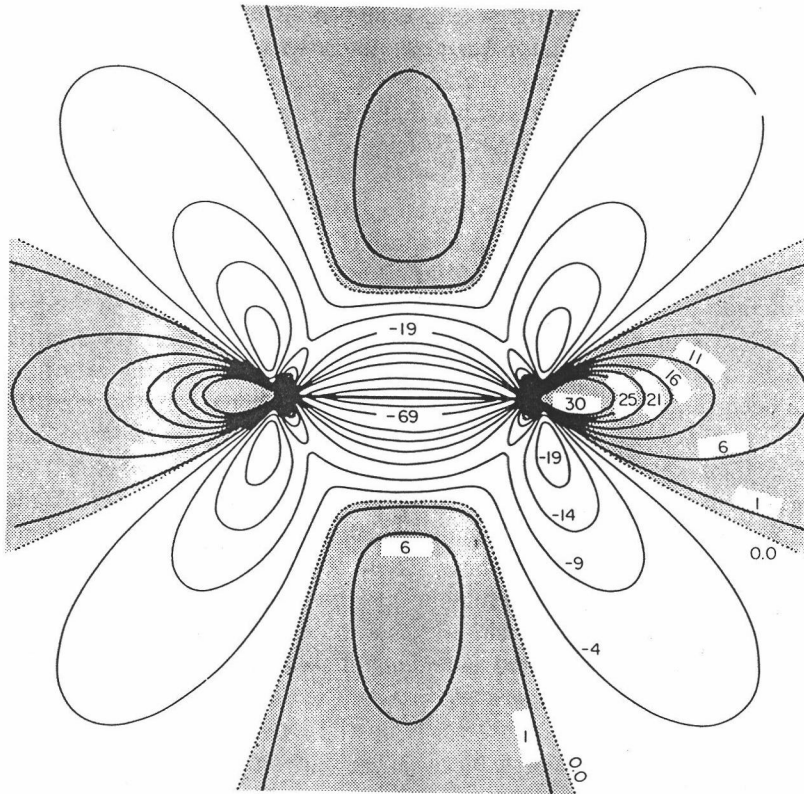


Figure 4.5.2 Change in the static stress field predicted by simple Griffith crack. Stress increases at the crack tips and perpendicular to the crack at about half a crack length distance. The area immediately adjacent to the crack experiences a decrease in shear stress (from Das and Scholz, 1982).

- The aftershocks seem to respond to a uniform stress field that resembles very much the ambient regional tectonic stresses.
- T-axes are rotated with depth, probably as a response to increasing overburden pressure.
- Fault strength is highly variable, and the rupture of some extremely misoriented planes is only imaginable under sub-lithostatic pore pressures.
- Aftershocks are evenly distributed within the assumed area of mainshock slip.

We propose an alternative model of aftershock generation that elucidates some of the observed phenomena. We suggest that aftershocks were driven by the ambient regional stress rather than by an increase in shear stress, and that they were triggered by a sudden, mainshock-induced decrease in strength in the area adjacent to slip. A similar conclusion was drawn by Zoback and Beroza (1993) to explain the diversity of mechanisms in the Loma Prieta aftershock sequence. We believe that the weakening was caused by changes in pore pressure in a pre-fractured zone adjoining the rupture area.

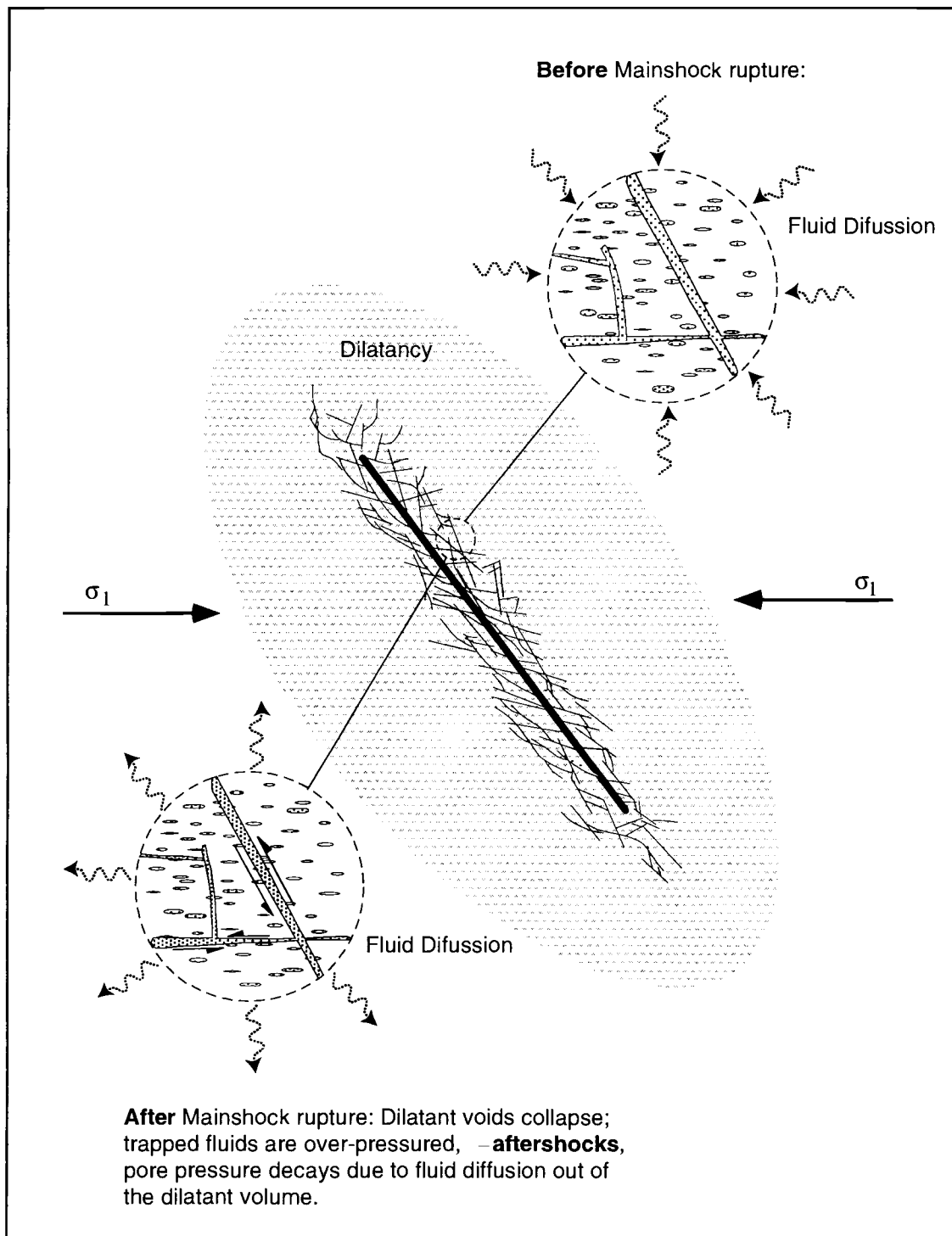
The brittle upper crust is almost universally permeated with fluids, and the significance of fluids in faulting has been recognized by many scholars. Induced seismicity at Denver and Rangeley (e.g., Healy *et al.*, 1968) and the observation of transitory surface effusion following some earthquakes, as well as hydrothermal vein systems found in ancient exhumed faults (Sibson, 1981) point out the importance of fluids on seismicity, and the effect seismicity has on fluid flows. Nur and Booker (1972) propose a model of fluid flow driven by changes in pore pressures due to volumetric strain accompanying faulting to explain the occurrence and time dependency of aftershocks. Their model predicts a clustering of aftershocks at the crack tips, which is indeed often observed, yet does not apply to the Scotts Mills events. To explain the geometry and mechanisms of the Scotts Mills sequence, a model that is closely confined to the area that slipped during the main event has to be found.

We suggest a possible mechanism based on dilatancy-diffusion models that were developed in the early seventies to explain a variety of precursory effects (Nur, 1972; Whitcomb *et al.*, 1973; Scholz *et al.*, 1973). Dilatancy is a phenomena that is well known

from laboratory fracture experiments. It denotes the increase in void space due to micro-cracking and crack-opening in rocks under high shear stress. Nur (1972) explained observed changes in v_p/v_s ratios prior to earthquakes by dilatancy and subsequent filling of the newly formed voids due to pore fluid diffusion. If we adopt this model and extend it to the time after the rupture we obtain the following scenario: As shear stress increases, dilatancy will initiate in a volume around the fault zone (Figure 4.5.3). We know that even well-developed fault zones are surrounded by zones of pervasively fractured rock (Chester and Logan, 1986). Because of this fractal character of fault roughness we believe that dilatancy will be particularly pronounced in the region adjacent to the main fault. As cracks open, pore fluid diffusion will inflate the spaces until pore pressure is reestablished (Figure 4.5.3). This is when the mainshock rupture occurs. Along with a coseismic stress drop the open cracks collapse, over-pressuring the captured fluids in the process. The high pore pressures cause a decrease in effective stress as well as fault strength in the region neighboring the main fault. Slip on preexisting, weak fractures is driven by the ambient, tectonic stresses and recorded as aftershocks (Figure 4.5.3). Their rate will decay as pore pressure becomes hydrostatic again due to fluid diffusion out of the dilatant, over-pressured volume.

This model provides but one possible mechanism for weakening the region immediately adjacent to the rupture area; others resulting in similar effects could certainly be thought of. In our proposed model aftershocks would set in instantaneously after mainshock slippage, and then decay with time according to the hydraulic diffusivity of rock. The fault zone would then act as an ephemeral window into the regional tectonic stress field.

Figure 4.5.3 Synoptic model of fault zone and outline of mechanism for aftershock generation. The fault is surrounded by pervasively fractured rock. As shear stress increases dilatancy occurs in a volume adjacent to the fault. Fluids will fill the newly open cracks and fractures. Due to the stress drop accompanying the mainshock rupture, the cracks and fractures collapse, over-pressuring the trapped fluids. The increased pore pressure causes a reduction of the effective stress, thus lowering the strength in the area adjacent to the fault. Aftershocks occur on the weak fracture planes until pore pressure decreases towards hydrostatic values due to fluid diffusion out of the dilatant volume.



BIBLIOGRAPHY

- Aki, K., P. G. Richards, *Quantitative Seismology, Theory and Methods*, Freeman, San Francisco, 1980.
- Ansell, J. H. and E. G. C. Smith, Detailed structure of a mantle seismic zone using the homogeneous station method, *Nature* 253: 518-520, 1975.
- Bakun, W. H., G. C. P. King, and R. S. Cockerham, Seismic slip, aseismic slip, and the mechanics of repeating earthquakes on the Calaveras fault, California, *Earthquake Source Mechanics. AGU Geophys. Mono. 37*, ed. S. Das, C Scholz, and J. Boatwright. Washington D.C.: American Geophysical Union, pp. 195-207, 1986.
- Beroza, G.C. and Zoback, M. D., Mechanism Diversity of the Loma Prieta Aftershocks and the Mechanics of Mainshock-Aftershock Interactions. *Science* 259: 210-213, 1993.
- Blakeley, R., R. Wells, T. Yelin, M. E. Dougherty, and A. M. Trehu, Faults and earthquakes in the Willamette Valley and Portland Basin, a regional perspective from newly acquired aeromagnetic data, *Abstracts, 92nd Annual Cordilleran Section, Geol. Soc. Am.* 28: 50, 1996.
- Bouchon, M., A simple method to calculate Green's functions for elastic layered media, *Bull. Seismol. Soc. Am.* 71: 959-971, 1981.
- Bouchon, M., The complete synthesis of seismic crustal phases at regional distances, *J. Geophys. Res.* 87: 1735-1741, 1982
- Braunmiller J., J. L. Nabelek, B. Leitner, T. Quamar, The Klamath Falls, Oregon, earthquake sequence: Source mechanisms from regional data, *Geophys. Res. Lett.* 22: 105-108, 1995.
- Buland, R., The mechanics of locating earthquakes, *Bull. Seismol. Soc. Am.* 66: 173-187, 1976.
- Burridge, R., and L. Knopoff, Body force equivalents for seismic dislocations, *Bull. Seismol. Soc. Am.* 54: 1875-1888, 1964.

- Byerlee, J., Friction of rocks, *Pure Appl. Geophys.* 116: 615-626, 1978.
- Carver, D., D. Worley, and T. Yelin, Digital recordings of the 25 March, 1993, Scotts Mills, Oregon, Earthquake, *U.S. Geol. Surv. Open-File Rept. 93-535*, 1993.
- Chester, F. M. and J. M. Logan, Implications for mechanical properties of brittle faults from observations of the Punch Bowl fault zone, California, *Pure Appl. Geoph.* 124: 79-106, 1986.
- Crosson, R. S., Small Earthquakes, structure, and tectonics of the Puget Sound region, *Bull. Seismol. Soc. Am.* 62: 1133-1171, 1972.
- Crosson, R. S., Crustal structure modeling of earthquake data 2. Velocity structure of the Puget Sound region, *J. Geophys. Res.* 81: 3047-3054, 1976.
- Crosson, R. S., Review of seismicity in the Puget Sound region from 1970 through 1978, in *Proc. of Workshop XIV, Earthquake hazards of the Puget Sound Region, Washington, U.S. Geol. Surv. Open-File Rep. 83-19*: 6-18, 1983.
- Das, S. and K. Aki, Fault planes with barriers: A versatile earthquake model, *J. Geophys. Res.* 82: 5658-5670, 1977.
- Das, S. and Scholz, C. Off-fault aftershock clusters caused by shear stress increase? *Bull. Seismol. Soc. Am.* 71: 1669-75, 1982.
- Deschamps, A. and G. C. P. King, Aftershocks of the Campania-Lucania (Italy) earthquake of 23 November 1980, *Bull. Seismol. Soc. Am.* 74: 2483-2517, 1984.
- Douglas, A., Joint Epicentre Determination. *Nature* 215: 47-48, 1967.
- Dziewonski, A. M., J. E. Frantzen, and J. H. Woodhouse. Centroid-moment tensor solutions for April-June 1983. *Phys. Earth Planet. Inter.* 33: 243-249, 1983.
- Evernden, J. F., Identification of earthquakes and explosions by use of teleseismic data, *J. Geophys. Res.* 74: 3828-3856, 1969.

- Fan, G., S. Beck, T. C. Wallace, The Seismic Source Parameters of the 1991 Costa Rica Aftershock Sequence: Evidence for a Transcurrent Plate Boundary, *J. Geophys. Res.* 98: 15,759-15,778, 1993.
- Geiger, L., Herdbestimmung bei Erdbeben aus den Ankunftszeiten, *Königl. Ges. der Wiss. Göttingen* 4: 331-339, 1910.
- Gephart, J. and Forsyth, D.W., An Improved Method for Determining the Regional Stress Tensor Using Earthquake Focal Mechanism Data: Application to the San Fernando Earthquake Sequence. *J. Geophys. Res.* 89: 9305-9320, 1984.
- Gephart, J. W., FMSI: A FORTRAN program for inverting fault/slickenside and earthquake focal mechanism data to determine the regional stress tensor, *Computers & Geosci.* 16: 953-989, 1990.
- Gilbert F., Excitation of the normal modes of the earth by earthquake sources, *Geophys. J. R. Astron. Soc.* 22: 223-226, 1970.
- Hampton, E. R., Geology and ground water of the Mollala-Salem slope area, northern Willamette Valley, Oregon, *U.S. Geol. Surv. Water Supply Pap.* 1997, 1972.
- Harmesen, S. C., The Little Skull Mountain, Nevada, Earthquake of 29 June 1992: Aftershock Focal Mechanisms and Tectonic Stress Field Implications. *Bull. Seismol. Soc. Am.* 84: 1484-1505, 1994.
- Hauksson, E., State of Stress from Focal Mechanisms Before and After the 1992 Landers Earthquake Sequence, *Bull. Seismol. Soc. Am.* 84: 917-934, 1994.
- Healy, J. H., W. W. Rubey, D. T. Griggs, and C. B. Raleigh, The Denver earthquakes, *Science* 161: 1301-1310, 1968.
- Herrmann, R., S. Park, and C. Wang, The Denver earthquakes of 1967-1968, *Bull. Seismol. Soc. Am.* 71: 731-745, 1981.
- Huang, P. Y., S. C. Solomon, E. A. Bergman, and J. L. Nabelek, Focal depths and mechanisms of Mid-Atlantic ridge earthquakes from body wave inversion, *J. Geophys. Res.* 91: 579-598, 1986.

- Hubbert, M. K., and W. W. Rubey, Role of pore fluid pressure in the mechanics of overthrust faulting, *Bull. Geol. Soc. Am.* 70: 115-166, 1959.
- Iio, Y., Depth-dependent change in the focal mechanism of shallow earthquakes: Implications for brittle-plastic transition in a seismogenic region. *J. Geophys. Res.* 101: 11,209-11,216, 1996.
- Jacobsen, R. S., Map of Oregon seismicity, 1841-1986, *Oregon Dept. of Geol. and Min. Ind. Geological Map Series GMS-49*, 1986.
- Jaeger, J. C., and N. G. W. Cook, *Fundamentals of Rock Mechanics*, Chapman and Hall Ltd., London, 1971.
- Jordan, T. H., K. A. Sverdrup, Teleseismic location techniques and their application to earthquake clusters in the South-Central Pacific, *Bull. Seismol. Soc. Am.* 71: 1105-1130, 1981.
- Kanamori, H. and G. Stewart, Seismological aspects of the Guatemala earthquake of Feb. 4 1976, *J. Geophys. Res.* 83: 3427-3434, 1978.
- Koch K., Moment tensor inversion of local earthquake data-I. Investigation of the method and its numerical stability with model calculations, *Geophys. J. Int.* 106: 305-319, 1991a.
- Koch K., Moment tensor inversion of local earthquake data-II. Application to aftershocks of the May 1980 Mammoth Lakes earthquakes, *Geophys. J. Int.* 106: 321-332, 1991b.
- Kostrov, B. V., and S. Das, Evaluation of stress and displacement fields due to an elliptical plane shear crack, *Geophys. J. Roy. Astr. Soc.* 78: 19-33, 1984.
- Ma, L. R., R. S. Crosson, and R. S. Ludwin, Focal mechanisms of western Washington earthquakes and their relationship to regional tectonic stress, *U.S. Geol. Surv. Open-File Rep. 91-441-D*, 1991.
- Madin, I., G. Priest, M. Mabey, S. Malone, T. Yelin, and D. Meier, March 25, 1993 Scotts Mills earthquake-western Oregon's wake-up call, *Oregon Geology* 55: 51-56, 1993.

- Mao, J. W., G. F. Panza, and P. Suhaldoc, Linearized waveform inversion of local and near-regional events for source mechanisms and rupturing processes, *Geophys. J. Int.* 116: 784-798, 1994.
- McGarr, A., Some Constraints on Levels of Shear Stress in the Crust From Observations and Theory, *J. Geophys. Res.* 85: 6231-6238, 1980.
- Mendoza, C. and S. H. Hartzell, Aftershock pattern and mainshock faulting, *Bull. Seismol. Soc. Am.* 78: 1438-1449, 1988.
- Menke, W., *Geophysical data analysis: Discrete Inverse Theory*, Academic Press, Inc., 1984.
- Nabelek, J. and Xia, G., Moment-tensor analysis using regional data: Application to the 25 March, 1993, Scotts Mills, Oregon, earthquake, *Geophysical Research Letters* 22: 13-16, 1995.
- Nabelek, J., Determination of earthquake source parameters from inversion of body-waves, Ph.D. thesis, Mass. Inst. of Tech., 1984.
- Nafe, J. E., C. L. Drake, Variation with depth in shallow and deep water marine sediments of porosity, density, and the velocities of compressional and shear waves, *Geophysics* 22: 523-552, 1957.
- Nur, A., and J. R. Booker, Aftershocks caused by pore fluid flow? *Science* 175: 885-887, 1972.
- Nur, A., Dilatancy, Pore Fluids, and Premonitory Variations of t_s/t_p Travel Times, *Bull. Seismol. Soc. Am.* 62: 1217-1223, 1972.
- Oppenheimer, D., Aftershock Slip Behavior of the 1989 Loma Prieta, California Earthquake, *Geophysical Research Letters* 17: 1199-1202, 1990.
- Oppenheimer, D., W. H. Bakun, and A. G. Lindh, Slip partitioning of the Calaveras fault, California, and prospects for future earthquakes, *J. Geophys. Res.* 95: 8483-8498, 1990.

- Pavlis, G. L. and J. R. Booker, Progressive Multiple Event Location (PMEL), *Bull. Seismol. Soc. Am.* 73: 1753-1777, 1983.
- Pujol, J., Comments on the joint determination of hypocenters and station corrections, *Bull. Seismol. Soc. Am.* 78: 1179-1189, 1988.
- Ritsema, J., and T. Lay, Rapid source mechanism determination of large ($M_w \geq 5.5$) earthquakes in the western United States, *Geophys. Res. Lett.* 20: 1611-1614, 1993.
- Saikia, C. K., and R. B. Herrmann, Application of waveform modeling to determine focal mechanisms of four 1982 Miramichi aftershocks, *Bull. Seismol. Soc. Am.* 75: 1021-1040, 1985.
- Saikia, C. K., and R. B. Herrmann, Moment tensor solutions for three 1982 Arkansas swarm earthquakes by waveform modeling, *Bull. Seismol. Soc. Am.* 76: 709-723, 1986.
- Scholz, C. H., L. R. Sykes, and Y. P. Aggarwal, Earthquake prediction: a physical basis, *Science* 181: 803-810, 1973.
- Schwartz, S. Y., J. W. Dewey, and T. Lay, Influence of fault plane heterogeneity on the seismic behavior in the southern Kurile Island arc, *J. Geophys. Res.* 94: 5637-5649, 1989.
- Schwartz, S. Y., Source Parameters of the 1991 Costa Rica and 1992 Cape Mendocino, California, Earthquakes from Inversion of Local Amplitude Ratios and Broad Band Waveforms, *Bull. Seismol. Soc. Am.* 85: 1560-1575, 1995.
- Sheriff, R. E., and L. P. Geldart, *Exploration seismology*, Cambridge University Press, 1983.
- Sibson, R., Fluid flow accompanying faulting: evidence and models, *Earthquake Prediction, an International Review. M. Ewing Ser. 4*, ed. D. Simpson and P. Richards., . Washington D.C.: American Geophysical Union, pp. 593-604, 1981.
- Stump, B., and L. R. Johnson, The determination of source properties by the linear inversion of seismograms *Bull. Seismol. Soc. Am.* 67: 1489-1502, 1977.

- Thomas, G. C., R. S. Crosson, D. L. Carver, and T. S. Yelin, The 25 March Scotts Mills, Oregon, Earthquake and Aftershock Sequence: Spatial Distribution, Focal Mechanisms, and the Mount Angel Fault, *Bull. Seismol. Soc. Am.* 86: 925-935, 1996.
- Thurber, C. H., Earthquake locations and three-dimensional crustal structure in the Coyote Lake area, Central California, *J. Geophys. Res.* 88: 8226-8236, 1983.
- Trehu, A., I. Asudeh, T. Brooker, J. Luetgert, W. Mooney, J. Nabelek, and Y. Nakamura, Crustal architecture of the Cascadia forearc, *Science* 265: 237-243, 1994.
- Utsu, T., Aftershocks and earthquake statistics (III). *J. Fac. Science, Hokkaido Univ. Series VII (Geophysics)* 3: 379-441, 1971.
- Vetter, U. R., and A. S. Ryall, Systematic change of focal mechanisms with depth in the Western Great Basin, *J. Geophys. Res.* 88: 8237-8250, 1983.
- Wang, K., T. Mulder, G. C. Rogers, and R. D. Hyndman, Case of low coupling stress on the Cascadia subduction fault, *J. Geophys. Res.* 100: 12,907-12,918, 1995.
- Ward, S. H., *Editor, Geotechnical and Environmental Geophysics*, Soc. Expl. Geoph., 1990.
- Werner, K. S., E. P. Graven, T. A. Berkman, and M. J. Parker, Direction of maximum horizontal compressional in western Oregon determined by borehole breakouts, *Tectonics* 10: 948-958, 1991.
- Werner, K. S., J. L. Nabelek, R. Yeats, and S. Malone, The Mt. Angel Fault: Implications of seismic reflection data and the Woodburn, Oregon, earthquake sequence of August 1990, *Oregon Geology* 54: 112-117, 1992.
- Whitcomb, J. H., J. D. Garmany, and D. L. Anderson, Earthquake prediction: Variation of Seismic Velocities before the San Francisco Earthquake, *Science* 180: 632-641, 1973.
- Xia, G., Moment tensor inversion for regional earthquakes in the Pacific Northwest, unpublished M.S. thesis, Oregon State University 1994.

Yeats, R. S., E. P. Graven, K. S. Werner, C. Goldfinger, and T. Popowski, Tectonics of the Willamette Valley, Oregon, *U.S. Geol. Surv. Professional Paper* 1560: 183 - 222, 1996.

APPENDICES

APPENDIX A

This Appendix contains observed and synthetic waveforms of all earthquakes analyzed in this study. Event and Source parameters are summarized in Table 2.5.3.

Event 1, 1.0 - 3.0 Hz 3 pole filter

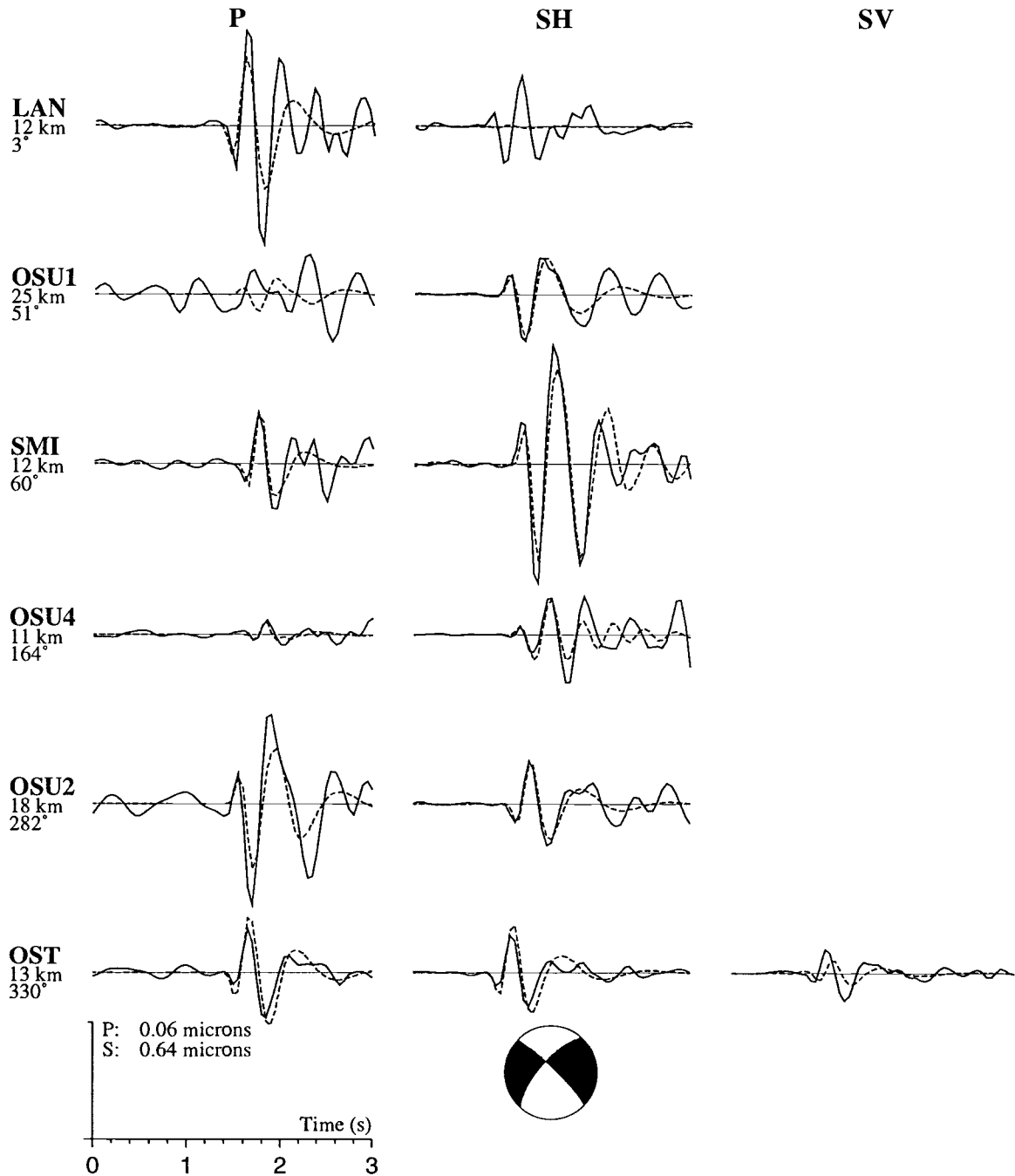


Figure A.1 Observed (solid lines) and synthetic (dashed lines) seismograms. First Column is station name, hypocentral distance, and event-station azimuth.

Event 2, 0.4 - 3.0 Hz 3 pole filter

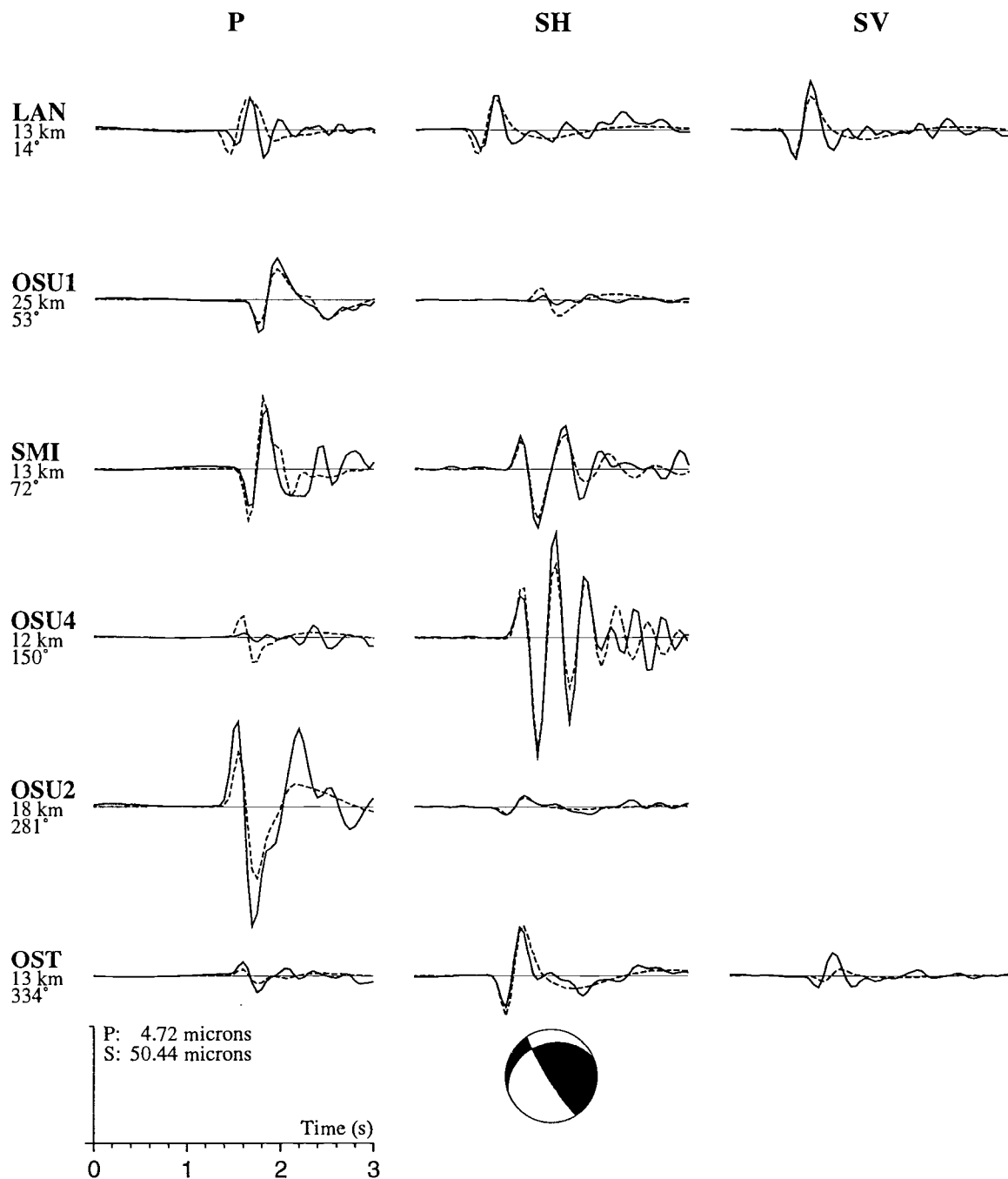


Figure A.2 Observed (solid lines) and synthetic (dashed lines) seismograms. First Column is station name, hypocentral distance, and event-station azimuth.

Event 3, 1.0 - 5.0 Hz 6 pole filter

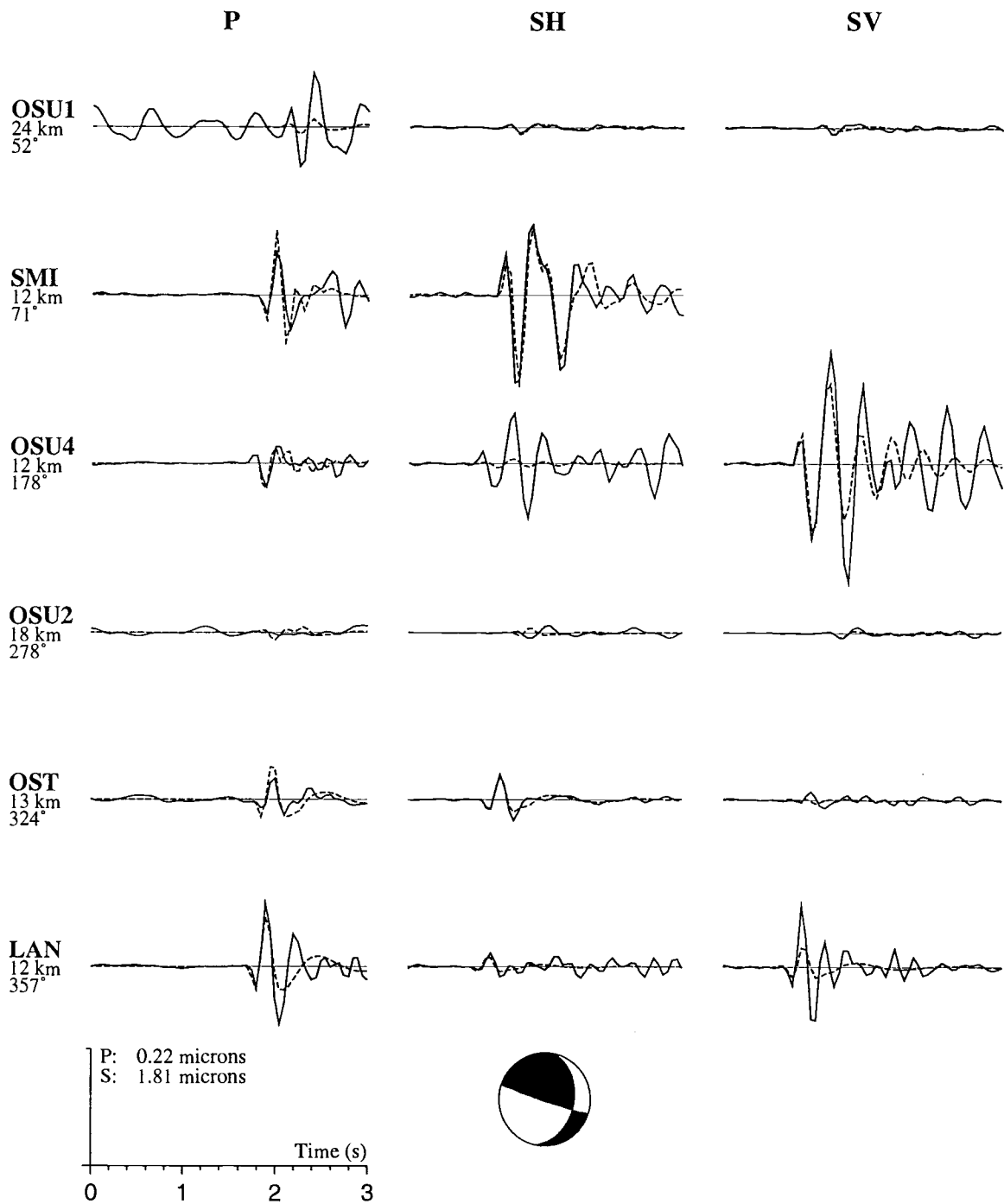


Figure A.3 Observed (solid lines) and synthetic (dashed lines) seismograms. First Column is station name, hypocentral distance, and event-station azimuth.

Event 4, 1.0 - 3.0 Hz 3 pole filter

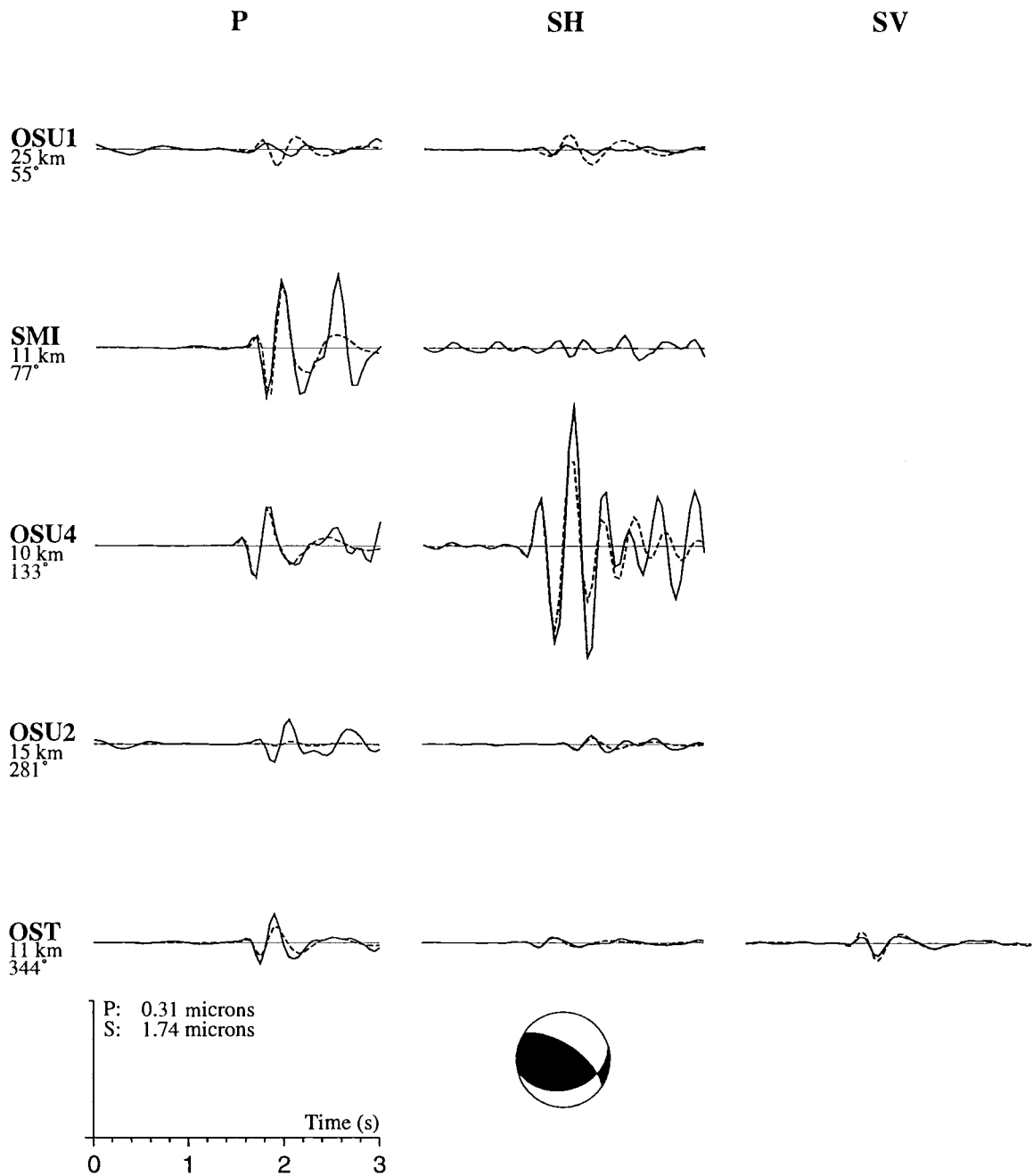


Figure A.4 Observed (solid lines) and synthetic (dashed lines) seismograms. First Column is station name, hypocentral distance, and event-station azimuth.

Event 5, 1.5 - 5.0 Hz 3 pole filter

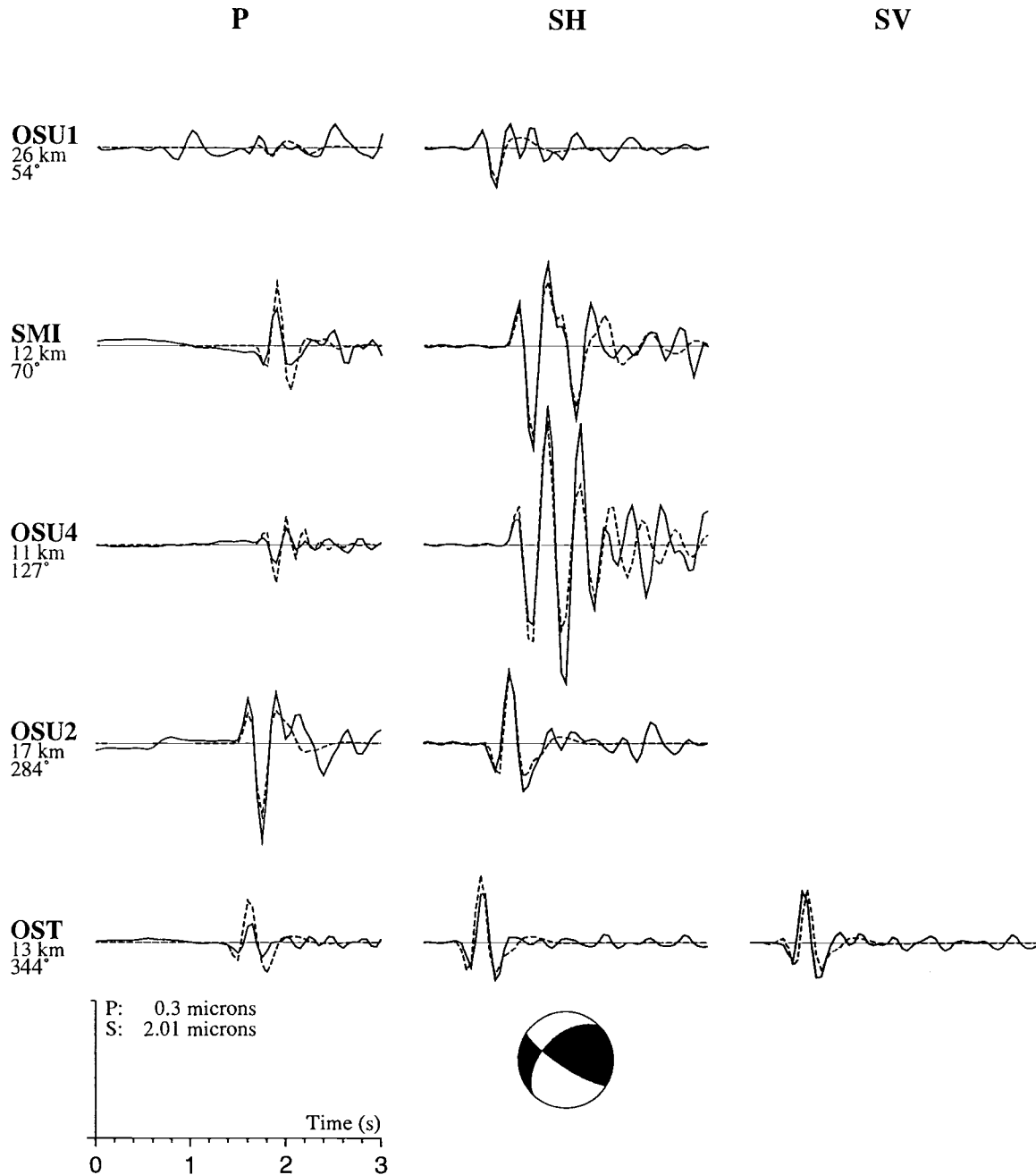


Figure A.5 Observed (solid lines) and synthetic (dashed lines) seismograms. First Column is station name, hypocentral distance, and event-station azimuth.

Event 6, 0.4 - 3.0 Hz 3 pole filter

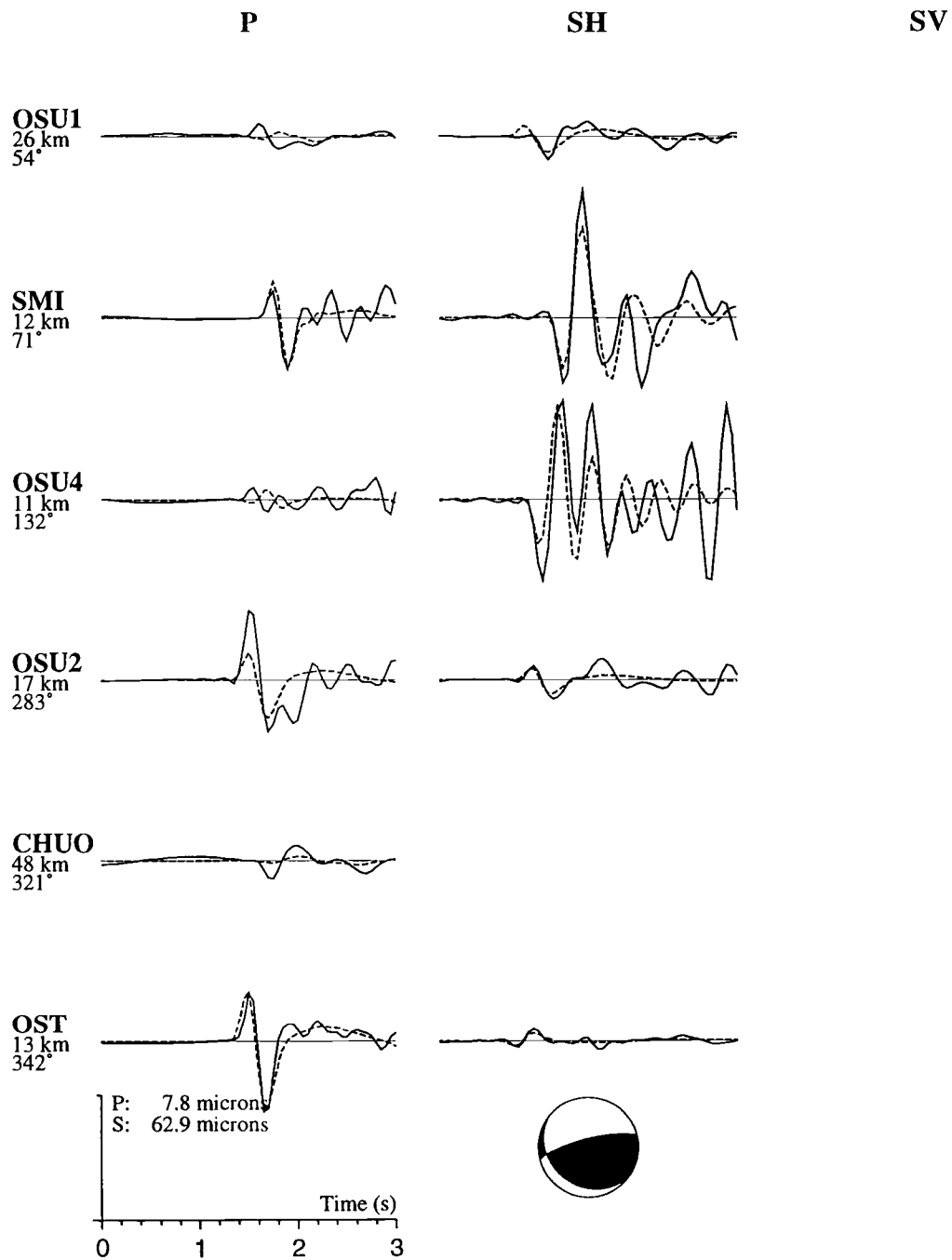


Figure A.6 Observed (solid lines) and synthetic (dashed lines) seismograms. First Column is station name, hypocentral distance, and event-station azimuth.

Event 7, 0.5 - 3.0 Hz 3 pole filter

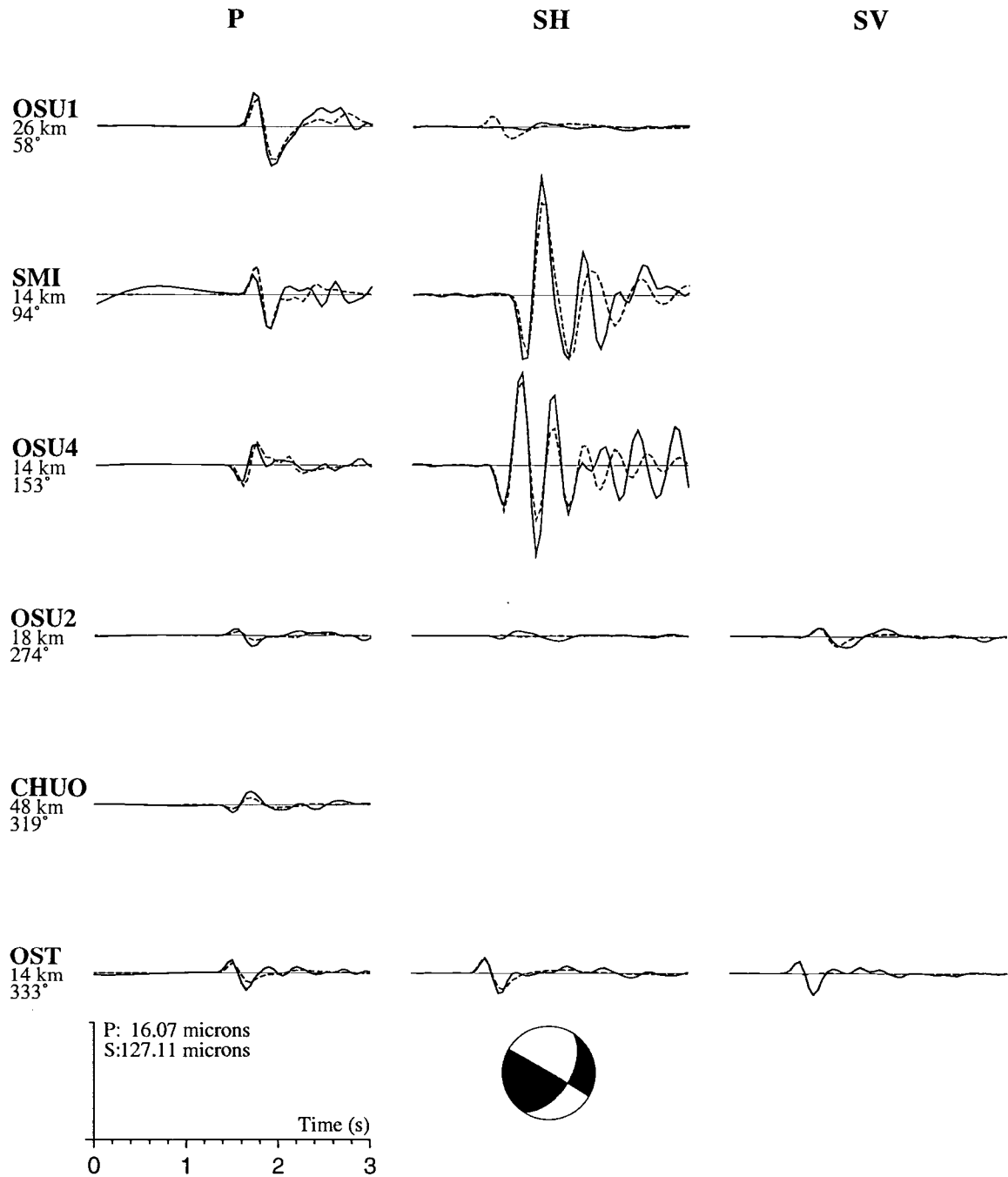


Figure A.7 Observed (solid lines) and synthetic (dashed lines) seismograms. First Column is station name, hypocentral distance, and event-station azimuth.

Event 8, 0.5 - 3.0 Hz 3 pole filter

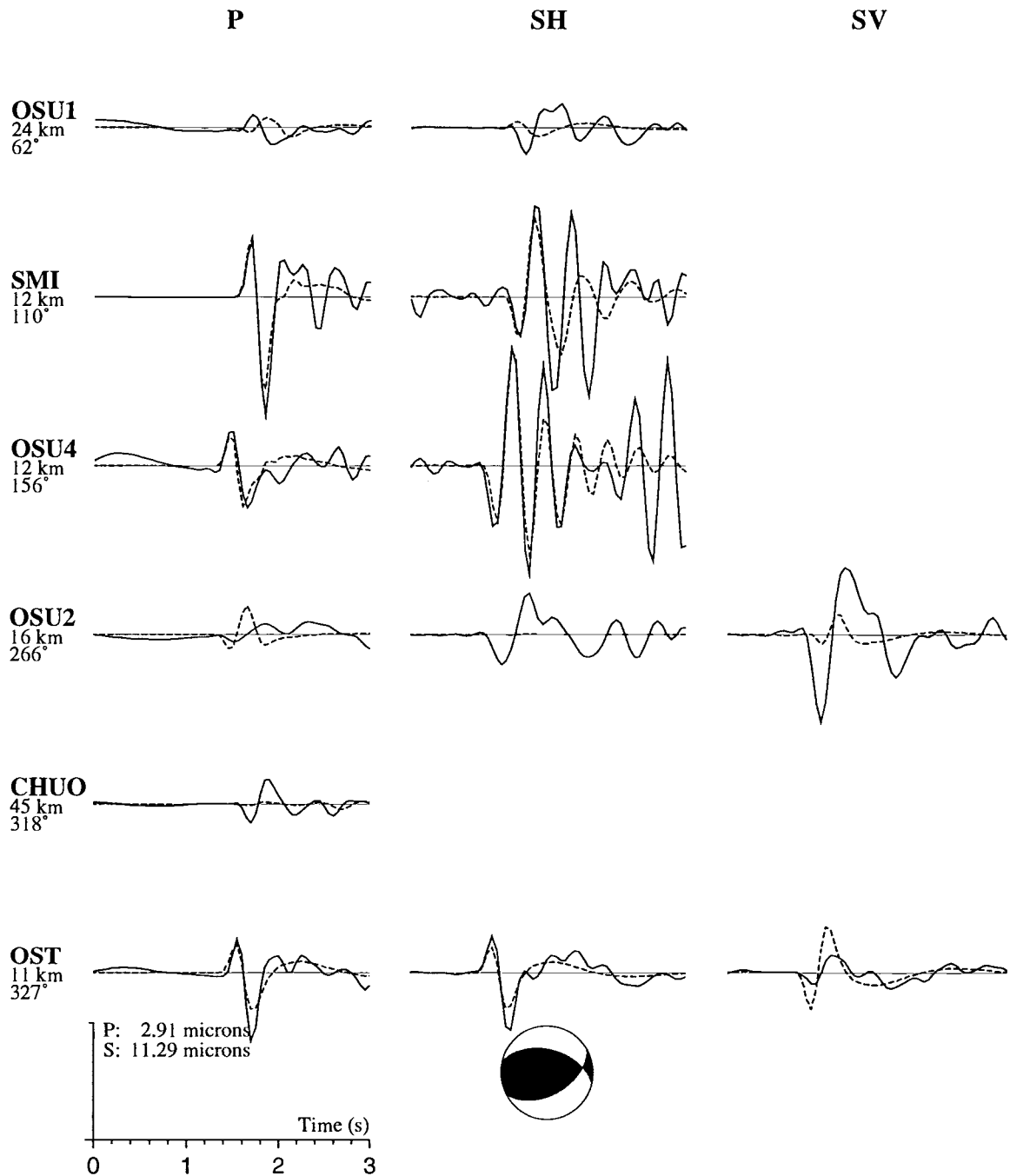


Figure A.8 Observed (solid lines) and synthetic (dashed lines) seismograms. First Column is station name, hypocentral distance, and event-station azimuth.

Event 9, 1.0 - 3.0 Hz 3 pole filter

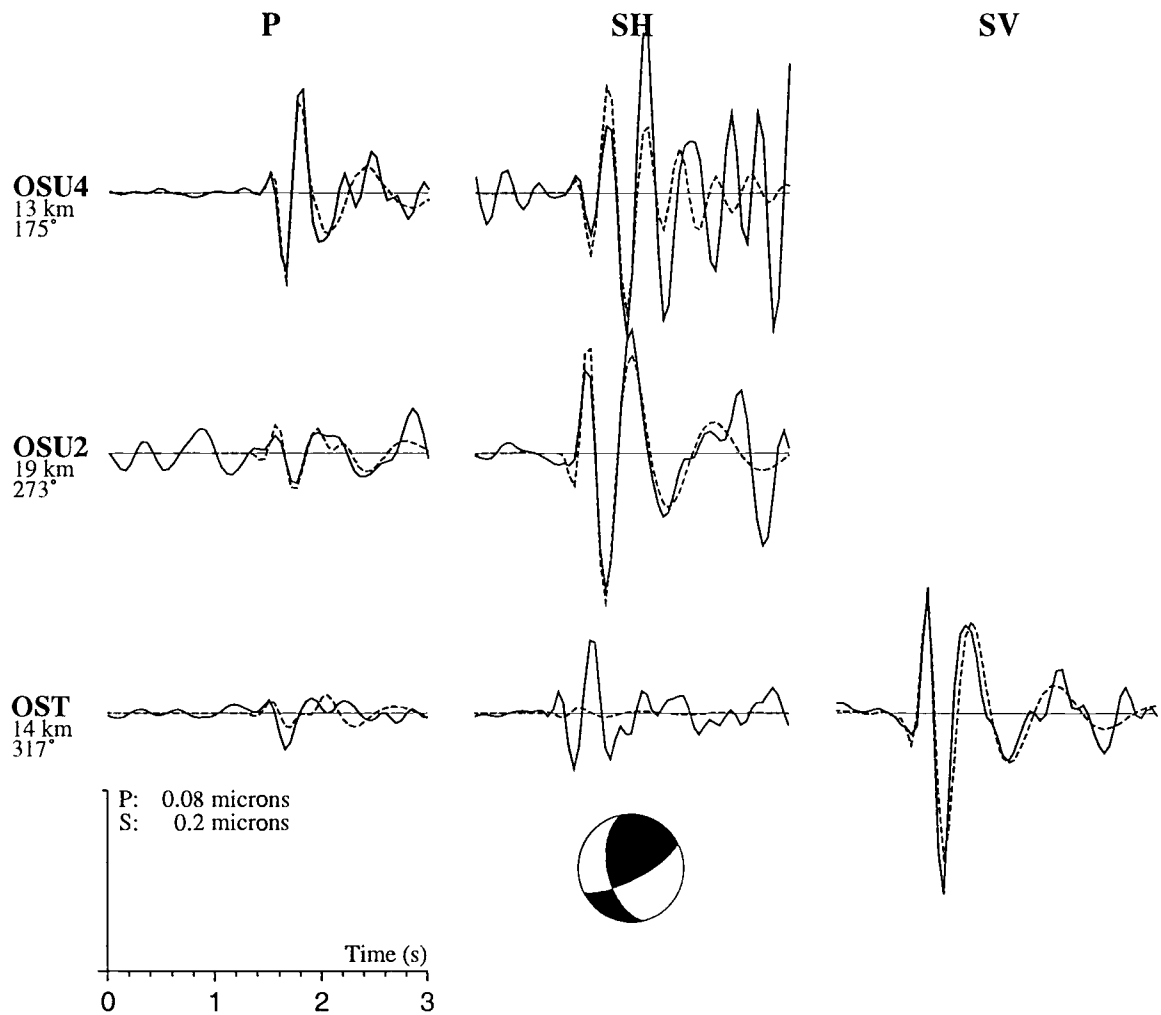


Figure A.9 Observed (solid lines) and synthetic (dashed lines) seismograms. First Column is station name, hypocentral distance, and event-station azimuth.

Event 10, 0.7 - 3.0 Hz 3 pole filter

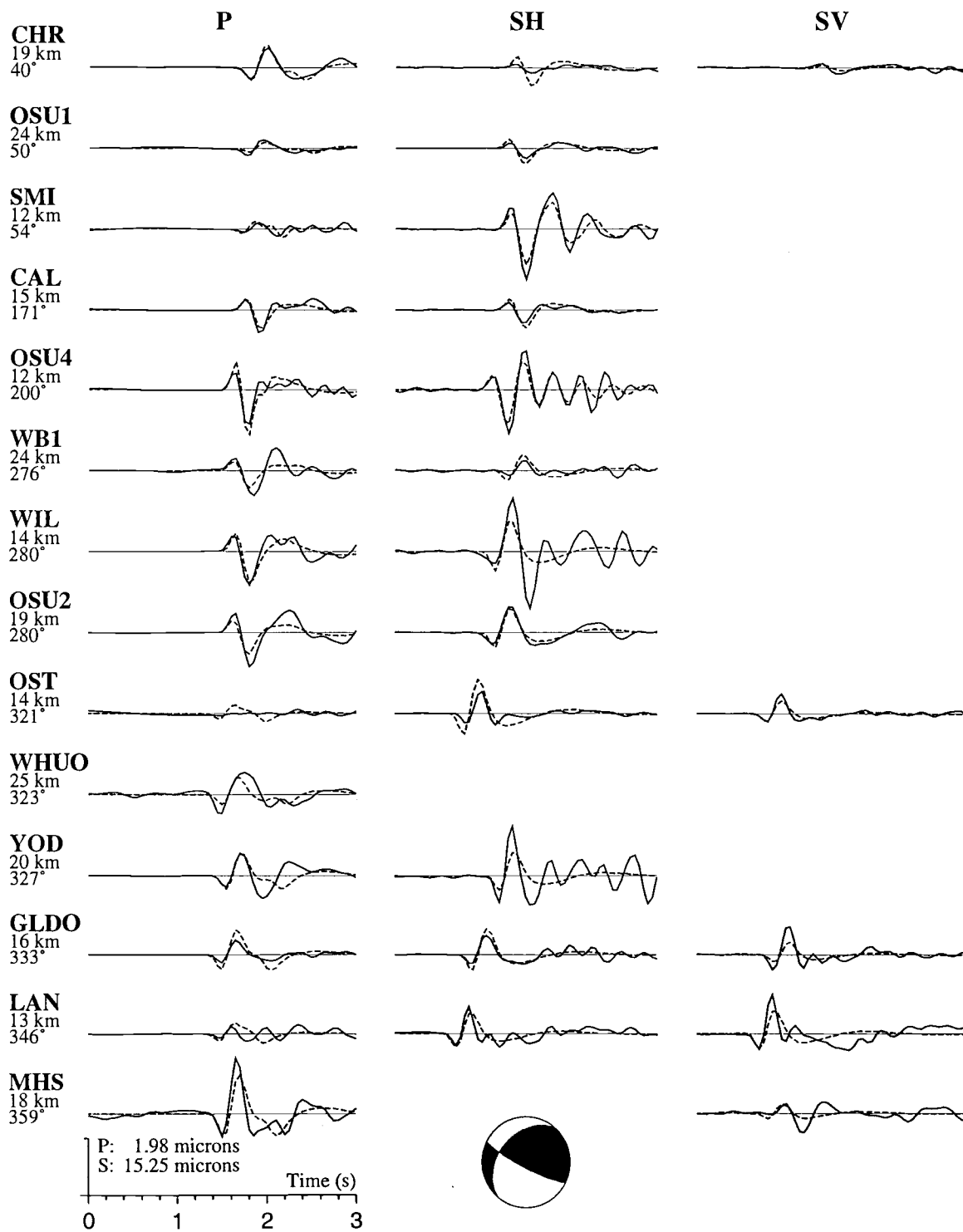


Figure A.10 Observed (solid lines) and synthetic (dashed lines) seismograms. First Column is station name, hypocentral distance, and event-station azimuth.

Event 11, 0.7 - 3.0 Hz 3 pole filter

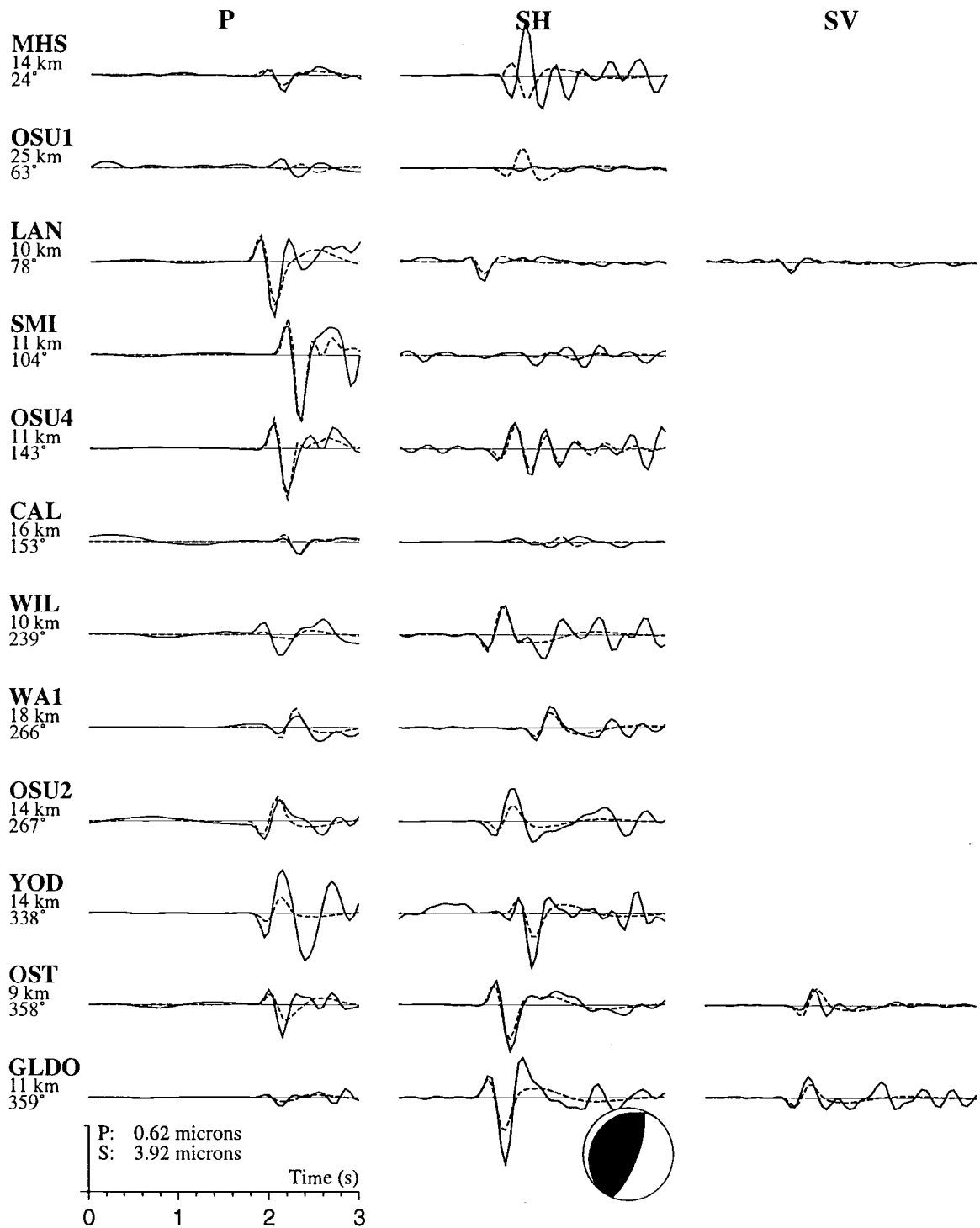


Figure A.11 Observed (solid lines) and synthetic (dashed lines) seismograms. First Column is station name, hypocentral distance, and event-station azimuth.

Event 12, 0.4 - 3.0 Hz 3 pole filter

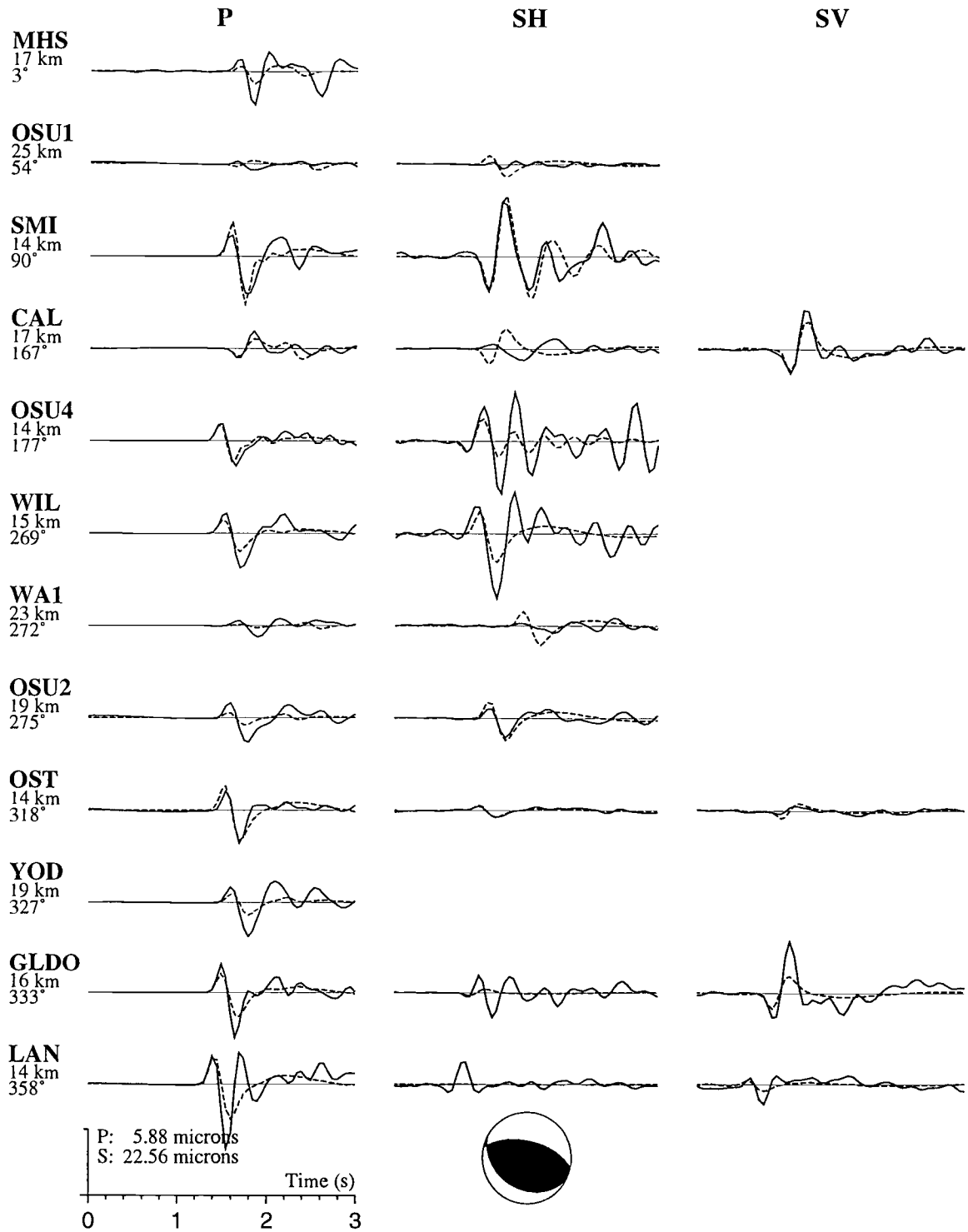


Figure A.12 Observed (solid lines) and synthetic (dashed lines) seismograms. First Column is station name, hypocentral distance, and event-station azimuth.

Event 13, 0.7 - 3.0 Hz 3 pole filter

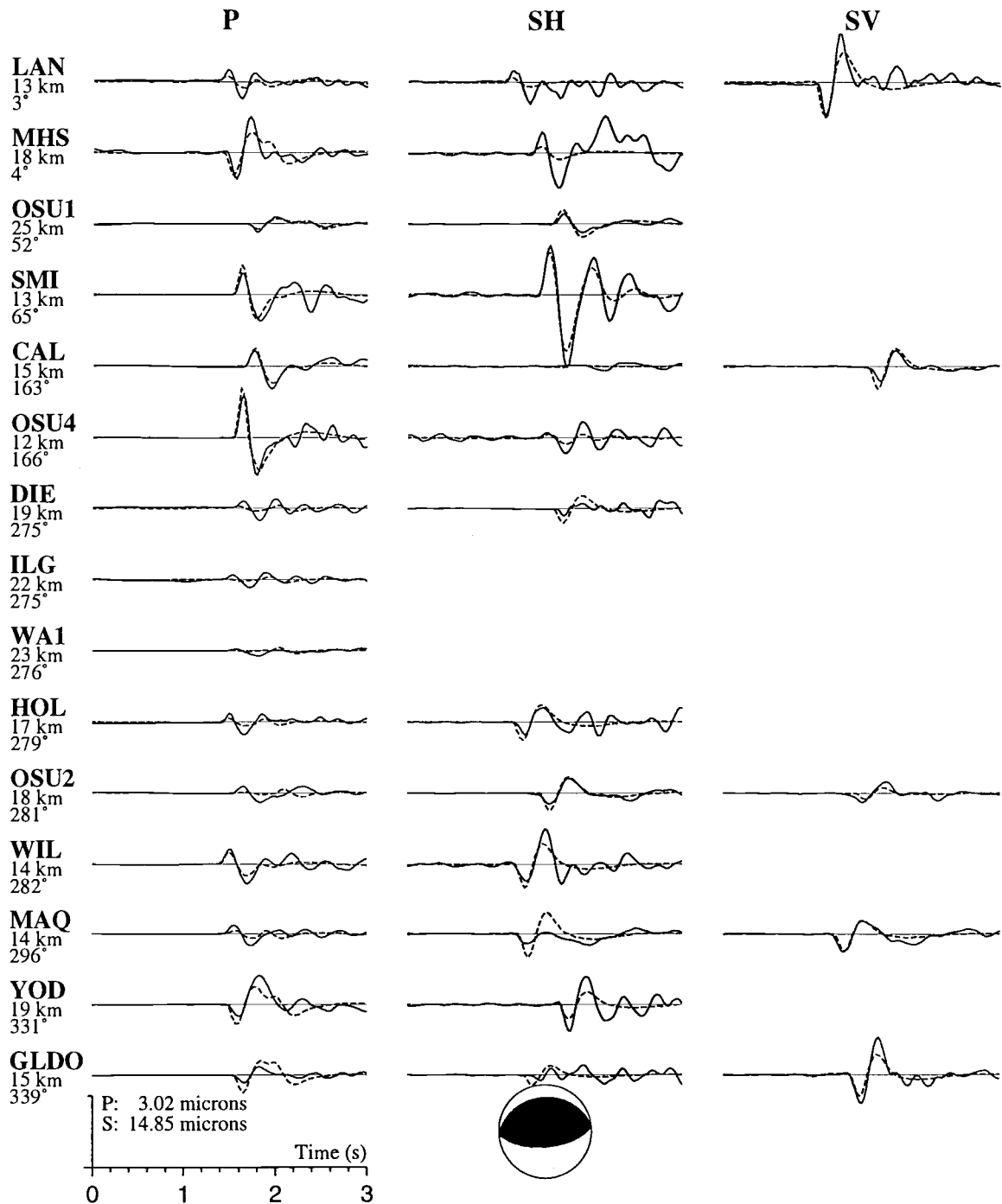


Figure A.13 Observed (solid lines) and synthetic (dashed lines) seismograms. First Column is station name, hypocentral distance, and event-station azimuth.

Event 14, 1.0 - 3.0 Hz 3 pole filter

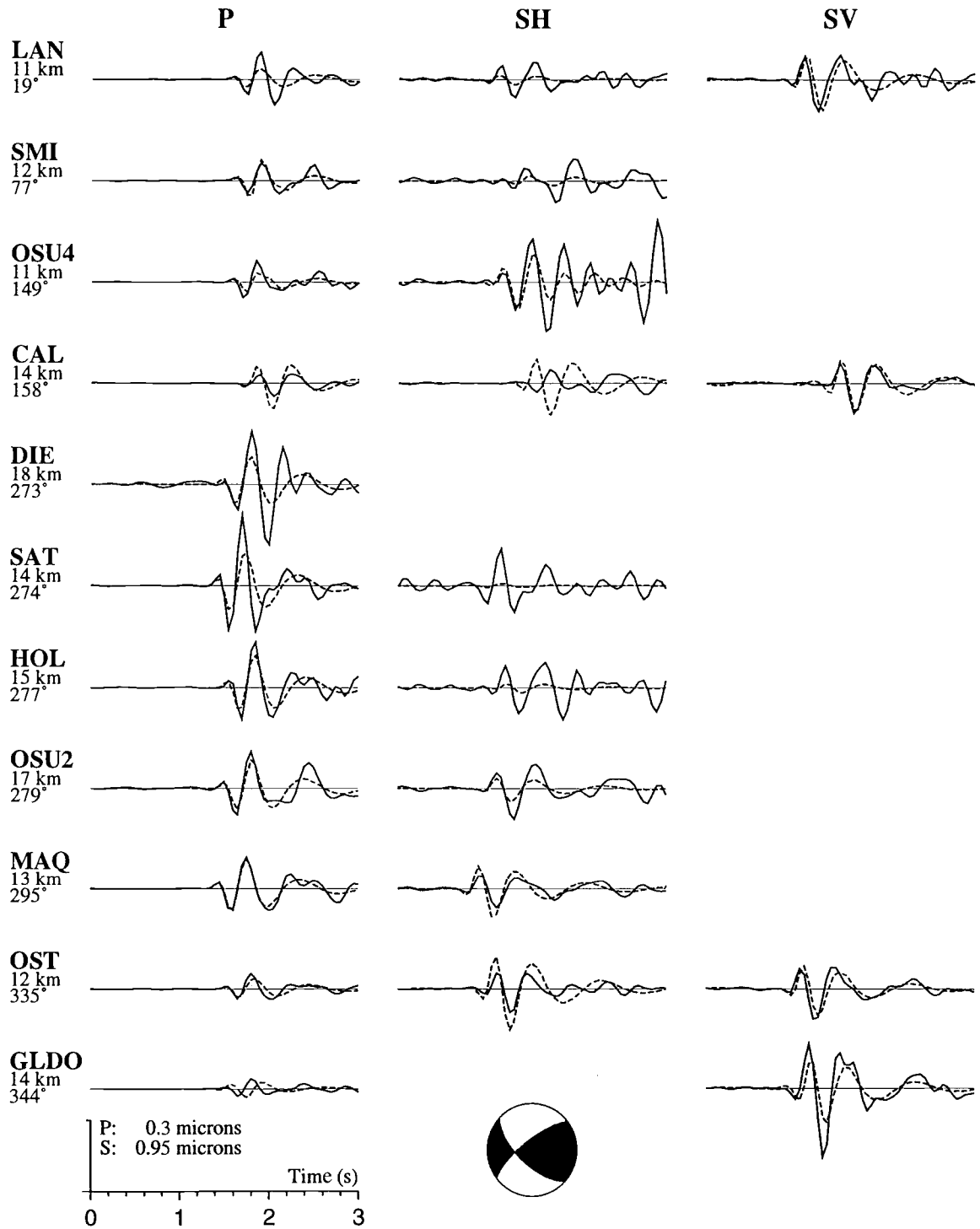


Figure A.14 Observed (solid lines) and synthetic (dashed lines) seismograms. First Column is station name, hypocentral distance, and event-station azimuth.

Event 15, 0.7 - 3.0 Hz 3 pole filter

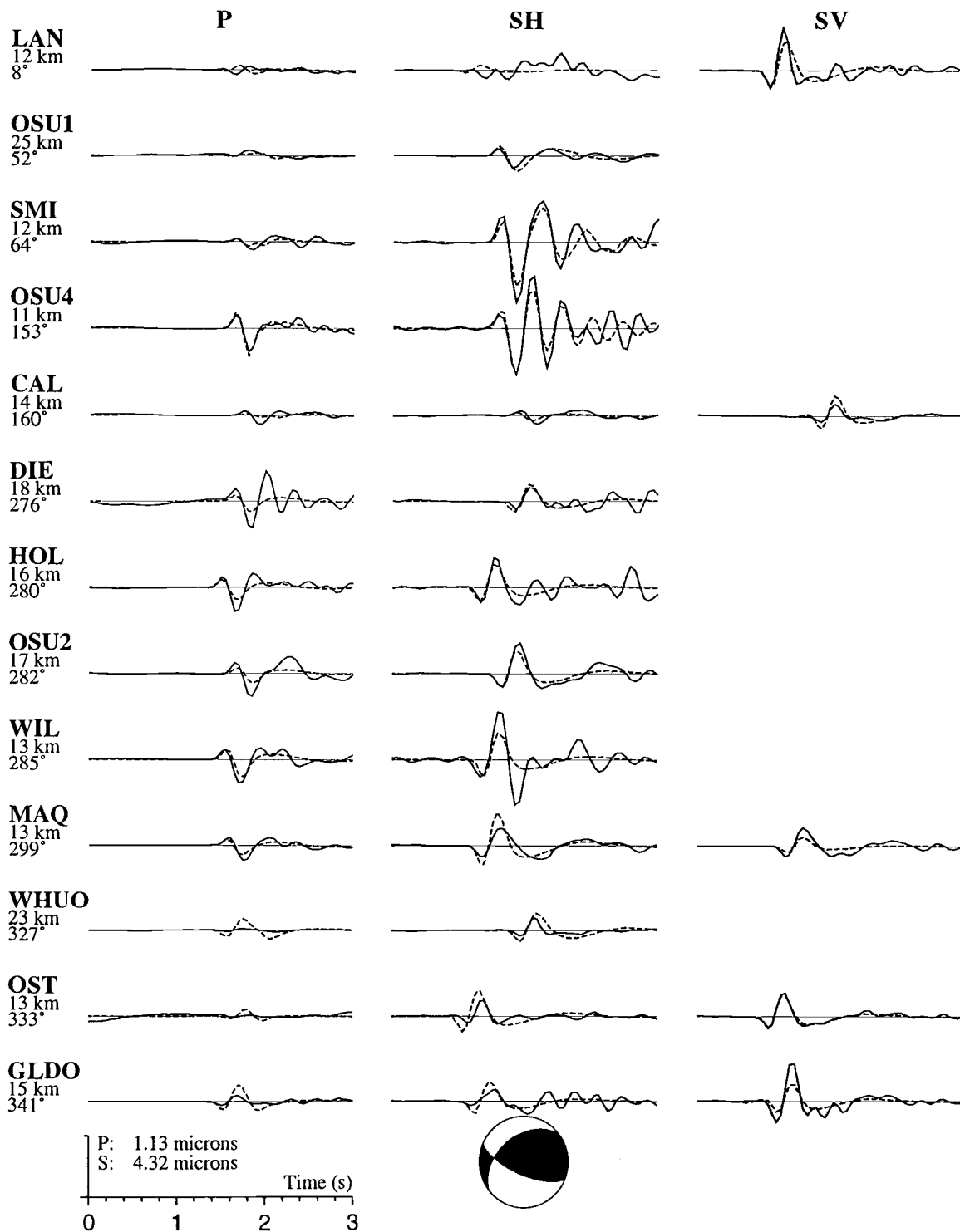


Figure A.15 Observed (solid lines) and synthetic (dashed lines) seismograms. First Column is station name, hypocentral distance, and event-station azimuth.

Event 16, 1.5 - 3.0 Hz 3 pole filter

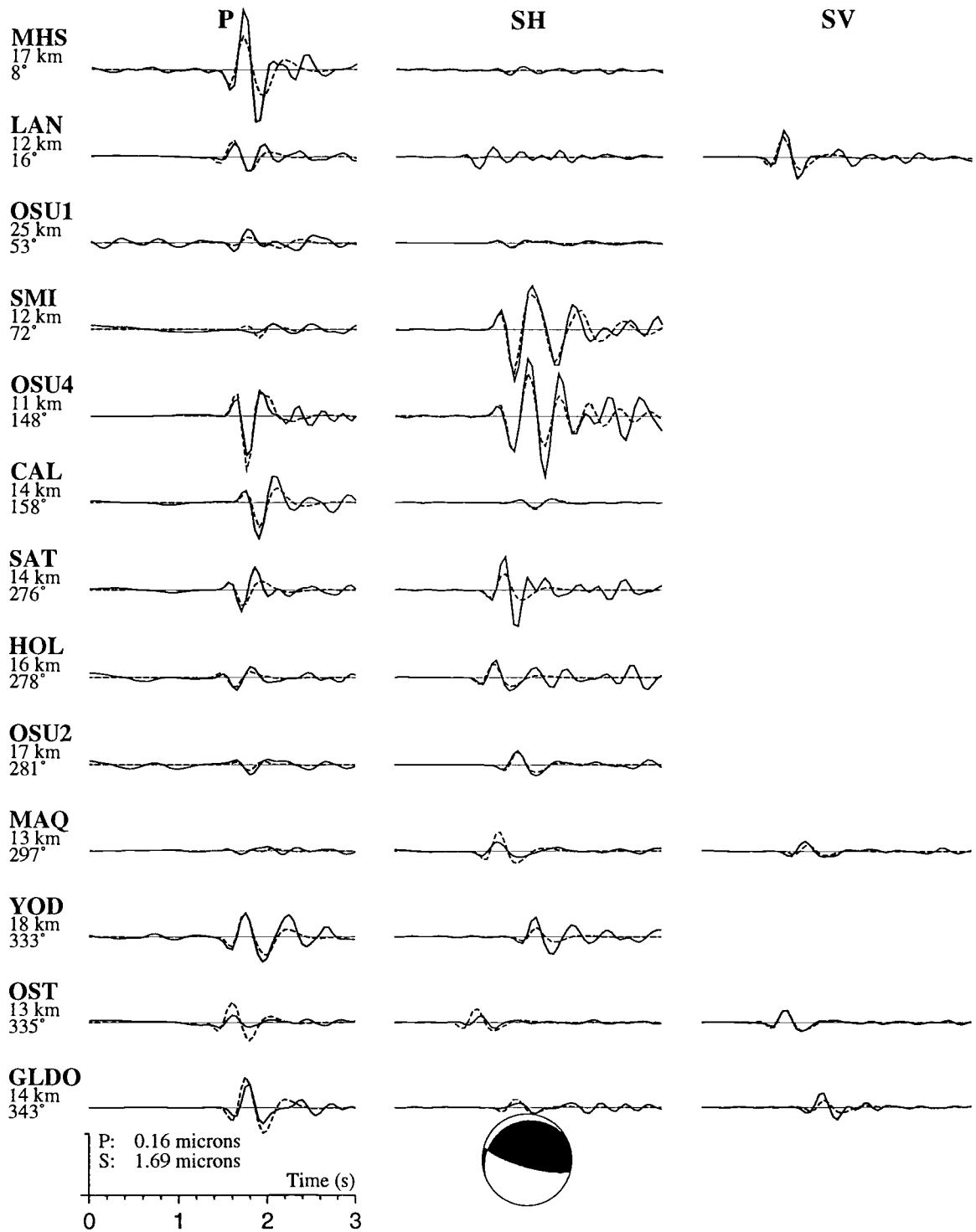


Figure A.16 Observed (solid lines) and synthetic (dashed lines) seismograms. First Column is station name, hypocentral distance, and event-station azimuth.

Event 17, 1.0 - 3.0 Hz 3 pole filter

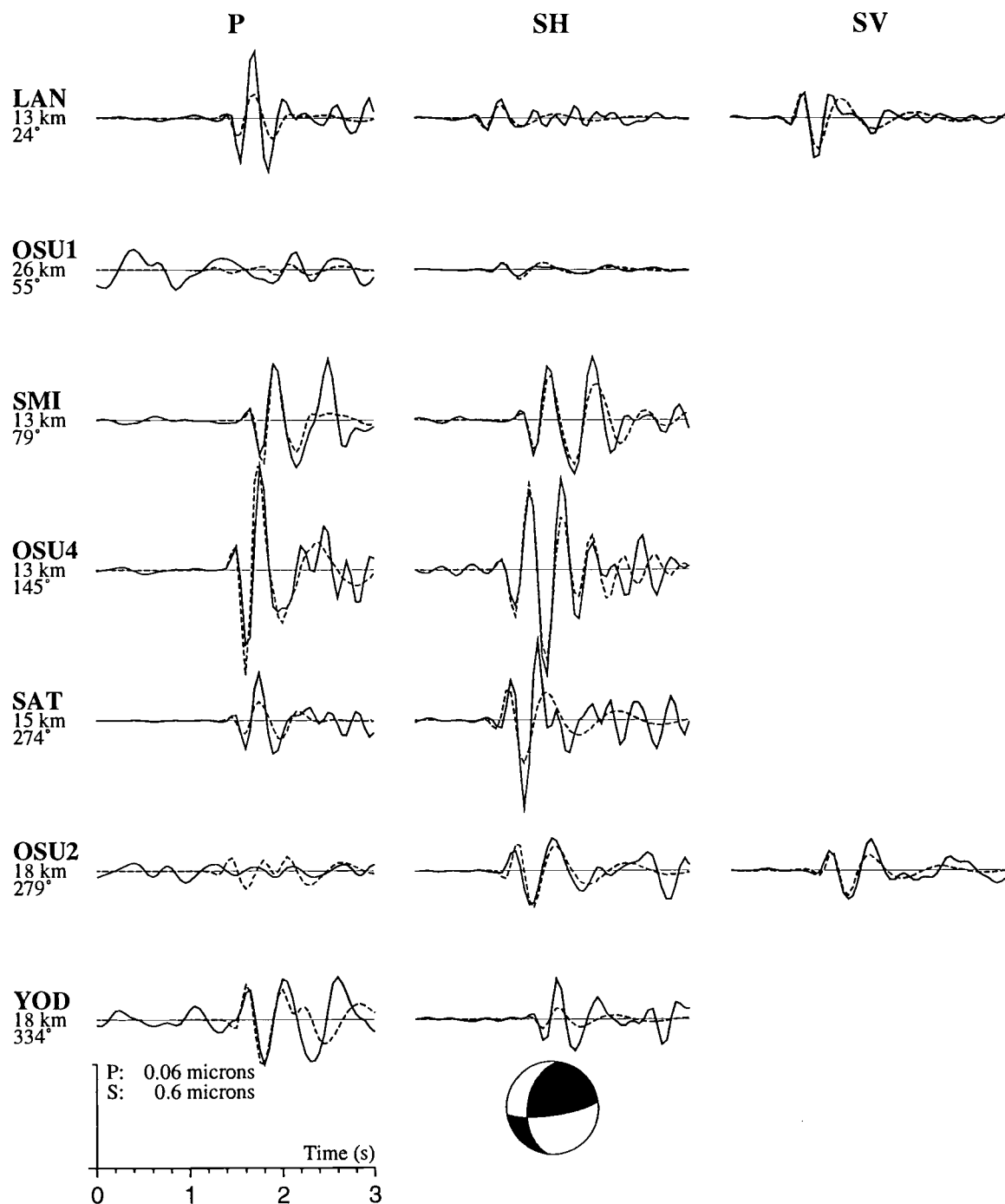


Figure A.17 Observed (solid lines) and synthetic (dashed lines) seismograms. First Column is station name, hypocentral distance, and event-station azimuth.

Event 18, 1.0 - 3.0 Hz 3 pole filter

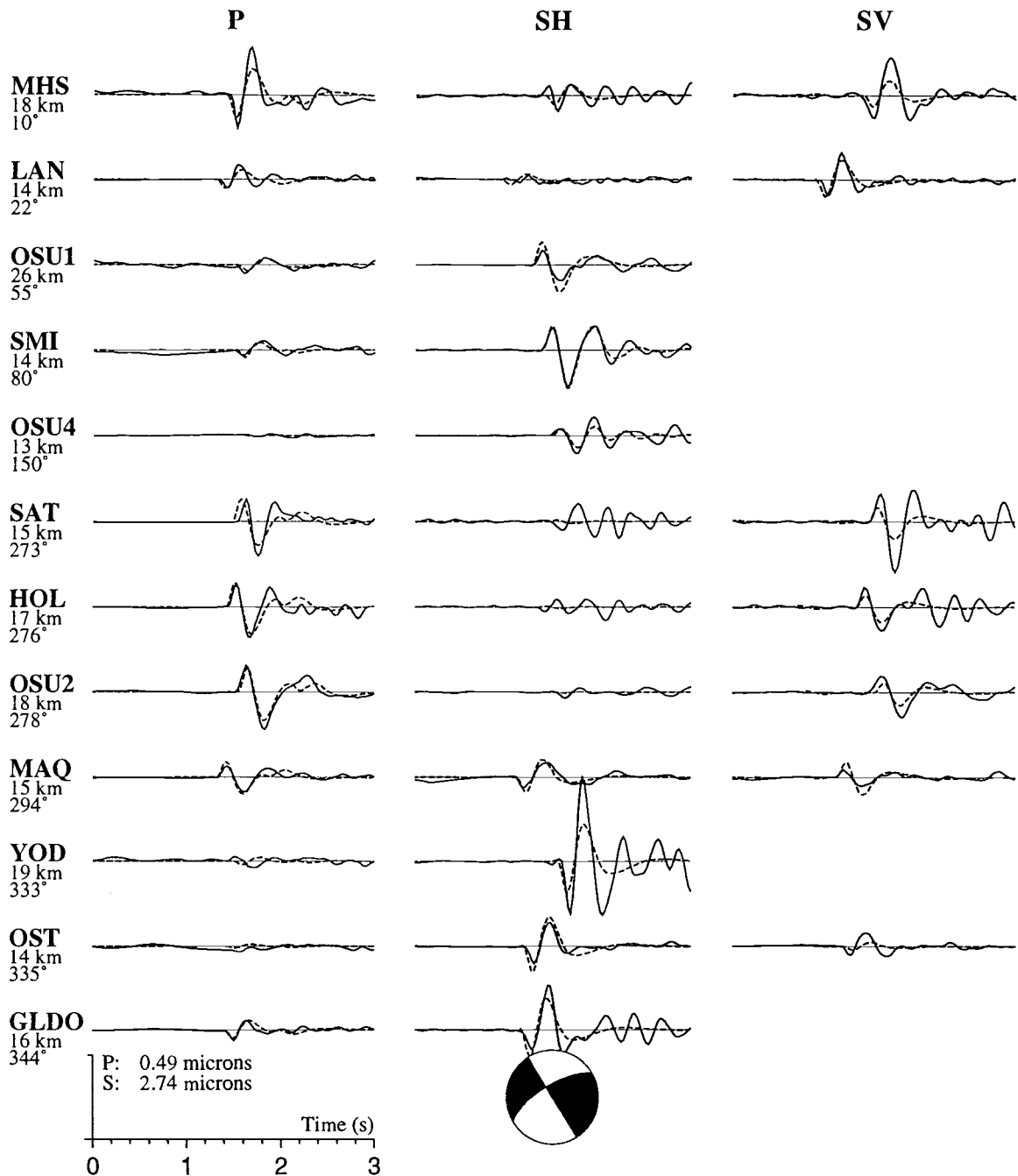


Figure A.18 Observed (solid lines) and synthetic (dashed lines) seismograms. First Column is station name, hypocentral distance, and event-station azimuth.

Event 19, 1.0 - 5.0 Hz 6 pole filter

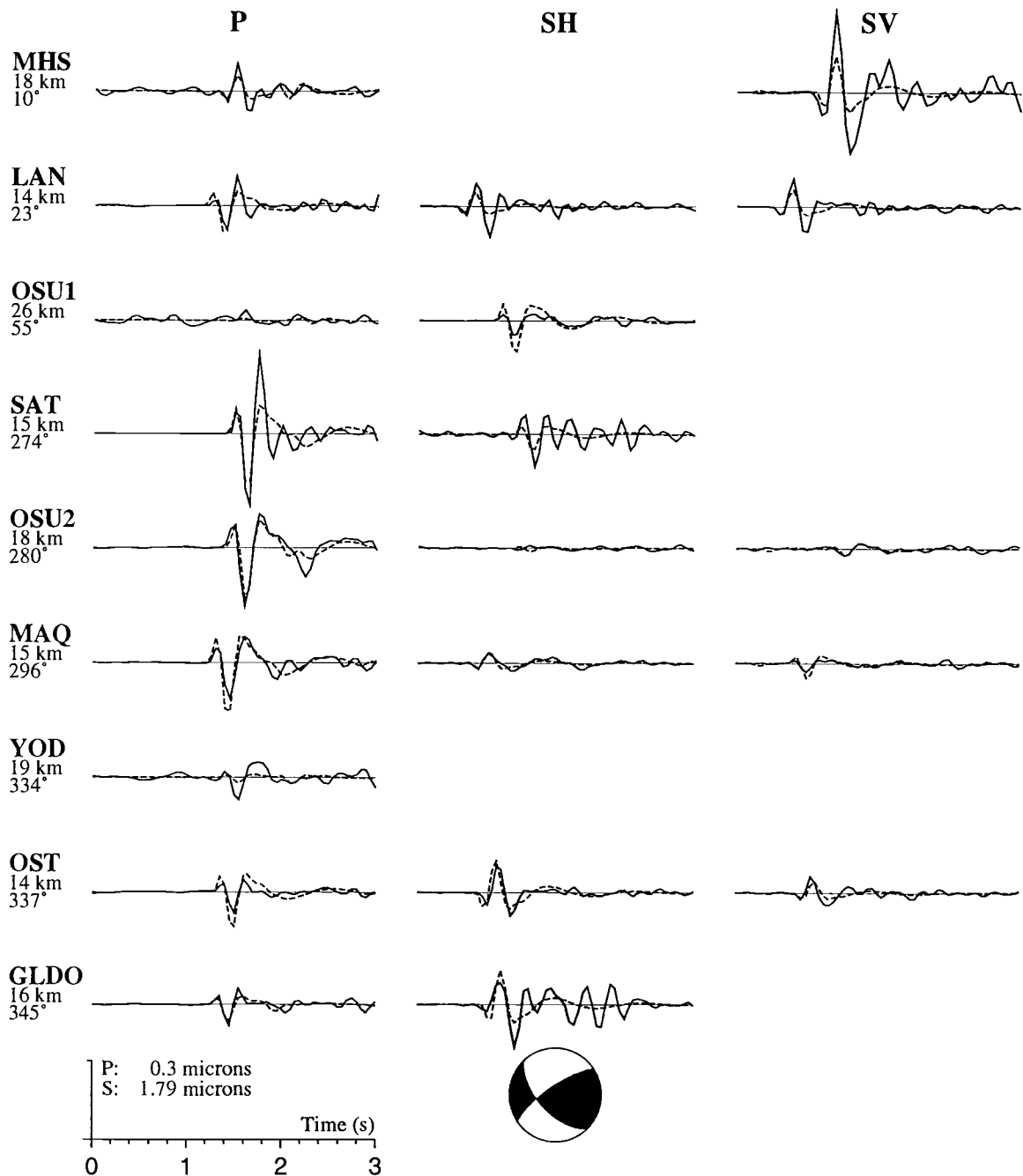


Figure A.19 Observed (solid lines) and synthetic (dashed lines) seismograms. First Column is station name, hypocentral distance, and event-station azimuth.

Event 20, 1.5 - 3.0 Hz 3 pole filter

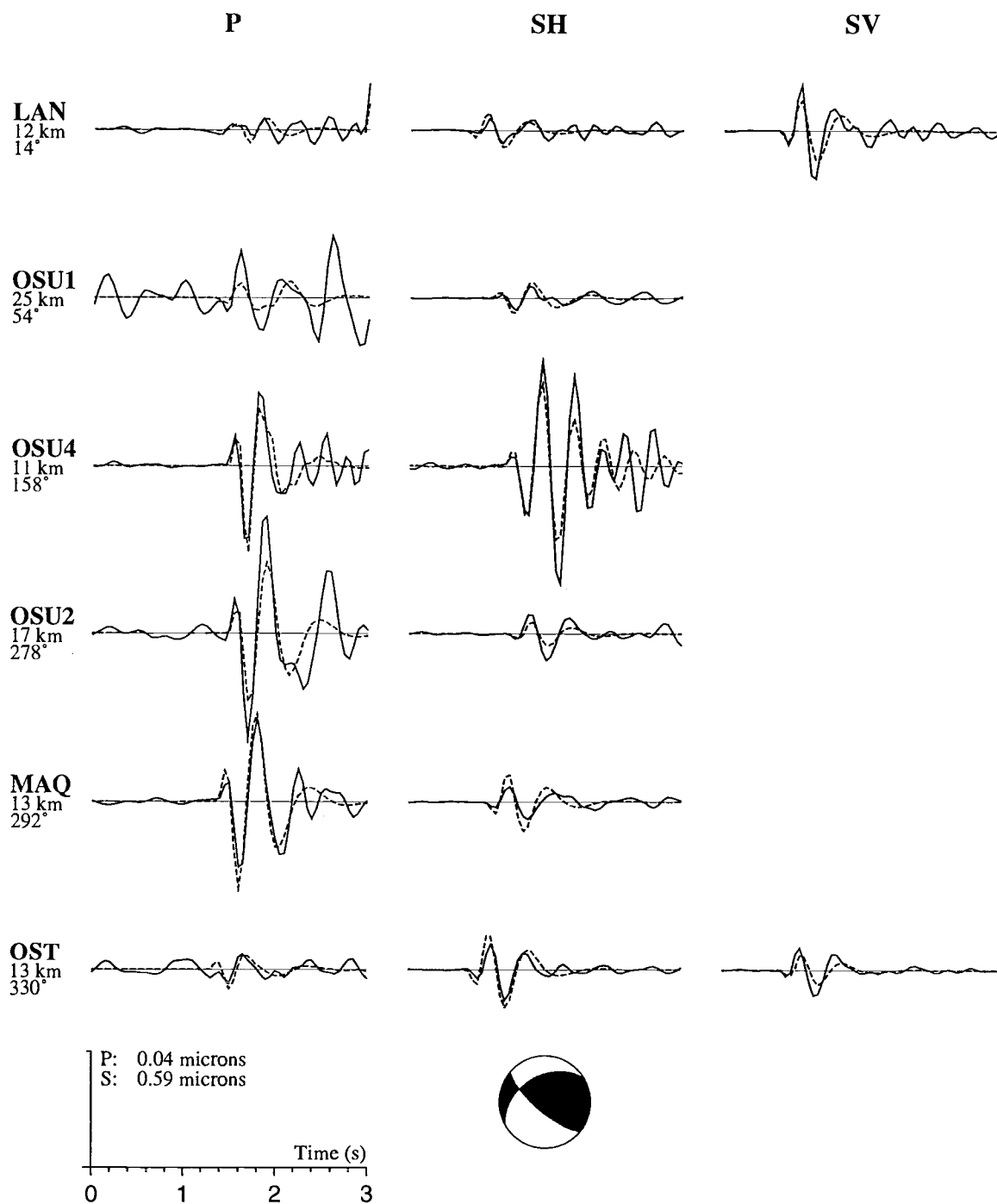


Figure A.20 Observed (solid lines) and synthetic (dashed lines) seismograms. First Column is station name, hypocentral distance, and event-station azimuth.

Event 21, 1.0 - 3.0 Hz 3 pole filter

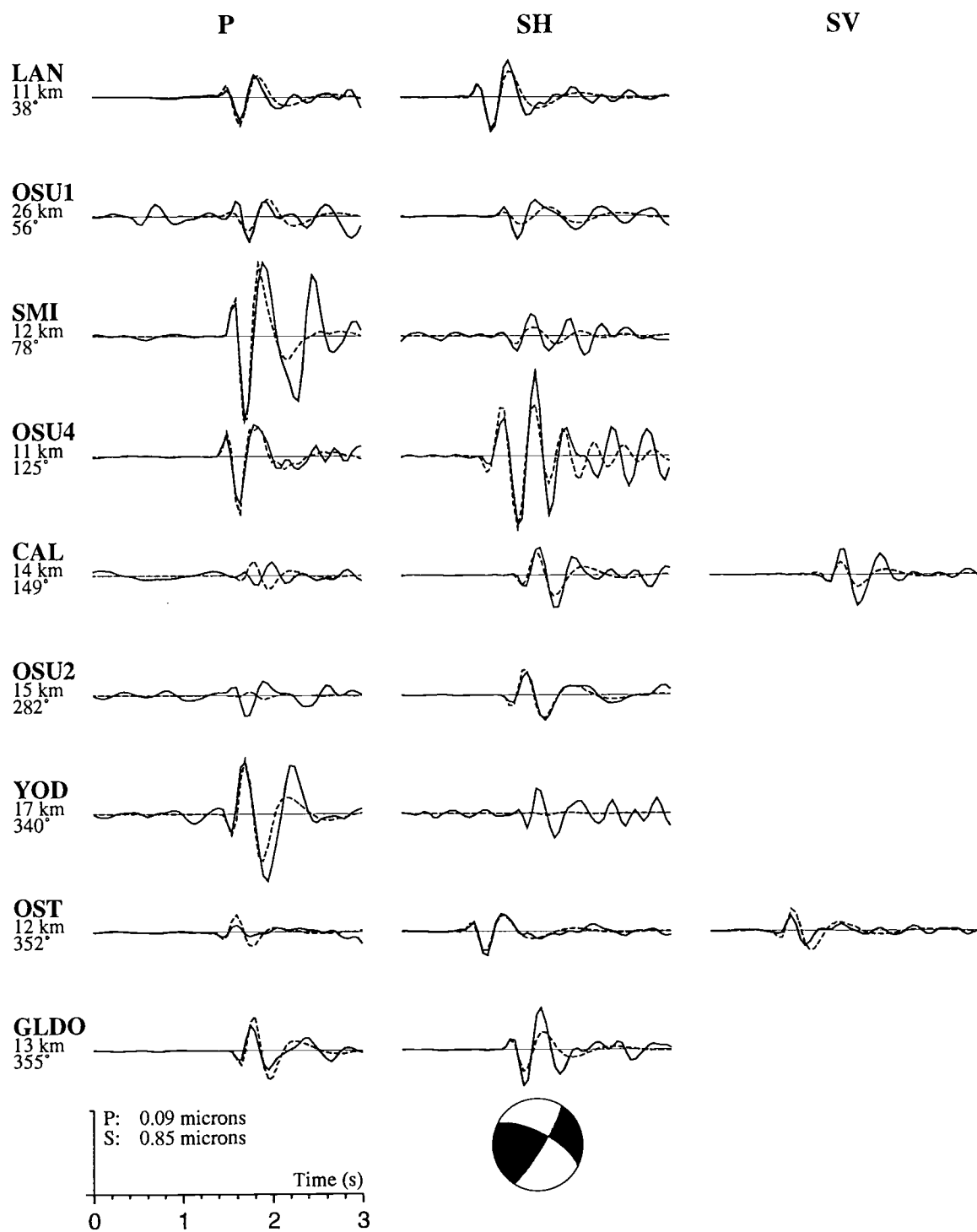


Figure A.21 Observed (solid lines) and synthetic (dashed lines) seismograms. First Column is station name, hypocentral distance, and event-station azimuth.

Event 22, 1.0 - 3.0 Hz 3 pole filter

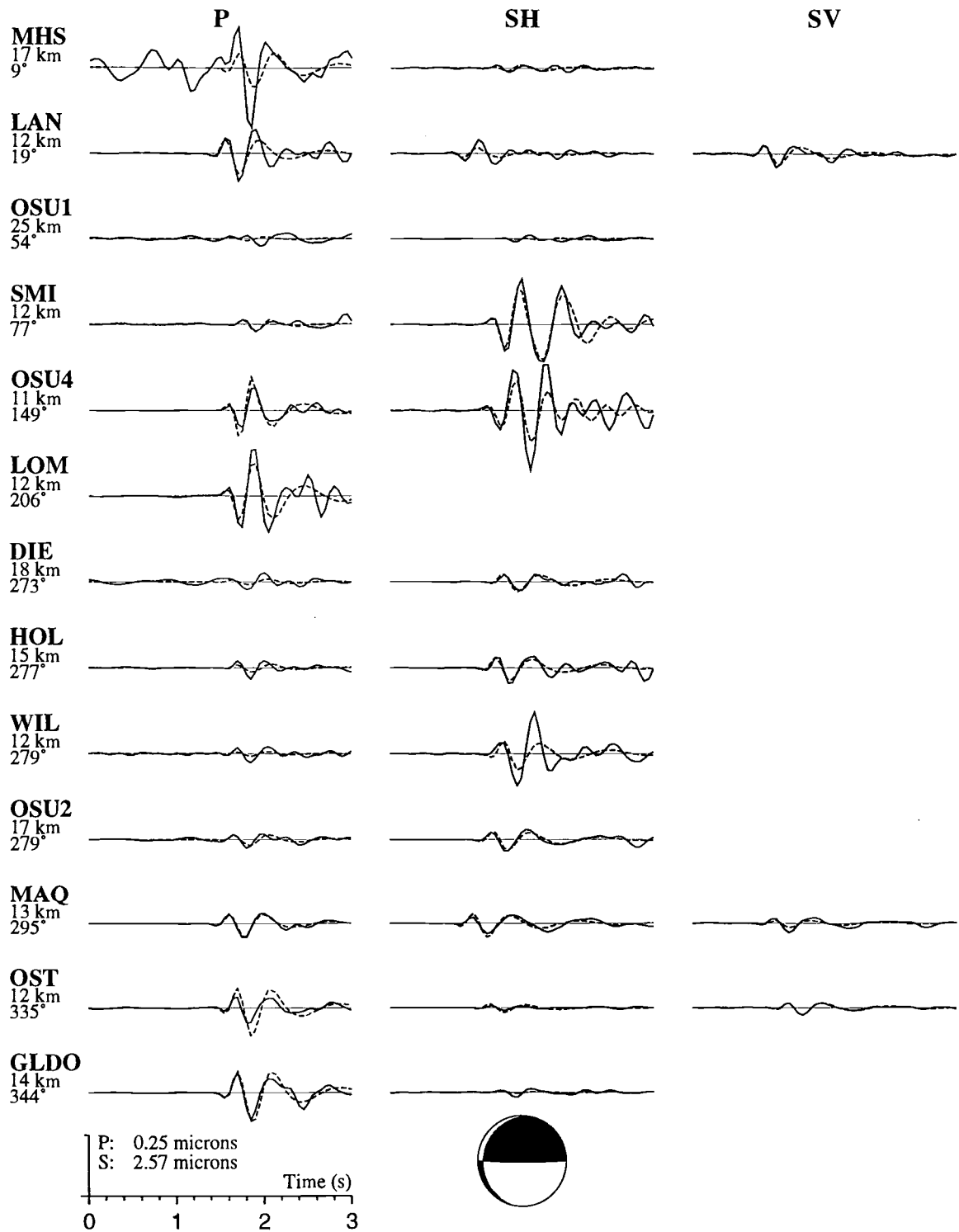


Figure A.22 Observed (solid lines) and synthetic (dashed lines) seismograms. First Column is station name, hypocentral distance, and event-station azimuth.

Event 23, 0.8 - 3.0 Hz 3 pole filter

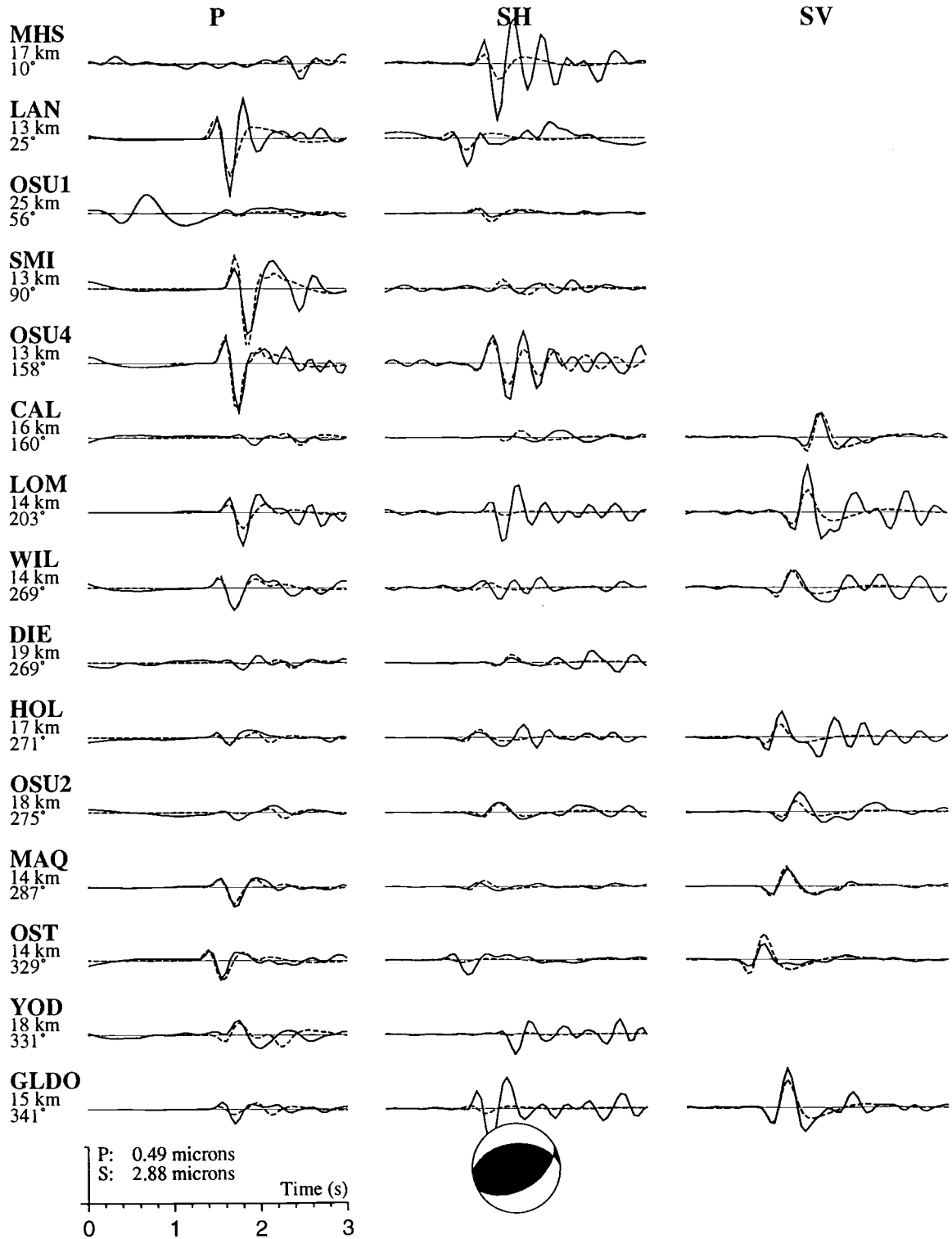


Figure A.23 Observed (solid lines) and synthetic (dashed lines) seismograms. First Column is station name, hypocentral distance, and event-station azimuth.

Event 24, 0.7 - 5.0 Hz 6 pole filter

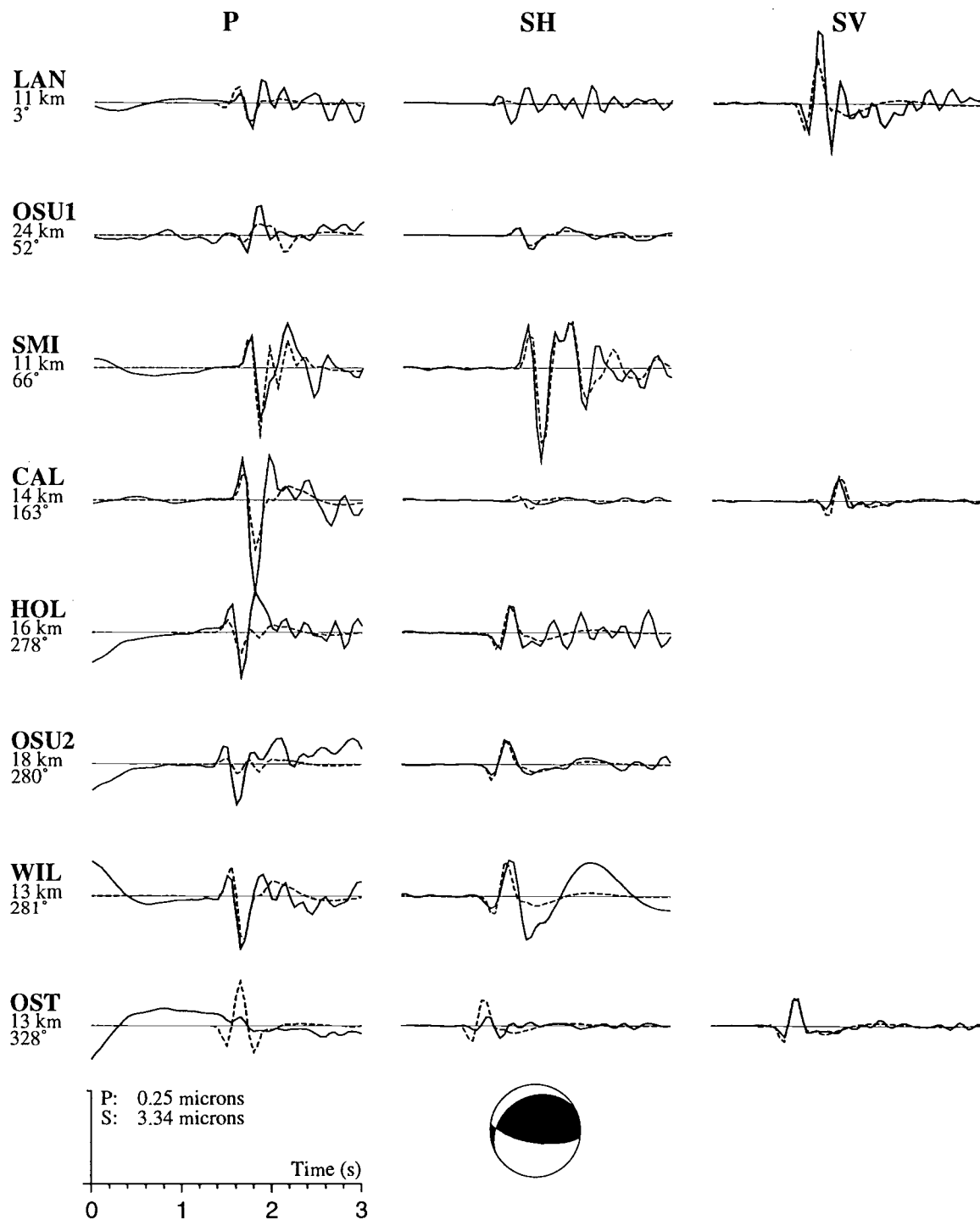


Figure A.24 Observed (solid lines) and synthetic (dashed lines) seismograms. First Column is station name, hypocentral distance, and event-station azimuth.

Event 25, 1.0 - 3.0 Hz 3 pole filter

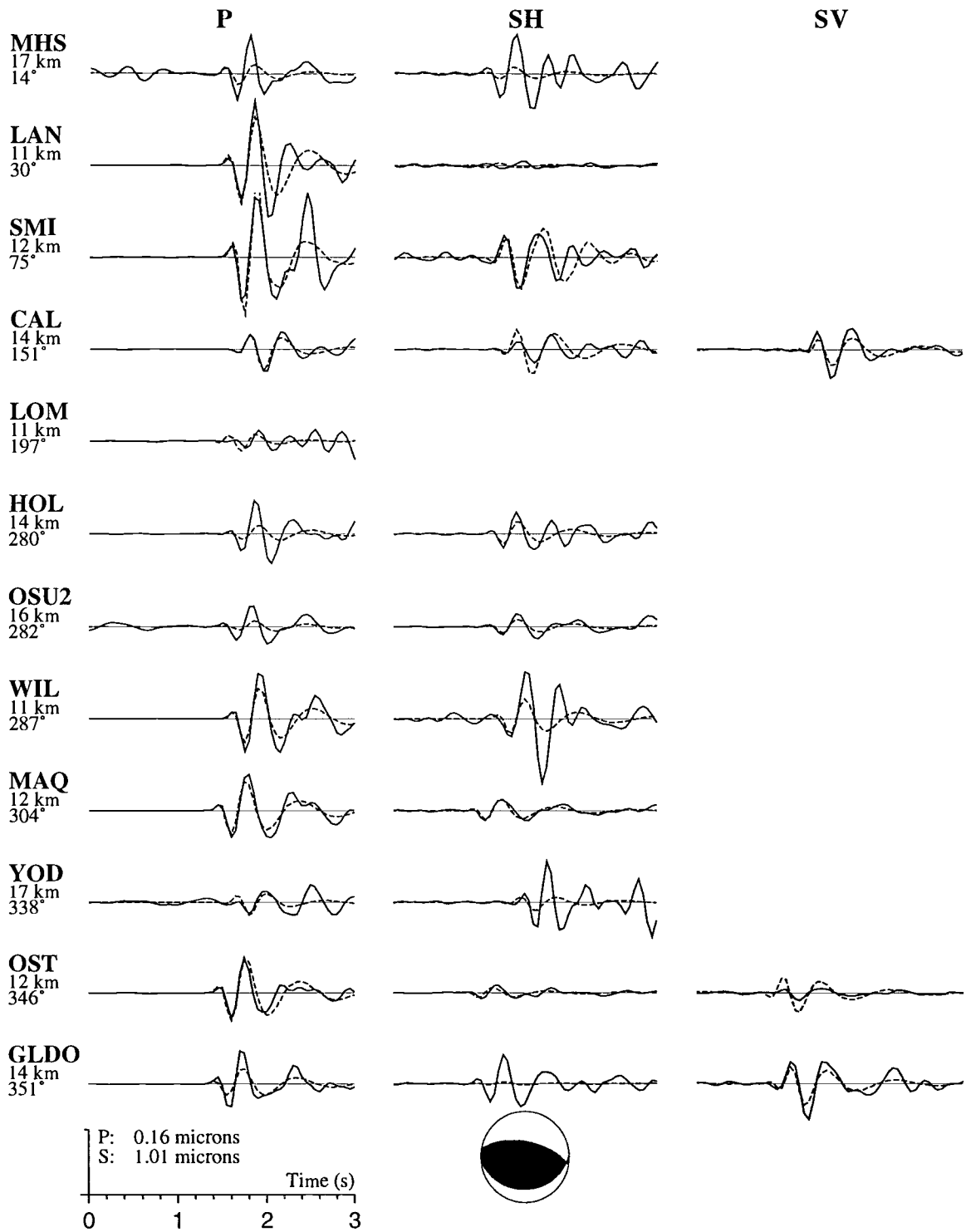


Figure A.25 Observed (solid lines) and synthetic (dashed lines) seismograms. First Column is station name, hypocentral distance, and event-station azimuth.

Event 26, 1.5 - 3.0 Hz 3 pole filter

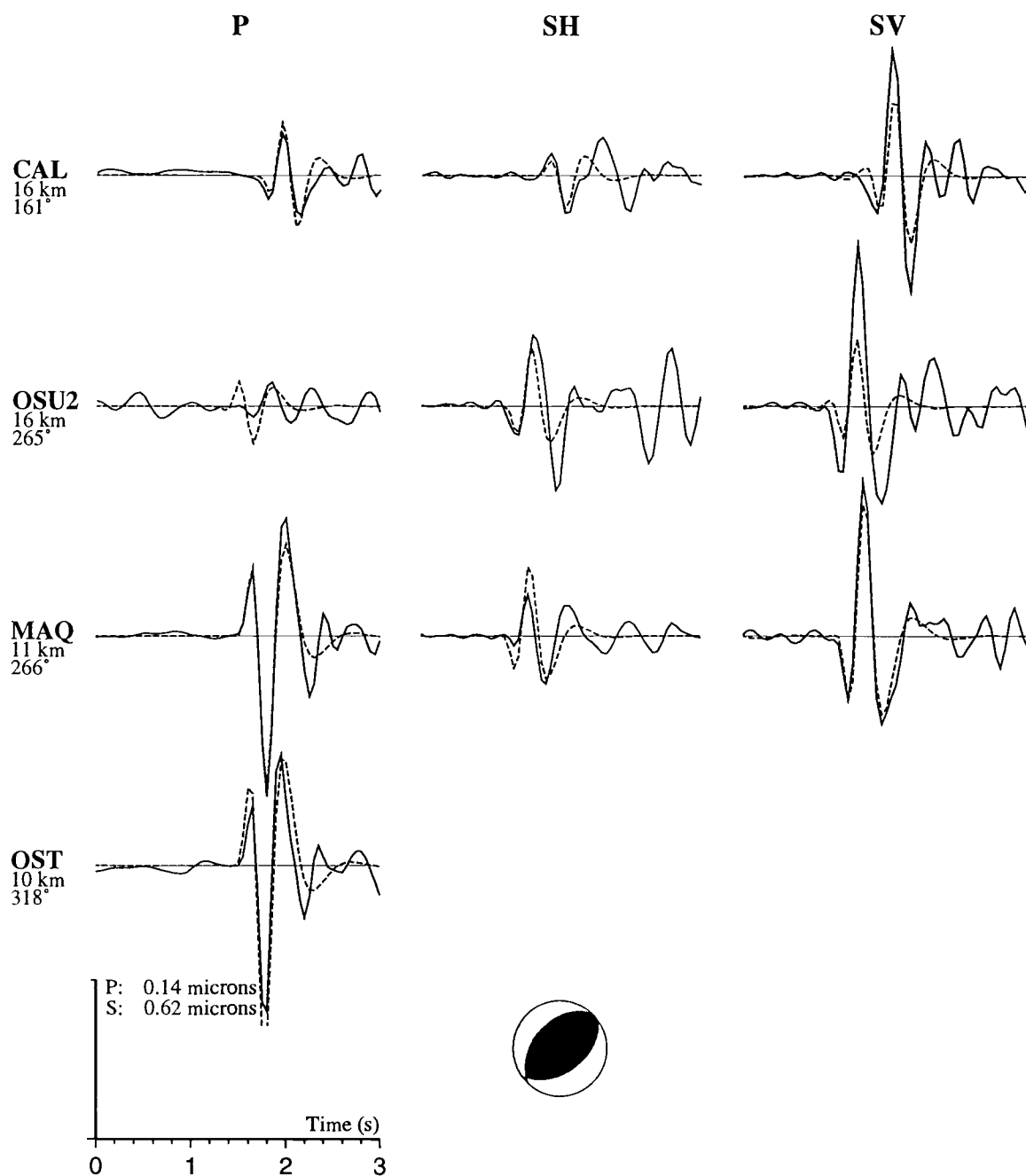


Figure A.26 Observed (solid lines) and synthetic (dashed lines) seismograms. First Column is station name, hypocentral distance, and event-station azimuth.

Event 27, 1.0 - 3.0 Hz 3 pole filter

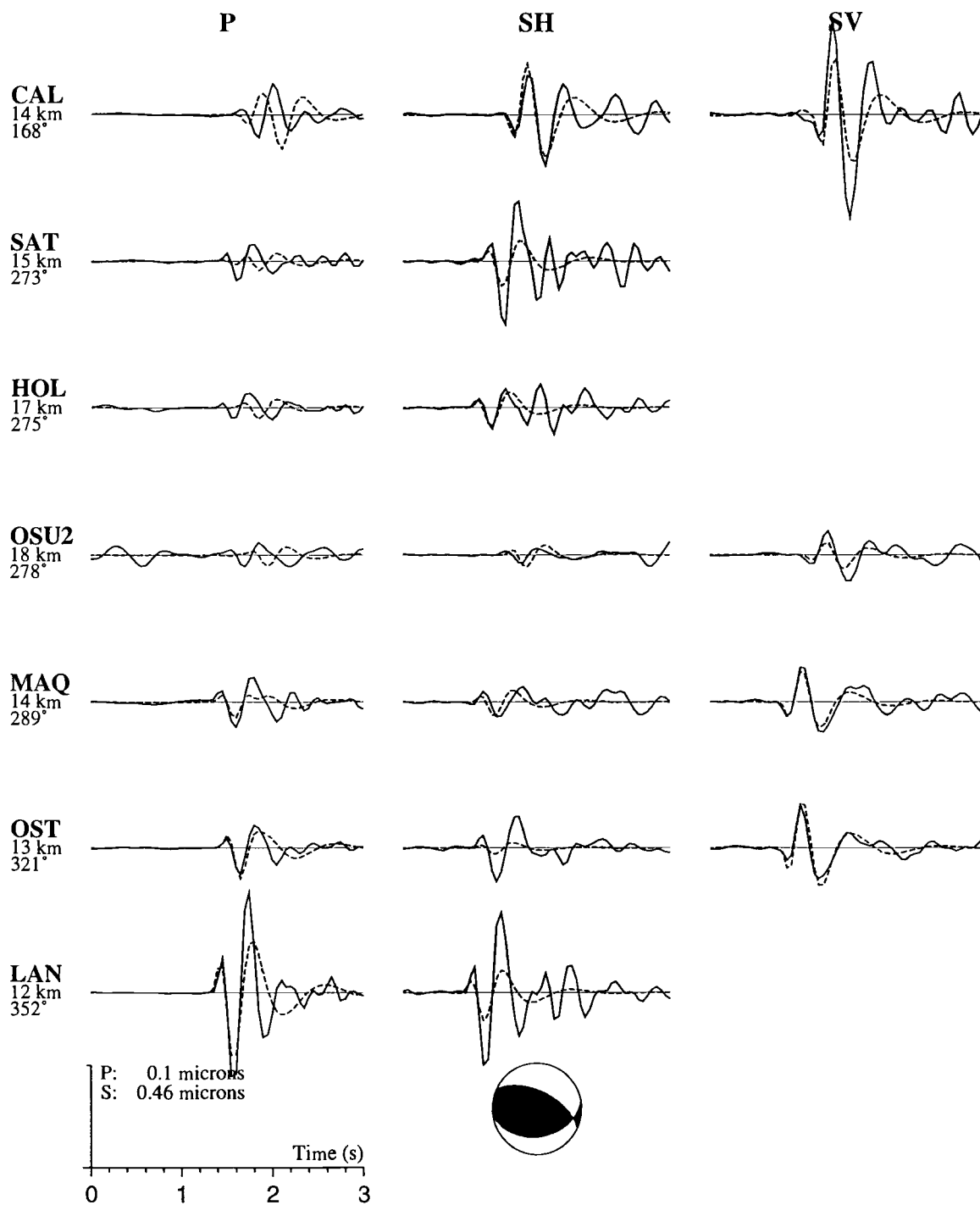


Figure A.27 Observed (solid lines) and synthetic (dashed lines) seismograms. First Column is station name, hypocentral distance, and event-station azimuth.

Event 28, 1.0 - 3.0 Hz 3 pole filter

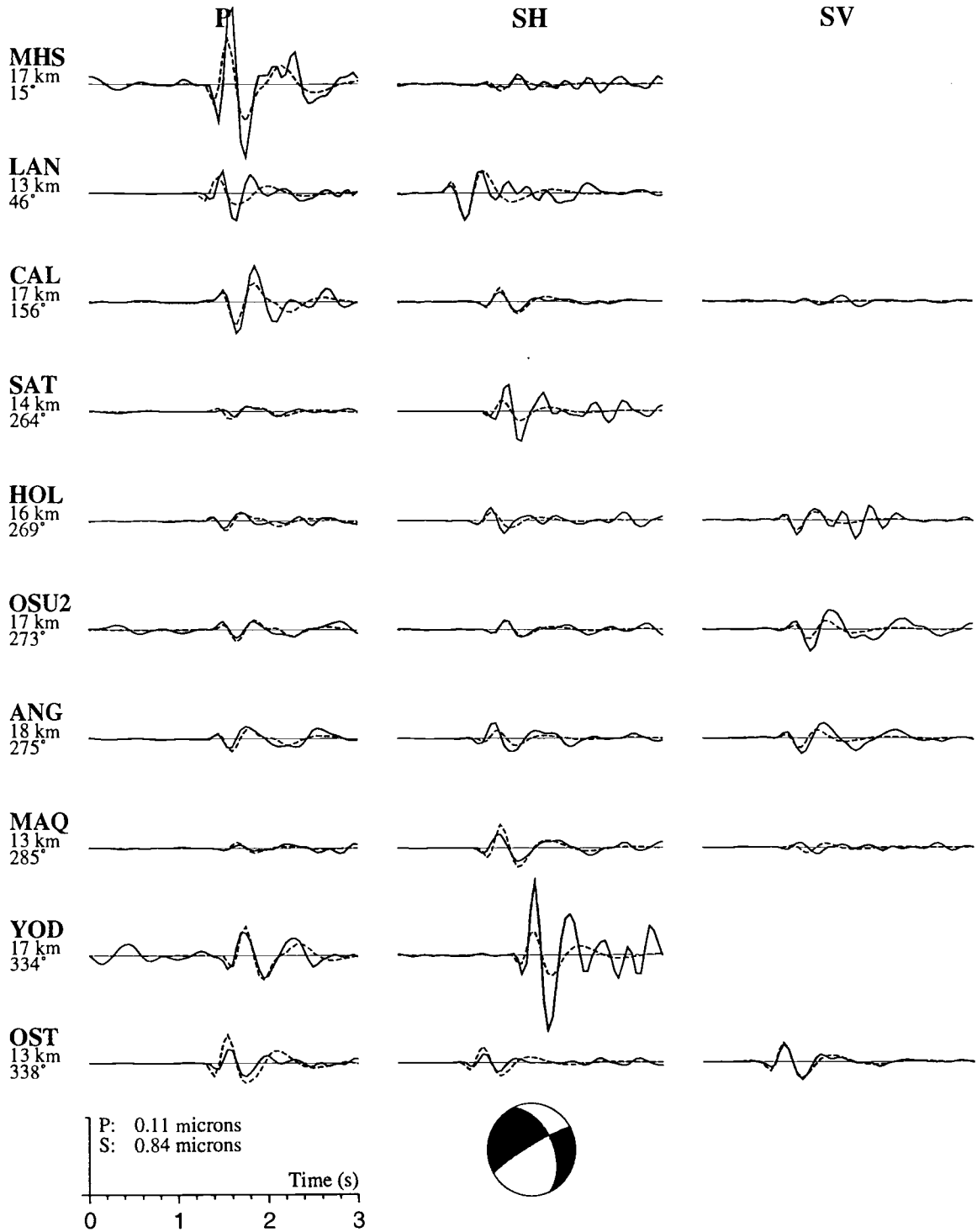


Figure A.28 Observed (solid lines) and synthetic (dashed lines) seismograms. First Column is station name, hypocentral distance, and event-station azimuth.

Event 29, 1.0 - 3.0 Hz 3 pole filter

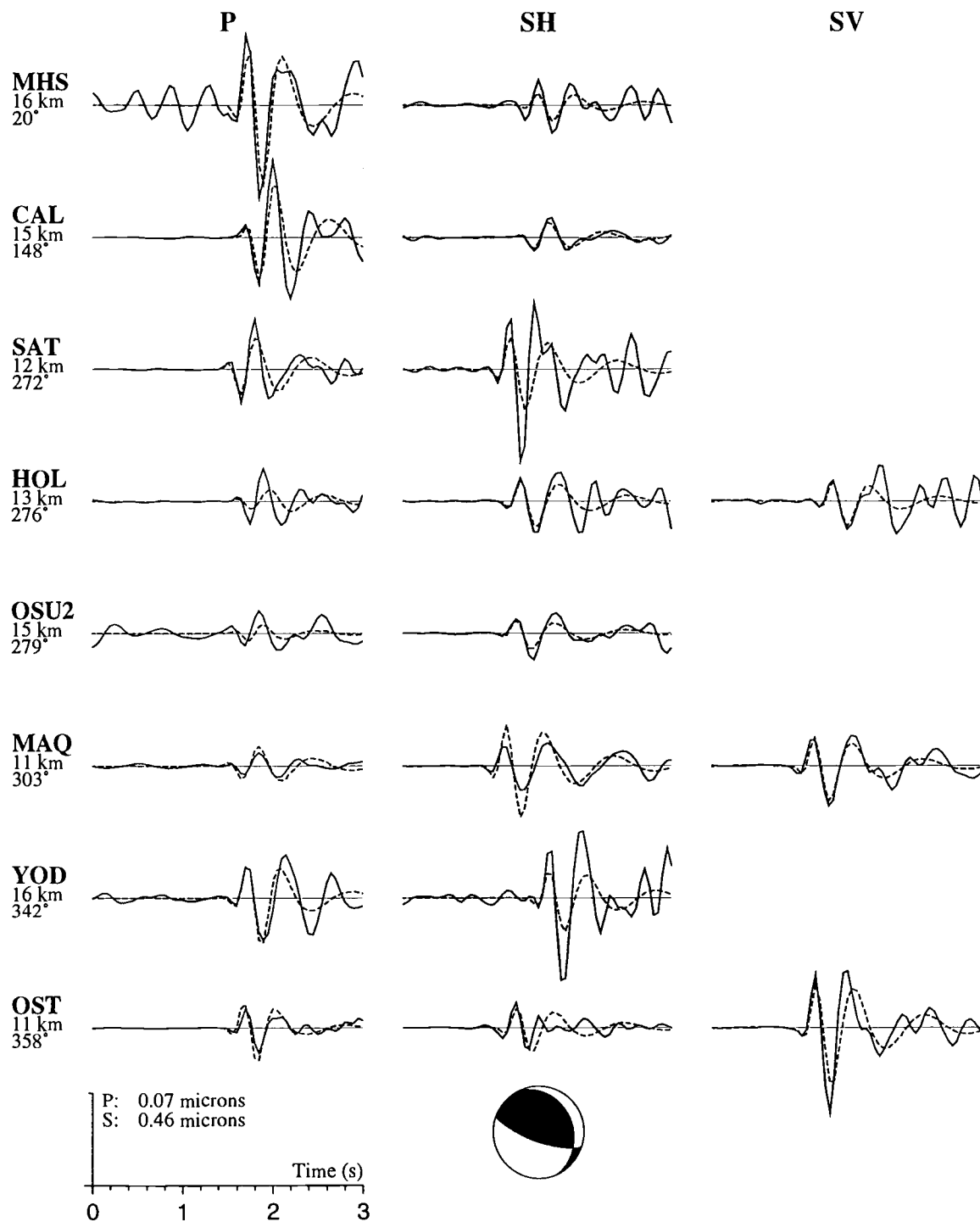


Figure A.29 Observed (solid lines) and synthetic (dashed lines) seismograms. First Column is station name, hypocentral distance, and event-station azimuth.

Event 30, 1.0 - 3.0 Hz 3 pole filter

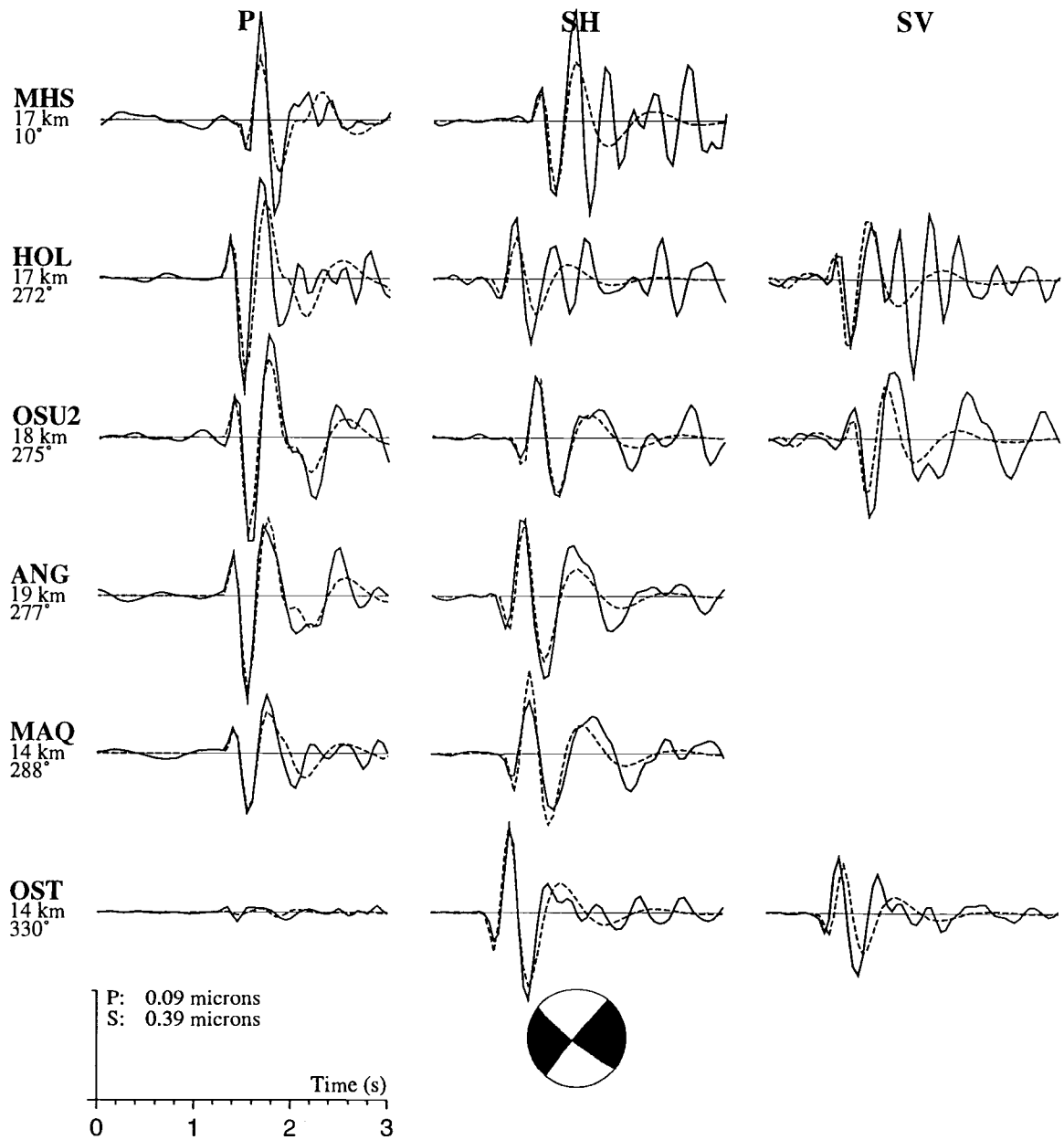


Figure A.30 Observed (solid lines) and synthetic (dashed lines) seismograms. First Column is station name, hypocentral distance, and event-station azimuth.

Event 31, 1.5 - 3.0 Hz 3 pole filter

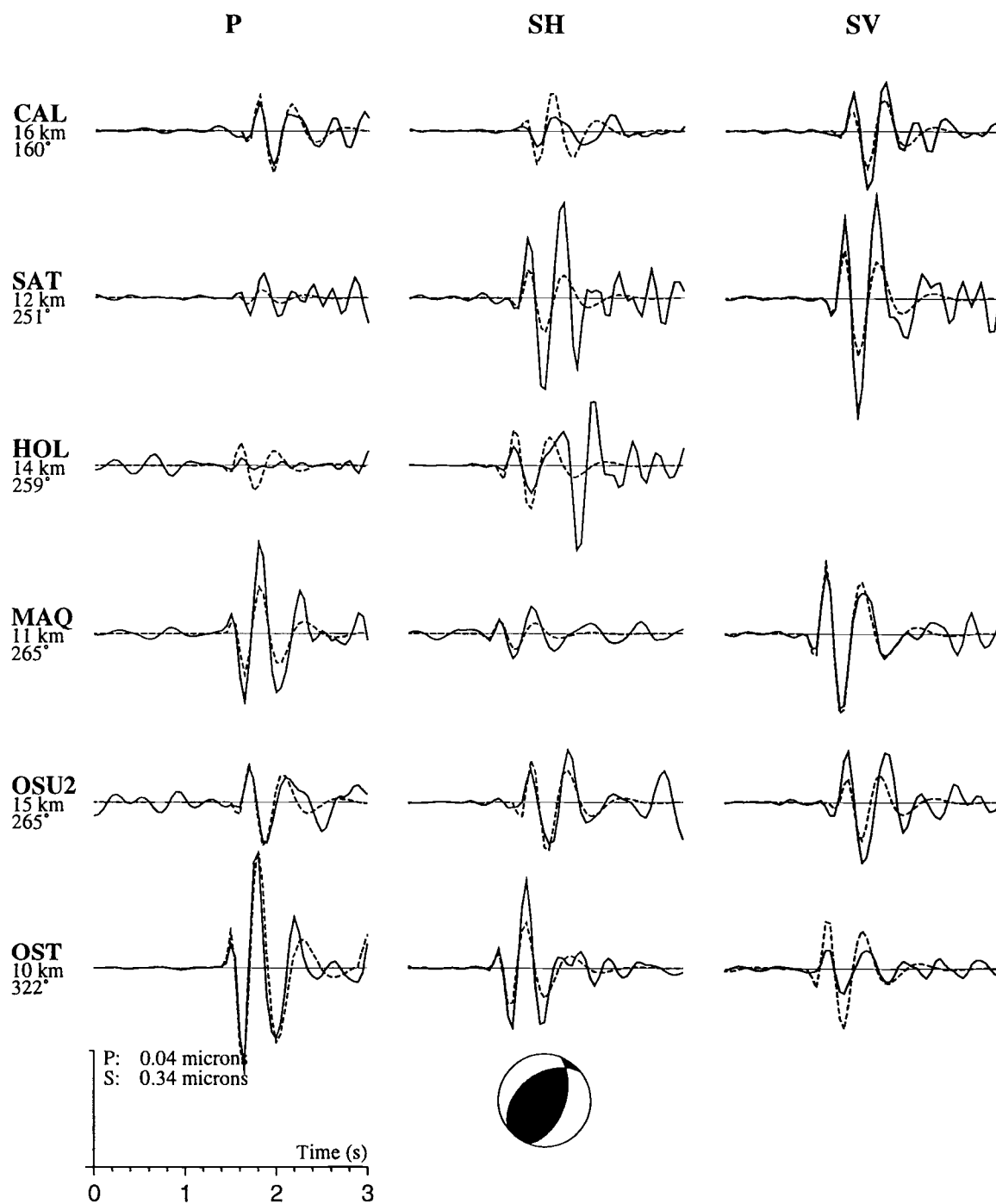


Figure A.31 Observed (solid lines) and synthetic (dashed lines) seismograms. First Column is station name, hypocentral distance, and event-station azimuth.

Event 32, 1.0 - 3.0 Hz 3 pole filter

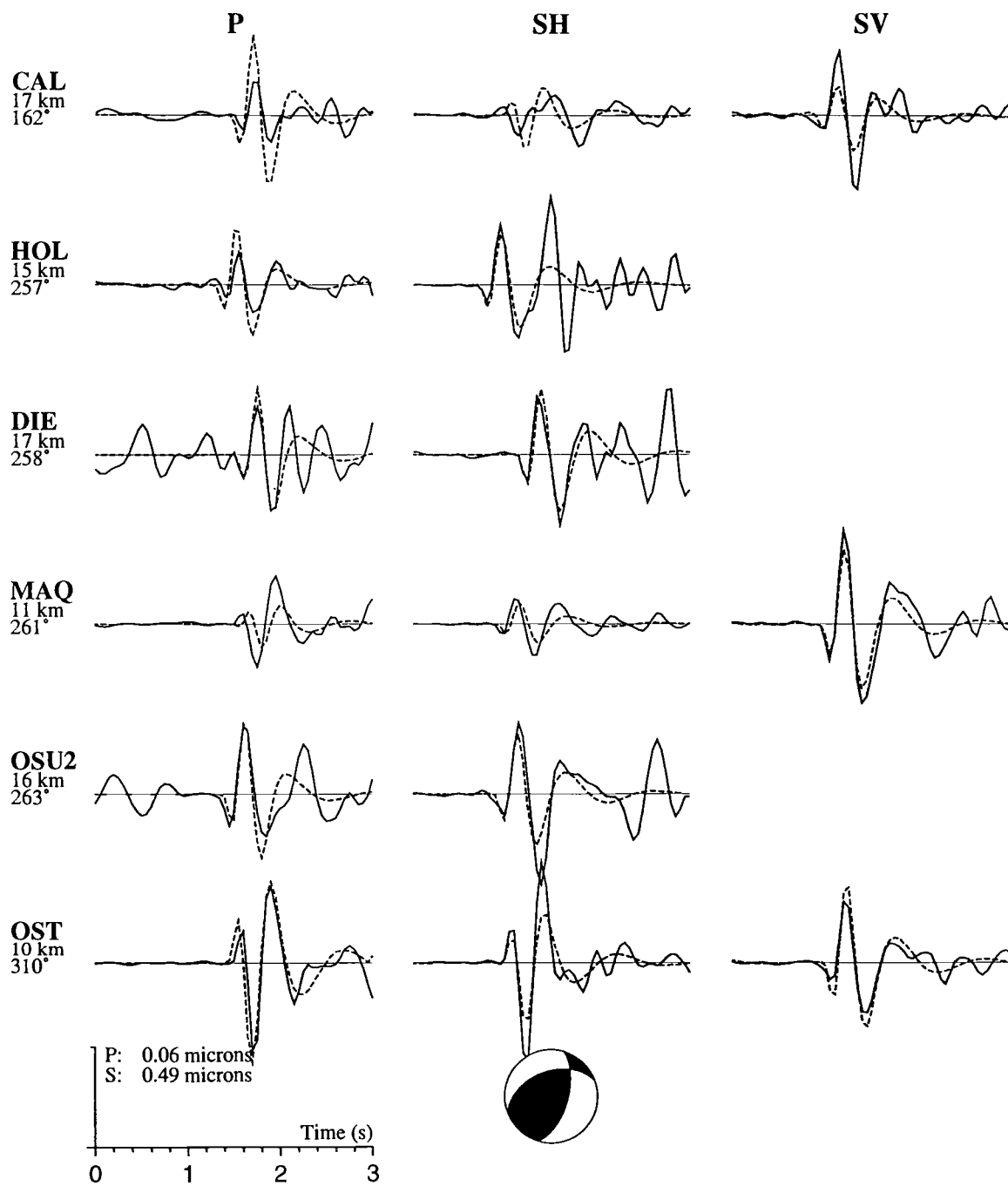


Figure A.32 Observed (solid lines) and synthetic (dashed lines) seismograms. First Column is station name, hypocentral distance, and event-station azimuth.

Event 33, 1.0 - 5.0 Hz 3 pole filter

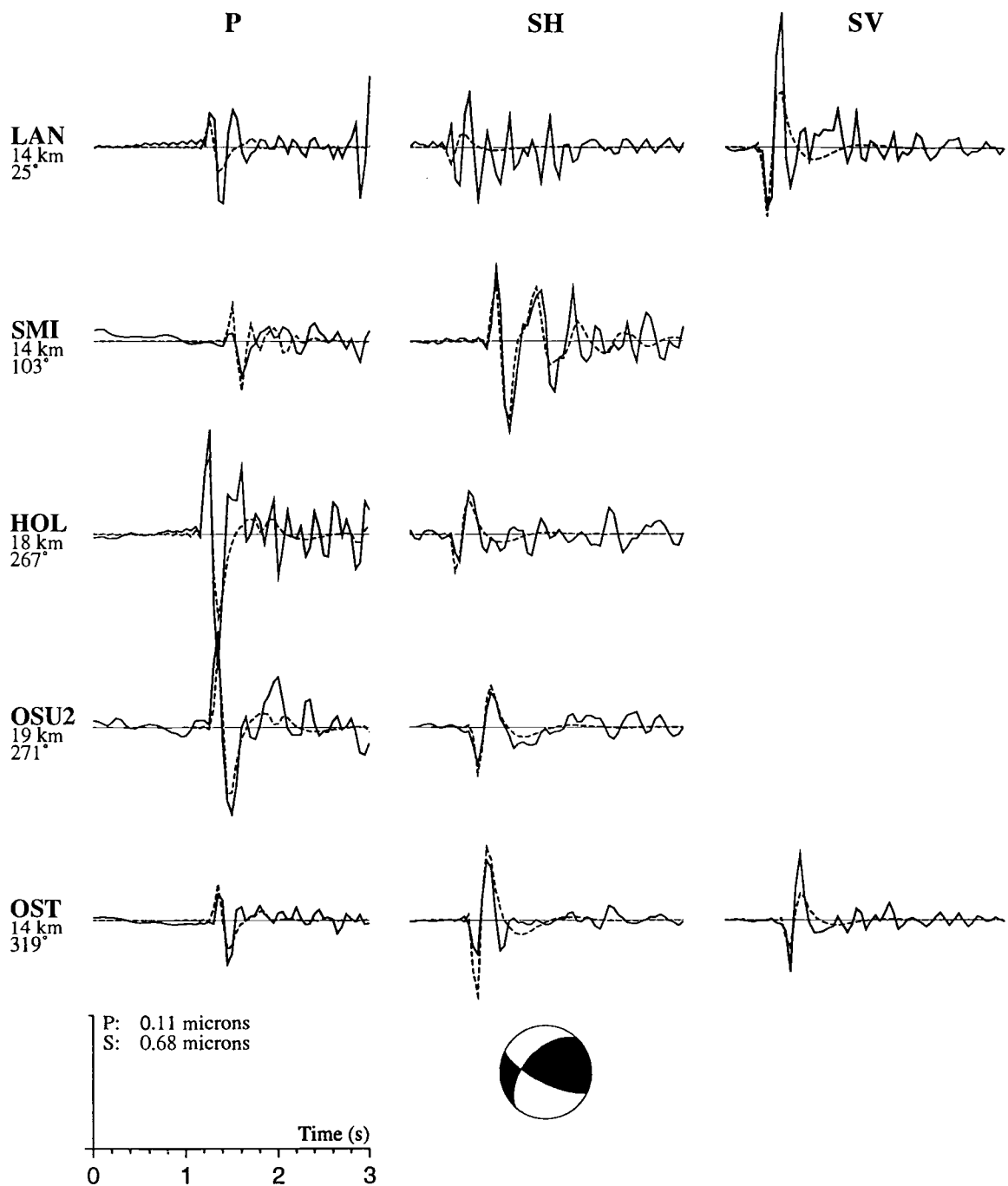


Figure A.33 Observed (solid lines) and synthetic (dashed lines) seismograms. First Column is station name, hypocentral distance, and event-station azimuth.

Event 34, 1.0 - 3.0 Hz 3 pole filter

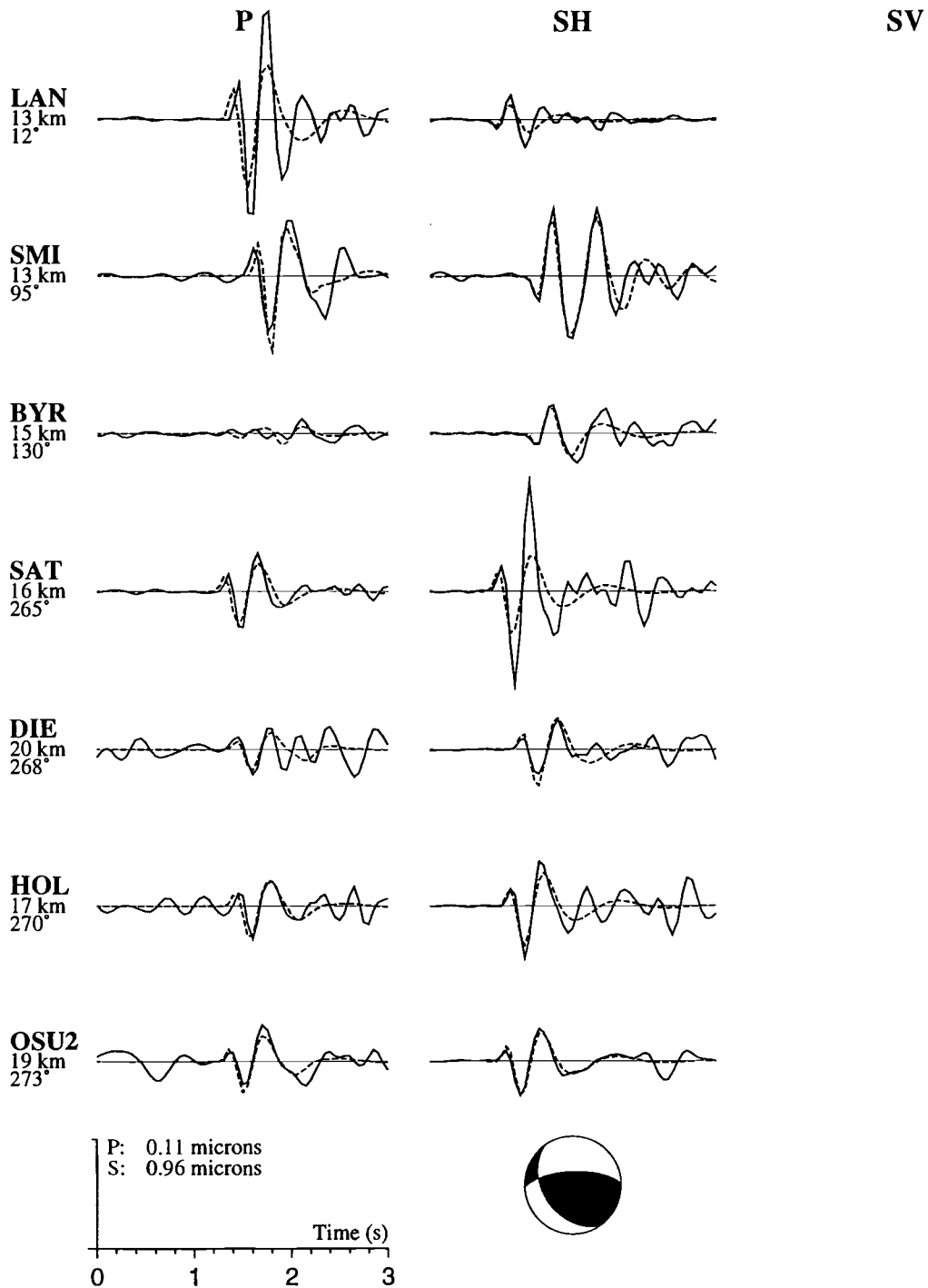


Figure A.34 Observed (solid lines) and synthetic (dashed lines) seismograms. First Column is station name, hypocentral distance, and event-station azimuth.

Event 35, 1.5 - 3.0 Hz 3 pole filter

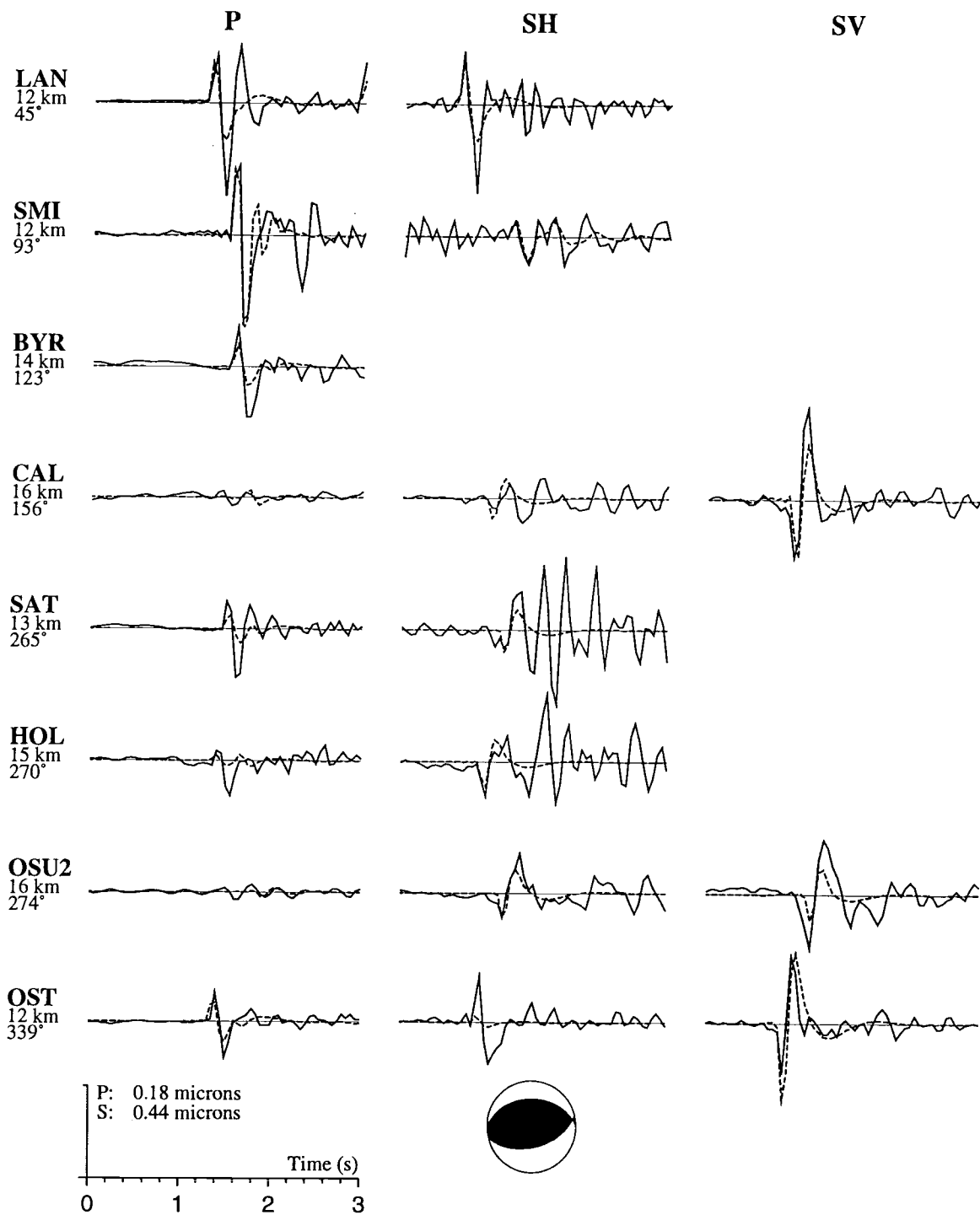


Figure A.35 Observed (solid lines) and synthetic (dashed lines) seismograms. First Column is station name, hypocentral distance, and event-station azimuth.

Event 36, 1.5 - 3.0 Hz 3 pole filter

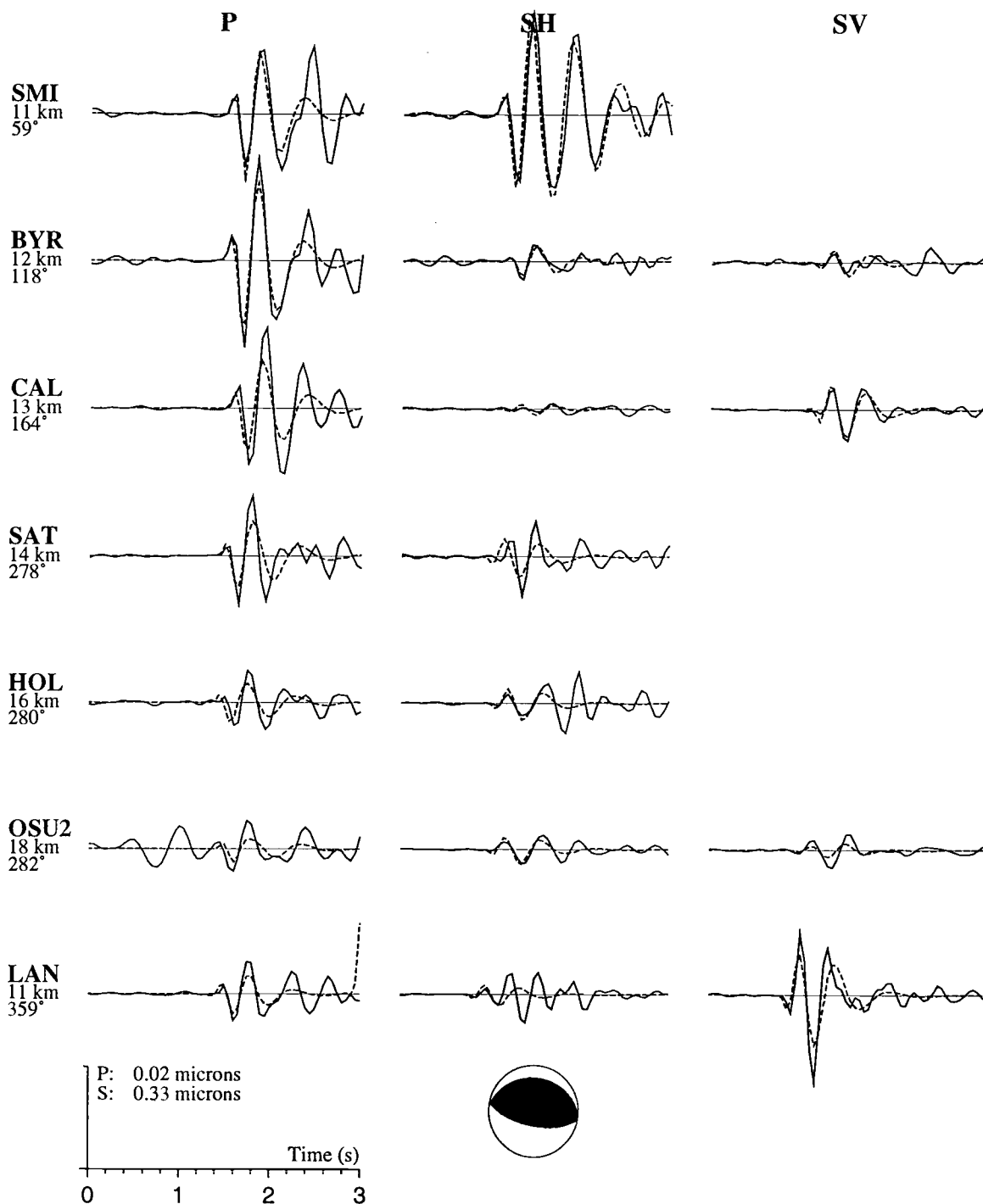


Figure A.36 Observed (solid lines) and synthetic (dashed lines) seismograms. First Column is station name, hypocentral distance, and event-station azimuth.

Event 37, 1.5 - 3.0 Hz 3 pole filter

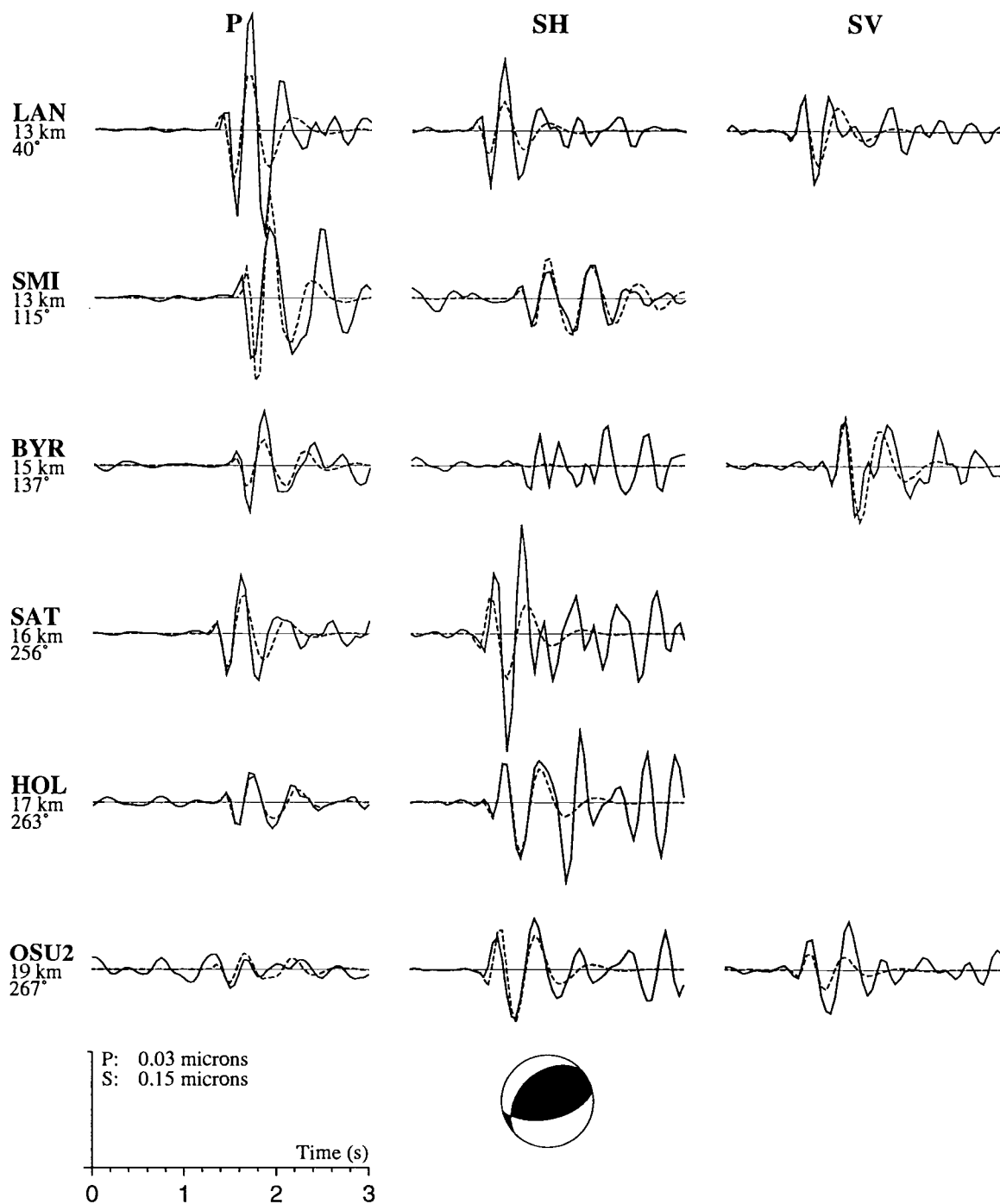


Figure A.37 Observed (solid lines) and synthetic (dashed lines) seismograms. First Column is station name, hypocentral distance, and event-station azimuth.

Event 38, 1.5 - 3.0 Hz 3 pole filter

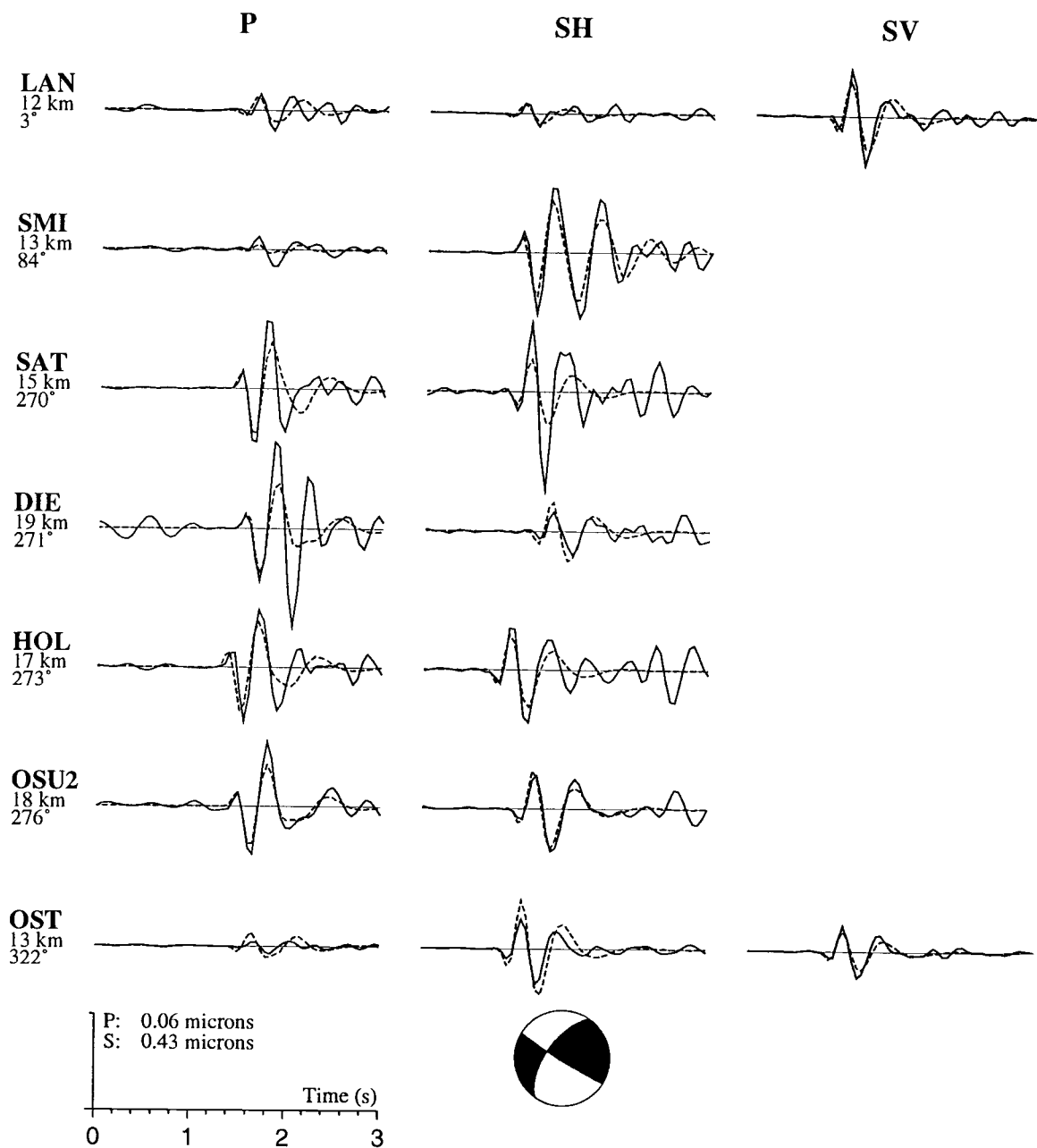


Figure A.38 Observed (solid lines) and synthetic (dashed lines) seismograms. First Column is station name, hypocentral distance, and event-station azimuth.

Event 39, 1.5 - 3.0 Hz 3 pole filter

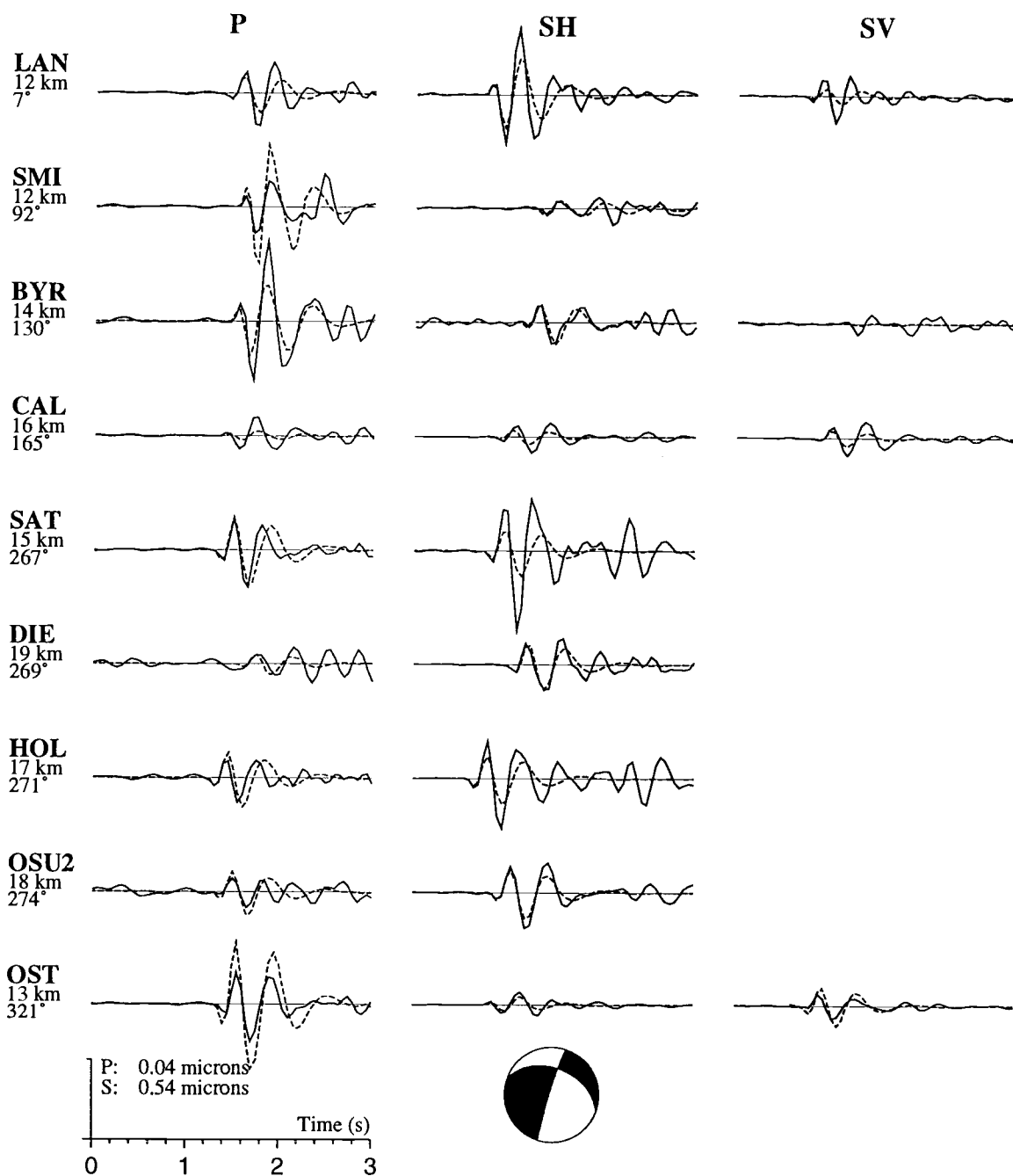


Figure A.39 Observed (solid lines) and synthetic (dashed lines) seismograms. First Column is station name, hypocentral distance, and event-station azimuth.

Event 40, 1.0 - 5.0 Hz 3 pole filter

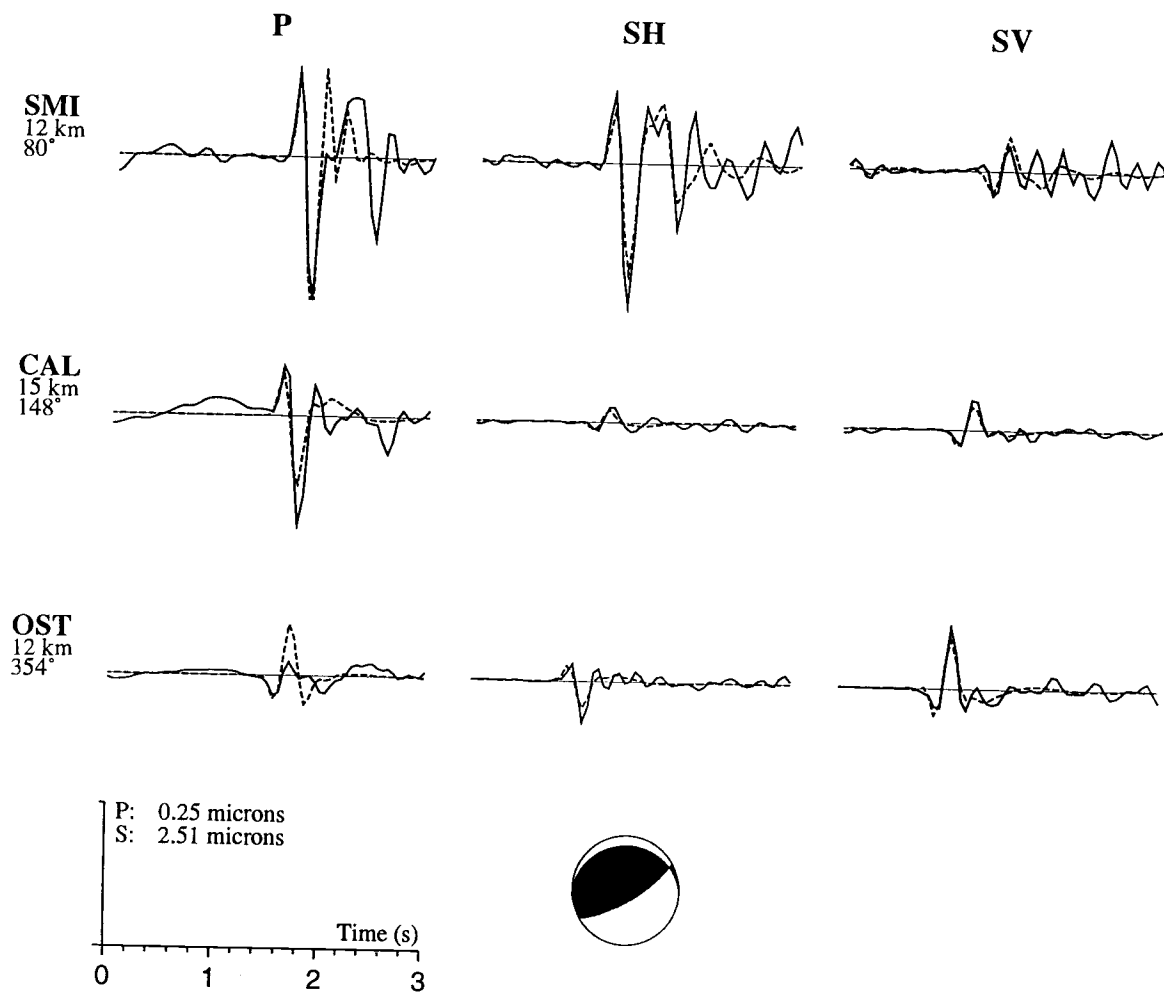


Figure A.40 Observed (solid lines) and synthetic (dashed lines) seismograms. First Column is station name, hypocentral distance, and event-station azimuth.

Event 41, 1.0 - 2.0 Hz 6 pole filter

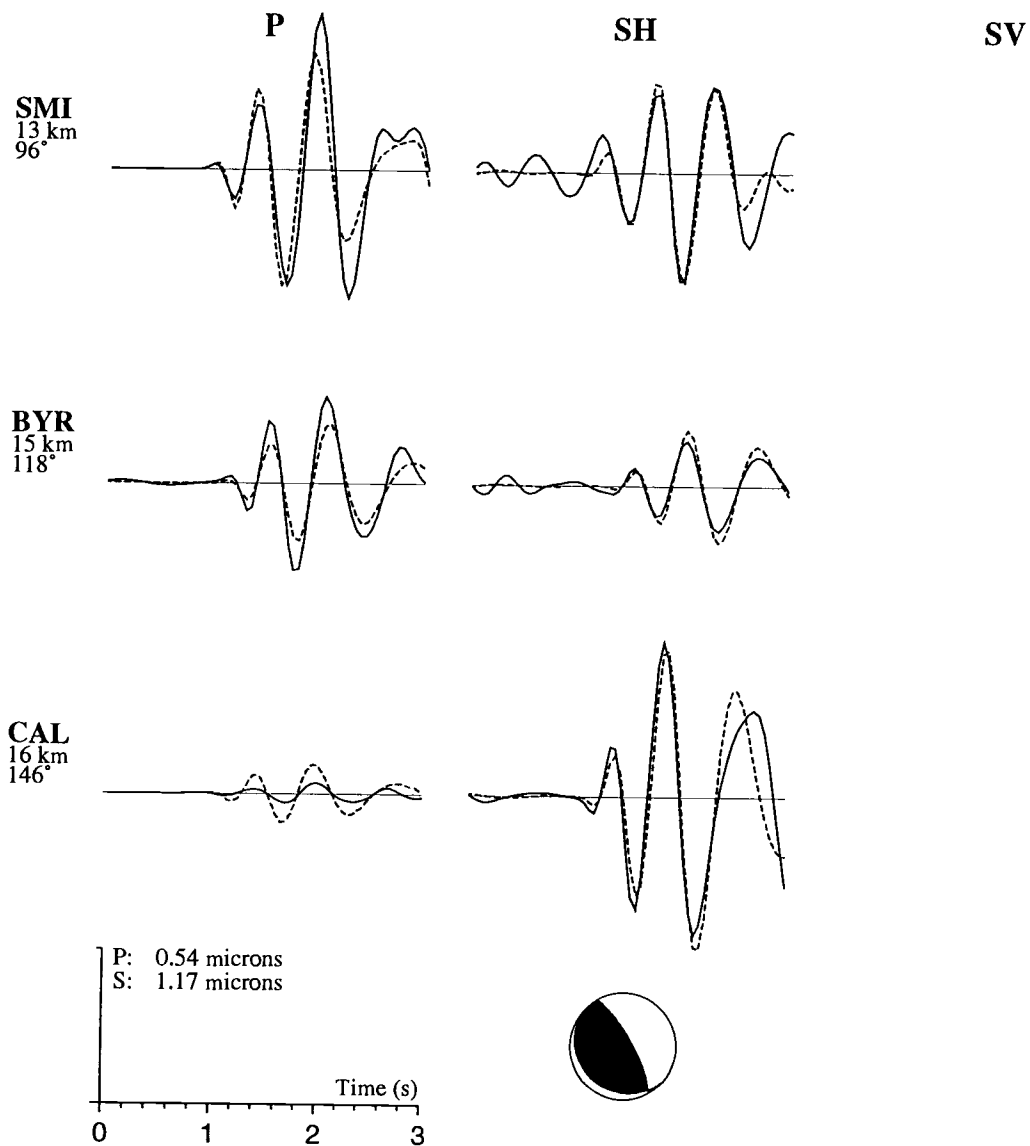


Figure A.41 Observed (solid lines) and synthetic (dashed lines) seismograms. First Column is station name, hypocentral distance, and event-station azimuth.

APPENDIX B

This appendix contains the code for the joint determination of hypocenter parameters and station corrections. It is written as a function file for the numeric computation software MATLAB[®]. This “language”, though not particular fast, is very well suited for matrix calculations. When taking advantage of several sparse matrix computations, each iteration, involving singular value decomposition of a 1931×221 data kernel, took few minutes on a SUN Sparc 10 workstation. And around five iterations were enough to converge to a solution. This makes it feasible for data sets of this scale. If there was no data point at a station for a particular event, the partial derivatives for this event in the data kernel were set to zero. There are two parameters conditioning convergence: *tol* is a threshold for the largest change in model parameters, and *Nit* is the maximum number of iterations. The code, bristling with comments, is hopefully self explanatory. Table B.1 describes the inputs to, and Table B.2 the outputs of the code. All inputs and outputs are MATLAB[®] vectors and matrices. They can be imported and exported as simple ASCII column files.

Table B.1 JHD Input data

Input	Description	Size
D	Matrix containing P and S arrival times for all events. If no data is available, value in D must be set to zero.	I×J
e	Matrix containing pick uncertainties.	I×J
m0	Matrix containing starting model: event locations (UTM) and origin times (seconds).	J×4
STALOC	Matrix containing station coordinates (UTM). P and S arrivals are treated as two independent stations with the same coordinates.	I×3
s0	Vector containing starting model for station corrections (seconds).	I×1
c0	V_p/V_s starting value.	scalar

I ... number of P and S arrivals. J ... number of events.

Table B.2 JHD Output data

Output	Description	Size
G	Data kernel containing the partial derivatives.	$I \cdot J + 4 \times 4 \cdot J + I + 1$
r	Matrix containing residuals.	$I \times J$
m	Matrix containing model parameters after inversion: x, y, z in UTM coordinates and origin times in seconds.	$J \times 4$
s	Vector containing station corrections (seconds).	$I \times 1$
c	V_p/V_s ratio after inversion.	scalar
Sd	Vector containing singular values ordered by size.	$4 \cdot J + I + 1 \times 1$
R	Resolution matrix.	$4 \cdot J + I + 1 \times 4 \cdot J + I + 1$
RMS	Matrix containing RMS residuals for each event after each iteration.	$J \times Nit + 1$
RMScum	Vector containing RMS residuals for all events at each iteration.	$1 \times Nit + 1$

I ... number of *P* and *S* arrivals. J ... number of events. Nit ... number of iterations.

Listing B.1

```
function [G,r,dm,m,s,c,Sd,R,RMS,RMScum]=jhd(D,m0,s,c,e,STALOC)

% This routine performs a joint hypocenter inversion. Input is data
% matrix D, a IxJ matrix of arrival times, with I = number of stations
% and J = number of events, e, IxJ matrix of pick uncertainties, m0, a
% Jx4 matrix containing the starting model for event locations and
% origin times, STALOC, a Ix3 matrix of station locations, s, a vector
% containing the starting model for the station corrections, and c,
% starting value for Vs/Vp ratio.

%=====
% PARAMETER SETTINGS

% p velocity of half space
vp = 5.5;
% s velocity of half space
vs = c * vp;

% J ... number of earthquakes
J=41;
% I ... number of arrival times of jth earthquake = # of stations,
% I=Is+Ip
% Is ... # of S arrivals, Ip # of P arrivals

Ip=25;
```

```

Is=22;
I=Is+Ip;

% Nit ... max. number of iterations
Nit=10;
% convergence criteria; if largest change in model parameter falls
% below tol, inversion stops
tol = 0.001;

%=====

% Initializing matrices and parameters
m=m0;
s=s0;
c=c0;
dm = eye(1, J*4+I+1);
it = 0;
dist=zeros(I,J);
tt=zeros(I,J);
r=zeros(I,J);
G = zeros(I*J+4,J*4+I+1);

%=====

% Iteration starts
while it < Nit & max(abs(dm)) > tol

it = it + 1;
ssump = sum(s(1:Ip));
ssums = sum(s(Ip+1:I));
nm(:,1:3)=m(:,1:3);

% Calculate travel time for model

for j = 1:J

    for i = 1:Ip
        dist(i,j)=norm( STALOC(i,1:3) - nm(j,1:3) );
        tt(j,i) = 1/vp * dist(i,j);
        % rows are tt's for jth earthquake
    end

    for i = Ip+1:I
        dist(i,j)=norm( STALOC(i,1:3) - nm(j,1:3) );
        tt(j,i) = 1/(c*vp) * dist(i,j);
        % rows are tt's for jth earthquake
    end

end

% Calculate Residuals r = D - t0 - Tmodel - s
for j = 1:J
    t0(j)=m(j,4);
    for i=1:I
        if D(i,j) == 0;
            r(i,j) = 0;
        else
            r(i,j) = D(i,j) - t0(j) - tt(j,i) - s(i);
        end
    end
end
end

```

```

%RMS residual for jth earthquake
  nrz(j) = nnz(r(:,j));
  RMS(it,j) = sqrt(sum(r(:,j).^2)/nrz(j));
end

%RMS residual for all earthquakes
RMScum(it) = sqrt(sum(sum(r.^2))/nnz(r));

% Calculate data kernel from partial derivatives
%=====

% partial derivatives for locations and origin times
% J ... number of earthquakes

for j=1:J

  for i = 1:Ip
% partial derivatives of hypocenter location

% P arrivals:
    for l=1:3
      if D(i,j) == 0;
        G(i+(j-1)*I,l+(j-1)*4) = 0;
      else
        G(i+(j-1)*I,l+(j-1)*4) = -1*(STALOC(i,l)-nm(j,l))/ ...
          (vp^2 * tt(j,i));
      end
    end
  end

% S arrivals:
  for i=Ip+1:I
    for l=1:3
      if D(i,j) == 0;
        G(i+(j-1)*I,l+(j-1)*4) = 0;
      else
        G(i+(j-1)*I,l+(j-1)*4) = -1*(STALOC(i,l)-nm(j,l))/ ...
          ((c*vp)^2 * tt(j,i));
      end
    end
  end

% partial derivatives for poisson ratio, 0 for p arrivals
  if D(i,j) == 0;
    G(i+(j-1)*I,4*J+1) = 0;
  else
    G(i+(j-1)*I,4*J+1) = -(tt(j,i))/(c);
  end
end

  for i = 1:I
% partial derivatives for origin time
    if D(i,j) == 0;
      G(i+(j-1)*I,4+(j-1)*4) = 0;
    else
      G(i+(j-1)*I,4+(j-1)*4) = 1;
    end
  end

% partial derivatives for station correction =1 for station used, 0
% otherwise i.e. diagonal matrix

```

```

    if D(i,j) == 0;
        G(i+(j-1)*I,4*J+1+i) = 0;
    else
        G(i+(j-1)*I,4*J+1+i) = 1;
    end

% constraint equations sum(sp) = 0 and sum(ss) = 0
    lam =1;
    G(J*I+1,4*J+2:4*J+1+Ip) = lam*ones(1,Ip);
    G(J*I+2,4*J+2+Ip:4*J+1+I) = lam*ones(1,Is);
% soft constraint for WA1 and WB1 to be similar
    G(J*I+3,4*J+1+21) = 1;
    G(J*I+3,4*J+1+22) = -1;
    G(J*I+4,4*J+1+44) = 1;
    G(J*I+4,4*J+1+45) = -1;

    end
end

% Inversion
%=====

n=I*J+4;
% get variance matrix from pick uncertainties
er=e(:);
er(I*J+1) = 1;
er(I*J+2) = 1;
er(I*J+3) = 1;
er(I*J+4) = 1;
sigma=spdiags(er,0,n,n);

d = r(:);
d(J*I+1) = -ssump;
d(J*I+2) = -ssums;
d(J*I+3) = 0;
d(J*I+4) = 0;

% distance dependent weights
w=zeros(1,I*J+4);
for j=1:J
    for i=1:I

% dwgt ... distance in km from which data get down weighted
        dwgt=75;
        if dist(i,j) < dwgt
            w(i+(j-1)*I) = 1;
        else
            w(i+(j-1)*I) = (1+dist(i,j)/dwgt)^(-1);
        end

% these weights determine the hardness of the constraints
        w(I*J+1) = 200;
        w(I*J+2) = 200;
        w(I*J+3) = 30;
        w(I*J+4) = 30;
    end
end

dw=spdiags(w',0,n,n);
W=inv(sigma)*dw;

```

```

de = W*d;
Ge = W*G;
d = de;
G = Ge;

% Singular Value Decomposition
[U,S,V] = svd(G,0);

% p ... number of model parameters = 4xJ + I + 1, or smaller if
% singular values are truncated
p=4*J+I+1;
% Define damping constant
damp=10*eye(212);
S = S + damp;
Sd=diag(S);
Sp=spdiags(Sd(1:p),0,p,p);
Up=U(:,1:p);
Vp=V(:,1:p);
% resolution matrix
R=Vp*Vp';

% dm ... change in model parameter
dm = Vp * inv(Sp) * Up' * d ;

% dm contains 4xJ hypocenter and origin time perturbations, perturbation
% for Vs/Vp ratio, and I station correction perturbations
%=====

% Calculate new model
for j=1:J
    for l=1:3
        m(j,l) = (nm(j,l) + dm(1+(j-1)*4));
    end
    m(j,4) = t0(j) + dm(4+(j-1)*4);
end
c=c+dm(4*J+1);
for i=1:I
    s(i)=s(i)+dm(4*J+1+i);
end

% End of iteration loop
end

%=====

% Calculate RMS residual for last model parameters
for j = 1:J
    for i = 1:Ip
        nm(j,1:3) = m(j,1:3);
        dist(i,j)=norm( STALOC(i,1:3) - nm(j,1:3) );
        tt(j,i) = 1/vp * dist(i,j);
    end

    for i = Ip+1:I
        nm(j,1:3) = m(j,1:3);
        dist(i,j)=norm( STALOC(i,1:3) - nm(j,1:3) );
        tt(j,i) = 1/(c*vp) * dist(i,j);
    end
end

for j = 1:J

```



```
% Calculate Residuals  $r = D - t_0 - T_{\text{model}} - s$ 
t0(j)=m(j,4);
for i=1:I
    if D(i,j) == 0;
        r(i,j) = 0;
    else
        r(i,j) = D(i,j) - t0(j) - tt(j,i) - s(i);
    end
end

% RMS residual for jth earthquake
nrz(j) = nnz(r(:,j));
RMS(it+1,j) = sqrt(sum(r(:,j).^2)/nrz(j));
end
RMScum(it+1) = sqrt(sum(sum(r.^2))/nnz(r));
```